Title	Analysis and Implementation of Mixed-Mode Cohesive Zone Formulations for Cardiovascular Biomechanics Applications
Author(s)	Ó Máirtín, Éamonn
Publication Date	2013-02-18
Item record	http://hdl.handle.net/10379/3403

Analysis and Implementation of Mixed-Mode Cohesive Zone Formulations for Cardiovascular Biomechanics Applications

by

Éamonn Ó Máirtín, B.E. (2008)

**A thesis submitted to the National University of Ireland as fulfilment
of the requirements for the Degree of Doctor of Philosophy.**

**Mechanical and Biomedical Engineering,
College of Engineering and Informatics,
National University of Ireland, Galway.**

October 2012

Supervisor of Research: Dr. J. P. McGarry

Acknowledgements

Abstract

A comprehensive theoretical analysis of potential-based and non-potential-based cohesive zone models (CZMs) under mixed-mode conditions is presented. Using the well established Xu-Needleman (XN) CZM, it is demonstrated that unphysical repulsive normal tractions occur for potential-based CZMs under mixed-mode conditions when the mode II work of separation is greater than mode I work of separation. A modified form of the XN potential function (McGarry et al., 2012) is shown to significantly reduce the range of interface separations for which repulsive normal tractions occur. Normal-tangential coupling is then analysed for non-potential-based CZMs, demonstrating that correct penalisation of mixed-mode over-closure is not trivially achieved when a compression occurs at the interface. Two non-potential-based CZMs (McGarry et al., 2012) are shown to correctly penalise mixed-mode over-closure, in contrast to the non-potential CZM of van den Bosch et al. (2006). Finally, it is demonstrated that normal-tangential coupling must be based on the magnitude of interface separation in order to achieve fully mode-independent work of separation.

CZMs are then used to simulate mixed-mode interface behaviour in three applied studies relating to the field of cardiovascular biomechanics: (i) In the first applied study, the traction distribution along a stent-coating interface is investigated in order to develop an enhanced understanding of the mechanisms of stent-coating debonding. Specifically, the influence of material and geometrical parameters on stent-coating interface tractions is analysed and conditions leading to mode I, mode II and mixed-mode coating delamination are uncovered; (ii) In the second applied study, interlayer dissection in an inhomogeneous abdominal aortic aneurysm (AAA) wall is simulated. Three patient-specific AAA geometries are reconstructed. Dissection is found to be primarily mode II in nature, accompanied by interface compression. The location and extent of interlayer dissection is found to be highly dependent on AAA geometry. Most importantly, predicted dissection locations are found to differ from locations of peak von Mises stress in the AAA wall; (iii) In the third applied study, mixed-mode debonding and rebonding of an endothelial cell from a silicone substrate is simulated. Cytoskeletal remodelling is found to be highly influenced by the form of the CZM used to describe the cell-substrate interface. The XN potential function leads to the computation of physically unrealistic repulsive normal tractions which prevent cell rebonding to the substrate. In contrast, such unphysical behaviour is not predicted when the modified potential function of McGarry et al. (2012) is used, and predicted cytoskeletal remodelling is found to correlate closely with published experimental data.

Table of Contents

Nomenclature	
CZM	Cohesive Zone Model
XN model	Xu and Needleman model
MP model	Modified Potential model
VB model	van den Bosch model
NP model	Non-Potential-Based model
SMC model	Separation Magnitude Coupling model
σ_A	Stress at a crack tip
a	Major axis crack length
b	Minor axis crack length
B	Plate thickness
k_t	Stress concentration factor
ρ	Radius of curvature of a crack
x_0	Distance between the nuclei of two adjoining atoms
K_I	Stress intensity factor
K_{I_C}	Critical stress intensity
$\mathcal{G}$	Energy release rate
$\mathcal{G}_c$	Critical energy release rate
P	Potential energy
$\mathcal{A}$	Crack area
E	Young's modulus
σ^f	Failure stress
a^c	Critical crack length
Ξ	Total energy
W_s	Work required to create new surfaces
P_o	Potential energy of an uncracked plate
γ_s	Material surface energy
γ_p	Plastic work per unit area
σ_{YS}	Uniaxial yield strength of the material
γ_L	Plastic zone length
u_y	Displacement behind effective crack tip

$\emptyset$	Work of separation at the interface
q	$\emptyset_t/\emptyset_n$
r	Traction free normal separation following complete shear separation
$\underline{\Delta}$	Interface separation vector
δ	Interface characteristic length
T	Interface traction
σ_{max}	Maximum normal traction without tangential separation
τ_{max}	Maximum tangential traction without normal separation
Σ_a	Non-dimensional arch deformation
$\varepsilon_{circumf}$	Circumferential strain
AAA	Abdominal Aortic Aneurysm
ILT	Intraluminal thrombus

1 Introduction

1.1 Rationale and Objective

Cohesive zone models (CZMs) are constitutive laws containing a description of normal and tangential interface behaviour. Typically, interface tractions are defined in terms of interface separation. CZMs have been used to predict interface failure for a wide range of applications including crack propagation in porous materials, ductile materials and coating failure evaluation in diamond-coated tools (Nakamura and Wang, 2001; Li and Chandra, 2003; Hu et al., 2008). Following on from the pioneering work of Barenblatt (1959) and Dugdale (1960), numerous types of CZMs have been proposed in the literature including bilinear, trapezoidal, piece-wise linear and exponential forms of CZM. An exponential form of CZM is shown in Figure 1-1.
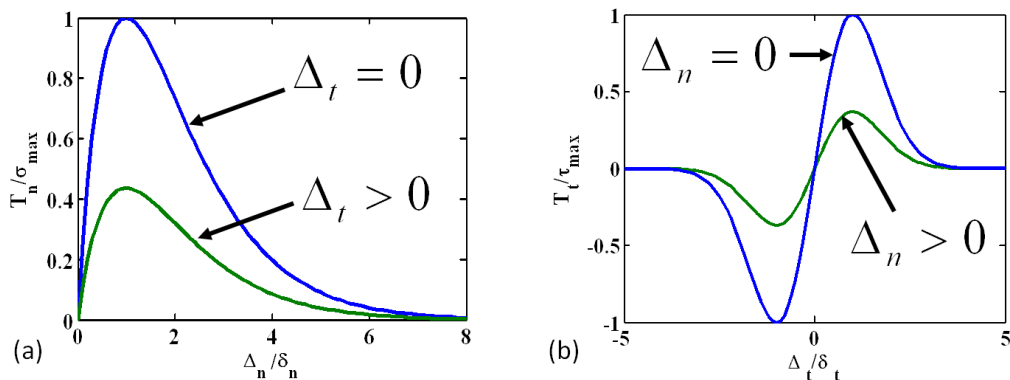
Figure 1-1: Coupled exponential form of cohesive zone model. (a) Normalised normal traction (T_n/σ_{max}) as a function of normalised normal separation (Δ_n/δ_n). The magnitude of normal traction reduces following tangential (mode II) separation $(\Delta_t > 0)$ (b) Normalised tangential traction (T_t/τ_{max}) as a function of normalised tangential separation (Δ_t/δ_t). The magnitude of tangential traction reduces following normal (mode I) separation $(\Delta_n > 0)$.

CZMs can be coupled or uncoupled. In an uncoupled cohesive zone law, the normal traction is independent of the tangential component of the separation vector and vice versa. However, uncoupled CZMs are limited to specific cases where interface failure is constrained to occur in a single predefined direction - either mode I separation (pure normal separation with no tangential separation) or mode II separation. In the context of cardiovascular biomechanics, however, failure mechanisms are often complex as a result of complex loading distributions

(e.g. coating debonding from a stent surface during deployment, arterial fracture) requiring the use of coupled mixed-mode CZM formulations, whereby all components of the interface traction vector depend on both the normal and tangential interface separation components. In a coupled CZM, a physically realistic coupling requires that normal interface separation reduces the resistance to tangential separation and vice versa, as shown in Figure 1-1.

CZMs can be broadly categorised into **potential-based** and **non-potential-based** formulations. In a potential-based model, interface tractions are derived from an interface potential function where the work performed during interface separation is path-independent. In the case of non-potential-based models, integration of the specified traction-separation relationships does not result in a unified potential function and the work performed during interface separation is path-dependent. Previous analyses have not fully uncovered a range of non-physical artefacts associated with potential-based formulations under conditions of mixed-mode separation and compression. In this work, a thorough assessment of the frequently adopted potential of Xu and Needleman (1993) is performed. Additionally, it is shown that physically realistic interface behaviour is not trivially achieved for non-potential-based formulations.

The **main objectives** of this thesis are: (i) to perform a thorough analysis of potential-based and non-potential-based cohesive zone formulations in mixed-mode interface over-closure (compression) and separation, and (ii) to predict mixed-mode failure in cardiovascular applications using cohesive zone modelling. Following from the two main objectives listed above, the work presented in this thesis can broadly be divided into two main categories:

- **Analysis:** A theoretical (Chapter 3) and computational (Chapter 4) assessment of two existing CZMs and four novel CZMs, proposed by McGarry et al. (2012), under mixed-mode conditions is presented.
- **Application** of CZMs in order to predict mixed-mode interface behaviour for three cardiovascular applications, namely: a cardiovascular device

(coated stent); a cardiovascular tissue (aortic aneurysm); and a cardiovascular cell phenotype (endothelial cell).

An outline of the format of this thesis, ranging from theoretical analysis of mixed-mode cohesive zone behaviour to finite element implementation for cardiovascular biomechanics applications, is provided below in Figure 1-2.
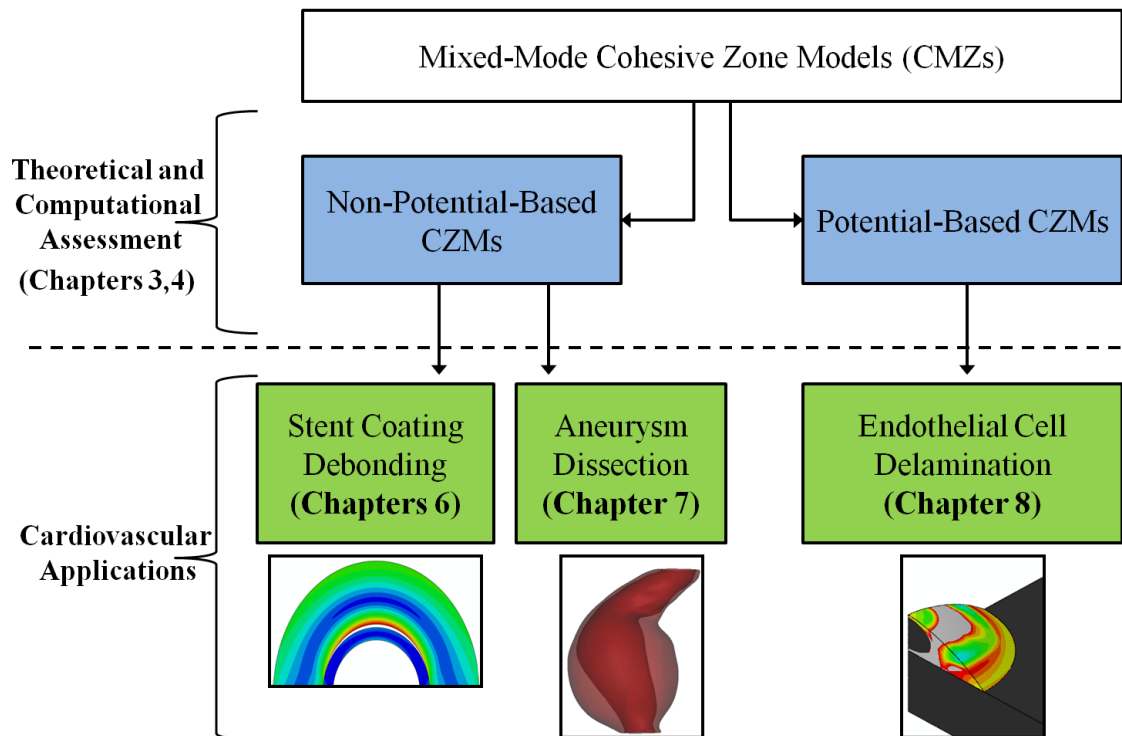
Figure 1-2: Outline of the work performed in this thesis from initial theoretical analysis to the application of cohesive zone formulations to predict mixed-mode interface behaviour in cardiovascular applications.

1.2 Theoretical Analysis and Computational Assessment

In **Chapter 3** of this thesis, a thorough theoretical analysis of novel and existing potential-based and non-potential-based CZMs is presented. One of the main objectives of this section is to present a complete characterisation of unphysical interface behaviour associated with the frequently adopted potential of Xu and Needleman (XN) (Xu and Needleman, 1993) under mixed-mode separation conditions. Additionally, it is demonstrated that realistic interface behaviour is not trivially achieved in cases of mixed-mode interface compression (over-closure) for potential and non-potential-based formulations. It is demonstrated that a potential-based formulation, proposed by McGarry et al. (2012), provides a significant improvement on the XN formulation (Xu and Needleman, 1993) during mixed-mode interface behaviour. Additionally, two novel non-potential-based CZMs are presented which provide a more realistic description of interface compression than the recently proposed model of van den Bosch et al. (2006) (VB model). A final non-potential-based formulation based on separation magnitude is presented which provides mode-independent interface behaviour. Following on from this theoretical analysis, further analysis of the mixed-mode behaviour of each cohesive zone formulation using highly mode sensitive finite element case studies is carried out in Chapter 4.

In **Chapter 4** of this thesis, a finite element computational assessment of the mixed-mode behaviour of potential and non-potential-based CZMs in separation and over-closure is performed. The case study of a bi-layered arch is first considered. The bi-layered arch is an ideal test case to assess the influence of coupling parameters on computed interface tractions. Additionally, an analytical solution has been developed (Parry and McGarry, 2012) whereby the traction magnitude is constant along the arch interface, with a sinusoidal distribution of normal and shear tractions. Mode mixity is a function of position on the arch interface. If cohesive zone formulation coupling terms result in a bias towards mode I or mode II separation, the analytical solution will not be reproduced. Hence the bi-layered arch is used to identify the most suitable cohesive zone for the highly mode sensitive application presented in Chapter 6 (stent coating

delamination), where it is critical that the cohesive zone does not introduce a bias towards mode I or mode II debonding.

The second section of Chapter 4 presents a finite element assessment of CZM performance under conditions of mixed-mode over-closure (tangential displacement accompanied by normal compression). It is crucial that CZMs can appropriately penalise mixed-mode interface compression, and as demonstrated in Chapter 3, this is not trivially satisfied for all formulations. Using the case study of a coating on the compressive region of a stent hinge, it is demonstrated that failure of a CZM to penalise mixed-mode over-closure leads to erroneous predictions of coating stress and hence a failure to correctly predict coating buckling. Having established robust cohesive zone formulations for interface separation and over-closure in Chapters 3 and 4, the focus of the remainder of the thesis is on the use of these CZMs for cardiovascular applications ranging from cardiovascular devices, tissue and cells. A brief summary of each application is provided next.

1.3   Cardiovascular Applications

1.3.1   Computational Investigation of Stent Coating Debonding

Drug-eluting stents (DES) have significantly reduced the rate of stent restenosis. However, late stent thrombosis has been reported in 1.7% of cases, often leading to patient mortality Iakovou et al. (2005). Numerous studies have suggested that coating debonding is a significant factor in the clinical complications associated with DES (Hoffmann et al., 2002; Kollum et al., 2005; Otsuka et al., 2007; Levy et al., 2009). The Food and Drug Administration does not provide guidelines on computational analysis and design techniques for coated stents (FDA, 2012). The main objective of **Chapter 6** is to develop a broad understanding of the computed traction distributions along a stent-coating interface during stent deployment and an enhanced understanding of the mechanisms of stent coating debonding. Firstly, an elastic stent is considered to develop a fundamental understanding of interface traction behaviour. The influence of geometrical parameters (strut length, stent

thickness and coating thickness) on stent-coating interface tractions is presented. Secondly, interface traction distributions are presented for an elastic-plastic stent, where complex interface traction distributions are computed.

1.3.2 Computational Investigation of Aneurysm Dissection

An abdominal aortic aneurysm (AAA) is a permanent dilation of the infrarenal aorta. A mortality rate of 90% is associated with the rupturing of a AAA with AAA rupture reported as the 13th highest cause of death in the western world by Vorp and Geest (2005). However, the reliable evaluation of the susceptibility of a specific AAA to rupture does not currently exist. Shear dissection has been suggested as a possible mechanism of AAA rupture initiation. In **Chapter 7**, shear dissection between the individual wall layers of three patient-specific AAA geometries is predicted. The location and extent of interlayer dissection is found to be strongly influenced by the AAA geometry.

1.3.3 Computational Investigation of Endothelial Cell Delamination

The realignment of cells seeded onto flexible substrates under conditions of cyclic tension has been demonstrated in several in-vivo studies. The cellular morphology and the actin cytoskeleton have been shown to align in the direction of minimum strain (Wang et al., 1995; Wang et al., 2001). In **Chapter 8**, mixed-mode debonding and rebonding of an endothelial cell from a silicone substrate under cyclic loading conditions is simulated. An active contractility formulation is implemented to describe cell cytoskeletal remodelling. It is shown that unphysical behaviour is computed if the potential-based Xu-Needleman CZM is used to describe the cell-substrate interface, significantly influencing the extent of cytoskeletal remodelling. A modified potential-based formulation is shown to overcome the unphysical problems associated with the Xu-Needleman formulation.

1.4 Thesis Structure

- A description of fundamental fracture mechanics theory is presented in **Chapter 2** where both linear elastic and elastic-plastic theories are discussed. A thorough review of CZMs proposed in the literature is also presented. Particular attention is directed towards two main categories of CZMs; potential-based and non-potential-based CZMs.

- A rigorous theoretical analysis of potential-based and non-potential-based mixed-mode CZMs is provided in **Chapter 3**. Specifically, the performance of each CZM is assessed in the context of mixed-mode interface separation and over-closure (compression). The influence of CZM coupling parameters on interface behaviour is investigated. This chapter provides a significant advance on previous theoretical analyses of CZMs, uncovering the importance of CZM coupling terms in mixed-mode separation and over-closure.

- In **Chapter 4**, a further assessment of the performance of each CZM during mixed-mode interface separation and mixed-mode interface compression is presented. In this chapter, a mode sensitive finite element case study is used to uncover any inherent bias towards mode I or mode II separation in CZMs. A second finite element case study is implemented to assess the ability of CZMs to correctly penalise mixed-mode over-closure.

- A thorough literature review of the evolution of cardiovascular stent design is provided in **Chapter 5**. Background information on stent and coating materials is provided with a particular focus on drug-eluting stents. The clinical implications of coating delamination are also discussed. This review chapter provides necessary background information and motivation for the extensive analysis of stent coating delamination in Chapter 6.

- In **Chapter 6**, the influence of stent material properties and geometry on the stress state at a stent-coating interface is investigated and predictions

of coating delamination are provided. Firstly, in order to gain an in-depth understanding of the mechanics of coating delamination, elastic coatings on elastic stent substrates are simulated. Following from this, the influence of stent plasticity on coating delamination is investigated. This chapter reveals, for the first time, the complex traction state at the stent-coating interface and demonstrates that several modes of delamination should be considered in the design of stent coatings.

- In **Chapter 7**, cohesive zone modelling is used to simulate interlayer dissection in an aneurysm wall. Three patient-specific geometries are analysed. Extensive mode II interlayer dissection is predicted and the importance of simulating a tri-layered inhomogeneous wall is highlighted. This chapter provides a significant advance on previous finite element approaches to aneurysm rupture prediction, which have been limited to the computation of von Mises stress distributions in homogeneous aneurysm walls without consideration of damage mechanisms.

- The final cardiovascular CZM application, presented in **Chapter 8**, entails the mixed-mode debonding of an endothelial cell from a silicone substrate during cyclic stretching. Unphysical interface tractions are computed when the Xu-Needleman CZM (Xu and Needleman, 1993) is used to simulate cell-substrate interface behaviour, whereas a modified potential model eliminates the prediction of non-physical behaviour, resulting in accurate predictions of cytoskeletal remodelling. This chapter highlights the importance of coupling terms in potential-based CZMs and, using the modified potential model, provides novel and accurate predictions of cytoskeletal remodelling due to cyclic substrate straining.

- A discussion of the main findings of this thesis is presented in **Chapter 9** together with concluding remarks and future considerations arising from the work.

1.5 References

Barenblatt, G. I. (1959) The formation of equilibrium cracks during brittle fracture. General ideas and hypotheses. Axially-symmetric cracks. *Journal of Applied Mathematics and Mechanics,* 23**,** 622-636.

Dugdale, D. S. (1960) Yielding of steel sheets containing slits. *Journal of the Mechanics and Physics of Solids,* 8**,** 100-104.

FDA (2012) U.S. Food and Drug Administration, date accessed 06/09/2012.

Hoffmann, R., Mintz, G. S., Haager, P. K., Bozoglu, T., Grube, E., Gross, M., et al. (2002) Relation of stent design and stent surface material to subsequent in-stent intimal hyperplasia in coronary arteries determined by intravascular ultrasound. *The American journal of cardiology,* 89**,** 1360-1364.

Hu, J., Chou, Y. K.&Thompson, R. G. (2008) Cohesive zone effects on coating failure evaluations of diamond-coated tools. *Surface and Coatings Technology,* 203**,** 730-735.

Iakovou, I., Schmidt, T., Bonizzoni, E., Ge, L., Sangiorgi, G. M., Stankovic, G., et al. (2005) Incidence, predictors, and outcome of thrombosis after successful implantation of drug-eluting stents. *JAMA: the journal of the American Medical Association,* 293**,** 2126-2130.

Kollum, M., Farb, A., Schreiber, R., Terfera, K., Arab, A., Geist, A., et al. (2005) Particle debris from a nanoporous stent coating obscures potential antiproliferative effects of tacrolimus-eluting stents in a porcine model of restenosis. *Catheterization and cardiovascular interventions,* 64**,** 85-90.

Levy, Y., Mandler, D., Weinberger, J.&Domb, A. J. (2009) Evaluation of drug-eluting stents' coating durability-"Clinical and regulatory implications. *Journal of Biomedical Materials Research Part B: Applied Biomaterials,* 91**,** 441-451.

Li, H.&Chandra, N. (2003) Analysis of crack growth and crack-tip plasticity in ductile materials using cohesive zone models. *International Journal of Plasticity,* 19**,** 849-882.

McGarry, J. P., Ó Máirtín, É., Parry, G.&Beltz, G. E. (2012) Potential-based and non-potential-based cohesive zone formulations under mixed-mode separation and over-closure. Part I: Theoretical Analysis. *Journal of the Mechanics and Physics of Solids,* In Submission.

Nakamura, T.&Wang, Z. (2001) Simulations of Crack Propagation in Porous Materials. *Journal of Applied Mechanics,* 68**,** 242-251.

Otsuka, Y., Chronos, N. A. F., Apkarian, R. P.&Robinson, K. A. (2007) Scanning electron microscopic analysis of defects in polymer coatings of three commercially available stents: comparison of BiodivYsio, Taxus and Cypher stents. *Journal of Invasive Cardiology,* 19**,** 71.

Parry, G.&McGarry, P. (2012) An analytical solution for the stress state at stent-coating interfaces. *Journal of the Mechanical Behavior of Biomedical Materials,* 10**,** 183-196.

van den Bosch, M. J., Schreurs, P. J. G.&Geers, M. G. D. (2006) An improved description of the exponential Xu and Needleman cohesive zone law for mixed-mode decohesion. *Engineering Fracture Mechanics,* 73**,** 1220-1234.

Vorp, D. A.&Geest, J. P. V. (2005) Biomechanical determinants of abdominal aortic aneurysm rupture. *Arteriosclerosis, Thrombosis, and Vascular Biology,* 25**,** 1558.

Wang, H., Ip, W., Boissy, R.&Grood, E. S. (1995) Cell orientation response to cyclically deformed substrates: Experimental validation of a cell model. *Journal of Biomechanics,* 28**,** 1543-1552.

Wang, J. H. C., Goldschmidt-Clermont, P., Wille, J.&Yin, F. C. P. (2001) Specificity of endothelial cell reorientation in response to cyclic mechanical stretching. *Journal of Biomechanics,* 34**,** 1563-1572.

Xu, X. P.&Needleman, A. (1993) Void nucleation by inclusion debonding in a crystal matrix. *Modelling and Simulation in Materials Science and Engineering,* 2**,** 417-418.

2. Background to Fracture Mechanics Theory and Cohesive Zone Modelling

2.1. Introduction

Since the modelling of interface fracture is a consistent theme throughout this thesis, a review of some of the fundamentals of fracture mechanics theory is discussed in Section 2.2 of this chapter. In Section 2.3 a thorough review of commonly implemented cohesive zone models is presented with particular attention directed towards potential-based and non-potential-based cohesive zone formulations. Additionally, a brief review of numerical methods used to describe crack propagation in finite element software is provided in Section 2.4. It should be noted that continuum mechanics theory relevant to this thesis is presented in Appendix A.

2.2. Fracture Mechanics Theory

2.2.1. Linear Elastic Fracture Mechanics

2.2.1.1. Material Flaws and the Stress Concentration Effect

A mathematical analysis of elliptical holes in flat plates was carried out by Inglis (1913) providing the first quantitative result linking material flaws and stress concentration effects. The model consists of a plate containing an elliptical hole with an applied stress perpendicular to the major axis of the ellipse as shown in Figure 2-1. It is assumed that the ellipse is not affected by the plate boundary. The stress at the tip of the major axis is determined to be;

$$\sigma_A = \sigma \left(1 + \frac{2a}{b} \right) \tag{2.1}$$

The stress concentration factor, k_t, is defined as the ratio σ_A/σ. Thus if the hole is circular $(a = b)$, then $k_t = 3$. If the major axis length, a, increases relative to b, then the elliptical hole becomes more like a sharp crack. It is easier to represent the stress at point A by

$$\sigma_A = \sigma \left(1 + 2 \sqrt{\frac{a}{\rho}} \right)$$

(2.2)

where ρ is defined as the radius of curvature given by;

$$\rho = \frac{b^2}{a}$$

(2.3)

When $a \gg b$, then Equation (2.2) is given as;

$$\sigma_A = 2\sigma \sqrt{\frac{a}{\rho}}$$

(2.4)

However, this equation predicts an infinite stress at the tip of an infinitely sharp crack $(\rho = 0)$. Therefore, theoretically, a material containing a sharp crack should fail upon the application of an infinitesimal load. This caused concern and motivated Griffith (Griffith, 1921) to develop fracture criterion based on energy as opposed to local material stress. Real materials are made of atoms and therefore the minimum radius a crack tip can have is on the order of an atomic radius. An estimate of the local stress concentration at the tip of an atomically sharp crack can be given as;

$$\sigma_A = 2\sigma \sqrt{\frac{a}{x_o}}$$

(2.5)

where x_0 is defined as the distance between the nuclei of two adjoining atoms. The analysis of Inglis (1913) was based on a continuum assumption which does not hold at the atomic level.

An element subject to in-plane stresses is shown near the tip of a crack in an elastic material in Figure 2-2. The equations below show that each stress component is proportional to a single constant, K_I.

$$\sigma_{xx} = \frac{K_I}{\sqrt{2\pi r}}cos\left(\frac{\theta}{2}\right)\left[1 - sin\left(\frac{\theta}{2}\right)sin\left(\frac{3\theta}{2}\right)\right] \tag{2.6}$$

$$\sigma_{yy} = \frac{K_I}{\sqrt{2\pi r}}cos\left(\frac{\theta}{2}\right)\left[1 + sin\left(\frac{\theta}{2}\right)sin\left(\frac{3\theta}{2}\right)\right] \tag{2.7}$$

$$\tau_{xy} = \frac{K_I}{\sqrt{2\pi r}}cos\left(\frac{\theta}{2}\right)sin\left(\frac{\theta}{2}\right)cos\left(\frac{3\theta}{2}\right) \tag{2.8}$$

This constant, called the stress intensity factor, provides a complete description of the crack tip conditions in a linear elastic material. This theory is based upon the fact that fracture will occur at a critical stress intensity, K_{I_C}, if a material fails locally due to a critical combination of stress and strain. Thus, K_{I_C} is a measure of fracture toughness or material resistance.

For a plate such as that shown in Figure 2-3, the stress intensity factor is defined as;

$$K_I = \sigma\sqrt{\pi a} \tag{2.9}$$

Crack failure occurs when $K_I = K_{I_C}$. K_{I_C} is assumed to be a size-independent material property. The relationship between material resistance, K_I and energy release rate, $\mathcal{G}$, can be given as;

$$\mathcal{G} = \frac{K_I^2}{E} \tag{2.10}$$

2.2.1.2. The Griffith Energy Balance

In this approach, fracture occurs when the energy available for crack growth is sufficient to overcome the resistance of the material. The energy criterion for fracture was first proposed by Griffith (1921). However, the idea of the energy release rate was first proposed by Irwin and Kies (1952). The proposed equations of Irwin (1957) were closely related to the equations of Griffith but provided a more convenient solution for many engineering problems. The energy release rate,

$\mathcal{G}$, is defined as the rate of change in potential energy, P, with crack area, $\mathcal{A}$, for a linear elastic material. When the energy release rate is equal to the critical energy release rate $(\mathcal{G} = \mathcal{G}_c)$, fracture initiates. Considering a crack length of $2a$ in an infinite plate subjected to tensile stress as shown in Figure 2-3, the energy release rate is defined as;

$$\mathcal{G} = -\frac{dP}{d\mathcal{A}} \qquad (2.11)$$

or

$$\mathcal{G} = \frac{\pi\sigma^2 a}{E} \qquad (2.12)$$

where E is the material Young's modulus, σ is the applied stress, and a is half of the crack length. It follows that the critical energy release rate is given as;

$$\mathcal{G}_c = \frac{\pi\sigma_f^2 a_c}{E} \qquad (2.13)$$

where σ^f and a^c are the failure stress and the critical crack length respectively.

The fracture toughness, $\mathcal{G}_c$, is assumed to be independent of the geometry of the cracked body as long as the material is reasonably homogenous and that the material behaviour is linear elastic. A number of factors can lead to nucleation of fracture. For instance, microscopic surface roughness at the tip of the flaw or a sharp microcrack near the tip of the flaw could produce adequate local stress concentrations to promote failure. The analysis of Griffith involved the influence of overall global energy balance on crack growth. That is, sufficient potential energy is required in the material to overcome the surface energy of the material. The following equations describe the Griffith energy balance for a small increase in crack area, $d\mathcal{A}$, under equilibrium conditions;

$$\frac{d\Xi}{d\mathcal{A}} = \frac{dP}{d\mathcal{A}} + \frac{dW_s}{d\mathcal{A}} = 0 \qquad (2.14)$$

$$-\frac{dP}{d\mathcal{A}} = \frac{dW_s}{d\mathcal{A}} \qquad (2.15)$$

where Ξ is the total energy, P is the potential energy consisting of external forces and internal strain energy and W_s is work required to create new surfaces.

14

Following on from the work of Inglis (1913), it was shown that;

$$P = P_o - \frac{\pi \sigma^2 a^2 B}{E}$$ (2.16)

where B is plate thickness and P_o is defined as the potential energy of an uncracked plate. The work required to create new surfaces is given as;

$$W_s = 4aB\gamma_s$$ (2.17)

where γ_s is the material surface energy.

The failure stress is then given as;

$$\sigma_f = \left(\frac{2E\gamma_s}{\pi a}\right)^{1/2}$$ (2.18)

The above equation is only suitable for brittle materials. In order to investigate the fracture stress of materials capable of plastic flow, such as metals, the Griffith equations were modified by Irwin (1948) and Orowan (1949). The revised equation for fracture stress is given as;

$$\sigma_f = \left(\frac{2E\left(\gamma_s + \gamma_p\right)}{\pi a}\right)^{1/2}$$ (2.19)

where γ_p is the plastic work per unit area of the created surface and is typically much larger than γ_s.

2.2.1.3. *Accounting for Crack Tip Plasticity-Extending the Validity of LEFM Theory*

Infinite stresses are predicted at the crack tip for linear elastic stress analysis of sharp cracks. However, stresses at the crack tip are finite in real materials as the crack tip radius must be finite (Anderson, 1995). Crazing effects in polymers and plasticity in metals leads to further relaxation of stress concentrations at the crack tip. As the inelastic region at the crack tip increases, linear elastic predictions become more inaccurate. Therefore, nonlinear material behaviour at the crack tip must be accounted for in crack problems involving plasticity. The Irwin approach

and the strip yield model can be used to extend the validity of linear elastic fracture mechanics theory to estimate the size of the crack tip yielding zone.

2.2.1.3.1. *The Irwin Approach*

The elastic-plastic boundary is estimated by using an elastic stress analysis in the Irwin approach. The normal stress, σ_{yy}, on the crack plane ($\theta = 0$) in a linear elastic material is defined by;

$$\sigma_{yy} = \frac{K_I}{\sqrt{2\pi r}} \tag{2.20}$$

where K_I is the stress intensity factor. The boundary between the elastic and plastic regions can be estimated when stresses in the above equation reach a yield criterion. In the case of a plane stress problem, material yielding occurs when $\sigma_{yy} = \sigma_{YS}$, where σ_{YS} is the uniaxial yield strength of the material. The first order estimate of the plastic zone region can be estimated by;

$$r_y = \frac{1}{2\pi}\left(\frac{K_I}{\sigma_{YS}}\right)^2 \tag{2.21}$$

Considering Figure 2-4, the stress distribution at $r \leq r_y$ can be represented by a horizontal line located at $\sigma_{yy} = \sigma_{YS}$ if strain hardening is neglected. However the above equation is based on an elastic crack tip solution. With yielding, stresses at the crack tip must redistribute in such a way as to maintain equilibrium. The hatched area represents stresses that would be present in an elastic material but cannot be reached in an elastic-plastic material as they exceed σ_{YS}. A second order estimate of plastic zone size, r_p, is described by;

$$\sigma_{YS} r_p = \int_0^{r_y} \sigma_{yy}\, dr = \int_0^{r_y} \frac{K_I}{\sqrt{2\pi r}}\, dr \tag{2.22}$$

Integrating and solving for r_p then gives;

$$r_p = \frac{1}{\pi}\left(\frac{K_I}{\sigma_{YS}}\right)^2 \tag{2.23}$$

Comparing this with Equation (2.21), it is clear that the second order estimate is twice the size of that based on the elastic crack tip solution.

2.2.1.3.2. The Strip Yield Model

The strip yield model was proposed by Dugdale (1960) and Barenblatt (1962). This analysis consisted of a long crack at the crack tip in a nonhardening material in plane stress where a through crack in an infinite plate was assumed (Figure 2-5). The model consists of a crack length of $2a + 2\gamma$ where γ_L is the plastic zone length. A closure stress equal to σ_{YS} is applied at each crack tip as shown in Figure 2-5(b). Two elastic solutions (a through crack under remote tension and through crack with closure stresses at the tip) are superimposed to approximate elastic-plastic behaviour. Unlike the Irwin approach where a stress singularity is computed at the crack tip, the stresses in the strip yield zone are finite for this model. A normal force, F, is applied to the crack at a distance x from the centre axis of the crack as shown in Figure 2-5(b) in order to estimate the stress intensity due to the closure stress. The stress intensities for the two crack tips are then given as;

$$K_{I(+a)} = \frac{F}{\sqrt{\pi a}} \sqrt{\frac{a + x}{a - x}} \qquad (2.24)$$

and

$$K_{I(-a)} = \frac{F}{\sqrt{\pi a}} \sqrt{\frac{a - x}{a + x}} \qquad (2.25)$$

if the plate is assumed to be of unit thickness. The closure force at a point within the strip yield zone is equal to;

$$F = -\sigma_{YS} dx \qquad (2.26)$$

By replacing a with $a + \gamma_L$ and summing the contribution from both crack tips, the total stress intensity at each crack tip as a result of the closure stresses is obtained;

$$K_{closure} = -\frac{\sigma_{YS}}{\sqrt{\pi(a+\gamma_L)}} \int_a^{a+r} \left\{ \sqrt{\frac{a+\gamma_L+x}{a+\gamma_L-x}} \right.$$

$$\left. + \sqrt{\frac{a+\gamma_L-x}{a+\gamma_L+x}} \right\} dx \tag{2.27}$$

$$= -2\sigma_{YS}\sqrt{\frac{a+\gamma_L}{\pi}} \int_a^{a+\gamma} \frac{dx}{\sqrt{(a+\gamma_L)^2-x^2}}$$

and solving this integral gives;

$$K_{closure} = -2\sigma_{YS}\sqrt{\frac{a+\gamma_L}{\pi}} \cos^{-1}\left(\frac{a}{a+\gamma_L}\right) \tag{2.28}$$

Noting that the stress intensity from the remote tensile stress $\left(K_\sigma = \sigma\sqrt{\pi(a+\gamma_L)}\right)$ must balance with $K_{closure}$, and solving for the plastic zone size, γ_L, gives;

$$\gamma = \frac{\pi}{8}\left(\frac{K_I}{\sigma_{YS}}\right)^2 \tag{2.29}$$

which is very similar to the Irwin approximation for plastic zone size (Equation (2.23)).

2.2.1.4. *Limits to LEFM Validity*

Linear elastic fracture mechanics is valid as long as nonlinear material deformation is confined to a small region surrounding the crack tip. Plasticity corrections such as the strip yield and Irwin models are rough estimations of elastic-plastic behaviour and can extend the validity of LEFM. However, when nonlinear behaviour becomes significant, the idea of stress intensity should be discarded and instead crack tip parameters which account for material behaviour such as crack tip opening displacement (CTOD) and the J integral should be adopted. Critical values of CTOD and J give almost size-independent measures of material fracture toughness even for cases where there is significant crack tip plasticity.

2.2.2. Elastic-Plastic Fracture Mechanics

2.2.2.1. Crack Tip Opening Displacement

When attempting to measure the critical stress intensity in a number of steels, it was discovered that the materials were too tough to be characterised by LEFM methods (Wells, 1961). It was realised that a new set of fracture mechanics principles were required to characterise this new class of metals. Wells noticed that even prior to fracture, the crack faces in these tough materials had moved apart due to the fact that plastic deformation had blunted the initially sharp crack (Figure 2-6 (a)). He demonstrated that the extent of crack blunting was proportional to the material toughness. This led to the establishment of the crack tip opening displacement (CTOD) as a useful fracture criterion. In the limit of small scale yielding, Wells related the stress intensity factor, K_I, and CTOD. Irwin demonstrated that plasticity at the crack tip makes the crack behave as if it is longer (Irwin, 1960). Considering a crack with a small plastic zone (Figure 2-6 (b)), it was realised that CTOD (δ) could be estimated by computing the displacement at the crack tip assuming an effective crack length of $a + r_y$ (Figure 2-6 (b)). The displacement behind the effective crack tip is defined as;

$$u_y = \frac{\kappa + 1}{2\mu} K_I \sqrt{\frac{r_y}{2\pi}} \tag{2.30}$$

where μ is the shear modulus and $\kappa = 3 - 4v$ in plane strain and $\kappa = (3 - v)/(1 + v)$ in plane stress. As shown in Equation (2.21), the Irwin correction for plasticity in plane stress is;

$$r_y = \frac{1}{2\pi} \left(\frac{K_I}{\sigma_{YS}} \right)^2 \tag{2.31}$$

And following substitution of Equation (2.31) into Equation (2.30), the crack tip opening displacement, δ is defined as;

$$\delta = 2u_y = \frac{4}{\pi} \frac{K_I^2}{\sigma_{YS} E} \tag{2.32}$$

The crack tip opening displacement is related to the energy release rate, $\mathcal{G}$, by;

$$\delta = \frac{4}{\pi} \frac{\mathcal{G}}{\sigma_{YS}} \quad (2.33)$$

Therefore, in the limit of small scale yielding, CTOD is related to $\mathcal{G}$ and K_I by Equation (2.32) and Equation (2.33).

2.2.2.2. The J-integral

The J-integral is a measure of the intensity of deformation at a notch or crack tip and involves the energy release required for crack growth. It can be used for both linear and nonlinear material response. Rice (1967) idealised elastic-plastic deformation as nonlinear elastic and thus provided a foundation for extending fracture mechanics theory well beyond the limits of LEFM. He demonstrated that the nonlinear energy release rate (change of potential energy with crack area), J, could be written as a path-independent line integral. J was also shown to characterise the stresses and strains at the crack tip in a nonlinear material by Hutchinson (1968) and Rice and Rosengren (1968). Uniaxial stress-strain behaviour for elastic-plastic and nonlinear elastic materials is shown in Figure 2-7. The loading curve is identical for both material types but the unloading curves differ. The nonlinear material unloads along the same loading path whereas the elastic-plastic material unloads along a path with the same slope as the initial Young's modulus. For a linear material response, the J-integral can be related to stress intensity factors. Abaqus/Standard (Abaqus, 2009) provides methods for the numerical evaluation of the J-integral such as the domain integral method and virtual crack extension method (Parks, 1977; Shih et al., 1986). For nonlinear elastic materials, $\mathcal{G}$ is replaced by J to give;

$$J = -\frac{dP}{d\mathcal{A}} \quad (2.34)$$

where P is potential energy and $\mathcal{A}$ is crack area. The potential energy is defined as;

$$P = S - F_{ext} \quad (2.35)$$

where S is strain energy stored in the body and F_{ext} is the work done by external forces.

2.2.2.3. Evaluation of J-integral in Two Dimensions

The J-integral is defined in two dimensions as;

$$J = \lim_{\Gamma \to 0} \int_{\Gamma} \boldsymbol{n}.\boldsymbol{H}.\boldsymbol{z} \, d\Gamma \tag{2.36}$$

where Γ denotes a contour starting on the bottom crack surface and finishing on the top surface (Figure 2-8). The limit $\Gamma \to 0$ indicates that the integral shrinks onto the crack tip. $\boldsymbol{n}$ is the outward normal to Γ, $\boldsymbol{z}$ is a unit vector in the virtual crack extension direction. $\boldsymbol{H}$ is defined by;

$$\boldsymbol{H} = W\boldsymbol{I} - \boldsymbol{\sigma}.\frac{\partial \boldsymbol{u}}{\partial \boldsymbol{x}} \tag{2.37}$$

For elastic material, W is defined as the elastic strain energy whereas for elastic-plastic or elastic-viscoplastic material behaviour, W is defined as the elastic strain energy density plus the plastic dissipation. From the work of Shih et al. (1986), Equation (2.36) can be rewritten as;

$$J = -\oint_{C+C_{+}+\Gamma+C_{-}} \boldsymbol{m}.\boldsymbol{H}.\bar{\boldsymbol{z}} \, d\Gamma - \int_{C_{+}+C_{-}} \boldsymbol{t}.\frac{\partial \mathbf{u}}{\partial \mathbf{x}}.\bar{\boldsymbol{z}} d\Gamma \tag{2.38}$$

where $\bar{\boldsymbol{z}}$ is an adequately smooth weighting function within the region enclosed by the closed contour $C + C_{+} + \Gamma + C_{-}$. It has the value $\bar{\boldsymbol{z}} = \boldsymbol{z}$ on Γ and $\bar{\boldsymbol{z}} = 0$ on C. $\boldsymbol{m}$ is the outward normal to the domain enclosed by the closed contour with $\boldsymbol{m} = -\boldsymbol{n}$ on Γ and $\boldsymbol{t} = \boldsymbol{m}.\boldsymbol{\sigma}$ being the surface traction on crack surfaces C_{+} and C_{-}. The closed contour integral can be converted into the domain integral by using the divergence theorem;

$$J = -\int_{A} \left(\frac{\partial}{\partial \boldsymbol{x}}\right).(\boldsymbol{H}.\bar{\boldsymbol{z}}) \, d\Gamma - \int_{C_{+}+C_{-}} \boldsymbol{t}.\frac{\partial \boldsymbol{u}}{\partial \boldsymbol{x}}.\bar{\boldsymbol{z}} d\Gamma \tag{2.39}$$

where A is the domain enclosed by the closed contour $C + C_{+} + \Gamma + C_{-}$ and includes the crack tip region as $\Gamma \to 0$.

2.2.2.4. Evaluation of J-integral in Three Dimensions

The *J*-integral can be extended to three dimensions when a crack with a tangentially continuous front is considered (Figure 2-9). Again, the local direction of virtual crack extension is given by **z** which is perpendicular to the crack front and lies in the crack plane. The *J*-integral defined in the plane perpendicular to the crack front is defined as;

$$J = \lim_{\Gamma \to 0} \int_{\Gamma} \boldsymbol{n}.\boldsymbol{H}.\boldsymbol{z} \, d\Gamma \qquad (2.40)$$

The definition of *J* in Equation (2.34) was supported by the experimental work of Begley and Landes (1972) and Landes and Begley (1972). *J* was measured experimentally by introducing cracks of various lengths in geometrically similar test specimens made of the same material and subjecting the specimens to an applied load. Load-displacement graphs were plotted for each test specimen and the area under each curve was defined as *U*, the energy absorbed by the specimen. For a specimen of thickness *B* to which an edge crack is applied, the *J*-integral is defined as;

$$J = -\frac{1}{B}\left(\frac{\partial U}{\partial a}\right)_{\Delta} \qquad (2.41)$$

By plotting *U* against crack length at various fixed displacements, *J* is computed by evaluating the slope to the tangent of each test curve (Figure 2-10).

2.3. Cohesive Zone Modelling

2.3.1. Introduction

Cohesive zone models are used to describe the delamination or crack propagation mechanism which occurs at the interface between two surfaces (Barenblatt, 1959; Dugdale, 1960; Camacho and Ortiz, 1996; Abdul-Baqi and Van der Giessen, 2001; Ural et al., 2009; Yan and Shang, 2009). Cohesive zones describe all failure modes at a discontinuity in an interface, which leads to the development of a cohesive zone law, specifying the relationship between the interface tractions and

displacements. A plethora of cohesive zone models have been proposed in the literature. The traction-separation relationships of commonly adopted cohesive zone models are illustrated in Table 2-1.

The concept of the cohesive zone model was first proposed by Barenblatt (1959) for modelling fracture in perfectly brittle materials as a possible alternative to the fracture mechanics concept. The notion of the cohesive zone model was subsequently developed by Dugdale (1960) to model the yielding of thin elastic-plastic sheets containing slits. The ability to predict coating delamination and crack propagation is of vital importance in many types of industries. Cohesive zone models have been used to model crack propagation in porous materials (Nakamura and Wang, 2001), ductile materials (Li and Chandra, 2003) and to model coating failure in diamond-coated tools (Hu et al., 2008). The cohesive zone model concept (referred to as the fictitious crack model) was used by Hillerborg et al. (1976) to assess crack formation and growth in concrete. The integrity of welded joints is greatly influenced by yield stress mismatch between the weld metal and the base material (Schwalbe et al., 1994; Schwalbe and Kocak, 1997). Therefore, Lin et al. (1999) implemented a cohesive zone to assess the effect of strength mismatch in welded joints. Among other findings, it was reported that there was no effect of strength mismatch for larger weld thicknesses. Metals such as steel and aluminium are coated with polymers in order to improve final surface finish (Graziano, 2000). As a result, cohesive zone formulations have been implemented to model the delamination process at a steel-polymer interface (Graziano, 2000; Van den Bosch et al., 2007). The process of crazing in polymers has also been investigated through the use of the cohesive zone method. In the work of Tijssens et al. (2000), different mechanisms leading to polymer crazing were evaluated based on micromechanical considerations using a cohesive zone. Thermal barrier coatings are used to protect metallic components from extremely high temperatures in power generation turbines and aircraft industries (Wei and Hutchinson, 2008). These thermal barrier coatings can consist of multiple layers. In the work of Wei and Hutchinson (2008), a potential-based cohesive zone model was used to describe the fracture process at a Ni/Al_2O_3 interface.

Cohesive zone models have also been implemented to model plaque rupture (Gasser and Holzapfel, 2007; Ferrara and Pandolfi, 2008) and the dissection process in healthy arteries (Gasser and Holzapfel, 2007). The interface debonding process in adhesively bonded pipe joints was assessed by means of the cohesive zone method by Ouyang and Li (2009), to predict the torsional load capacity in these structures. The rate-dependent failure behaviour of thin structural adhesives subjected to mode I loading was assessed by Marzi et al. (2009), using a bi-linear cohesive zone model. Important information regarding energy emission during crack initiation was evaluated. In a recent computational study, the cohesive zone method was used to predict polymer coating delamination from the surface of commercially available cardiovascular stent designs (Hopkins et al., 2010). A design curve for the conditions leading to Mode I coating delamination from the tensile surface of a stent was determined. Computed patterns of coating delamination showed very strong correlation with published experimental images. The cohesive zone concept has recently been used to describe the debonding process at carbon nanotube composite interfaces (Zhu and Luo, 2011).

Experimental determination of a suitable cohesive model can be challenging. Experimental methods to assess the suitability of cohesive zone employed for large failure process zones were presented by Sørensen and Jacobsen (2003). Two commonly used experimental techniques were discussed; the direct tension test, assuming uniform damage evolution across a test specimen and the *J*-integral approach (Li and Ward, 1989). In the direct tension test, an extensometer measures the relative displacement of two points across the failure plane of a specimen subjected to uniaxial tension. This test provides information as to the shape of the cohesive zone up to peak traction. The evolution of damage across the width of the specimen must be uniform however, which is difficult to achieve experimentally. The cohesive zone can also be derived from the *J*-integral approach and end opening of the cohesive zone (Rice, 1967). Sørensen and Jacobsen (2003) determined the *J*-integral by subjecting a double cantilever beam (DCB) to bending moments. The *J*-integral is used to characterise the failure zone assuming bulk elastic behaviour, small displacements and small strains. It is

evaluated in the region enclosing the process zone and crack tip. Differentiating the measured fracture resistance encountered during crack growth with respect to the crack opening displacement determines the *J*-integral. It is possible to estimate the shape of the cohesive zone from the shape of the fracture resistance-opening displacement relationship. In the research of Fuchs and Major (2011), a novel test rig was fabricated to determine the cohesive zone model shape and parameters required for analysing the fracture process in glass fibre reinforced epoxy resin composites. A digital image correlation system coupled with a high speed camera was used to measure small crack opening displacements allowing for accurate determination of cohesive zone characteristic distance. The cohesive zone was utilised for the numerical simulation of crack growth in homogeneous and inhomogeneous polyethylene samples by Janko et al. (2012). Material inhomogeneity is known to have a significant influence on crack initiation and evolution. The choice of cohesive zone and material parameters was determined from experimental data. Simulations revealed that the specific arrangement of polyethylene grades in bimaterial specimens had a significant influence on the resulting crack growth. These findings are very relevant due to the increasing use of multilayered polyethylene pipes in industry (Hutar et al., 2010).

Cohesive zone models can be coupled or uncoupled. In an uncoupled cohesive zone law, the normal traction is independent of the tangential opening displacement and the tangential traction is independent of the normal opening displacement (van den Bosch et al., 2006). In a coupled cohesive zone law, both tractions depend on both the normal and tangential opening displacements. Uncoupled cohesive zone models are of limited use unless interface separation is constrained to occur in a single predefined direction (e.g. either mode I or mode II separation). Typically, however, cohesive zone models are applied to engineering problems where the mode of interface separation is not predefined, requiring the use of mixed-mode formulations, whereby all components of the traction vector depend on both the normal and tangential interface separations, in order to provide a physically realistic response. For example if an interface undergoes a

complete separation in the tangential direction, the resistance to a subsequent normal separation should be significantly reduced or eliminated.

2.3.2. Potential-Based and Non-Potential-Based Cohesive Zone Models

Two main categories of cohesive zone models have been proposed in the literature; potential-based models (path-independent) and non-potential-based models (path-dependent) where tractions are not derived from an interface potential. A review of both types of models is presented in this section.

2.3.2.1. *Potential-Based Cohesive Zone Models*

A potential-based function involves defining physical field quantities as a function of position at a continuum or atomistic level (Park et al., 2009). An interface potential characterises the overall fracture behaviour and represents the work done when two opposing surfaces at an interface undergo a relative separation $\underline{\Delta}$ (Xu and Needleman, 1993). The first derivative of the potential provides the cohesive tractions at the fracture surfaces and the second derivative provides the interface stiffness. Potential-based functions have been used for many mixed-mode fracture applications (Needleman, 1987; Needleman, 1990; Beltz and Rice, 1991; Xu and Needleman, 1993). The toughness and ductility of plastically deforming solids is limited by the nucleation of voids from inclusions and second phase particles. A polynomial-based potential function which first provided a phenomenological description of normal separation was proposed by Needleman (1987). This formulation was used to describe the process of void nucleation by inclusion debonding in an isotropically hardening elastic-viscoplastic matrix from initial debonding through to complete decohesion. The cohesive zone law was embedded in a continuum elastic-plastic description of solids joined at the interface. Computed decohesion occurred either in a ductile or in a brittle manner depending on the ratio of the inclusion radius to the characteristic length. In order to account for larger shear displacements, an exponential-based potential was proposed by Needleman (1990) to analyse the decohesion of a viscoplastic block from a rigid substrate. This exponential form of cohesive law originated from the universal relationship between binding energies and atomic separation of bimetallic interfaces (Rose et al., 1981; Rose et al., 1983). Decohesion initiated in

a predominantly tensile or shear type separation based on the ratio of the maximum traction to the interface strength. The influence of size scale, interfacial properties and loading rate on defect-dominated decohesion were presented. In a related manuscript, a potential function was implemented to analyse the specific mode of decohesion between a viscoplastic block and rigid substrate (Needleman, 1990b). An exponential function was defined for the normal traction response while a periodic function was utilised to characterise tangential traction. Decohesion was significantly influenced by the ratio of the block size to characteristic length. It was reported that the mode of decohesion changed from a uniform type of separation along the interface to a crack-like propagation as the ratio of block size to characteristic length increased. This potential-based formulation was again implemented for the micromechanical modelling of interface decohesion by Needleman (1992).

Following on from the work of Needleman (1987), a cohesive law was implemented by Tvergaard 1990 to analyse fibre debonding in a whisker-reinforced metal-matrix composite. Failure was predicted to initiate by a process of void formation near the sharp edges at the fibre ends. A periodic exponential-based potential model was developed by Beltz and Rice (1991) to assess the competition between dislocation emission and cleavage decohesion at a crack tip in a crystal. Periodic shear dependence described the transfer of attraction from one atom to another during shearing (dislocation) of atomic planes. In contrast to previous models used to describe nucleation, which were based on elasticity theory for complete dislocations (Mason, 1979; Rice and Thomson, 1974), a Peierls-type stress versus displacement relationship was implemented to describe dislocation nucleation on a slip plane ahead of the crack tip. Mixed-mode loading conditions were considered. It was determined that the tension across the slip plane slightly reduced the critical load for dislocation emission. The influence of loading angle on ductile or brittle decohesion was discussed. Actual crystal slip plane orientation was reported to influence whether the crack emanated from dislocation emission or cleavage decohesion. This result was corroborated by experimental work involving symmetric bicrystals of copper (Wang and

Anderson, 1991). A one-dimensional potential-based model was proposed by Tvergaard and Hutchinson (1993), where the effective displacement was used to account for mode-mixity. This potential was used to assess the influence of plasticity and mixed-mode loading on interface toughness between an elastic-plastic solid and a solid which did not yield plastically. Crack growth resistance was predicted for a range of non-dimensional material parameters and mixed-mode loading conditions. Predicted crack growth patterns were not particularly sensitive to cohesive law parameter changes such as the normal and tangential critical characteristic distances ($\delta_n^c, \delta_{t,}^c$). Plasticity was found to enhance interface toughness for all modes of loading but especially for predominantly mode II loading due to plastic deformation outside the fracture process zone.

A potential-based model was implemented by Xu and Needleman (1993), for the micromechanical investigation of void nucleation in a crystal matrix. Constitutive properties were specified independently for the interface, the void-nucleating particles and the matrix. Comparison was made between a continuum crystalline plasticity constitutive model and a constitutive model based on flow theory of plasticity for the matrix. Decohesion was inhibited with the implementation of the crystalline model due to localised strains computed in the matrix and localised shear at the matrix-particle interface. The influence of the type of interface shear behaviour on decohesion was investigated with periodic shear displacement together with a shear response which allowed for complete shear decohesion used. The interface shear displacement definition did not have a significant influence on the course of decohesion in cases where the shear strength was either very high or very low relative to the normal interface strength. However, in intermediate cases, where the normal and shear strengths were similar, the shear traction characterisation was found to have a significant influence on decohesion behaviour. Complete decohesion was computed for the periodic potential depending on the specific parameter sets chosen. The interface strength and imposed stress state dictated whether or not decohesion preceded localisation. Localisation was found to reduce normal separation across the interface, inhibiting decohesion. It was reported however that localisation can itself lead to

decohesion due to large material localised strains or due to local shedding behaviour to nearby particles. Regarding the choice of constitutive model, little difference in void nucleation patterns was computed between models for a weak and compliant interface. This potential-based formulation was also utilised to simulate crack growth in brittle solids (Xu and Needleman, 1994). The cohesive law was capable of capturing crack patterns and crack progression velocities reported experimentally (Washabaugh and Knauss, 1994). The effect of high impact velocity on crack growth was investigated. A zigzag pattern of crack growth was computed prior to crack branching for a range of cohesive surface orientations.

In the research of Rahul-Kumar et al. (1999), a modified form of the Xu and Needleman potential (Xu and Needleman, 1994) and an inverse power law potential model for intermolecular attraction were used together with cohesive elements to describe polymer interfacial behaviour. Three tests were carried out to assess the accuracy of the models. The first simulation involved a t-peel test to determine the adhesion strength between two elastomers. The second test involved the simulation of a compressive shear test to analyse the adhesion between a viscoelastic elastomer and a rigid substrate. The model was capable of describing transition from stable to unstable fracture. The third simulation involved interface failure in a multilayer elasto-plastic polymer system. The modelling framework employed demonstrated the ability to predict crack nucleation and propagation in systems with complex microstructures and multiple layers. The exponential cohesive law of Xu and Needleman (1993) (XN) was implemented by Abdul-Baqi and Van der Giessen (2001), in order to study indentation-induced delamination of a strong film from a ductile substrate. The indentation technique has been adopted as a tool to characterise the properties of thin films and coatings. Delamination was found to be driven by the shear stress at the interface associated with plastic deformation in the substrate. However, interfacial normal stresses were found to have a significant influence on delamination, due to the coupling of the normal and tangential responses inherent in the XN law. The XN law was again adopted by Abdul-Baqi and Van der

Giessen (2002), for the prediction of indentation-induced cracking of hard coatings on ductile substrates. The cohesive zone formulation was used to describe the fracture process at the interface between the coating and the substrate. Through-thickness cracks were also modelled using cohesive surfaces, which had a finite strength and fracture energy. Coating cracks were computed in areas of high tensile radial stress.

A novel exponential form of potential-based cohesive law was developed by Jin et al. (2002) to simulate crack growth in ceramic/metal functionally graded materials using cohesive elements. Although ductile deformation was not accounted for, the transition in fracture mechanisms between metal and ceramic phases was accounted for by six cohesive parameters including peak cohesive tractions of both material phases, the cohesive energy densities and two cohesive gradation parameters. A damage variable was also included to account for irreversible material damage. The novel formulation was used to analyse crack growth in a titanium/titanium monoboride (TiB/ Ti) composite. It was determined that the load required to initiate crack formation was similar between the composite material and that of a pure Ti specimen. A potential-based cohesive zone model was proposed by Song et al. (2006), to simulate crack propagation in asphalt concrete. Numerical implementation of the model was performed by means of a subroutine using user element capability in Abaqus/Standard software. The proposed model was validated by comparison to closed form solutions and by the simulation of a double cantilever beam test. Cohesive parameters were calibrated to match experimental observations and mixed-mode crack propagation was simulated by using cohesive elements. The predicted crack propagation patterns were found to compare favourably well with the experimental results.

Thermal barrier coatings are used to protect metallic components from extremely high temperatures in power generation turbines and aircraft industries. These thermal barrier coatings consist of multiple layers. Thermal expansion mismatch between the ceramic layers and the thicker metallic component can produce large compressive stresses in the ceramic layers upon cool-down. In the work of Wei

and Hutchinson (2008), fracture in a thermal barrier composite was considered. The composite consisted of a porous ceramic layer with a low thermal conductivity on top of a fully dense layer of Al_2O_3, which was adhered to a metal (Ni alloy) layer bonded to the component. A potential-based cohesive zone model, based on two previous models (Needleman, 1990; Sun et al., 1993), was utilised to describe the delamination process at the Ni/Al_2O_3 interface in order to assess how interface properties such as the work of separation and normal strength at the ceramic-metal interface affected the toughness at the interface. It was evaluated that plasticity accompanying interface fracture is essential for the adherence of thermal barrier coatings. Even a Mode I loading on the materials induced shear on the interface around the crack tip due to plasticity on one side of the interface and the elastic mismatch between the materials. This work stressed the importance for the inclusion of a mixed-mode (coupled) cohesive zone for simulating this type of delamination process. Recently a polynomial potential-based model for mixed-mode fracture was proposed by Park et al. (2009), to provide additional control in the coupling between normal and tangential tractions when different mode I and mode II fracture energies are defined. This potential accounted for both intrinsic and extrinsic cohesive zone models. The path dependence of the work of separation in the proposed model was assessed while boundary conditions were imposed such that the normal and tangential tractions were set to zero if they exceeded a certain separation. Initial slope indicators were included to control the elastic fracture behaviour and shape parameters were employed to characterise the material softening response. The choice of boundary conditions limited the regions in which repulsive forces were encountered for mixed-mode separation. In contrast to the Xu and Needleman potential-based model (Xu and Needleman, 1993), the boundary conditions defined in this model allowed for the overall work of separation to be dependent on separation path. However, due to the imposed boundary conditions, a discontinuity (kink point) in the work of separation was reported for certain mixed-mode loading conditions. A simulation involving a mixed-mode bending test was carried out to validate the proposed model.

2.3.2.2. Non-Potential-Based Cohesive Zone Models

A number of path-dependent models have been proposed in the literature. The work of separation is dependent on the separation path for these formulations. Examples of these path-dependent models include; rigid-linear fracture models (Camacho and Ortiz, 1996; Ural et al., 2009), piece-wise (trapezoidal) models (Tvergaard and Hutchinson, 1992; Planas and Elices, 1993; Yan and Shang, 2009), bilinear (Geubelle and Baylor, 1998; Yan and Shang, 2009) and exponential fracture models (van den Bosch et al., 2006). An illustration of some of these models is provided in Table 2-1.

A path-dependent trapezoidal form of the traction-separation response was implemented to model the resistance of crack growth following the initiation of a crack at an interface in elastic-plastic solids in the work of Tvergaard and Hutchinson (1992). The cohesive formulation was used to predict material toughness in cases where fracture behaviour is characterised by void growth and coalescence and also highlighted the important role of plasticity in enhancing toughness in dual-phase solids. The governing parameters of this trapezoidal cohesive zone model were the work of fracture, the peak stress, the critical displacement ratio and the shape factors. The shape factors dictated where the peak stress and damage initiation points occurred. The proposed model was capable of simulating ductile fracture where numerous voids interact within the fracture process zone. A piece-wise linear softening function was employed in a study involving the asymptomatic analysis of a cohesive crack by Planas and Elices (1993). This work determined when simplified linear elastic fracture mechanics (LEFM) methods could be applied to a cohesive crack simulation and also provided methods for extracting information on softening behaviour of material from experimental data. It was reported that the effective crack opening prior to peak and the deviation from LEFM predictions could be very closely estimated by the length of the fracture softening curve. In the work of Ortiz and Suresh (1993), the mechanism of fracture in polycrystalline ceramics during cooling obeyed a bilinear cohesive law. This work investigated the residual stresses generated in these ceramics during cooling from fabrication temperature.

A rigid-linear fracture model was employed by Camacho and Ortiz (1996), to propagate numerous cracks along random paths in a brittle material. Radial cracking in axisymmetric simulations was evaluated through a continuum damage model. Following crack initiation, a friction algorithm was implemented to describe multi body dynamics. Heat conduction, thermal coupling and rate-dependent plasticity were also included in the calculations. Two case studies were presented to validate the predictive capability of the model; spall tests and dynamic crack propagation in a double cantilever beam specimen. Additionally, a simulation involving the subjection of alumina plates to impacts from steel pellets at a wide range of velocities was performed. In contrast to previous studies where interface fracture elements were initially applied along potential fracture surfaces (Xu and Needleman, 1994), an adaptive meshing technique was employed in this work by duplicating nodes along previous element boundaries which for allowed crack propagation along multiple paths. Radial, conical and lateral crack propagation patterns were computed which correlated well with experimental observations.

A quasi-linear cohesive law was implemented in the research of Geubelle and Baylor (1998), to analyse impact-induced delamination in polymeric matrix fibre reinforced composite laminates. In contrast to metals, polymeric matrix composite structures lack the ability to deform plastically in order to absorb the kinetic energy of an impact. These composite laminates are implemented in many engineering applications where they can be exposed to low velocity impacts. An example is an aircraft structure subjected to impact from runway debris. Cohesive elements were applied along inner layer boundaries and transverse plies to simulate the initiation and propagation of cracking. In contrast to the Xu and Needleman formulation (Xu and Needleman, 1993) where healing of fracture surfaces is possible upon unloading, healing of fracture surfaces for this formulation was inhibited by enforcing an internal residual strength variable. This internal strength variable was prescribed an initial value before loading and vanished upon complete interfacial failure. The model was able to capture the location of damage initiation and the failure processes associated with the

delamination event. Computed crack predictions agreed well with 2D line-impact experiments conducted on a graphite/epoxy doubly clamped composite plate (Choi et al., 1991a; Choi et al., 1991b). Yang and Thouless (2001) implemented a trapezoidal form of cohesive law to simulate mixed-mode fracture of plastically-deforming joints. Excellent predictions were obtained between numerical calculations and the large-scale plastic deformation in T-peel and lap shear tests of aluminium alloy bound by commercial adhesive. It was reported that this was the first time that the failure and deformation of plastically-deforming lap-shear joints had been predicted quantitatively. A bilinear cohesive law was implemented by Zavattieri and Espinosa (2001), to capture crack initiation, propagation, coalescence and branching in ceramic microstructures in a combined numerical and experimental approach. A stochastic model was utilised to describe the microfracture process. The Weibull distribution of interface strength was employed at the grain boundaries to account for chemical impurities, random grain boundary orientation and the glassy phase at grain boundaries. Simulations revealed good agreement between the computed and experimental crack pattern predictions and crack propagation velocities only when certain grain morphology and model parameters were chosen.

In the work of Zhang and Paulino (2005), a bilinear cohesive zone model was used for the analysis of functionally graded and homogenous materials undergoing dynamic failure. The influence of material gradation on mixed-mode and mode I fracture problems were assessed. The bilinear formulation was implemented to alleviate artificial compliance associated with the insertion of cohesive elements by allowing the adjustment of the initial stiffness similar to the formulation of Geubelle and Baylor (1998). In order to account for crack propagation in graded materials, material-dependent parameters were included in the bilinear formulation. These parameters accounted for fracture toughness reduction due to the interaction of material phases. A simulation involving mixed-mode crack growth in steel and functionally graded material plates was performed to demonstrate the applicability of the cohesive zone. Computed crack propagation angles and crack tip velocities were similar to those reported in

previous studies (Kalthoff and Winkler, 1988; Belytschko et al., 2003). A rate-independent bilinear model was employed in the research of Kandula et al. (2005), to model dynamic fracture of composite material. Fracture experiments were performed on composite specimens made of polyester resin with varying amounts of plasticiser to validate the numerical approach. The path-dependent van den Bosch (VB) exponential form of cohesive law was proposed by van den Bosch et al. (2006) to provide an alternative to the widely used Xu and Needleman (XN) law (Xu and Needleman, 1993) for mixed-mode applications. Unphysical mixed-mode behaviour associated with the XN law was demonstrated by assessing the work of separation and traction responses computed for a range of coupling parameters. The alternative formulation involved setting the q coupling parameter, which defines the ratio of the tangential to the normal work of separation, equal to unity and introducing a new parameter which allowed for independent fracture energies in the normal and tangential directions. The VB formulation was used to measure the mixed-mode delamination fracture toughness of unidirectional glass/epoxy composites, through the use of a mixed-mode bending apparatus. It was also used to describe, with reasonable accuracy, the work of separation under mixed-mode loading conditions when compared to previous experimental data (Benzeggagh and Kenane, 1996).

In the work of Shim et al. (2006), a displacement-based bilinear cohesive law based on the formulation of Jin et al. (2002), was employed to assess elastic-plastic crack growth resistance in ceramic/metal functionally graded material. Crack growth resistance was characterised by the J-integral approach developed by Rice (1967). Although crack growth was only considered for mode I conditions, the proposed model provided a more accurate prediction of crack growth patterns in the functionally graded composite material than other cohesive laws (Jin et al., 2002; Zhang and Paulino, 2005). During delamination of a polymer coating from a steel substrate, interface fibrillation can frequently occur. This failure mechanism is characterised by large bulk material deformations and large interfacial displacements. In the research of Van den Bosch et al. (2007), a generic cohesive law was introduced to describe uniform and non-uniform

interface fracture involving very large displacements. Polymer coating delamination was first assessed experimentally to validate existence of fibrils. For the large displacement formulation, no distinction was made between normal and tangential loading. Instead, only one constitutive relation was implemented for the interface traction and displacement by coupling the normal and tangential equations through a weighted sum of the tractions using two weight factors. The weight factors were then defined with respect to the total opening displacement. This large displacement formulation was then applied to three cohesive laws used to describe the fibrillation process; an exponential law (van den Bosch et al., 2006), a cohesive law based on experimental observations of soft polymer delamination under mode I loading (Zosel, 1998; O Connor and Willenbacher, 2004) and a bilinear model commonly implemented in the literature (Espinosa et al., 2000; Zhang and Paulino, 2005). Four simulations involving deformation of a laminate structure were performed to assess the macroscopic response, quantified by the force-displacement curves and dissipated energy, for small and large displacement formulations for each cohesive law. No differences were computed between the small and large deformation laws for pure mode I and pure mode II loading. However, significant differences were computed between the two categories for mixed-mode loading conditions.

Ural et al. (2009), employed bilinear damage-based cohesive zone model to simulate crack propagation under cyclic loading of cast aluminium alloy. The model accounted for damage evolution and crack retardation. This was achieved through the use of a damage-dependent traction-separation relation coupled with an equation governing damage evolution in the material. The actual rate of damage in the material was characterized by three material parameters; damage accumulation, crack retardation and stress threshold. A good correlation was obtained between the simulated results and experimental fatigue test results for an aluminium alloy under different load ratios. The ability of the model to predict crack retardation was confirmed by the fact that crack retardation was computed in the lower but not in the higher loading ratio. This pattern was also observed experimentally. Crack retardation was also predicted following a single stress

overload. In this case, computed crack retardation occurred as a result of residual stresses in the plastic region of the material. Another study involved the assessment of the process of interfacial delamination in PZT (piezoelectric) thin films, where exponential, bilinear and trapezoidal models were presented Yan and Shang (2009). The fracture process along the Cr (chromium)/PZT interface was investigated using these models. The cohesive strength and work of separation were found to be the dominant parameters in such a simulation. However, the interface characteristic parameter did not seem to have as great an effect on the fracture response. In this study, it was found that the bilinear model was best suited to describing the delamination process. The results also demonstrated that the critical interfacial stress for crack initiation was lower than the rupturing strength of bulk PZT or Cr material. In recent years, a great interest has been directed towards the improvement of lithium ion batteries for applications such as grid storage and electric vehicles where batteries are subjected to high rates of charge and discharge (Grantab and Shenoy, 2011). The design process would be aided significantly if microstructural battery damage could be predicted. Bower and Guduru (2012) implemented a bilinear cohesive model to simulate fracture in lithium ion insertion electrode materials. Surface and cohesive zone elements were used to model crack nucleation and propagation at the lithium–electrode interface. The tractions were related to displacements using a constitutive equation adapted from Ortiz and Pandolfi (1999). A large compressive stiffness was included to prevent cracks from overlapping during simulation.

2.4. Numerical Methods for Modelling Crack Propagation in Finite Element Analysis

Cohesive surfaces are often aligned with finite element mesh boundaries leading to a predefined crack propagation path. Although denser finite element meshes can capture multiple crack paths (Papoulia et al., 2006), patterns of crack branching are still limited to predefined paths which may influence crack prediction. Additionally, predefined fracture surfaces can affect material stiffness in the vicinity of the crack tip which can also lead to numerical inaccuracies (Remmers et al., 2008). One method of simulating fracture in finite element

software is to implement a user-defined subroutine (UINTER), written in Fortran code, to define specific cohesive zone model equations at an interface. For this method, the failure path or discontinuity is predefined. Another popular method of simulating fracture in which the failure path is predefined involves applying specialised cohesive elements along the fracture interface and defining failure criterion for each cohesive element specified by a constitutive law. When this failure criterion is met, the cohesive elements are deleted and the interface crack proceeds (Ortiz and Pandolfi, 1999; Pandolfi et al., 1999; Ural and Vashishth, 2006; Paulino et al., 2008; Samimi et al., 2011).

Extended finite element methods (XFEM and GFEM) have been presented in recent years to simulate crack path prediction beyond predefined paths (Camacho and Ortiz, 1996; Wells and Sluys, 2001; Moes and Belytschko, 2002; Remmers et al., 2003; Zhang and Paulino, 2005; Remmers, 2006; Yang and Deeks, 2007; Remmers et al., 2008; Ng and Dai, 2012). The partition of unity (PU) method was implemented by Belytschko and Black (1999), in order to minimise remeshing while solving a linear elastic fracture mechanics problem. This method allows for discontinuities to be simulated independent of the mesh in finite element software (Natarajan et al., 2010). This creates greater flexibility in modelling moving boundary problems without actually changing the underlying mesh, while the set of failure criterion evolve with the interface geometry. However, a number of numerical problems have been associated with this technique. In the work of Camacho and Ortiz (1996), initially rigid cohesive surfaces were inserted at inter-element boundaries. Fracture could progress along these new cohesive surfaces if a critical condition was met. This abrupt introduction of alternative crack surfaces can lead to numerical problems however as discussed by Papoulia et al. (2003). In an effort to alleviate dynamic fracture numerical instabilities, a time-dependent cohesive segment method was formulated by Remmers et al. (2008). Three applications (tensile and shear loading of a block and crack growth at a bi-material interface) provided evidence of the ability of the new technique to model fast crack propagation in brittle solids. Special attention must be taken for element numerical integration if the failure approximation becomes discontinuous; in 3D

simulations, problems with continuity in the equations can lead to poor accuracy of the derivatives close to high gradient regions such as crack fronts (Natarajan et al., 2010). To overcome these numerical issues encountered at corner points or crack fronts, a generalised finite element method (GFEM) has been proposed (Strouboulis et al., 2001). The two main capabilities of this method, as outlined by Strouboulis et al. (2001), are that it can deal with overlapping meshes at the crack domain boundary and also can provide a numerical solution to boundary value problems encountered in the region of corner points, voids and cracks.

2.5. References

Abaqus (2009) Abaqus Theory Manual, Version 6.9-1,. *User Documentation, Dassault Systems*.

Abdul-Baqi, A.&Van Der Giessen, E. (2001) Indentation-induced interface delamination of a strong film on a ductile substrate. *Thin Solid Films,* 381, 143-154.

Abdul-Baqi, A.&Van Der Giessen, E. (2002) Numerical analysis of indentation-induced cracking of brittle coatings on ductile substrates. *International Journal of Solids and Structures,* 39, 1427-1442.

Anderson, T. L. (1995) Fracture mechanics: fundamentals and applications, 1995. *CRC Boca Raton*.

Barenblatt, G. I. (1959) The formation of equilibrium cracks during brittle fracture. General ideas and hypotheses. Axially-symmetric cracks. *Journal of Applied Mathematics and Mechanics,* 23, 622-636.

Barenblatt, G. I. (1962) The mathematical theory of equilibrium cracks in brittle fracture. *Advances in applied mechanics,* 7, 104.

Begley, J. A.&Landes, J. D. (1972) The J-integral as a fracture criterion. *Astm Stp,* 514, 1-20.

Beltz, G. E.&Rice, J. R. (1991) Dislocation nucleation versus cleavage decohesion at crack tips. *Modeling the Deformation of Crystalline Solids: Physical Theory, Application and Experimental Comparisons. Warrendale, PA,* 457-480.

Belytschko, T.&Black, T. (1999) Elastic crack growth in finite elements with minimal remeshing. *International Journal for Numerical Methods in Engineering,* 45, 601-620.

Belytschko, T., Chen, H., Xu, J.&Zi, G. (2003) Dynamic crack propagation based on loss of hyperbolicity and a new discontinuous enrichment. *International Journal for Numerical Methods in Engineering,* 58, 1873-1905.

Benzeggagh, M. L.&Kenane, M. (1996) Measurement of mixed-mode delamination fracture toughness of unidirectional glass/epoxy composites with mixed-mode bending apparatus. *Composites science and technology,* 56, 439-449.

Bower, A. F.&Guduru, P. R. (2012) A simple finite element model of diffusion, finite deformation, plasticity and fracture in lithium ion insertion electrode materials. *Modelling and Simulation in Materials Science and Engineering,* 20, 045004.

Camacho, G. T.&Ortiz, M. (1996) Computational modelling of impact damage in brittle materials. *International Journal of Solids and Structures,* 33, 2899-2938.

Choi, H. Y., Downs, R. J.&Chang, F. K. (1991a) A new approach toward understanding damage mechanisms and mechanics of laminated composites due to low-velocity impact: Part I-experiments. *Journal of Composite Materials,* 25, 992-1011.

Choi, H. Y., Wu, H. Y. T.&Chang, F. K. (1991b) A new approach toward understanding damage mechanisms and mechanics of laminated

composites due to low-velocity impact: Part II-analysis. *Journal of Composite Materials,* 25**,** 1012-1038.

Dugdale, D. S. (1960) Yielding of steel sheets containing slits. *Journal of the Mechanics and Physics of Solids,* 8**,** 100-104.

Espinosa, H. D., Dwivedi, S.&Lu, H. C. (2000) Modeling impact induced delamination of woven fiber reinforced composites with contact/cohesive laws. *Computer Methods in Applied Mechanics and Engineering,* 183**,** 259-290.

Ferrara, A.&Pandolfi, A. (2008) Numerical modelling of fracture in human arteries. *Computer methods in biomechanics and biomedical engineering,* 11**,** 553-567.

Fuchs, P. F.&Major, Z. (2011) Experimental Determination of Cohesive Zone Models for Epoxy Composites. *Experimental Mechanics,* 51**,** 779-786.

Gasser, T. C.&Holzapfel, G. A. (2007) Modeling plaque fissuring and dissection during balloon angioplasty intervention. *Annals of Biomedical Engineering,* 35**,** 711-723.

Gehlen, P. C.&Kanninen, M. F. (1969) An atomic model for cleavage crack propagation in Alpha iron. DTIC Document.

Geubelle, P. H.&Baylor, J. S. (1998) Impact-induced delamination of composites: a 2D simulation. *COMPOS PART B: ENG,* 29**,** 589-602.

Grantab, R.&Shenoy, V. B. (2011) Location-and Orientation-Dependent Progressive Crack Propagation in Cylindrical Graphite Electrode Particles. *Journal of the Electrochemical Society,* 158**,** A948.

Graziano, F. (2000) Coil and sheet coating. *Metal Finishing,* 98**,** 175-176.

Griffith, A. A. (1921) The phenomena of rupture and flow in solids. *Philosophical transactions of the royal society of london. Series A, containing papers of a mathematical or physical character,* 221**,** 163-198.

Hillerborg, A., Modeer, M.&Petersson, P. E. (1976) Analysis of crack formation and crack growth in concrete by means of fracture mechanics and finite elements. *Cement and concrete research,* 6**,** 773-781.

Hopkins, C. G., McHugh, P. E.&McGarry, J. P. (2010) Computational Investigation of the Delamination of Polymer Coatings During Stent Deployment. *Annals of Biomedical Engineering,* 38**,** 2263-2273.

Hu, J., Chou, Y. K.&Thompson, R. G. (2008) Cohesive zone effects on coating failure evaluations of diamond-coated tools. *Surface and Coatings Technology,* 203**,** 730-735.

Hutar, P., Nahlik, L., Sestakova, L., Sevcik, M., Knesl, Z.&Nezbedova, E. (2010) A fracture mechanics assessment of surface cracks existing in protective layers of multi-layer composite pipes. *Composite structures,* 92**,** 1120-1125.

Hutchinson, J. W. (1968) Singular behaviour at the end of a tensile crack in a hardening material. *Journal of the Mechanics and Physics of Solids,* 16**,** 13-31.

Inglis, C. E. (1913) Stresses in a cracked plate due to the presence of cracks and sharp corners. *Transaction of Naval Architects (London),* 60**,** 213.

Irwin, G. R. (1948) Fracture dynamics. *Fracturing of metals,* 147**,** 166.

Irwin, G. R. (1957) Analysis of stresses and strains near the end of a crack traversing a plate. *J. appl. Mech.*

Irwin, G. R. (1960) Plastic zone near a crack and fracture toughness. Mechanical and Metallurgical Behaviour of Sheet Materials.

Irwin, G. R.&Kies, J. A. (1952) Fracturing and fracture dynamics. *Welding Journal,* 31**,** 95s-100s.

Janko, M., Ecker, W., Pinter, G.&Kolednik, O. (2012) Numerical Simulation of Crack Growth in Polyethylene Composites by Means of the Cohesive Zone Model. Wiley Online Library.

Jin, Z. H., Paulino, G. H.&Dodds Jr, R. H. (2002) Finite element investigation of quasi-static crack growth in functionally graded materials using a novel cohesive zone fracture model. *Journal of Applied Mechanics,* 69**,** 370.

Kalthoff, J. F.&Winkler, S. (1988) Failure mode transition at high rates of shear loading. *DGM Informationsgesellschaft mbH, Impact Loading and Dynamic Behavior of Materials,* 1**,** 185-195.

Kandula, S. S. V., Abanto-Bueno, J., Geubelle, P. H.&Lambros, J. (2005) Cohesive modeling of dynamic fracture in functionally graded materials. *International Journal of Fracture,* 132**,** 275-296.

Landes, J. D.&Begley, J. A. (1972) The Effect of Specimen Geometry on J/c.

Li, H.&Chandra, N. (2003) Analysis of crack growth and crack-tip plasticity in ductile materials using cohesive zone models. *International Journal of Plasticity,* 19**,** 849-882.

Li, V. C.&Ward, R. J. (1989) A novel testing technique for post-peak tensile behaviour of cementitious materials. *Fracture Toughness and Fracture Energy Testing Methods for Concrete and Rocks. AA Balkema Publishers, Rotterdam***,** 183-195.

Lin, G., Meng, X. G., Cornec, A.&Schwalbe, K. H. (1999) The effect of strength mis-match on mechanical performance of weld joints. *International Journal of Fracture,* 96**,** 37-54.

Marzi, S., Hesebeck, O., Brede, M.&Kleiner, F. (2009) A rate-dependent cohesive zone model for adhesively bonded joints loaded in mode I. *Journal of adhesion science and technology,* 23**,** 881-898.

Mason, D. D. (1979) Segregation-induced embrittlement of grain boundaries. *Philosophical Magazine A,* 39**,** 455-468.

Moes, N.&Belytschko, T. (2002) Extended finite element method for cohesive crack growth. *Engineering Fracture Mechanics,* 69**,** 813-833.

Nakamura, T.&Wang, Z. (2001) Simulations of Crack Propagation in Porous Materials. *Journal of Applied Mechanics,* 68**,** 242-251.

Natarajan, S., Mahapatra, D. R.&Bordas, S. (2010) Integrating strong and weak discontinuities without integration subcells and example applications in an XFEM/GFEM framework. *International Journal for Numerical Methods in Engineering,* 83**,** 269-294.

Needleman, A. (1987) A continuum model for void nucleation by inclusion debonding. *Journal of Applied Mechanics,* 54**,** 525-531.

Needleman, A. (1990) An analysis of tensile decohesion along an interface. *Journal of the Mechanics and Physics of Solids,* 38**,** 289-324.

Needleman, A. (1990b) An analysis of decohesion along an imperfect interface. *International Journal of Fracture,* 42**,** 21-40.

Needleman, A. (1992) Micromechanical modelling of interfacial decohesion. *Ultramicroscopy,* 40**,** 203-214.

Ng, K.&Dai, Q. (2012) Tailored Extended Finite-Element Model for Predicting Crack Propagation and Fracture Properties within Idealized and Digital Cementitious Material Samples. *Journal of engineering mechanics,* 138**,** 89.

O Connor, A. E.&Willenbacher, N. (2004) The effect of molecular weight and temperature on tack properties of model polyisobutylenes. *International journal of adhesion and adhesives,* 24**,** 335-346.

Orowan, E. (1949) Fracture and strength of solids. *Reports on progress in physics,* 12**,** 185.

Ortiz, M.&Pandolfi, A. (1999) Finite-deformation irreversible cohesive elements for three-dimensional crack-propagation analysis. *International Journal for Numerical Methods in Engineering,* 44**,** 1267-1282.

Ortiz, M.&Suresh, S. (1993) Statistical properties of residual stresses and intergranular fracture in ceramic materials. *Transactions-American Society of Mechanical Engineers-Journal of Applied Mechanics,* 60**,** 77-77.

Ouyang, Z.&Li, G. (2009) Cohesive zone model based analytical solutions for adhesively bonded pipe joints under torsional loading. *International Journal of Solids and Structures,* 46**,** 1205-1217.

Pandolfi, A., Krysl, P.&Ortiz, M. (1999) Finite element simulation of ring expansion and fragmentation: The capturing of length and time scales through cohesive models of fracture. *International Journal of Fracture,* 95**,** 279-297.

Papoulia, K. D., Sam, C. H.&Vavasis, S. A. (2003) Time continuity in cohesive finite element modeling. *International Journal for Numerical Methods in Engineering,* 58**,** 679-701.

Papoulia, K. D., Vavasis, S. A.&Ganguly, P. (2006) Spatial convergence of crack nucleation using a cohesive finite-element model on a pinwheel-based mesh. *International Journal for Numerical Methods in Engineering,* 67**,** 1-16.

Park, K., Paulino, G. H.&Roesler, J. R. (2009) A unified potential-based cohesive model of mixed-mode fracture. *Journal of the Mechanics and Physics of Solids,* 57**,** 891-908.

Parks, D. M. (1977) The virtual crack extension method for nonlinear material behavior. *Computer Methods in Applied Mechanics and Engineering,* 12**,** 353-364.

Paulino, G. H., Celes, W., Espinha, R.&Zhang, Z. J. (2008) A general topology-based framework for adaptive insertion of cohesive elements in finite element meshes. *Engineering with Computers,* 24**,** 59-78.

Planas, J.&Elices, M. (1993) Asymptotic analysis of a cohesive crack: 2. Influence of the softening curve. *International Journal of Fracture,* 64**,** 221-237.

Rahul-Kumar, P., Jagota, A., Bennison, S. J., Saigal, S.&Muralidhar, S. (1999) Polymer interfacial fracture simulations using cohesive elements. *Acta Materialia,* 47**,** 4161-4169.

Remmers, J. J. C. (2006) Discontinuities in materials and structures: a unifying computational approach.

Remmers, J. J. C., Borst, R.&Needleman, A. (2003) A cohesive segments method for the simulation of crack growth. *Computational Mechanics,* 31**,** 69-77.

Remmers, J. J. C., De Borst, R.&Needleman, A. (2008) The simulation of dynamic crack propagation using the cohesive segments method. *Journal of the Mechanics and Physics of Solids,* 56**,** 70-92.

Rice, J. R. (1967) A path independent integral and the approximate analysis of strain concentration by notches and cracks. DTIC Document.

Rice, J. R.&Rosengren, G. F. (1968) Plane strain deformation near a crack tip in a power-law hardening material. *Journal of the Mechanics and Physics of Solids,* 16**,** 1-12.

Rice, J. R.&Thomson, R. (1974) Ductile versus brittle behaviour of crystals. *Philosophical Magazine,* 29**,** 73-97.

Rose, J. H., Ferrante, J.&Smith, J. R. (1981) Universal binding energy curves for metals and bimetallic interfaces. *Physical Review Letters,* 47**,** 675-678.

Rose, J. H., Smith, J. R.&Ferrante, J. (1983) Universal features of bonding in metals. *Physical Review B,* 28**,** 1835-1845.

Samimi, M., Van Dommelen, J. A. W.&Geers, M. G. D. (2011) A self-adaptive finite element approach for simulation of mixed-mode delamination using cohesive zone models. *Engineering Fracture Mechanics*.

Schwalbe, K. H.&Kocak, M. (1997) Mis-matching of interfaces and welds. *Proceedings of the Second International Symposium on Mis-Matching of Welds*

Schwalbe, K. H., Kocak, M.&European Structural Integrity, S. (1994) *Mis-matching of Welds: Papers Presented at the International Symposium on Mis-Matching of Welds--Performance of Strength Mis-Matched Welded Or Bonded Joints, Reinstorf-Luneburg, Germany, 26-28 May 1993*, Mechanical Engineering Publications.

Shih, C. F., Moran, B.&Nakamura, T. (1986) Energy release rate along a three-dimensional crack front in a thermally stressed body. *International Journal of Fracture,* 30**,** 79-102.

Shim, D. J., Paulino, G. H.&Dodds, R. H. (2006) J resistance behavior in functionally graded materials using cohesive zone and modified boundary layer models. *International Journal of Fracture,* 139**,** 91-117.

Song, S. H., Paulino, G. H.&Buttlar, W. G. (2006) Simulation of crack propagation in asphalt concrete using an intrinsic cohesive zone model. *Journal of engineering mechanics,* 132**,** 1215.

Sørensen, B. F.&Jacobsen, T. K. (2003) Determination of cohesive laws by the J integral approach. *Engineering Fracture Mechanics,* 70**,** 1841-1858.

Strouboulis, T., Copps, K.&Babuska, I. (2001) The generalized finite element method. *Computer Methods in Applied Mechanics and Engineering,* 190**,** 4081-4193.

Sun, Y., Beltz, G. E.&Rice, J. R. (1993) Estimates from atomic models of tension-shear coupling in dislocation nucleation from a crack tip. *Materials Science and Engineering: A,* 170**,** 67-85.

Tijssens, M. G. A., Van Der Giessen, E.&Sluys, L. J. (2000) Modeling of crazing using a cohesive surface methodology. *Mechanics of Materials,* 32**,** 19-35.

Tvergaard, V. (1990) Effect of fibre debonding in a whisker-reinforced metal. *Name: Materials Science and Engineering, A: Structural Materials: Properties, Microstructure and Processing*.

Tvergaard, V.&Hutchinson, J. W. (1992) The relation between crack growth resistance and fracture process parameters in elastic-plastic solids. *Journal of the Mechanics and Physics of Solids,* 40**,** 1377-1397.

Tvergaard, V.&Hutchinson, J. W. (1993) The influence of plasticity on mixed mode interface toughness. *Journal of the Mechanics and Physics of Solids,* 41**,** 1119-1135.

Ural, A., Krishnan, V. R.&Papoulia, K. D. (2009) A cohesive zone model for fatigue crack growth allowing for crack retardation. *International Journal of Solids and Structures,* 46**,** 2453-2462.

Ural, A.&Vashishth, D. (2006) Cohesive finite element modeling of age-related toughness loss in human cortical bone. *Journal of Biomechanics,* 39**,** 2974-2982.

van den Bosch, M. J., Schreurs, P. J. G.&Geers, M. G. D. (2006) An improved description of the exponential Xu and Needleman cohesive zone law for mixed-mode decohesion. *Engineering Fracture Mechanics,* 73**,** 1220-1234.

van den Bosch, M. J., Schreurs, P. J. G.&Geers, M. G. D. (2007) A cohesive zone model with a large displacement formulation accounting for interfacial fibrilation. *European Journal of Mechanics-A/Solids,* 26**,** 1-19.

Wang, J. S.&Anderson, P. M. (1991) Fracture behavior of embrittled FCC metal bicrystals. *Acta metallurgica et materialia,* 39**,** 779-792.

Washabaugh, P. D.&Knauss, W. G. (1994) A reconciliation of dynamic crack velocity and Rayleigh wave speed in isotropic brittle solids. *International Journal of Fracture,* 65**,** 97-114.

Wei, Y.&Hutchinson, J. W. (2008) Toughness of Ni/Al2O3 interfaces as dependent on micron-scale plasticity and atomistic-scale separation. *Philosophical Magazine,* 88**,** 3841 - 3859.

Wells, A. A. (1961) Unstable crack propagation in metals: cleavage and fast fracture.

Wells, G. N.&Sluys, L. J. (2001) A new method for modelling cohesive cracks using finite elements. *International Journal for Numerical Methods in Engineering,* 50**,** 2667-2682.

Xu, X. P.&Needleman, A. (1993) Void nucleation by inclusion debonding in a crystal matrix. *Modelling and Simulation in Materials Science and Engineering,* 2**,** 417-418.

Xu, X. P.&Needleman, A. (1994) Numerical simulations of fast crack growth in brittle solids. *Journal of the Mechanics and Physics of Solids,* 42**,** 1397-1434.

Yan, Y.&Shang, F. (2009) Cohesive zone modeling of interfacial delamination in PZT thin films. *International Journal of Solids and Structures,* 46**,** 2739-2749.

Yang, Q. D.&Thouless, M. D. (2001) Mixed-mode fracture analyses of plastically-deforming adhesive joints. *International Journal of Fracture,* 110**,** 175-187.

Yang, Z. J.&Deeks, A. J. (2007) Fully-automatic modelling of cohesive crack growth using a finite element-scaled boundary finite element coupled method. *Engineering Fracture Mechanics,* 74**,** 2547-2573.

Zavattieri, P. D.&Espinosa, H. D. (2001) Grain level analysis of crack initiation and propagation in brittle materials. *Acta Materialia,* 49**,** 4291-4311.

Zhang, Z. J.&Paulino, G. H. (2005) Cohesive zone modeling of dynamic failure in homogeneous and functionally graded materials. *International Journal of Plasticity,* 21**,** 1195-1254.

Zhu, W. L.&Luo, D. M. (2011) The Application of the Cohesive Zone Model on the Analysis of Mechanical Properties of Carbon Nano-Tube Composites with Debonding Interface. *Proceedings of the 6th International Conference on Advanced Materials and Processing*

Zosel, A. (1998) The effect of fibrilation on the tack of pressure sensitive adhesives. *International journal of adhesion and adhesives,* 18**,** 265-271.

2.6. Tables and Figures
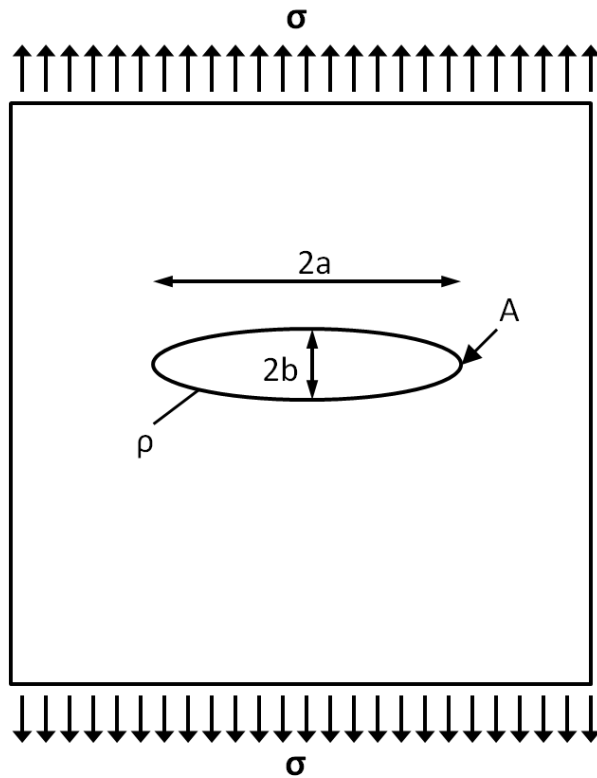
Figure 2-1: Elliptical hole in a flat plate where the plate is subjected to a tensile stress, σ. Point A is the location of the crack tip on the major axis of the ellipse. ρ denotes the radius of curvature of the ellipse.
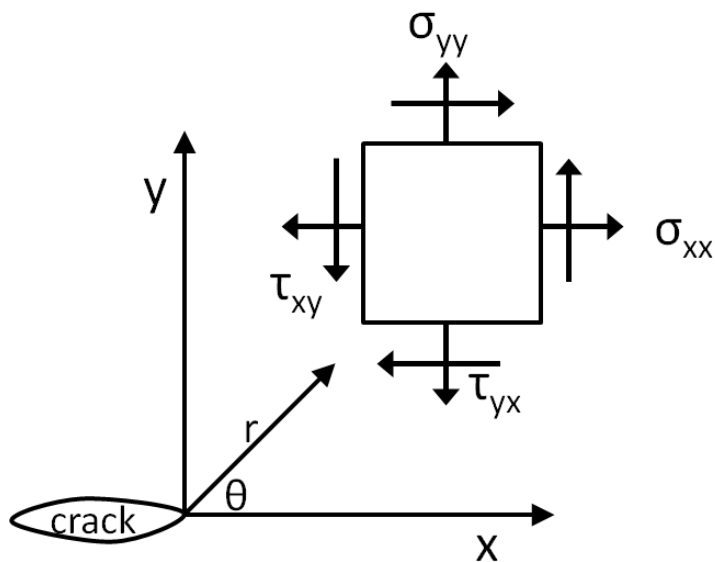
Figure 2-2: Schematic of an element of material located near a crack tip subjected to normal (σ) and shear (τ) stresses.
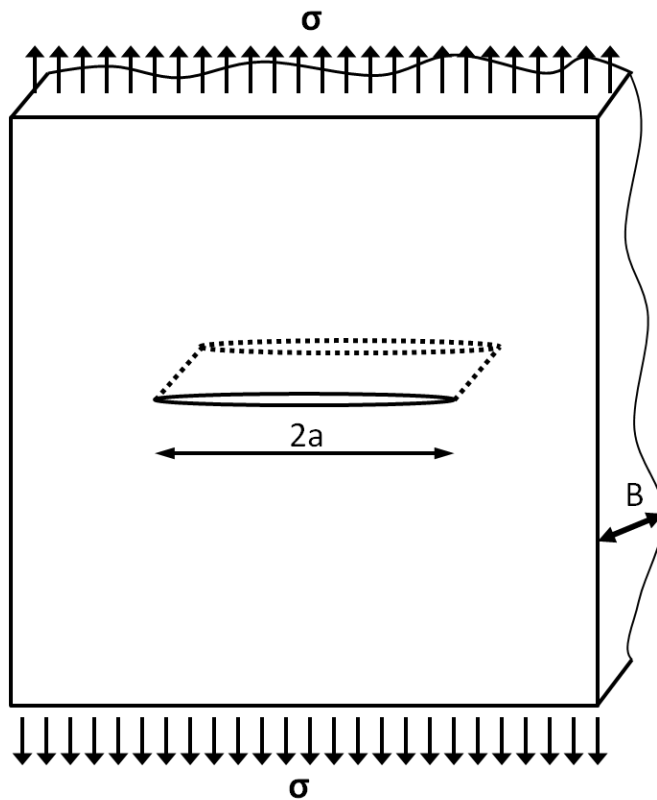
Figure 2-3: An infinite plate subjected to remote tensile stress containing a through thickness-crack. The term 'infinite' is used to emphasise that the plate width is $\gg 2a$.
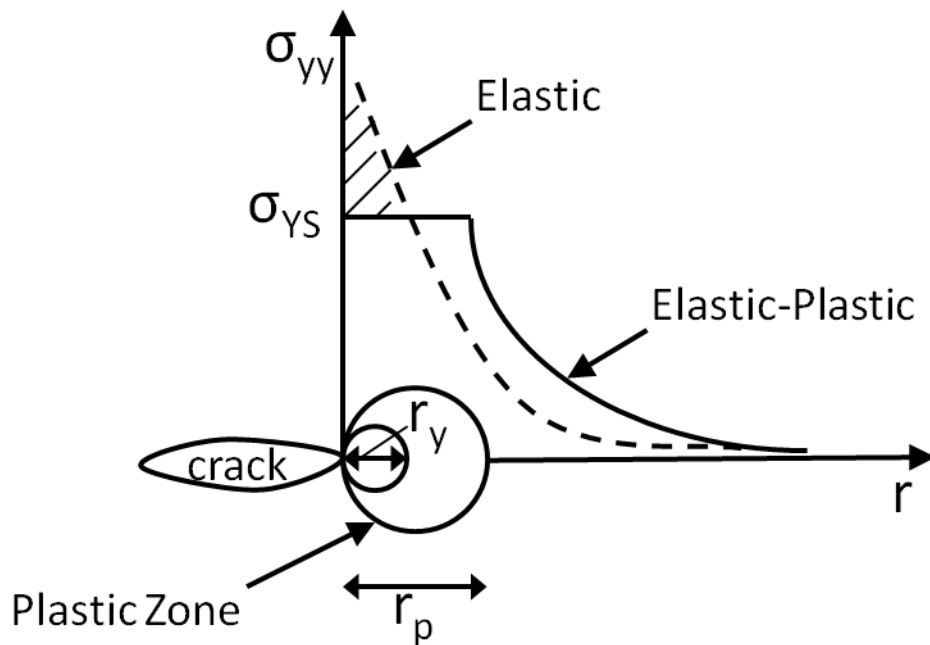
Figure 2-4: First order (r_y) and second order (r_p) approximations of plastic zone size based on the Irwin approach. The hatched area represents the work that must be redistributed to account for plasticity.
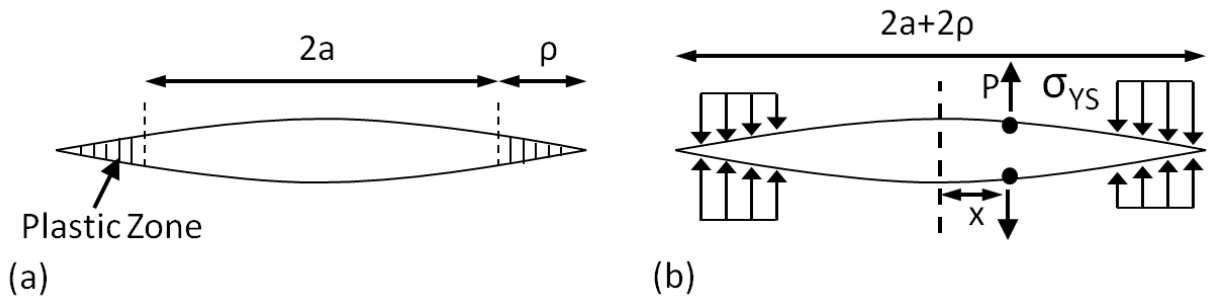
Figure 2-5: The strip yield model with (a) plastic zones at each end of the crack highlighted and (b) location of applied closure stresses, σ_{YS}.
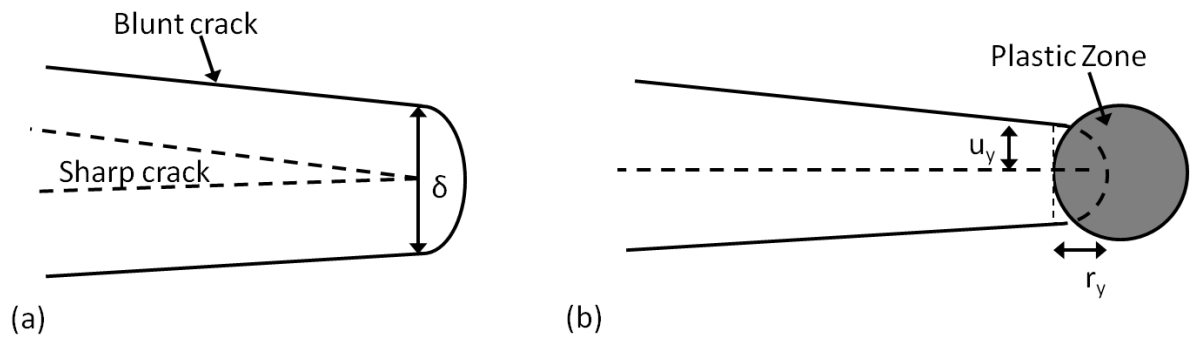
Figure 2-6: Crack tip opening displacement- (a) An initially sharp crack blunts following plastic deformation, resulting in a finite displacement, δ, at the crack tip. (b) Estimation of the crack tip opening displacement from displacement of the effective crack in the Irwin plastic zone correction.
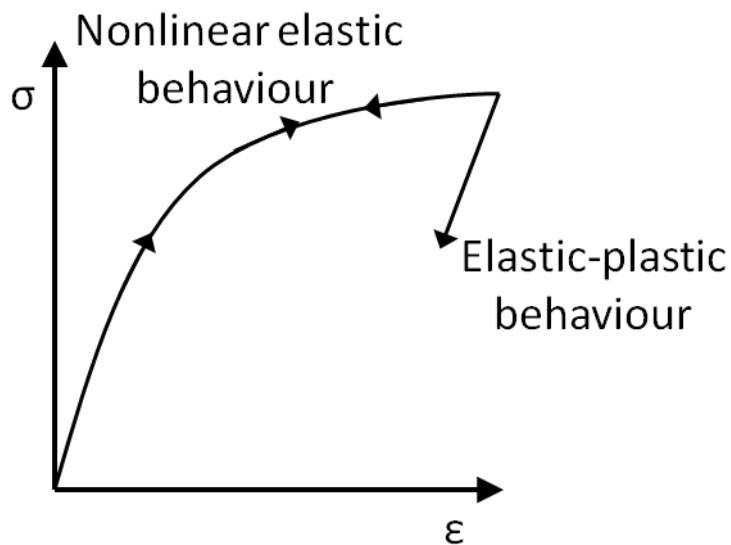
Figure 2-7: Comparison of stress-strain behaviour of nonlinear elastic and elastic-plastic materials.
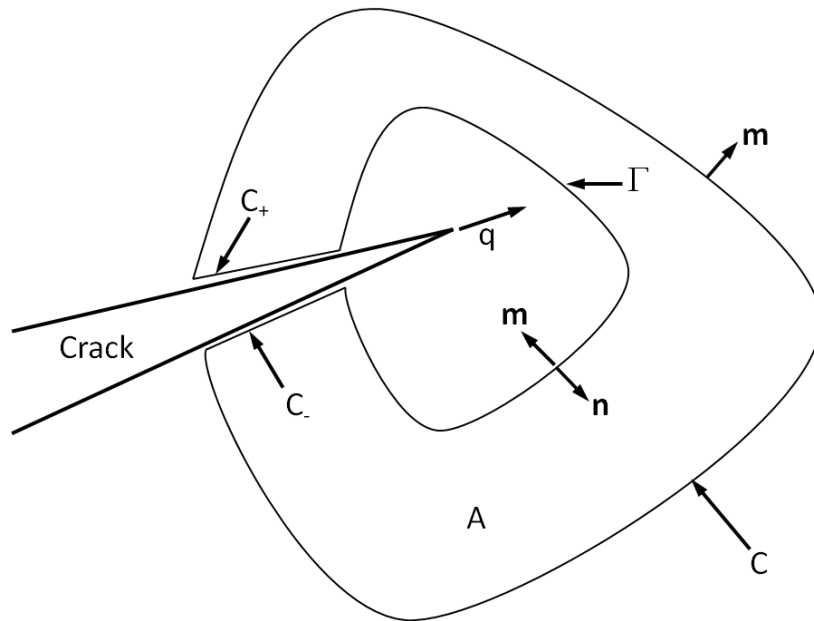
Figure 2-8: 2-D evaluation of the J-integral. The closed contour, $C + C_+ + \Gamma + C_-$ encloses a domain, A, that includes the crack tip region.
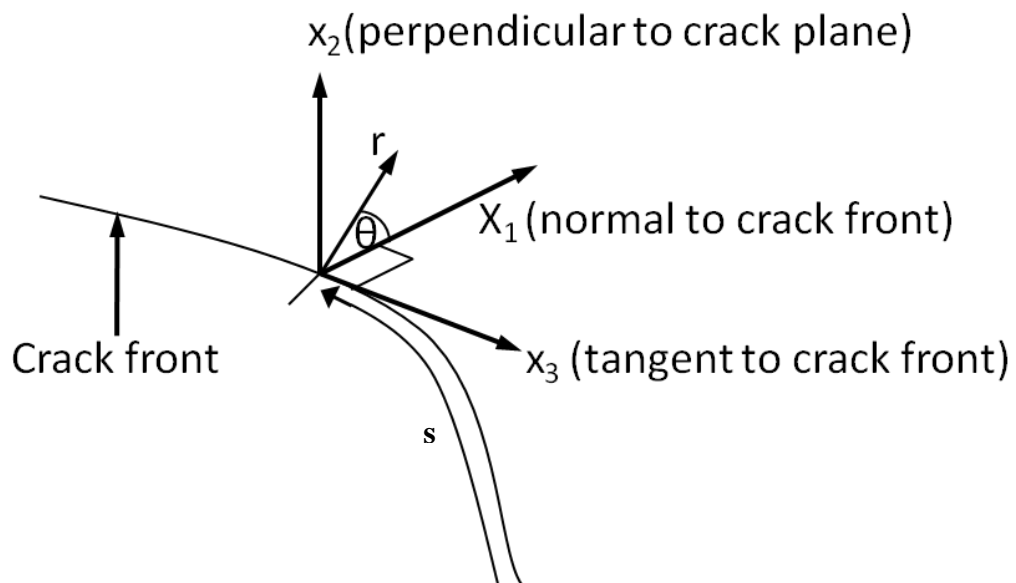
Figure 2-9: Definition of the local orthogonal Cartesian co-ordinates at the point, s, on the crack front. The crack is in the $x_1 - x_3$ plane.
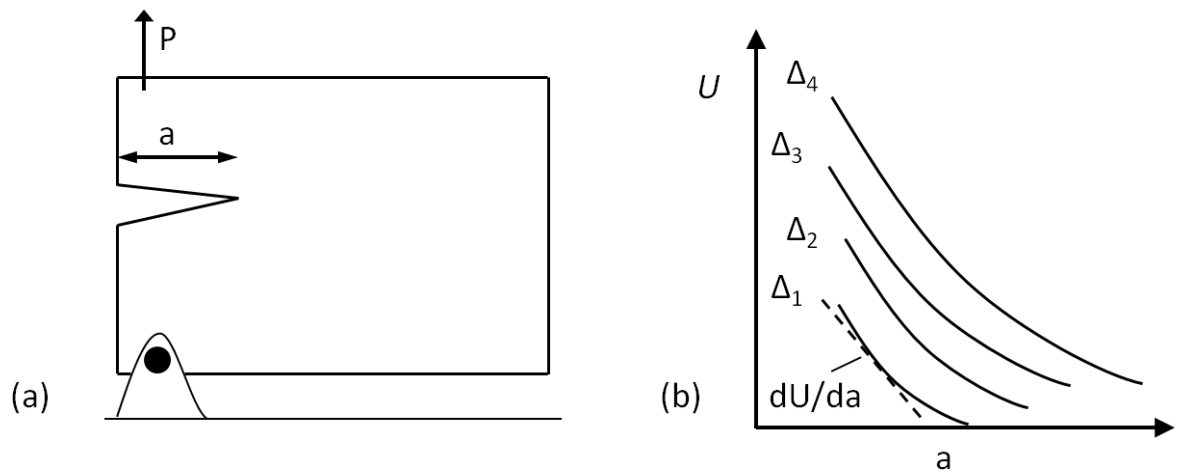
Figure 2-10: (a) Schematic of experimental investigation of J-integral where P is applied force and a is crack length. (b) The energy absorbed by a specimen, U, as a function of crack length, a. J is computed by evaluating the slope to the tangent of each test curve.
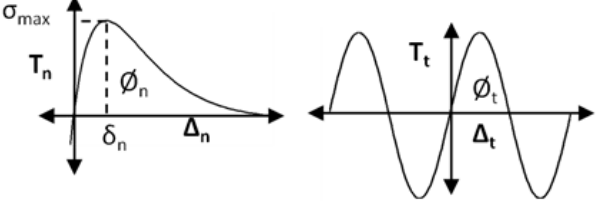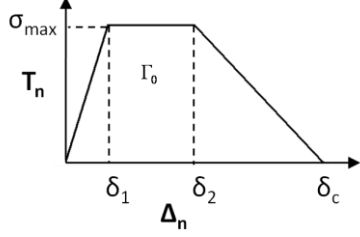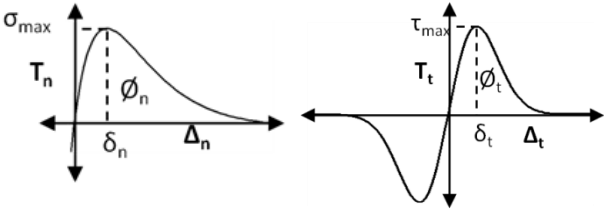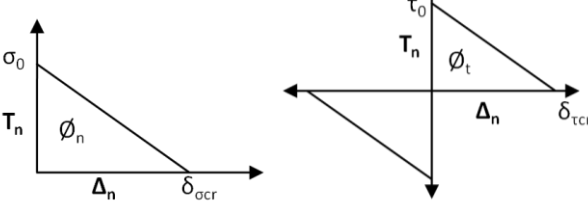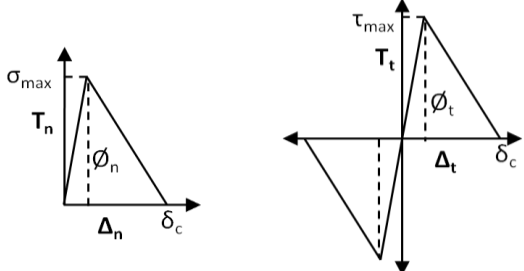
Model Representation	Model Type and Parameters
	Model Type: Exponential. Trigonometric fit for shear traction $\emptyset_n$ and $\emptyset_t$ are the work of normal and tangential separation respectively. σ_{max} is the peak normal strength. δ_n is the normal critical displacement. (Needleman, 1990b)
	Model Type: Trapezoidal Γ_0 is the work of separation. σ_{max} is the peak normal strength. δ_c is the critical displacement. δ_1 and δ_2 are shape factors. (Tvergaard and Hutchinson, 1992)
	Model Type: Exponential $\emptyset_n$ and $\emptyset_t$ are the work of normal and tangential separation respectively. σ_{max} is the peak normal strength. δ_n and δ_t are the normal and tangential critical displacements respectively. (Xu and Needleman, 1993)
	Model Type: Rigid-linear σ_0 and τ_0 are normal and shear stress at fracture initiation respectively. $\delta_{\sigma cr}$ and $\delta_{\tau cr}$ are normal and shear critical opening displacements respectively. (Camacho and Ortiz, 1996)
	Model Type: Bilinear σ_{max} and τ_{max} are the peak normal and tangential strengths respectively. δ_c is the critical opening displacement. (Geubelle and Baylor, 1998)

Table 2-1: Traction-separation relationships and description of commonly adopted cohesive zone models.

3. Theoretical Analysis of Potential-Based and Non-Potential-Based Cohesive Zone Formulations Under Mixed-Mode Separation and Over-closure

3.1. Introduction

In the present chapter, a thorough analysis of potential-based and non-potential-based cohesive zone formulations in mixed-mode over-closure and separation is presented. The focus of the first series of analyses presented in this chapter is the commonly implemented cohesive zone model of Xu-Needleman (Xu and Needleman, 1993) in which traction-separation relationships are obtained from the first derivatives of an interface potential function. This exponential form of cohesive zone law originated from the universal relationship between binding energies and atomic separation of bimetallic interfaces (Rose et al., 1981; Rose et al., 1983). The Xu-Needleman (XN) law has been used to describe many mixed-mode decohesion processes, including: interfacial delamination in piezoelectric thin films (Yan and Shang, 2009); coating failure evaluations of diamond-coated tools (Hu et al., 2008); the effect of bond strength and loading rate on the conditions governing the attainment of intersonic crack growth along interfaces (Needleman and Rosakis, 1999); the analysis of crack growth and crack-tip plasticity in ductile materials (Li and Chandra, 2003) and the analysis of crack propagation in porous materials (Nakamura and Wang, 2001).

In the Xu-Needleman (XN) model, normal and tangential behaviour is coupled via exponentially decaying functions of normal and tangential separation. The ratio of the work of tangential separation $(\emptyset_t)$ to the work of normal separation $(\emptyset_n)$, conventionally denoted using the symbol "q", determines the relative strength of the interface under mode I and mode II separation. A similar potential-based model was also proposed by Beltz and Rice (1992), in which a sinusoidal

tangential traction-separation relationship is coupled with an XN type normal traction-separation relationship. Again, the ratio of work of tangential separation to the work of normal separation provides a critical coupling parameter in this model. Several experimental studies have reported that the work of normal and tangential separation required for interfacial fracture are different (Dollhofer et al., 2000; Warrior et al., 2003; Yang et al., 2001). Mode II interface toughness has been reported to be stronger than mode I strength in numerous experimental studies involving ductile material (Cao and Evans, 1989; Chai and Liechti, 1992; Thouless, 1990; O'Dowd et al., 1992). However, the ratio of tangential to normal work, q, is arbitrarily set to unity for many mixed-mode implementations of the XN cohesive zone model (Rahulkumar et al., 2000; Yuan and Chen, 2003; Zavattieri et al., 2008). It should also be noted that a number of previous studies adopt a value of $q \approx 0.43$ so that both the normal and tangential maximum tractions have the same value when the normal and tangential interface characteristic distances are assumed to be equal (Abdul-Baqi and Van der Giessen, 2002; Hattiangadi and Siegmund, 2005; Hopkins et al., 2010). A range of values of q ranging from 0.025 to 10 were considered in the original application of the XN model to debonding of spherical inclusions in a metal matrix composite (Xu and Needleman, 1993). In the study of thin film delamination, values of q ranging from 0.086 to 0.7 were considered by Abdul-Baqi and Van der Giessen (2001), while most recently a value of $q = 0.5$ was used by Yan and Shang (2009).

A second coupling parameter used in the XN model is the traction free normal separation following complete shear separation (commonly denoted using the symbol "r" in the XN potential function). It was noted by Abdul-Baqi and Van der Giessen (2001) that physically realistic penalisation of normal over-closure was computed only if $r \geq q$. However, the majority of studies that use the XN model set $r = 0$ (Rahulkumar et al., 2000; Xu and Needleman, 1993; Zavattieri et al., 2008). Furthermore, a study by van den Bosch et al. (2006) suggested that physically realistic coupling is implemented by the XN model only when $q = 1$. An alternative non-potential cohesive zone formulation was proposed by the

authors, based on the XN traction-separation equations with $q = 1$, for cases where normal and tangential interface strengths differ.

To date, no comprehensive analysis of the XN CZM has been published in which the complete range of diverse interface behaviour under mixed-mode separation and mixed-mode over-closure has been characterised. In Section 3.2 of this chapter (Model Development) a comprehensive and rigorous analysis of the XN CZM is presented, significantly expanding on the initial analyses of Abdul-Baqi and Van der Giessen (2001) and van den Bosch et al. (2006). It is demonstrated in this chapter, for the first time, that no combination of model parameters exist to provide physically realistic behaviour under both mixed-mode separation and mixed-mode over-closure for the XN potential-based model. A modified potential-based (MP) model was proposed by McGarry et al. (2012) as an alternative to the XN model. In this chapter, a theoretical analysis of the performance of this modified model under mixed-mode conditions is presented, for the first time. Specifically, it is established in Section 3.2.1.6 that this modified potential-based model can significantly improve upon the XN model under mixed-mode conditions. In particular, improved coupling is demonstrated both for mixed-mode separation and over-closure.

While it is demonstrated in Section 3.2.1 that the MP model provides a significant improvement on the XN model, it should be noted that unphysical interface behaviour, uncovered in Sections 3.2.1.1-3.2.1.6, cannot be fully eliminated if a CZM is derived from a potential function. Therefore, non-potential-based CZMs are subsequently considered in Section 3.2.2. Firstly, it is demonstrated that the non-potential CZM proposed by van den Bosch et al. (2006) (VB) fails to provide physically realistic behaviour under mixed-mode over-closure. Two non-potential models (NP1, NP2) proposed by McGarry et al. (2012) as an alternative to the VB formulation are then analysed. It is demonstrated that both of these alternative formulations provide physically reasonable coupling under both mixed-mode separation and over-closure. Finally, a formulation that relies on separation magnitude for coupling of normal and tangential behaviour (SMC model) is

considered. This model possesses the ability to provide mode-independent work of separation, but it does not provide any penalisation of over-closure due the reliance of the coupling terms of the equations on separation magnitude.

3.2. Model Development

3.2.1. Potential-Based Formulations

3.2.1.1. Xu-Needleman Formulation

The XN cohesive zone law has frequently been used to model numerous fracture mechanics problems. This law is based on the definition of an interface potential, $\emptyset$, representing the work done when two opposing surfaces at an interface undergo a relative separation, $\underline{\Delta}$ (Xu and Needleman, 1993). The resulting tractions are given by;

$$\underline{T}(\underline{\Delta}) = \partial\emptyset(\underline{\Delta})/\partial\underline{\Delta} \tag{3.1}$$

The interface potential is given by;

$$\emptyset\,(\Delta_n, \Delta_t) = \emptyset_n + \emptyset_n \exp\left(-\frac{\Delta_n}{\delta_n}\right)$$

$$\left[\left\{1 - r + \frac{\Delta_n}{\delta_n}\right\}\left(\frac{1-q}{r-1}\right) - \left\{q + \left(\frac{r-q}{r-1}\right)\frac{\Delta_n}{\delta_n}\right\}exp\left(-\frac{\Delta_t^2}{\delta_t^2}\right)\right] \tag{3.2}$$

Coupling in this model is controlled through the parameters q and r;

where, $q = \emptyset_t/\emptyset_n \qquad r = \Delta_n^*/\delta_n$

$\emptyset_n$ and $\emptyset_t$ are the work of normal and tangential separation respectively. The normal and tangential components of the interface separation vector, $\underline{\Delta}$, are Δ_n and Δ_t respectively. The normal and tangential interface characteristic lengths are δ_n and δ_t respectively and Δ_n^* is the value of Δ_n after complete tangential separation takes place under the condition of normal tension being zero ($T_n = 0$).

Using Equations (3.1) and (3.2), the interfacial tractions are obtained as follows;

$$T_n = \frac{\partial \emptyset}{\partial \Delta_n} = \left(\frac{\emptyset_n}{\delta_n}\right) exp\left(-\frac{\Delta_n}{\delta_n}\right) \left\{ \frac{\Delta_n}{\delta_n} exp\left(-\frac{\Delta_t^2}{\delta_t^2}\right) \right.$$
$$\left. + \frac{1-q}{r-1}\left[1 - exp\left(-\frac{\Delta_t^2}{\delta_t^2}\right)\right]\left[r - \frac{\Delta_n}{\delta_n}\right]\right\}$$

(3.3)

$$T_t = \frac{\partial \emptyset}{\partial \Delta_t} = 2\left(\frac{\emptyset_n}{\delta_n}\right)\left(\frac{\delta_n}{\delta_t}\right)\frac{\Delta_t}{\delta_t}\left\{q + \left(\frac{r-q}{r-1}\right)\frac{\Delta_n}{\delta_n}\right\}$$
$$exp\left(-\frac{\Delta_n}{\delta_n}\right) exp\left(-\frac{\Delta_t^2}{\delta_t^2}\right)$$

(3.4)

The characteristic lengths δ_n and δ_t are given by;

$$\delta_n = \emptyset_n / \left(\sigma_{max} exp(1)\right)$$

(3.5)

$$\delta_t = \emptyset_t / \left(\tau_{max}(0.5\, exp(1))^{0.5}\right)$$

(3.6)

where σ_{max} is the maximum normal traction without tangential separation and τ_{max} is the maximum tangential traction without normal separation.

3.2.1.2. *Work of Separation in Xu-Needleman Cohesive Zone Law*

Figure 3-1(a) shows the work of separation as a function of both normal and tangential separations for $q > 1$. Two paths are compared to obtain the same final mixed-mode interface separation configuration. Undergoing interface separation along the path indicated by the green arrows from the unseparated configuration $(\Delta_n/\delta_n = \Delta_t/\delta_t = 0)$ to the final fully separated mixed-mode configuration $(\Delta_n/\delta_n = \Delta_t/\delta_t = 5)$, it is clear that the work done during initial normal separation is $\emptyset_n$ (in accordance with Equation (3.2)). As is also clear from Equation (3.2), the work done for full mixed-mode separation is also $\emptyset_n$. Therefore no subsequent work is done for tangential separation following initial normal separation. In contrast to the path indicated by the green arrows, the red arrows outline a path in which tangential separation is followed by normal separation. For $q > 1$, clearly the work done during the initial tangential separation is greater than $\emptyset_n$. However, the work of full mixed-mode separation

must be $\emptyset_n$, in accordance with Equation (3.2). Therefore, following initial tangential separation, negative work (red arrow) must be performed to achieve full mixed-mode separation. This negative work gradient results in negative (repulsive) normal tractions for mixed-mode separation conditions.

Figure 3-1(b) shows the work of separation as a function of both normal and tangential separations for $q < 1$. Considering the path outlined by the green arrows, the work done during initial normal separation is again $\emptyset_n$ and no subsequent work is done for tangential separation following normal separation. However, considering the path outlined by the red arrows, when $q < 1$, the work done during the initial tangential separation is less than $\emptyset_n$. Therefore, in the case where $q < 1$, following initial tangential separation, normal work is still required to reach full interface separation configuration as the value of work at full mixed-mode separation must be $\emptyset_n$. Therefore, positive normal tractions are computed following full tangential separation when $q < 1$. A more physical coupling of normal and tangential behaviour should ensure that, following complete tangential separation at the interface, zero work (and consequently zero traction) should be required for normal separation and vice versa. Tractions which exist following complete interface separation in either the tangential or normal component directions are hereafter referred to as residual tractions.

Figure 3-1 (c) shows the maximum normal traction * $T_{n,max}$ as a function of tangential separation. Residual normal tractions for mixed-mode interface separation are evident. The value of maximum normal traction, $T_{n,max}$ after complete tangential separation can be expressed as;

$$T_{n,max} = -\sigma_{max} exp(-r)\left(\frac{1-q}{r-1}\right) \tag{3.7}$$

Therefore, when $r = q$,

$$T_{n,max}/\sigma_{max} = exp(-r) \tag{3.8}$$

(*$T_{n,max}$ refers to the maximum normal traction encountered during normal separation for a given tangential separation Δ_t. For example, if $\Delta_t=0$, $T_{n,max}=\sigma_{max}$. $T_{t,max}$ is defined in a similar fashion.)

A coupling parameter set which has been widely chosen in literature is $q = 0.43$ and $r = 0$ (Abdul-Baqi and Van der Giessen, 2002; Hattiangadi and Siegmund, 2005; Hopkins et al., 2010) as this results in $\tau_{max} = \sigma_{max}$ for $\delta_n = \delta_t$. However, Figure 3-1(c) shows that *positive* residual normal tractions are computed as $\Delta_t/\delta_t \to \infty$ for $q = 0.43$ and $r = 0$. This phenomena occurs for all $q < 1$, as illustrated in Figure 3-1(b). When $q = 2$ and $r = 0$, *negative* residual normal tractions develop following increasing tangential separations. These unphysical residual tractions are an artefact of the path-independency of $\emptyset(\underline{\Delta})$, as illustrated in Figure 3-1((a),(b)). Residual normal tractions can be avoided only if $q = 1$ (in which case the parameter r is redundant-see Equations (3.3),(3.4)).

The residual normal tractions developed for $r \neq 0$ are analysed next. Residual normal tractions are computed when $r = q$ ($q \neq 1$) (Figure 3-1(c)). Figure 3-1(d) shows how a non-zero r value affects the normal traction-separation response. An ideal response is obtained for pure mode I separation as expected. Following initial tangential separation ($\Delta_t/\delta_t = 5$), with $q = 2$, the normal traction-separation response flips. The reason for this has been outlined in Figure 3-1(a). However, for $r = q = 2$ the normal traction-separation response is shifted to the right leading to unphysical repulsive normal tractions. This is an important point as previous researchers have used a coupling parameter set of $r = q = 0.5$ (Abdul-Baqi and Van der Giessen, 2001). The normal separation at which the maximum *or minimum* normal traction occurs for a range of tangential separations is given as;

$$(\Delta_n/\delta_n)^{max,min} = \frac{(Ar + A + 1)exp\left(-\frac{\Delta_t^2}{\delta_t^2}\right) - Ar - A}{(A + 1)exp\left(-\frac{\Delta_t^2}{\delta_t^2}\right) - A} \qquad (3.9)$$

where,

$A = (1 - q)/(r - 1)$

Therefore if $\Delta_t/\delta_t = 0$, then $(\Delta_n/\delta_n)^{max,min}$ occurs at 1. However, if $\Delta_t/\delta_t \rightarrow$ ∞ then $(\Delta_n/\delta_n)^{max,min}$ occurs at $r + 1$. This can clearly be seen in Figure 3-1(d). When $r = q$ $(q \neq 1)$, negative normal tractions are computed for $\Delta_n/\delta_n < r$ due to the shifting of the normal traction-separation response. The occurrence of residual positive normal tractions was considered by van den Bosch et al. (2006). However, the traction at $\Delta_n/\delta_n = 1$ was incorrectly reported as the peak traction for all values of Δ_t/δ_t. This is considered further in the Discussion section.

3.2.1.3. *Residual Tangential Tractions in Xu-Needleman Cohesive Zone Law*

The normal separation at which local maxima/minima tangential tractions occur is given as:

$$(\Delta_n/\delta_n)_{T_{t,max}/\tau_{max}}{}^{max,min} = r(1-q)/(r-q) \tag{3.10}$$

Figure 3-2 (a) shows that the maximum tangential traction response can be greatly affected, according to the specific parameter set chosen. Several previous studies have assumed $q = 1$ when implementing the XN model (Rahulkumar et al., 2000; Yuan and Chen, 2003; Zavattieri et al., 2008). For this specific case clearly the parameter r is redundant. However, for $q = 1$, unphysical tangential behaviour will be computed in cases of mixed-mode over-closure. Specifically, as illustrated in Figure 3-2(a), maximum tangential tractions reduce as the magnitude of normal over-closure increases for $q = 1$. In fact for large magnitudes of normal over-closure($\Delta_n/\delta_n < -1$), negative maximum tangential tractions are computed. In addition to the specific case where $q = 1$, this problem also occurs for all values of q when $r = 0$. As previously mentioned, several studies have assumed that $q = 0.43$ and $r = 0$. However, inaccuracies computed due to over-closure have not previously been investigated. A previous study by van den Bosch et al. (2006) (VB) suggests that penalisation of mode I normal over-closure will prevent the computation of reduced tangential traction in over-closure. In Chapter 4 of this thesis, a case study is presented that illustrates that this is not the case.

Also shown in Figure 3-2(a), repulsive tangential tractions develop during mixed-mode over-closure when $r < q$ as highlighted by van den Bosch et al. (2006). It is only when $r = q$ ($q \neq 1$) that a realistic physical response is obtained; maximum tangential tractions increase during mixed-mode over-closure and maximum tangential tractions decrease gradually with increasing normal separation. However, it has been demonstrated in the previous section (Figure 3-1(c-d)) that negative normal tractions are computed for mixed-mode separation when $r = q$ ($q \neq 1$) for $\Delta_n/\delta_n < r$ and residual normal tractions as $\Delta_t/\delta_t \rightarrow \infty$.

The evolution of repulsive tractions during mixed-mode over-closure for $q = 1$ is further illustrated by considering the interface potential $\emptyset$ (Figure 3-2(b)). For zero normal separation, $\partial\phi/\partial\Delta_t > 0$. This results in the expected form of pure mode II separation. However, normal over-closure leads to a decrease in $\partial\phi/\partial\Delta_t$. At $\Delta_n/\delta_n = -1$, $\partial\phi/\partial\Delta_t = 0$. This results in the unphysical behaviour whereby there is no resistance to tangential separation, despite compression of the interface. Further over-closure leads to $\partial\phi/\partial\Delta_t < 0$, resulting in repulsive tangential traction. While this may be appropriate at an atomic length scale, it is unphysical at the length scales of most engineering applications.

3.2.1.4. The Effect of Coupling Parameters on Maximum Normal and Tangential Tractions

In a study by Abdul-Baqi and Van der Giessen (2001), film delamination during indentation was simulated using the XN CZM. A number of parameter sets were considered in this study whereby $r \neq 0$ and $q \neq 1$. In order to further illustrate the unphysical behaviour that can be computed by the XN model one of the parameter sets implemented by Abdul-Baqi and Van der Giessen (2001), namely $r = 0.5$ and $q = 0.3$ is considered. Again, two separation paths are considered (Figure 3-3 (c)): Partial normal separation followed by shear separation (green arrows); partial tangential separation followed by normal separation (red arrows). It has been demonstrated in Figure 3-1(a),(b) that only the latter (red) path leads to

unphysical behaviour if $r = 0$. However, when $r \neq 0$, unphysical behaviour is computed for both paths.

Considering the green path, following initial normal separation, negative tangential work is computed during subsequent tangential separation ($\partial \phi / \partial \Delta_t < 0$). Resultant repulsive tangential tractions are illustrated in Figure 3-3(b) following initial normal separations of $\Delta_n / \delta_n = 2$ and $\Delta_n / \delta_n = 3$. The tangential response for pure mode II separation ($\Delta_n / \delta_n = 0$) is also shown in Figure 3-3(b) for comparison. The unphysical repulsive forces computed under mixed-mode conditions are characterised by a change in sign of the computed tractions. As $\Delta_n / \delta_n \to \infty$ the magnitude of negative tangential traction reduces.

Next, considering the red path: following initial tangential separation, negative normal work is computed during subsequent normal separation ($\partial \phi / \partial \Delta_n < 0$). This response is shown in terms of normal traction in Figure 3-3(a) ($\Delta_t / \delta_t = 2$). The normal traction-separation response is shifted and the maximum normal traction occurs at $r + 1$ as discussed in Section 3.2.1.2. The traction-separation curve for pure mode I separation ($\Delta_t / \delta_t = 0$) is also shown in Figure 3-3(a) for comparison.

3.2.1.5. *Summary of the XN Cohesive Zone Model*

- Due to the fact that the net tractions for this model are derived from an interface potential function, residual normal tractions are computed for mixed-mode conditions at the interface when $\emptyset_t > \emptyset_n$ or $\emptyset_n > \emptyset_t$, when the normal traction is expected to reduce to zero as $\Delta_t / \delta_t \to \infty$ (Figure 3-1(c)). Repulsive (negative) normal tractions develop when $\emptyset_t > \emptyset_n$ for mixed-mode conditions.

- Maximum normal traction ($T_{n,max}$) occurs when $\Delta_n / \delta_n = r + 1$ as $\Delta_t / \delta_t \to \infty$. Therefore the addition of the r coupling parameter leads to the development of repulsive normal tractions as $\Delta_t / \delta_t \to \infty$ (Figure 3-1(d)).

- When $q = 1$ ($\emptyset_t = \emptyset_n$), maximum tangential tractions ($T_{t,max}$) reduce as the magnitude of normal over-closure increases (Figure 3-2). For a certain

magnitude of normal over-closure $(\Delta_n/\delta_n < -1)$, repulsive tangential tractions develop.

3.2.1.6. Modified Potential Model (MP)

In an effort to overcome the problems uncovered above for the Xu-Needleman (XN) model, a modified form of the XN potential function is presented:

$$\emptyset\,(\Delta_n, \Delta_t) = \emptyset_n \left[1 + exp\left(\frac{-f(\Delta_t)\Delta_n}{\delta_n}\right)\left(\left(1 - r + \frac{f(\Delta_t)\Delta_n}{\delta_n}\right)\left(\frac{1-q}{r-1}\right)\right.\right.$$
$$\left.\left. - exp\left(-\frac{\Delta_t^2}{\delta_t^2}\right)\left(q + \frac{f(\Delta_t)\Delta_n}{\delta_n}\left(\frac{r-q}{r-1}\right)\right)\right)\right] \tag{3.11}$$

where;

$$f(\Delta_t) = 1 + m - m\,exp\left(-\frac{\Delta_t^2}{\delta_t^2}\right)$$

The new interface parameter, m, provides additional coupling between normal and tangential tractions. All other variables and parameters have the same meaning as defined for the XN model.

Once again, interface traction-separation relationships are obtained from $\underline{T}(\underline{\Delta}) = \partial\emptyset(\underline{\Delta})/\partial\underline{\Delta}$, giving the following expressions:

$$T_n = \frac{\partial \emptyset}{\partial \Delta_n}$$

$$= \emptyset_n \left[\left(\frac{(1-q)(f(\Delta_t)) - (r-q)exp\left(-\frac{\Delta_t^2}{\delta_t^2}\right)(f(\Delta_t))}{(r-1)\delta_n} \right) exp\left(\frac{-\Delta_n(f(\Delta_t))}{\delta_n}\right) \right.$$

$$(3.12)$$

$$\left. - \frac{\left((f(\Delta_t)) \left(\frac{(1-q)\left(\frac{\Delta_n(f(\Delta_t))}{\delta_n} - r + 1\right)}{r-1} \right) exp\left(\frac{-f(\Delta_t)\Delta_n}{\delta_n}\right)}{\delta_n} \right)}{\delta_n} \right]$$

$$T_t = \frac{\partial \emptyset}{\partial \Delta_t}$$

$$= \emptyset_n \left[\left(\frac{\left(2\Delta_t\, exp\left(-\frac{\Delta_t^2}{\delta_t^2}\right)\right)\left(\frac{(r-q)\Delta_n f(\Delta_t)}{(r-1)\delta_n}\right)}{\delta_t^2} \right. \right.$$

$$(3.13)$$

$$\left. - \frac{2m(r-q)\Delta_t\Delta_n exp\left(-2\frac{\Delta_t^2}{\delta_t^2}\right) + 2m(1-q)\Delta_t\Delta_n exp\left(-\frac{\Delta_t^2}{\delta_t^2}\right)}{\delta_t^2(r-1)\delta_n} \right) exp\left(\frac{-f(\Delta_t)\Delta_n}{\delta_n}\right)$$

$$\left. \frac{2m\Delta_t\Delta_n\left(\frac{(1-q)\left(\frac{\Delta_n f(\Delta_t)}{\delta_n} - r + 1\right)}{(r-1)} - exp\left(-\frac{\Delta_t^2}{\delta_t^2}\right)\left(\frac{(r-q)\Delta_n f(\Delta_t)}{(r-1)\delta_n} + q\right)\right)exp\left(\left(-\frac{\Delta_t^2}{\delta_t^2}\right) - \frac{\Delta_n f(\Delta_t)}{\delta_n}\right)}{\delta_t^2\delta_n} \right]$$

As with the XN model, the parameter, q, represents the ratio of work of pure mode II separation to the work of pure mode I separation. The parameter m controls the zone of influence of mode II behaviour for mixed-mode conditions. If $m = 0$, the potential function collapses to the XN model. An increasing value of m leads to a decreasing region in which mode II behaviour dominates. To illustrate this point, Figure 3-4 considers the case where $q = 2$. Three cases are considered, $m = 0$ (the XN model), $m = 1$, and $m = 5$. All three potential functions are identical for pure mode I separation and also for pure mode II separation. Clearly, when $m = 5$ the transition from mode II behaviour to mode I behaviour is confined to a narrow region near the mode II axis. In contrast, when $m = 0$ (XN model) the transition from mode II to mode I behaviour is very gradual. The implications of reducing the transition zone become clear when one considers a separation path that follows a line at a shallow angle to the mode II axis followed by normal separation, as shown in Figure 3-4. For the case of $m = 0$ (XN model), following the initial phase of the interface deformation, in which the separation is predominantly in the tangential direction, negative work of separation occurs during the second phase of the deformation in the normal direction. This results in repulsive normal tractions, as outlined in the XN section of this study. However, as the parameter m is increased, the region in which repulsive normal tractions occur is reduced. Considering the case of $m = 1$ (Figure 3-4 (b)), following the initial mixed-mode separation the negative gradient of $\emptyset$ encountered during the subsequent normal separation is significantly reduced from that computed for the XN model ($m = 0$) shown in Figure 3-4(a). Hence, the magnitude of repulsive normal tractions is reduced when $m > 0$. For $m = 5$, as shown in Figure 3-4(c), no significant repulsive normal tractions are computed for the same path. In this case the transition zone from mode II to mode I separation is sufficiently small such that the illustrated path does not encounter any negative gradients of $\emptyset$ during the second normal phase of the separation. It is important to note, however, that the possibility of computing repulsive normal tractions cannot be fully eliminated for any potential-based model where the mode II work of separation exceeds the mode I work of separation ($q > 1$). This is very clearly illustrated in Figure 3-4(c) ($m = 5$): despite the significantly reduced zone

in which repulsive normal tractions are computed, a pure mode II separation will necessarily lead to the computation of repulsive normal tractions. In fact for a given value of q, the magnitude of repulsive normal tractions computed following a pure mode II separation will be highest for potential surfaces with smaller transition zones between mode II and mode I separation.

Figure 3-5 (a) shows the tangential traction-separation curves for a mixed-mode separation at 20° to the mode II axis for the XN model and for the MP model with $m =$1, 2 and 5. The initial slope is identical for all models. Additionally, the peak traction is not strongly affected by the value of m in the MP model. It can be noted, however, that larger values of m lead to a more rapid decrease in tangential traction for increasing separation post peak. When this mixed-mode separation is followed by an increase in normal separation (with tangential separation held constant at $\Delta_t/\delta_t = 5$, a repulsive normal traction of $T_n/\sigma_{max} = -0.8$ is computed at $\Delta_n/\delta_t = 2$ for the XN model, as shown in Figure 3-5(b). Repulsive normal tractions reduce as normal separation increases, but in the case of the XN model, repulsive normal tractions are still evident at a normal separation of $\Delta_n/\delta_n = 8$. For the MP model with $m = 1$, the magnitude of repulsive normal tractions are significantly reduced from the XN case. Additionally, repulsive normal tractions are negligible when $\Delta_n/\delta_n \geq 4$. A further reduction is evident when $m = 2$, with no significant repulsive normal tractions being computed when $\Delta_n/\delta_n \geq 3$. Finally, it is demonstrated in Figure 3-5(b) that no repulsive normal tractions are computed during the normal separation phase when $m = 5$. Again, this corresponds to the potential plot of Figure 3-4(c), in which the reduced zone in which repulsive normal tractions are computed does not coincide with the separation path.

MP model potential surfaces for the case of $q < 1$ (work of mode II separation less than work of mode I separation) are presented in Figure 3-6. Specifically, it is assumed that $q = 0.43$, as is commonly implemented for the XN model. The case of $m = 0$ (the XN model) is presented in Figure 3-6(a). Once again a separation path is illustrated in which a mixed-mode separation is followed by a normal

separation. As detailed in the XN section of the current study, residual normal tractions must be overcome during the second (normal) phase of the separation despite the preceding full mixed-mode separation. As illustrated in Figure 3-6(b) and (c) for $m = 1$ and $m = 5$ respectively, the zone in which residual normal tractions are computed is reduced as the parameter m is increased. Hence, for $m = 5$ no residual normal tractions are computed during the second (normal) phase of the separation. Once again it is worth mentioning that the MP model is identical to the XN model in pure mode I and mode II separation.

Figure 3-7 (a) shows, for $q = 0.43$, the tangential traction-separation curves for mixed-mode separation (20° to the mode II axis) for the XN model and for the MP model with $m = 1, 2$ and 5. For all cases the tangential tractions reduce to zero at a tangential separation of $\Delta_t/\delta_t = 3$. However, it should be noted that an increase in the parameter m leads to an increase in the computed peak tangential traction beyond the peak mode II traction (τ_{max}). For the case of $m = 5$, a peak tangential traction of $T_t/\tau_{max} \approx 1.7$ is computed during the first (mixed-mode) phase of the deformation. The reduction of the residual normal traction zone for high values of m results in a strong influence of the normal work of separation $\emptyset_n$ on mixed-mode separations, even when the mode angle is tending towards mode II. Figure 3-7(b) shows the normal traction-separation curves during the second (normal) phase of the separation path, when tangential separation is held constant at a value of $\Delta_t/\delta_t = 5$. No residual tractions are computed for the MP model for $m = 5$, as the mixed-mode path followed during the first phase of the deformation extends beyond the residual normal traction zone of the potential surface. However, as m is reduced, the magnitude and region of residual normal tractions is increased. For $m = 1$ a residual normal traction of $T_n/\sigma_{max} = 0.3$ is computed at $\Delta_n/\delta_n = 2$. When $\Delta_n/\delta_n \geq 4$, computed residual normal tractions are not significant. However, for the XN model ($m = 0$), residual normal tractions are still evident when the normal separation is increased to $\Delta_n/\delta_n = 6$.

Figure 3-8 shows the potential surface for the MP model ($m = 1$) for the case of $q = 1$. It should be recalled that the XN model fails to correctly penalise mixed-

mode over-closure for $q = 1$ (see Figure 3-2(b)), with a negative gradient of $\emptyset$ in the tangential direction leading to repulsive tangential tractions. In contrast to the XN model, increasing over-closure in the MP model is accompanied by increasing gradients of $\emptyset$ in the tangential direction. This leads to an increasing penalisation of tangential separation with increasing normal over-closure, resulting in a physically realistic penalisation of mixed-mode over-closure. It should be noted however, that for $\Delta_t/\delta_t > 1$ the gradient of $\emptyset$ in the tangential direction becomes negative, leading to reduced penalisation of tangential separation, and repulsive tangential tractions at high values of Δ_t/δ_t. Despite this limitation, the MP model represents an improvement on the XN model where resistance to tangential separation is reduced for the entire over-closure regime. The relationship between tangential traction and normal separation for the MP model for $q = 1$ is further examined in Figure 3-8(b). The XN model ($m = 0$) is included for comparison, again highlighting the unphysical reduction in maximum tangential traction, $T_{t,max}$, with increasing normal over-closure ($\Delta_n < 0$). In contrast to the XN model, the MP model correctly penalises mixed-mode over-closure, with maximum tangential traction increasing with increasing normal over-closure for all cases considered. An increase in the coupling parameter, m, results in an increased penalisation of mixed-mode over-closure. In separation ($\Delta_n > 0$), the MP relationship between $T_{t,max}$ and Δ_n is very similar to the XN model. However, as highlighted in Figure 3-8(c) for $m = 5$ a slight increase in $T_{t,max}/\tau_{max}$ to a value of 1.11 can be observed for $0 < \Delta_n/\delta_n < 0.35$. This affect is less pronounced for $m = 2$ and is not significant for $m = 1$.

3.2.2. Non-Potential-Based Formulations

3.2.2.1. Van den Bosch (VB) Formulation

A recent study has proposed an improved cohesive zone model for mixed-mode conditions (van den Bosch et al., 2006). Essentially this model uses the traction-separation equations for the XN CZM for $q = 1$ and then applies independent scaling factors in the normal and tangential directions to prescribe the peak tractions. The resultant traction-separation relationships are given as:

$$T_n = \left(\frac{\emptyset_n}{\delta_n}\right)\frac{\Delta_n}{\delta_n} exp\left(-\frac{\Delta_n}{\delta_n}\right) exp\left(-\frac{\Delta_t^2}{\delta_t^2}\right) \tag{3.14}$$

$$T_t = 2\left(\frac{\emptyset_t}{\delta_t}\right)\frac{\Delta_t}{\delta_t}\left\{1 + \frac{\Delta_n}{\delta_n}\right\} exp\left(-\frac{\Delta_n}{\delta_n}\right) exp\left(-\frac{\Delta_t^2}{\delta_t^2}\right) \tag{3.15}$$

$\emptyset_n$ and $\emptyset_t$ (the work of mode I and mode II separation, respectively) are independent model parameters. Traction-separation relationships are not derived from a potential function, so the work done during mixed-mode separation is path-dependent, in contrast to the XN CZM. Such a non-potential CZM eliminates several problems associated with mixed-mode separation (as described in the previous section). However, given that this model is based on XN traction-separation relationships for $q = 1$, unphysical behaviour is similarly computed in mixed-mode over-closure. This is illustrated in Figure 3-9(a), which shows the work done when a normal displacement of $\Delta_{n,max}$ is followed by a complete tangential separation, whereby Δ_t increases from 0 to ∞. In addition to total work, the work of normal separation and the work of tangential separation are plotted and both normal separation and over-closure are considered. Model parameters are chosen such that $\emptyset_t = 0.34\emptyset_n$ so that $\tau_{max}=0.8\,\sigma_{max}$. Firstly, as shown in Figure 3-9(a), this model provides a monotonic increase in total work with increasing $\Delta_{n,max}$ as reported previously by van den Bosch et al. (2006). However, focusing on the over-closure regime, the work of tangential separation

reduces with increasing normal over-closure. In fact, for large values of normal over-closure $(\Delta_n/\delta_n < -1)$ negative tangential work is computed, resulting in repulsive tangential forces. A case study is presented in Chapter 4 of this thesis to demonstrate that this unphysical behaviour in mixed-mode over-closure can lead to inaccurate simulation of coating buckling from a stent surface.

3.2.2.2. *Non-Potential-Based (NP1) Formulation*

In order to correct the unphysical behaviour of the VB CZM in mixed-mode over-closure, a modified form of the tangential traction-separation relationship, proposed by McGarry et al. (2012), is presented in this section. The term $\left(1 + \frac{\Delta_n}{\delta_n}\right)$ in Equation (3.15) is removed, thus eliminating reductions in peak tangential traction during mixed-mode over-closure. The resultant traction-separation relationships are expressed as:

$$T_n = \sigma_{max} exp(1) \left(\frac{\Delta_n}{\delta_n}\right) exp\left(-\frac{\Delta_n}{\delta_n}\right) exp\left(-\frac{\Delta_t^2}{\delta_t^2}\right) \tag{3.16}$$

$$T_t = \tau_{max} \sqrt{2exp(1)} \left(\frac{\Delta_t}{\delta_t}\right) exp\left(-\frac{\Delta_n}{\delta_n}\right) exp\left(-\frac{\Delta_t^2}{\delta_t^2}\right) \tag{3.17}$$

where σ_{max} and τ_{max} are the peak tractions for mode I and mode II separation, respectively.

Figure 3-9 (b) shows the work done when a normal displacement of $\Delta_{n,max}$ is followed by a complete tangential separation again with $\tau_{max}=0.8\,\sigma_{max}$. The tangential work, W_t, increases with increasing normal over-closure, providing a physically realistic representation of mixed-mode over-closure, in contrast to the VB model. However, it should be noted that a slight reduction in W_{total} is computed as $\Delta_{n,max}$ initially increases from 0. This is due to a rapid decrease in tangential work as $\Delta_{n,max}$ increases from 0. This is in contrast to the monotonic increase in W_{total} computed by the VB model (Figure 3-9 (a)).

3.2.2.3. Non-Potential-Based (NP2) Formulation

It should be noted that the three CZMs presented thus far (XN, VB and NP1) have different forms for mode I and mode II separation. In all three cases normal tractions for mode I separation are of the form $\left(\frac{\Delta_n}{\delta_n}\right) exp\left(-\frac{\Delta_n}{\delta_n}\right)$ while tangential tractions for mode II separation are of the form $\left(\frac{\Delta_t}{\delta_t}\right) exp\left(-\frac{\Delta_t^2}{\delta_t^2}\right)$. Therefore, no model parameters can be chosen so that identical mode I and mode II traction-separation relationships are obtained for these three models. In order to overcome this limitation, a non-potential-based formulation (NP2) is presented:

$$T_n = \sigma_{max}exp(1)\left(\frac{\Delta_n}{\delta_n}\right) exp\left(-\frac{\Delta_n}{\delta_n}\right) exp\left(-\sqrt{\frac{\overline{\Delta_t^2}}{\delta_t^2}}(\sqrt{2}-1)\right) \qquad (3.18)$$

$$T_t = \tau_{max}exp(1)\left(\frac{\Delta_t}{\delta_t}\right) exp\left(-\sqrt{\frac{\overline{\Delta_t^2}}{\delta_t^2}}\right) exp\left(\left(-\frac{\Delta_n}{\delta_n}\right)(\sqrt{2}-1)\right) \qquad (3.19)$$

This model provides identical behaviour in mode I and mode II separation when $\sigma_{max} = \tau_{max}$ and $\delta_n = \delta_t$. Additionally, it can easily be demonstrated that identical normal and tangential components of the traction vector are obtained for 45° mixed-mode separation ($\Delta_n = \Delta_t$).

In order to assess the mixed-mode behaviour of NP2 when $\tau_{max} \neq \sigma_{max}$, Figure 3-9(c) shows the work done when a normal displacement of $\Delta_{n,max}$ is followed by a complete tangential separation when $\tau_{max}=0.8 \sigma_{max}$. Firstly, in contrast to the VB model (Figure 3-9(a)) and to NP1 (Figure 3-9 (b)), it should be noted that the ratio the of work of mode I separation to the work of mode II separation is identical to the ratio of σ_{max} to τ_{max}, as expected given the identical forms of mode I and mode II traction-separation. A drawback of NP2 is that a monotonic increase in W_{total} is not obtained for increasing $\Delta_{n,max}$ with a maximum value of

W_{total} being computed at $\Delta_{n,max}/\delta_n \approx 4.4$. Next, considering NP2 in over-closure, tangential work increases with increasing normal over-closure, providing physically realistic mixed-mode over-closure similar to that of NP1.

3.2.2.4. *Separation Magnitude Coupling (SMC)Formulation*

Finally, a third non-potential-based model is considered (SMC) in which the effective separation $(\Delta_n^2/\delta_n^2 + \Delta_t^2/\delta_t^2)$ is used to couple the normal and tangential interface tractions, as shown in Equations (3.20) and (3.21):

$$T_n = \sigma_{max}exp(1)\left(\frac{\Delta_n}{\delta_n}\right) exp\left(-\sqrt{\left(\frac{\Delta_n^2}{\delta_n^2} + \frac{\Delta_t^2}{\delta_t^2}\right)}\right) \tag{3.20}$$

$$T_t = \tau_{max}exp(1)\left(\frac{\Delta_t}{\delta_t}\right) exp\left(-\sqrt{\left(\frac{\Delta_n^2}{\delta_n^2} + \frac{\Delta_t^2}{\delta_t^2}\right)}\right) \tag{3.21}$$

This model provides identical behaviour in mode I and mode II separation when $\sigma_{max} = \tau_{max}$ and $\delta_n = \delta_t$. Additionally, it is clear that the traction magnitude $\sqrt{T_n^2 + T_t^2}$ is independent of the mode mixity, depending only on the effective separation. Considering the mixed-mode behaviour of SMC when $\tau_{max} \neq \sigma_{max}$, Figure 3-9(d) shows the work done when a normal displacement of $\Delta_{n,max}$ is followed by a complete tangential separation when $\tau_{max}=0.8\,\sigma_{max}$. In contrast to the NP2 formulation, SMC provides a monotonic increase in W_{total} for increasing $\Delta_{n,max}$. However, it is clear from Equations (3.20, 3.21) and from Figure 3-9(d) that the SMC formulation provides identical traction-separation behaviour in over-closure and in separation. Therefore, as over-closure is not penalised in a physically realistic fashion it is suggested that the SMC model should be used for separation ($\Delta_n \geq 0$) only. In cases where both separation and over-closure may be encountered the SMC model could be used in separation with the NP2 formulation being used in over-closure. Such a scheme is computationally feasible

as the NP2 and SMC CZMs have an identical mode II traction-separation relationship.

3.2.2.5. *Comparison of NP1, NP2 and SMC Formulations*

In summary, three non-potential-based cohesive zone formulations have been presented in order to achieve physically realistic coupling between normal and tangential tractions in mixed-mode separation and mixed-mode over-closure. Figure 3-10(a) demonstrates that maximum normal traction, $T_{n,max}$ reduces with increasing tangential separation for all models (NP1, NP2, SMC). The details of the coupling differ between models with the steeper coupling terms ($exp-(\Delta_t^2/\delta_t^2)$) of NP1 leading to the disappearance of normal tractions at a low tangential separation ($\Delta_t/\delta_t \approx 3$) in contrast to NP2 and SMC. Figure 3-10(b) demonstrates that maximum tangential traction, $T_{t,max}$, reduces with increasing normal separation ($\Delta_n/\delta_n > 0$) for all models (NP1,NP2, SMC). However, as previously stated, only NP1 and NP2 provide a physically realistic penalisation of mixed-mode over-closure.

3.2.3. **Mixed-Mode Comparison of Cohesive Zone Formulations for All Separation Angles**

Finally, the ability of each model to provide mode-independent interface behaviour is considered. Again, model parameters are chosen such that $\sigma_{max} = \tau_{max}$ with separations at peak traction being identical for mode I and mode II separation. In Figure 3-11(a) the maximum traction magnitude ($|T|_{max} = max(\sqrt{T_n^2 + T_t^2})$) is plotted as a function of separation mode angle, θ, where $\theta = Tan^{-1}(\Delta_n/\Delta_t)$. A plot of the separation magnitude at which $|T|_{max}$ occurs ($|\Delta|_{max}$) is shown in Figure 3-11(b). As specified in Equations (3.20-3.21), the SMC formulation provides a mode-independent response. For NP2, identical behaviour is obtained for mode I, mode II and pure mixed-mode ($\theta = \pi/4$) separation. For NP1, the VB and XN models, the peak traction is highly mode-dependent, as is the separation magnitude at which it occurs. It should again be noted that while in Figure 3-11 model parameters are chosen so that $|T|_{max}^{\theta=0} =$

$|T|_{max}^{\theta=\pi/2}$ and $|\Delta|_{max}^{\theta=0} = |\Delta|_{max}^{\theta=\pi/2}$, the form of the traction-separation curve is different for mode I and mode II separation for NP1, VB and XN models.

3.3. Results and Discussion

In this chapter a thorough analysis of the potential-based XN CZM in mixed-mode separation and over-closure is performed. It is demonstrated that derivation of traction-separation relationships from a potential function results in non-physical behaviour under mixed-mode conditions. Specifically, repulsive normal tractions can be computed by potential-based CZMs during mixed-mode separation if $\emptyset_t > \emptyset_n$. Similarly, positive/adhesive residual normal tractions can be computed by potential-based CZMs following mode II or mixed-mode separation if $\emptyset_t < \emptyset_n$. In the present chapter, a modified potential-based (MP) cohesive zone model is presented in which the zone in which repulsive ($\emptyset_t > \emptyset_n$) or residual ($\emptyset_t < \emptyset_n$) normal tractions occur is reduced. It is demonstrated that the MP model can eliminate the computation of repulsive normal tractions following full mixed-mode separation when $\emptyset_t > \emptyset_n$, without significantly altering the maximum tangential traction from the prescribed value, during mixed-mode separation.   Considering that several experimental studies report that $\emptyset_t > \emptyset_n$ (Dollhofer et al., 2000; Warrior et al., 2003; Yang et al., 2001), the MP model provides a significant improvement on the XN model for mixed-mode applications. While the MP model has the ability to eliminate residual normal tractions for mixed-mode separations when $\emptyset_t < \emptyset_n$, it suffers from the drawback that maximum tangential traction are altered from the prescribed value. While the MP model offers significant improvements on the XN model for mixed-mode separation, it is very important to note that no potential-based model can avoid the computation of repulsive normal tractions following pure mode II separation if $\emptyset_t > \emptyset_n$. Previous studies of potential-based models have set the normal traction if the normal traction exceeds a certain value (Park et al., 2009) to overcome this problem. However, non-potential CZMs such as those presented in this study must be used to fully eliminate the possible computation of repulsive normal tractions during mixed-mode separation.

The XN model provides physically realistic coupling under mixed-mode separation only if the work of mode I and mode II separation are equal ($q = 1$). Based on this observation van den Bosch et al. (2006) proposed a coupled non-potential CZM (the VB model) that provides physically realistic coupling during mixed-mode separation. Using the XN traction-separation equations for $q = 1$, independent scaling factors were applied to the expressions for normal and tangential tractions in order to simulate cases where $\emptyset_t \neq \emptyset_n$. However, similar to the XN model for $q = 1$, the VB model does not provide correct penalisation of mixed-mode over-closure, with peak tangential tractions decreasing with increasing over-closure, becoming repulsive when the normal over-closure exceeds the characteristic distance. An alternative model (NP1) that is identical to the XN and VB models in pure mode I and pure mode II separation is presented, again with physically realistic coupling in mixed-mode separation. However, in contrast to the VB model, NP1 provides a physically realistic coupling in mixed-mode over-closure, i.e. the peak tangential traction increases with normal over-closure and repulsive tangential tractions are never computed. In a follow on case study in Chapter 4 of this thesis, it is demonstrated that excessive mixed-mode over-closure is computed at a stent-coating interface by the VB model, leading to an erroneous prediction of coating stress and buckling.

A potential limitation of the XN, MP, VB and NP1 formulations is that identical traction-separation relationships cannot be specified for mode I and mode II separation. Even if peak mode I and mode II tractions are equal ($\sigma_{max} = \tau_{max}$) and occur at the same effective separation ($\sqrt{2}\delta_n = \delta_t$) the work of tangential separation will be lower than the work of normal separation ($q \approx 0.607$). Therefore, an additional formulation (NP2) is presented in this chapter that provides identical "effective traction"-"effective separation" relationships for 90° (mode I), 0° (mode II) and 45° (pure mixed-mode) separation in addition to providing physically realistic behaviour in mixed-mode over-closure. A formulation (SMC) is also considered in which the effective separation is used for mixed-mode coupling, following from the work of Tvergaard and Hutchinson (1993), providing mode-independent behaviour in separation but no penalisation

of over-closure. It is demonstrated that NP2 provides a closer approximation to the mode-independent separation behaviour of SMC than the XN, VB or NP1 formulations. Given that NP2 is identical to SMC for 90° (mode I), 0° (mode II) and 45° (pure mixed-mode) separation, a framework can be readily implemented in which NP2 is applied if $\Delta_n < 0$ and SMC is applied if $\Delta_n \geq 0$.

The present study presents for the first time a complete characterisation of the well established XN model under conditions of mixed-mode separation and over-closure. The study by van den Bosch et al. (2006) provides a partial characterisation of the problems associated with the XN model, focusing on mixed-mode tractions when $q \leq 1$ ($\emptyset_t \leq \emptyset_n$). It was correctly reported that residual positive normal tractions can be computed following complete tangential separation. However, an incorrect expression for maximum residual normal traction was reported as it was assumed that the peak normal traction occurs at $\Delta_n/\delta_n = 1$ when $\Delta_t/\delta_t \to \infty$. In the present study it is demonstrated that peak normal tractions occur at $\Delta_n/\delta_n = r + 1$ when $\Delta_t/\delta_t \to \infty$ and that the maximum residual traction is given as $T_{n,max}/\sigma_{max} = -exp(-r)(1 - q/r - 1)$. Importantly, it is also demonstrated that negative (repulsive) normal tractions are computed when $\Delta_n/\delta_n < r$, when $r = q$ ($q \neq 1$). It can therefore be concluded that a large value for the r parameter of the XN model should not be adopted in an effort to minimise residual normal tractions when $\Delta_t/\delta_t \to \infty$. In the present study it is shown that both repulsive normal and repulsive tangential forces can be computed during mixed-mode separation when $q < r$.

3.4. Conclusion

In conclusion, a rigorous analysis of potential-based and non-potential-based cohesive zone formulations in mixed-mode over-closure and separation is presented in this chapter. The presented analyses provide valuable guidance for future implementation of the Xu-Needleman (XN) model and related potential-based CZMs for problems involving mixed-mode separation and over-closure. Repulsive normal tractions are computed for the XN model during mixed-mode separation if the work of tangential separation exceeds the work of normal separation ($\emptyset_t > \emptyset_n$) while positive residual normal tractions are computed following mode II or mixed-mode separation if $\emptyset_t < \emptyset_n$. Additionally, the XN model fails to provide correct penalisation of mixed-mode over-closure when the work of normal and tangential separation are equal ($q = 1$), with peak tangential tractions decreasing with increasing over-closure, becoming repulsive when the normal over-closure exceeds the characteristic distance. An alternative potential-based CZM (the MP model) is presented that improves upon the performance of the XN model under mixed-mode conditions. However, residual tractions cannot be fully eliminated for all mixed-mode separation paths using a potential-based formulation unless the work of normal and tangential separation are equal ($\emptyset_t = \emptyset_n$). A non-potential-based model (NP1) is presented which improves upon the performance of the VB model (van den Bosch et al., 2006) under conditions of mixed-mode over-closure. Finally, two non-potential-based models are presented that provide the option of achieving identical mode I and mode II behaviour, while providing reasonable coupling under mixed-mode conditions.

Further assessment of the performance of each CZM during mixed-mode interface separation and mixed-mode interface compression is presented in Chapter 4 using computational (finite element) analyses. A mode sensitive finite element case study is used to uncover any inherent bias towards mode I or mode II separation in CZMs. A second finite element case study is implemented to further assess the ability of CZMs to correctly penalise mixed-mode over-closure.

3.5. References

Abdul-Baqi, A.&Van Der Giessen, E. (2001) Indentation-induced interface delamination of a strong film on a ductile substrate. *Thin Solid Films,* 381**,** 143-154.

Abdul-Baqi, A.&Van Der Giessen, E. (2002) Numerical analysis of indentation-induced cracking of brittle coatings on ductile substrates. *International Journal of Solids and Structures,* 39**,** 1427-1442.

Beltz, G. E.&Rice, J. R. (1992) Dislocation nucleation at metal-ceramic interfaces. *Acta metallurgica et materialia,* 40**,** S321-S331.

Cao, H. C.&Evans, A. G. (1989) An experimental study of the fracture resistance of bimaterial interfaces. *Mechanics of Materials,* 7**,** 295-304.

Chai, Y. S.&Liechti, K. M. (1992) Asymmetric Shielding in lnterfacial Fracture Under/n-Plane Shear. *Journal of Applied Mechanics,* 59**,** 295-304.

Dollhofer, J., Beckert, W., Lauke, B.&Schneider, K. (2000) Fracture mechanical characterisation of mixed-mode toughness of thermoplast/glass interfaces. *Computational Materials Science,* 19**,** 223-228.

Hattiangadi, A.&Siegmund, T. (2005) An analysis of the delamination of an environmental protection coating under cyclic heat loads. *European Journal of Mechanics - A/Solids,* 24**,** 361-370.

Hopkins, C. G., McHugh, P. E.&McGarry, J. P. (2010) Computational Investigation of the Delamination of Polymer Coatings During Stent Deployment. *Annals of Biomedical Engineering,* 38**,** 2263-2273.

Hu, J., Chou, Y. K.&Thompson, R. G. (2008) Cohesive zone effects on coating failure evaluations of diamond-coated tools. *Surface and Coatings Technology,* 203**,** 730-735.

Li, H.&Chandra, N. (2003) Analysis of crack growth and crack-tip plasticity in ductile materials using cohesive zone models. *International Journal of Plasticity,* 19**,** 849-882.

McGarry, J. P., Ó Máirtín, É., Parry, G.&Beltz, G. E. (2012) Potential-based and non-potential-based cohesive zone formulations under mixed-mode separation and over-closure. Part I: Theoretical Analysis. *Journal of the Mechanics and Physics of Solids,* In Submission.

Nakamura, T.&Wang, Z. (2001) Simulations of Crack Propagation in Porous Materials. *Journal of Applied Mechanics,* 68**,** 242-251.

Needleman, A.&Rosakis, A. J. (1999) The effect of bond strength and loading rate on the conditions governing the attainment of intersonic crack growth along interfaces. *Journal of the Mechanics and Physics of Solids,* 47**,** 2411-2449.

O'Dowd, N. P., Stout, M. G.&Shih, C. F. (1992) Fracture toughness of alumina-niobium interfaces: experiments and analyses. *Philosophical Magazine A,* 66**,** 1037-1064.

Park, K., Paulino, G. H.&Roesler, J. R. (2009) A unified potential-based cohesive model of mixed-mode fracture. *Journal of the Mechanics and Physics of Solids,* 57**,** 891-908.

Rahulkumar, P., Jagota, A., Bennison, S. J.&Saigal, S. (2000) Cohesive element modeling of viscoelastic fracture: application to peel testing of polymers. *International Journal of Solids and Structures,* 37**,** 1873-1897.

Rose, J. H., Ferrante, J.&Smith, J. R. (1981) Universal binding energy curves for metals and bimetallic interfaces. *Physical Review Letters,* 47**,** 675-678.

Rose, J. H., Smith, J. R.&Ferrante, J. (1983) Universal features of bonding in metals. *Physical Review B,* 28**,** 1835-1845.

Thouless, M. D. (1990) Fracture of a model interface under mixed-mode loading. *Acta metallurgica et materialia,* 38**,** 1135-1140.

Tvergaard, V.&Hutchinson, J. W. (1993) The influence of plasticity on mixed mode interface toughness. *Journal of the Mechanics and Physics of Solids,* 41**,** 1119-1135.

van den Bosch, M. J., Schreurs, P. J. G.&Geers, M. G. D. (2006) An improved description of the exponential Xu and Needleman cohesive zone law for mixed-mode decohesion. *Engineering Fracture Mechanics,* 73**,** 1220-1234.

Warrior, N. A., Pickett, A. K.&Lourenco, N. S. F. (2003) Mixed-Mode Delamination-Experimental and Numerical Studies. *Strain,* 39**,** 153-159.

Xu, X. P.&Needleman, A. (1993) Void nucleation by inclusion debonding in a crystal matrix. *Modelling and Simulation in Materials Science and Engineering,* 2**,** 417-418.

Yan, Y.&Shang, F. (2009) Cohesive zone modeling of interfacial delamination in PZT thin films. *International Journal of Solids and Structures,* 46**,** 2739-2749.

Yang, Q. D., Thouless, M. D.&Ward, S. M. (2001) Elastic-plastic mode-II fracture of adhesive joints. *International Journal of Solids and Structures,* 38**,** 3251-3262.

Yuan, H.&Chen, J. (2003) Computational analysis of thin coating layer failure using a cohesive model and gradient plasticity. *Engineering Fracture Mechanics,* 70**,** 1929-1942.

Zavattieri, P. D., Hector Jr, L. G.&Bower, A. F. (2008) Cohesive zone simulations of crack growth along a rough interface between two elastic-plastic solids. *Engineering Fracture Mechanics,* 75**,** 4309-4332.

3.6. Tables and Figures
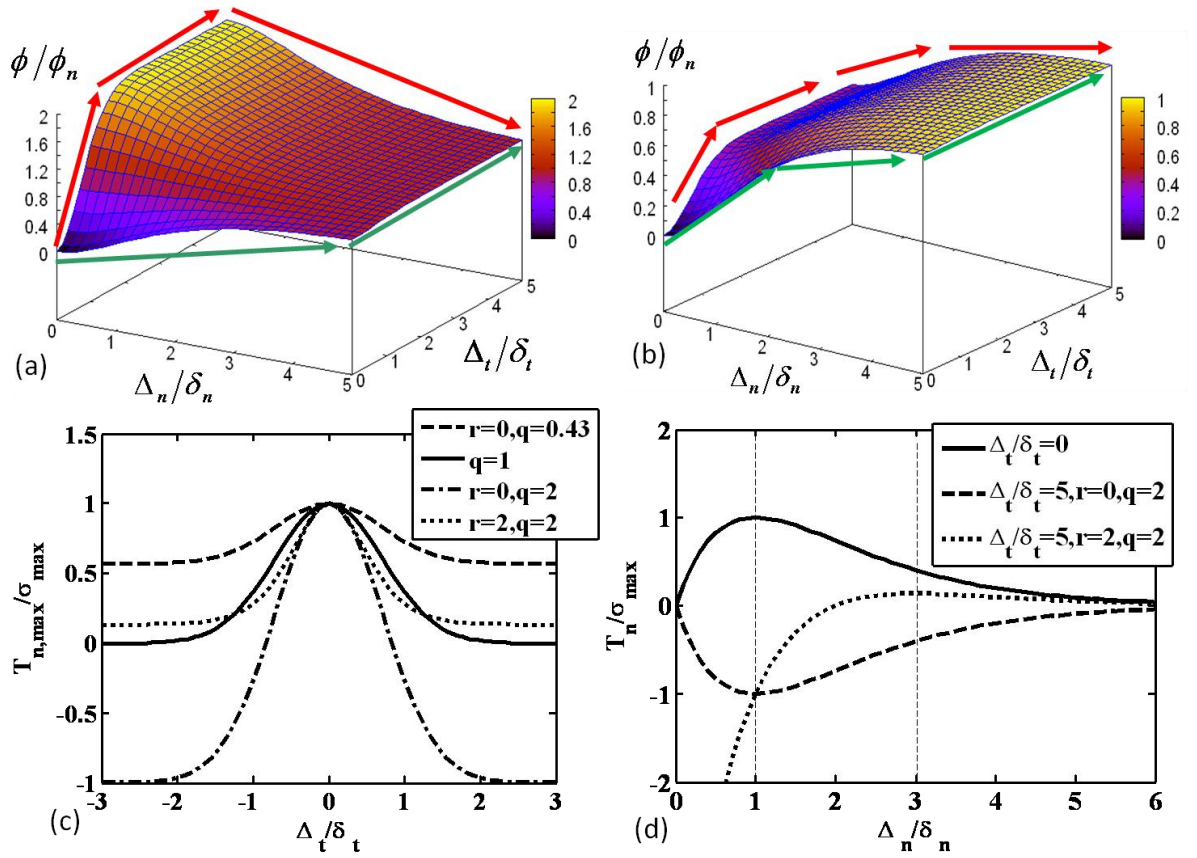
Figure 3-1: Normalised work of separation ($\emptyset/\emptyset_n$) as a function of normalised normal (Δ_n/δ_n) and normalised tangential (Δ_t/δ_t) components of the interface separation vector for the XN model: (a) $q = 2$, $r = 0$; (b) $q = 0.43$, $r = 0$. (c) Normalised maximum normal traction ($T_{n,max}/\sigma_{max}$) as a function of normalised tangential separation. (d) Normalised normal traction (T_n/σ_{max}) as a function of normalised normal separation (Δ_n/δ_n).

Figure 3-2: (a) Normalised maximum tangential traction ($T_{t,max}/\tau_{max}$) as a function of normalised normal separation (Δ_n/δ_n) for a range of r and q coupling parameters. (b) Normalised work of separation ($\emptyset/\emptyset_n$) as a function of normalised normal (Δ_n/δ_n) and normalised tangential (Δ_t/δ_t) components of the interface separation vector for $q = 1$.
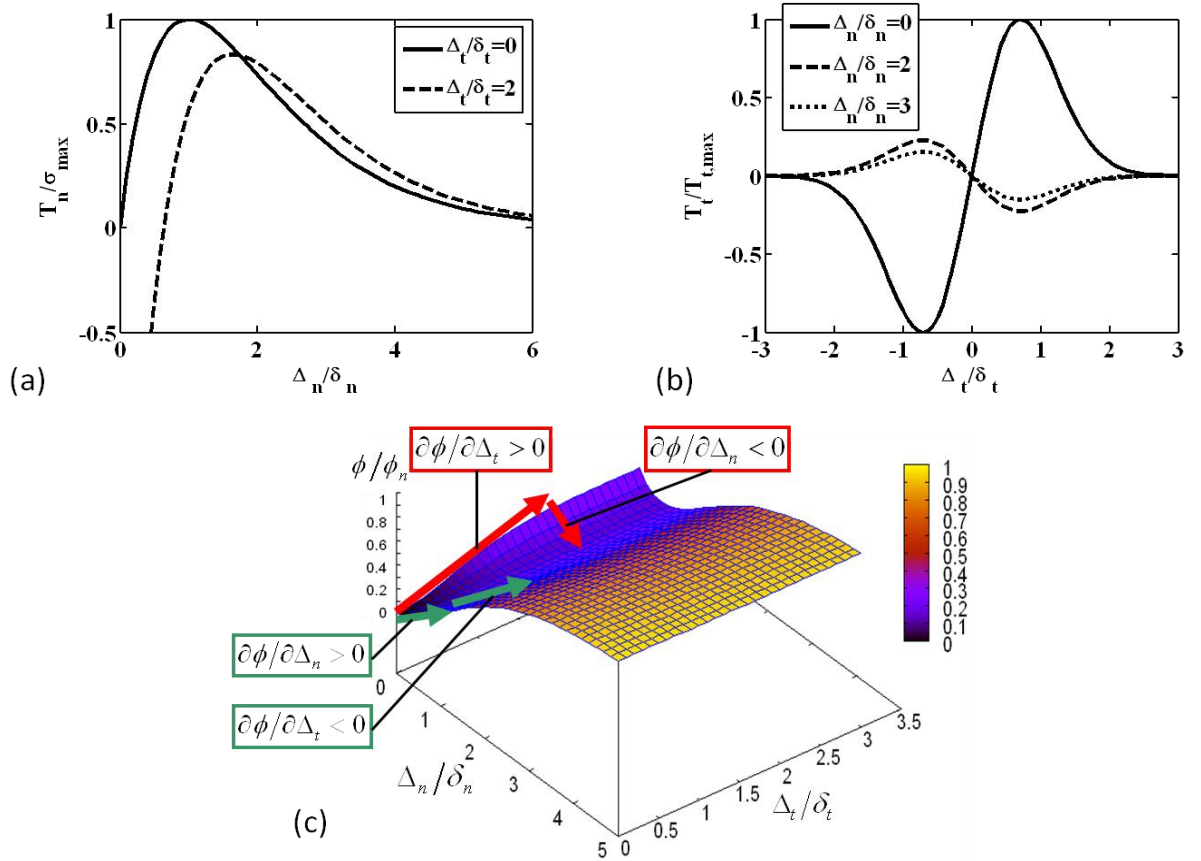
Figure 3-3: (a) Normalised normal traction (T_n/σ_{max}) as a function of normalised normal separation (Δ_n/δ_n) for increasing tangential separations (b) Normalised tangential traction (T_t/τ_{max}) as a function of tangential separation (Δ_t/δ_t) for increasing normal separations (c) Work of Separation as a function of normal (Δ_n/δ_n) and tangential (Δ_t/δ_t) separations. In all cases q=0.3, r=0.5.
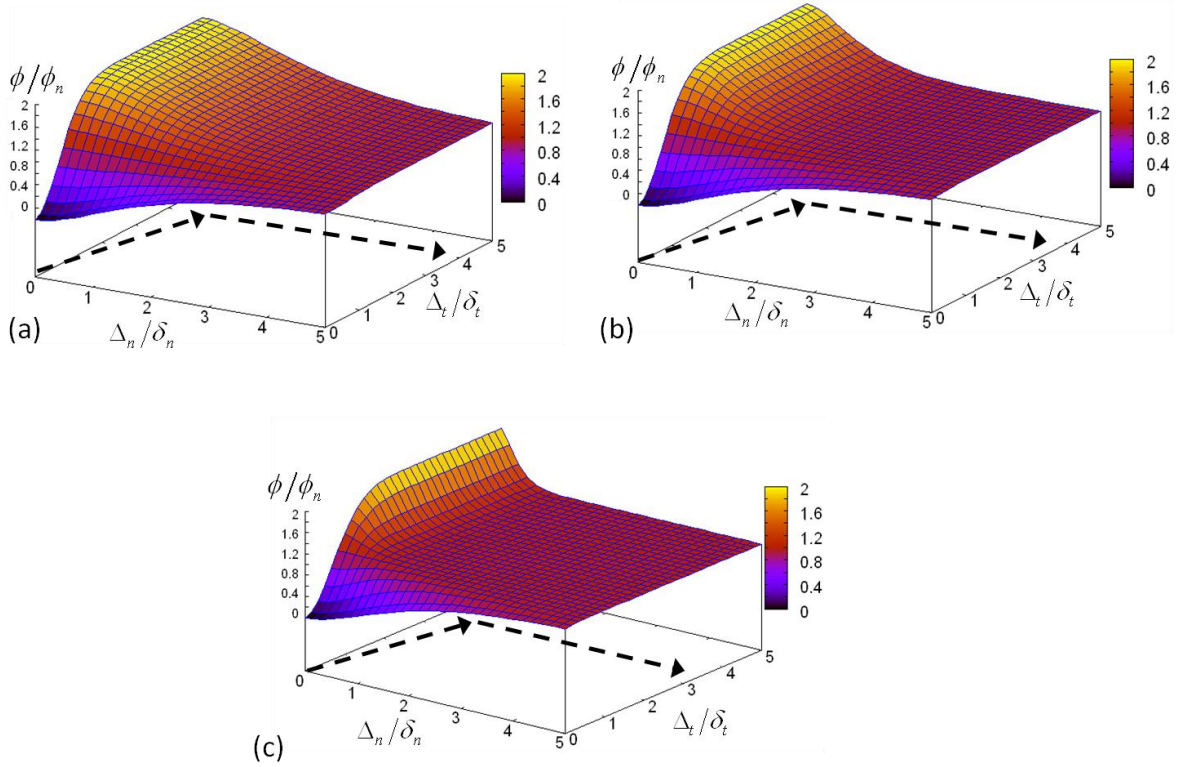
Figure 3-4: Normalised work of separation ($\emptyset/\emptyset_n$) as a function of normalised normal (Δ_n/δ_n) and normalised tangential (Δ_t/δ_t) components of the interface separation vector for the MP model with $q=2$ and $r=0$: (a) m=0 (XN model); (b) $m = 1$; (c) $m=5$. Dotted line indicates a path comprising of mixed-mode separation followed by normal separation.
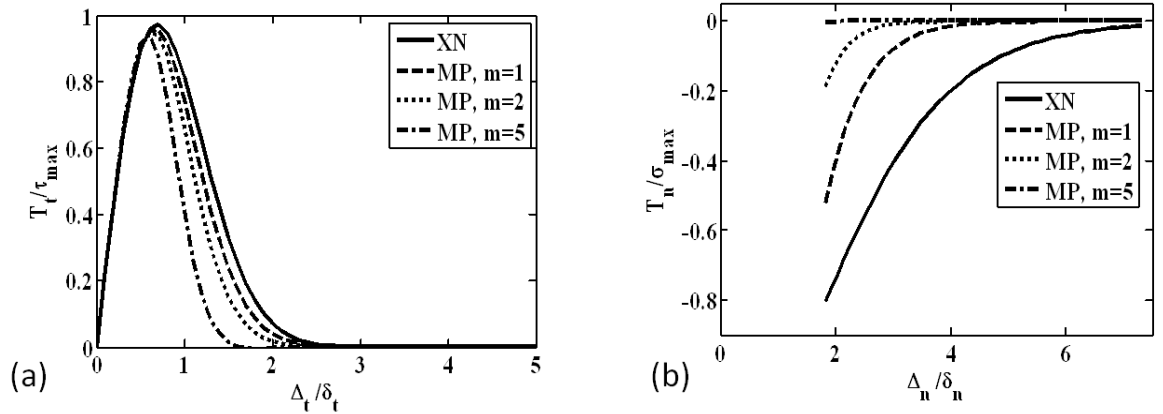
Figure 3-5: (a) Normalised tangential traction (T_t/τ_{max}) as a function of normalised tangential displacement (Δ_t/δ_t) for $q=2$ and $r=0$ during a mixed-mode separation where $Tan^{-1}(\Delta_n/\Delta_t) = 20^o$. (b) Normalised normal traction (T_n/σ_{max}) as a function of normalised normal displacement (Δ_n/δ_n) representing a normal separation subsequent to the mixed-mode separation shown in (a). Curves are shown for the XN model and the MP model ($m=1, 2$ and 5).
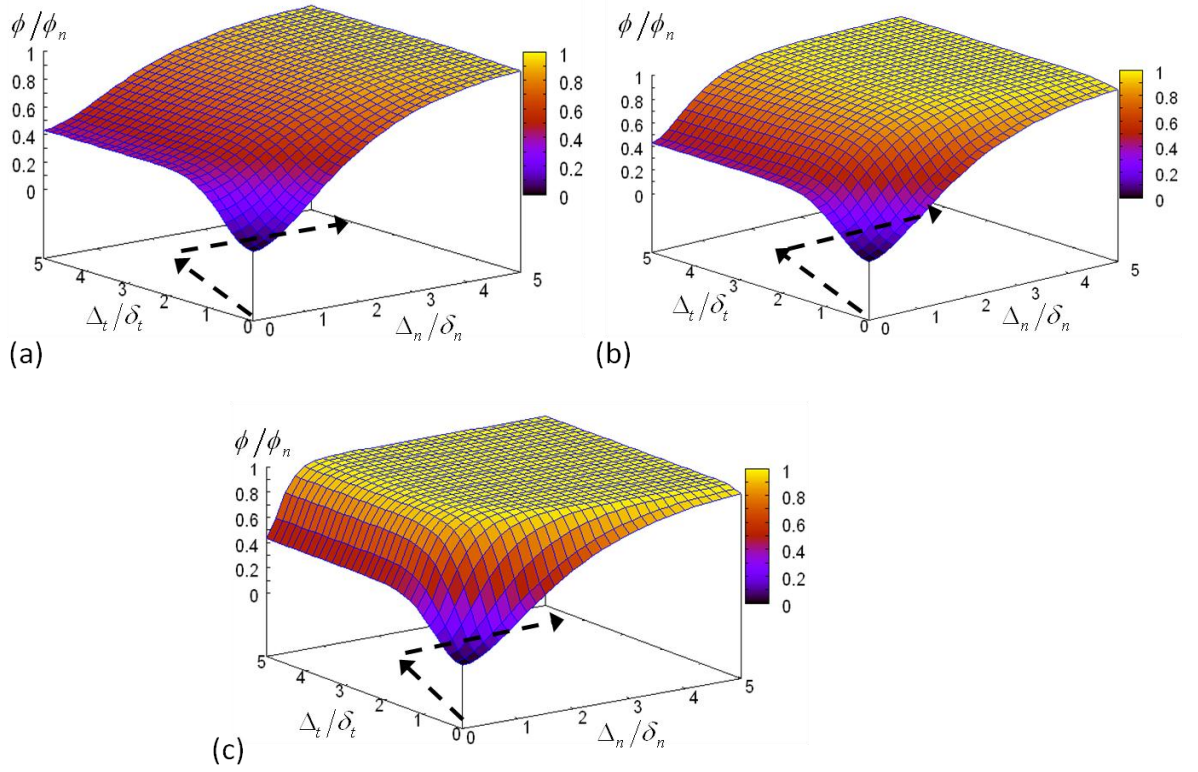
Figure 3-6: Normalised work of separation (ϕ/ϕ_n) as a function of normalised normal (Δ_n/δ_n) and normalised tangential (Δ_t/δ_t) components of the interface separation vector for the MP model with $q=0.43$ and $r=0$: (a) $m=0$ (XN model); (b) $m = 1$; (c) $m=5$. Dotted line indicates a path comprising of mixed-mode separation followed by normal separation.
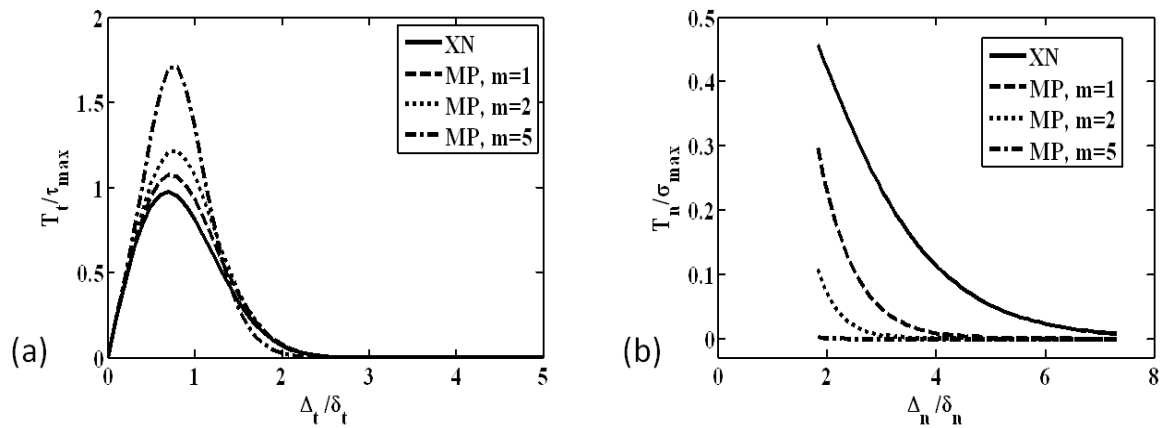
Figure 3-7: (a) Normalised tangential traction (T_t/τ_{max}) as a function of normalised tangential displacement (Δ_t/δ_t) for $q=0.43$ and $r=0$ during a mixed-mode separation where $Tan^{-1}(\Delta_n/\Delta_t) = 20^o$. (b) Normalised normal traction (T_n/σ_{max}) as a function of normalised normal displacement (Δ_n/δ_n) representing a normal separation subsequent to the mixed-mode separation shown in (a). Curves are shown for the XN model and the MP model ($m=1$, 2 and 5).
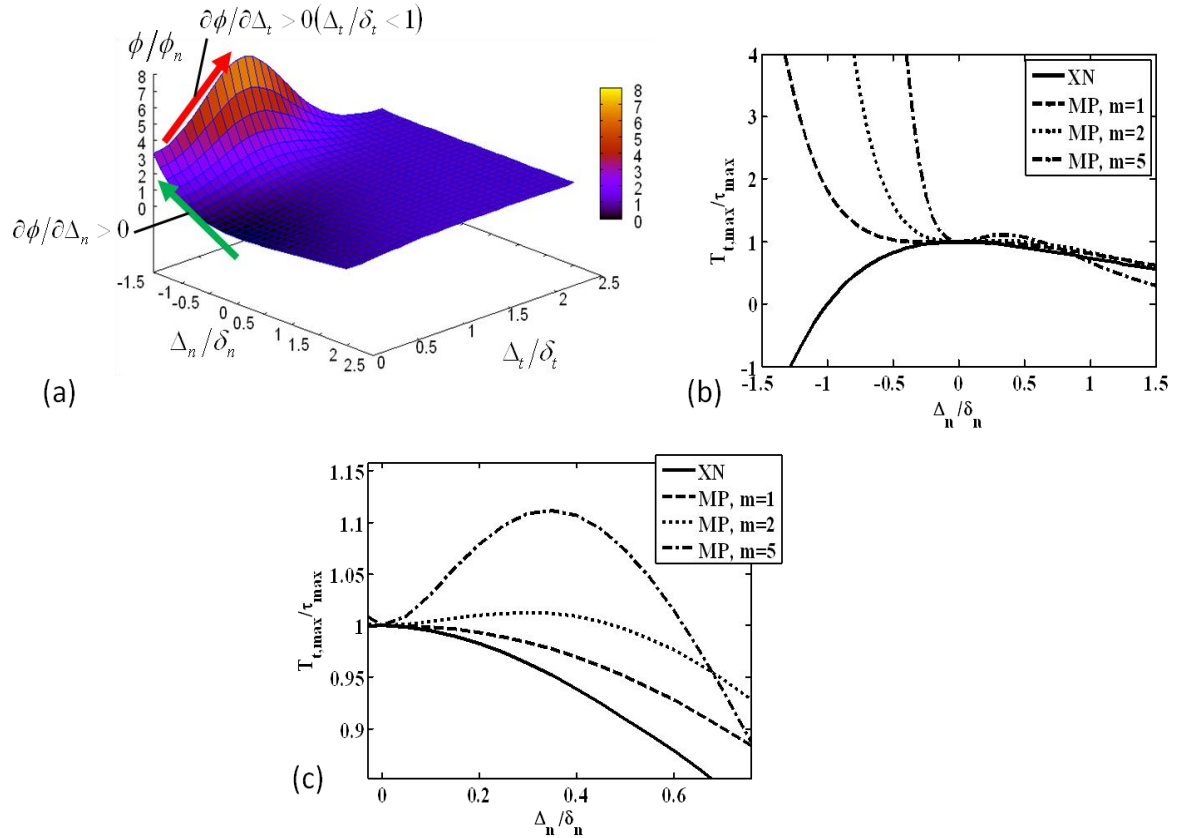
Figure 3-8: (a) Normalised work of separation $(\emptyset/\emptyset_n)$ as a function of normalised normal (Δ_n/δ_n) and normalised tangential (Δ_t/δ_t) components of the interface separation vector for the MP model with *m=1*, *q=1* and *r=0*. Green arrow highlights the positive gradient of $\emptyset$ w.r.t. Δ_n. Red arrow highlights the positive gradient of $\emptyset$ w.r.t. Δ_t indicating correct penalisation of mixed-mode over-closure, with resistance to tangential separation incre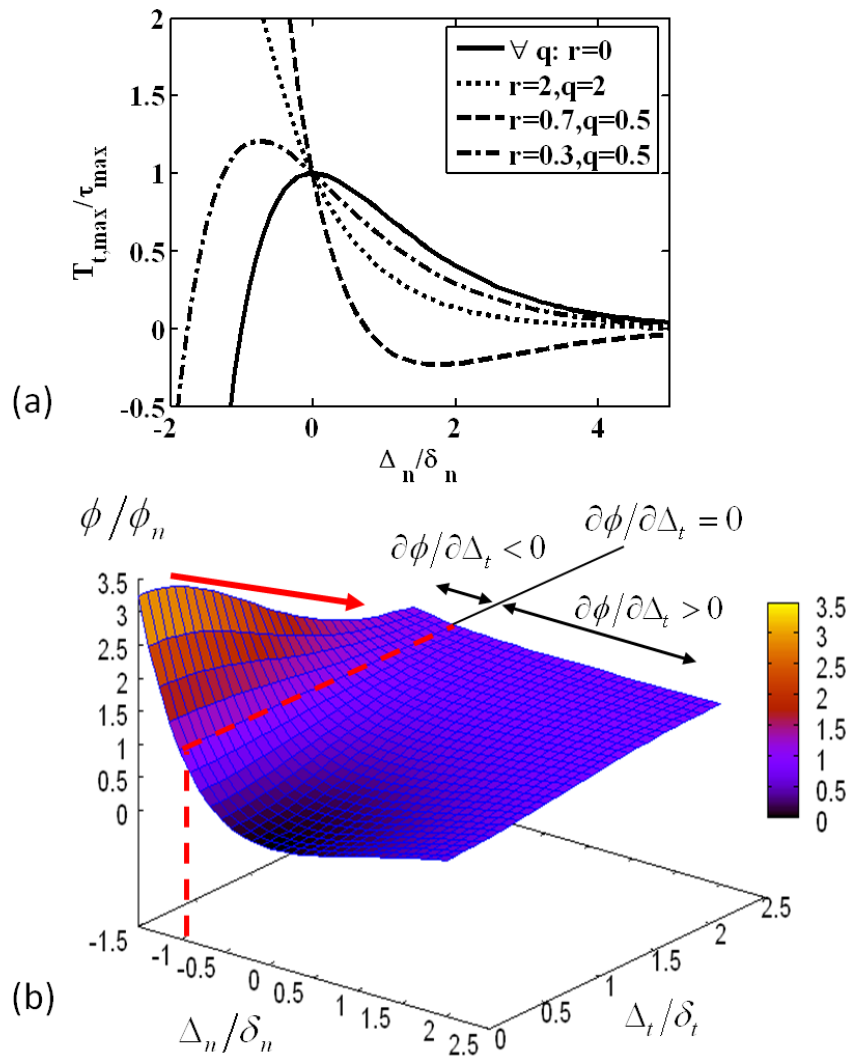asing with increasing normal over-closure. (b) Normalised maximum tangential traction $(T_{t,max}/\tau_{max})$ as a function of normalised normal separation (Δ_n/δ_n) for the MP model with *q=1* and *r=0*. Curves are shown in both separation and over-closure for *m=0* (XN model), *m=1*, *m=2* and *m=5*. (c) Zoomed-in plot of behaviour for low values of Δ_n/δ_n in separation.
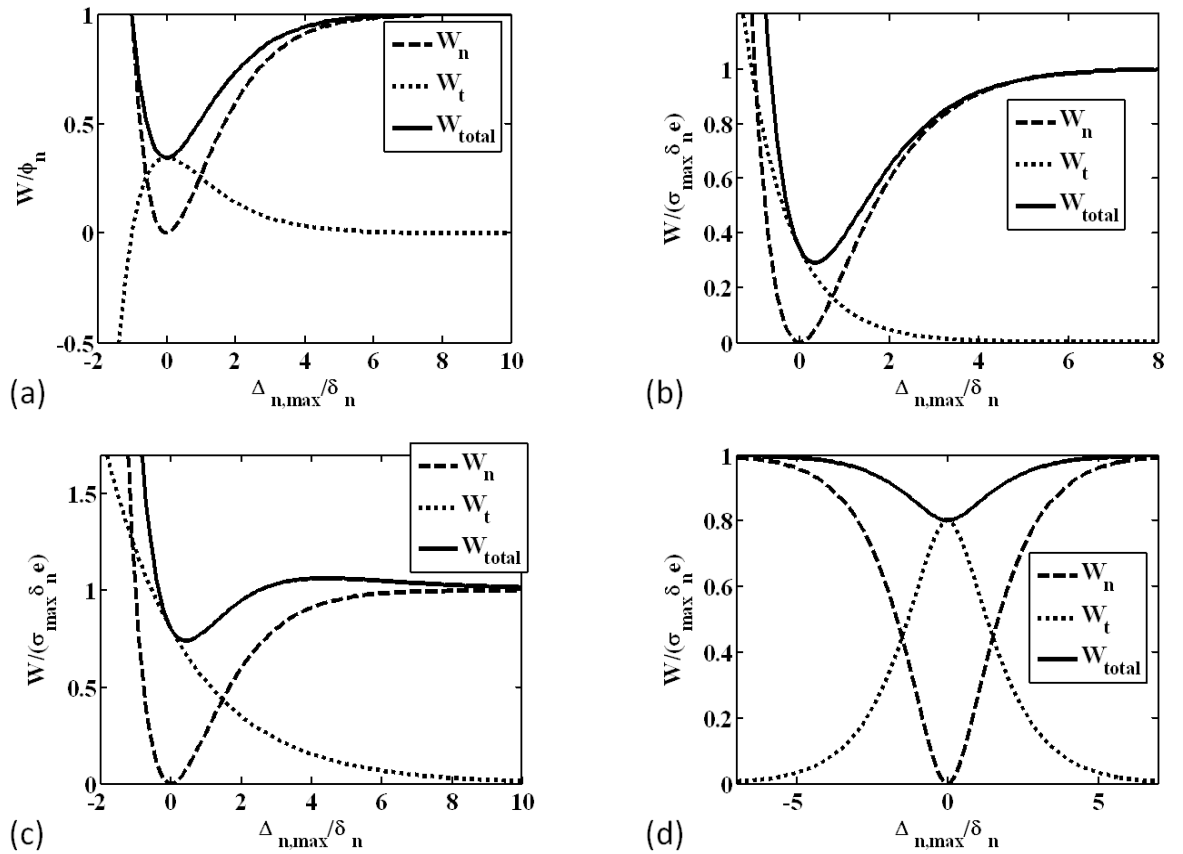
Figure 3-9: Normalised work performed where an interface first undergoes pure normal separation until $\Delta_n = \Delta_{n,max}$ followed by a complete tangential separation for (a) VB model: τ_{max}=0.8 σ_{max} , $\delta_n = \delta_t = 1$. (b) NP1model: τ_{max}=0.8 σ_{max}, $\delta_n = \delta_t = 1$ (c) NP2 model: τ_{max}=0.8 σ_{max}, $\delta_n = \delta_t = 1$(d) SMC model: τ_{max}=0.8 σ_{max}, $\delta_n = \delta_t = 1$
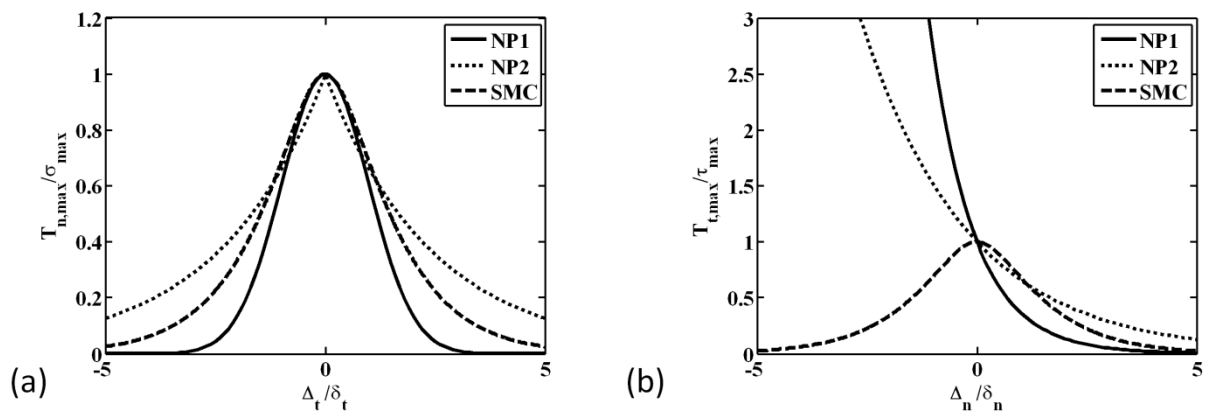
Figure 3-10: (a) Maximum normal traction, $T_{n,max}$, normalised by σ_{max}, as a function of normalised tangential separation (Δ_t/δ_t). (b) Maximum tangential traction, $T_{t,max}$, normalised by τ_{max}, as a function of normalised normal separation(Δ_n/δ_n). NP1: $\delta_n = 1; \delta_t = \sqrt{2}\delta_n$, NP2: $\delta_n = \delta_t = 1$, SMC: $\delta_n = \delta_t = 1$
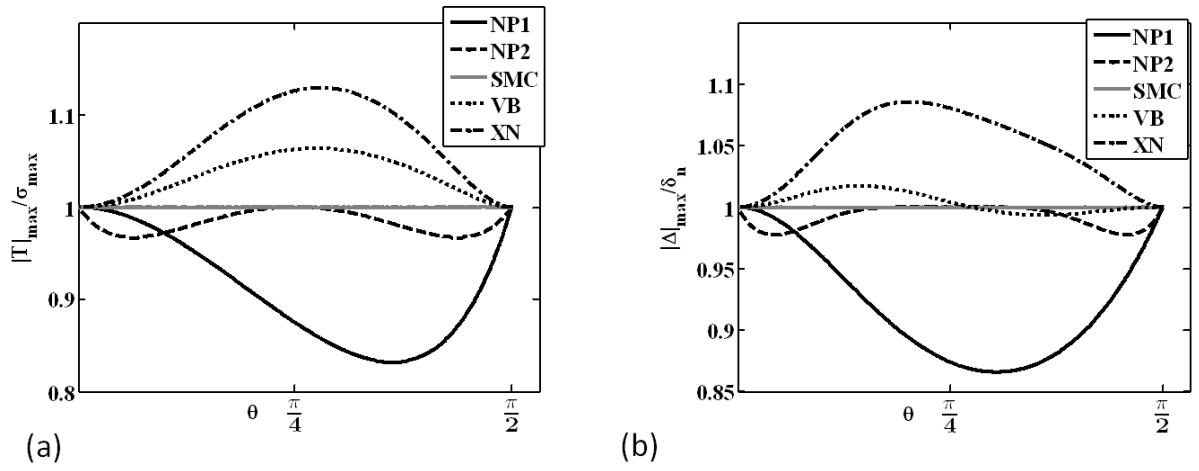
Figure 3-11: (a) Comparison of maximum effective traction ($|T|_{max}/\sigma_{max}$) as a function of mode angle for all CZMs. (b) Comparison of separation magnitudes at which maximum effective traction occurs ($|\Delta|_{max}/\delta_n$) as a function of mode angle for all CZMs. For all models $\sigma_{max} = \tau_{max}$. For XN, VB and NP1 models $\delta_t = \sqrt{2}\delta_n$. For NP2 and SMC models $\delta_n = \delta_t$.

4. Computational Assessment of Cohesive Zone Performance in Mixed-Mode Over-closure and Separation

4.1. Introduction

While cohesive zone models have been used extensively for a wide array of applications and loading conditions, few studies have rigorously investigated the effect of coupling terms on predicted behaviour during mixed-mode interface separation and over-closure. In Chapter 3, a thorough theoretical analysis of potential-based and non-potential-based cohesive zone models (CZMs) under conditions of mixed-mode separation and mixed-mode over-closure is presented. Problems are identified with the well established potential-based Xu-Needleman (XN) model (Xu and Needleman, 1993). A modified potential-based formulation and a number of non-potential-based models are also considered. A non-potential-based formulation has previously been proposed by van den Bosch et al. (2006) (VB model) in order to provide improved coupling under mixed-mode separation. However, in Chapter 3, it is shown that the VB model does not provide correct penalisation of mixed-mode over-closure. A new non-potential-based formulation (NP1) is presented and theoretical analyses demonstrate that correct coupling in both mixed-mode separation and in mixed-mode over-closure is provided by this formulation. Noting that it is not possible to prescribe identical mode I and mode II separation behaviour for the XN, VB and NP1 formulations, a second non-potential-based formulation (NP2) is investigated. Identical traction-separation relationships in mode I, mode II and in pure mixed-mode (45°) separation are achieved for this formulation. Theoretical analyses of Chapter 3 demonstrated that this formulation also provides correct penalisation of mixed-mode over-closure. Finally, following from the work of Tvergaard and Hutchinson (1993), a model in which the coupling terms are based on the separation magnitude (SMC model)

was considered in Chapter 3 in order to provide mode-independent behaviour under displacement controlled conditions.

This chapter extends on the theoretical analysis presented in Chapter 3 by providing a finite element computational assessment of the mixed-mode behaviour of potential and non-potential-based CZMs in separation and over-closure. In the first case study, a bi-layered arch is used to assess the influence of coupling parameters on computed interface tractions. A recently developed analytical solution for the stress state at the arch interface (Parry and McGarry, 2012) is briefly described, demonstrating symmetry between shear and normal tractions, with the traction magnitude being constant along the interface. The ability of the potential and non-potential-based cohesive zone models presented in Chapter 3 to replicate the analytical solution is then analysed. It is demonstrated that the normal-tangential coupling terms in a cohesive zone formulation can significantly affect computed traction and debonding patterns at the arch interface. Proportional mixed-mode separation is computed by the SMC formulation at all points along the interface, in accordance with the analytical solution. All other formulations considered deviate from the analytical solution, displaying a bias towards either mode I or mode II separation. Hence, the bi-layered arch is used to determine the most suitable cohesive zone for the highly mode sensitive application presented in Chapter 6 (stent coating delamination).

In the second case study, a finite element assessment of CZM performance under conditions of mixed-mode over-closure is presented. Specifically, the behaviour of a coating on the compressive region of a cardiovascular stent during expansion of the stent is considered. It is demonstrated that the non-potential-based VB model fails to correctly penalise mixed-mode over-closure of the coating into the stent surface, leading to an under-prediction of coating buckling on the compressive surface of the stent. In contrast, the non-potential-based formulations presented in Chapter 3 correctly penalise mixed-mode over-closure, leading to the simulation of significant coating buckling. It's important to emphasise that the behaviour of a coating on the compressive region of a stent is used as a test case

in order to assess of performance of CZMs under conditions of mixed-mode over-closure. This case study, which simply challenges the ability of CZMs to penalise mixed-mode over-closure, should be distinguished from the extensive study of stent-coating delamination presented in Chapter 6, where the focus is on the tensile region of the stent hinge. The two case studies in the present chapter simply serve to select appropriate CZMs for separation and over-closure for the extensive applied studies of Chapters 6 and 7.

4.2. Methods

4.2.1. Cohesive Zone Model Formulations

In this study, mixed-mode coating behaviour is computed necessitating the use of coupled cohesive zone formulations such as those presented in Chapter 3. 2-D cohesive zone formulations are implemented in the commercial finite element software Abaqus/Standard via a user defined interface subroutine (UINTER), where traction-separation relationships and the Jacobian are defined. In the first case study, the Xu-Needleman (XN), VB, NP1, NP2 and SMC formulations are used to model the interface of a bi-layered arch. In the second case study, three non-potential-based formulations are used to predict coating buckling: the VB formulation, the NP1 formulation and finally the SMC formulation, where the NP2 formulation is implemented during coating compression($\Delta_n < 0$).

4.2.2. Finite Element Model- Case Study I- Bi-layered Arch

The bi-layered arch is shown in Figure 4-1. A 2D idealisation is implemented and horizontal displacement is applied to the base of the arch. The entire semi-circular arch is modelled to avoid computational problems which occur when a quarter-circular model is implemented; a normal traction singularity is computed at the top of the arch ($\theta = 0$). Additionally, a multi point constraint slider boundary condition is implemented in the region at the bottom of the arch ($\theta = \pi/2$) in an effort to avoid associated computational problems in this region. Specifically, the slider boundary condition is enforced to ensure that the bottom coating node,

located at the interface, moves along a line defined by two nodes on the surface of the arch. A polar coordinate system (r, θ) is used. The interface is located at $r = R$ and the symmetry axis is also highlighted. The coating and substrate materials are identified as layers 1 and 2, of thickness h_1 and h_2 respectively. Elastic properties are assumed for the arch and coating materials where μ_1 and μ_2 are the shear moduli of layers 1 and 2, respectively with $\mu_2/\mu_1 = 2.5$. A Poisson's ratio of 0.3 is assumed. Unless otherwise stated, cohesive zone parameters are chosen so that peak mode I traction and peak mode II tractions are equal $(\sigma_{max}/E_c = \tau_{max}/E_c = 0.0001)$ with the peak occurring at the same effective separation in mode I and mode II separation $\left(|T|_{max}^{\theta=0} = |T|_{max}^{\theta=\pi/2}; \ |\Delta|_{max}^{\theta=0} = |\Delta|_{max}^{\theta=\pi/2} \right)$.

4.2.3. Finite Element Model- Case Study II-Stent Coating Buckling

The associated stent and coating geometry for case study II is shown in Figure 4-2. A 2D unit cell idealisation is utilised based on a commercially available stent design (McGarry et al., 2004) and stent deployment is simulated by imposing displacement boundary conditions on the strut ends. 316L stainless steel elastic-plastic material properties are assumed for the stent (Young's modulus 200GPa; Yield stress 264MPa; Ultimate tensile strength 595MPa; v=0.3) (McGarry et al., 2007). A porous titanium alloy coating (TiNOx) is simulated with properties assigned based on the literature (Young's modulus 92GPa; Yield stress 702.5MPa; Ultimate tensile strength 756.5MPa, v=0.35) (Asaoka et al., 1985). An interface strength of $\tau_{max} = \sigma_{max} = 50MPa$ is used for each cohesive zone model and interface characteristic distances are chosen so that peak tractions occur at a separation of 25nm in both mode I and mode II separation.

4.3. Results and Discussion

4.3.1. Case Study I- Bi-layered Arch

Laminated composite circular arches are used in numerous applications. As structural members in the aerospace and marine sectors, they are appreciated for their high strength to weight ratio. This structural element is also typical of stents. The problem of multilayer circular arch deformation has been investigated within the framework of beams (Chandrashekhara and Rao, 1996; Matsunaga, 2003; Malekzadeh, 2009), using different kinematic models in order to estimate the stress distribution in the structure. An exact solution derived in the framework of two dimensional linear elasticity has been recently established (Parry and McGarry, 2012). Such a solution is of great importance to describe the normal and shear stress components at the interface between the two materials of the arch. The analytical solution provides the interface tractions prior to delamination. The different CZMs presented in Chapter 3 are examined for the case of the semi-circular arch subjected to a prescribed displacement at its base.

An analytical solution for the stress state in the arch has been developed by Parry and McGarry (2012). Tractions along the interface (T_n, T_t) can be obtained from the analytical solution:

$$\frac{T_n(\theta)}{\mu_1} = -A \sin(\theta) \frac{U}{R} \tag{4.1}$$

$$\frac{T_t(\theta)}{\mu_1} = A \cos(\theta) \frac{U}{R} \tag{4.2}$$

where the constant, A, is a function of the geometric and material parameters of the bi-layered arch. μ_1 and μ_2 are the shear moduli of layers 1 and 2, respectively while R is the distance to the arch interface. It is worth noting that the traction magnitude $\left(T_{mag} = \sqrt{T_n{}^2 + T_t{}^2}\right)$ is constant along the interface. In order to

predict the delamination of the structure, finite element calculations are carried out with the different cohesive zone models. Firstly, in order to confirm the ability of the finite element model to replicate the analytical solution, a set of calculations is carried out, for which a very small prescribed displacement, U, is applied, so that the decohesion remains negligible. Cohesive zone parameters are chosen so that interface tractions are an order of magnitude lower than the interface strength, i.e. the interface behaviour is in the elastic regime and no debonding occurs. Additionally, interface characteristic lengths are chosen so that the interface stiffness is several orders of magnitude stiffer than the arch materials. Contour plots of the radial stress $\sigma_{rr}(r, \theta)$, shear stress $\sigma_{r\theta}(r, \theta)$ and the hoop stress $\sigma_{\theta\theta}(r, \theta)$ are shown in Figure 4-3. This plot shows how stresses are distributed inside the coating prior to delamination. The finite element calculation shows very good agreement with the analytical solution, except for a small region around a singularity at the base of the arch between the arch and coating materials ($r = R, \theta = \pi/2$) (Figure 4-3 (a)).

4.3.1.1. Debonding Simulations

Next, the XN, VB, NP1, NP2, and SMC cohesive zone models (CZMs) are used to predict debonding of the bi-layered arch. The elastic solution suggests that the interface provides a traction-dependent mode mixity. The mode angle depends on the coordinate along the interface, varying sinusoidally from pure mode II at the base of the arch to pure mode I at the top of the arch. The symmetry between normal and tangential tractions along the interface and the constant traction magnitude along the interface suggest that debonding patterns computed using a CZM at the interface will be highly sensitive to the normal-tangential coupling. Unless otherwise stated, cohesive zone parameters are chosen for the following analyses so that peak mode I traction and peak mode II tractions are equal ($\sigma_{max} = \tau_{max}$), with the peak occurring a the same effective separation in mode I and mode II separation. The variations of T_n and T_t along the interface at the onset of debonding are reported in Figure 4-4 (a)-(d) for the different CZMs, in addition to the analytical solution as a reference.

The traction distribution in the different models follow the general pattern of the analytical solution, namely a tensile normal traction T_n increasing from $T_n = 0$ at the bottom $(\theta = \pi/2)$ to a maximum value at top $(\theta = 0)$. Also, as expected, the absolute value of the shear traction, T_t, is maximum at the bottom of the arch and decreases with increasing θ, vanishing at the top. The XN model is examined in Figure 4-4 (a). The results indicate that the analytical solution is not exactly reproduced, except for pure mode I $(\theta = 0)$ and pure mode II $(\theta = \pi/2)$ separation. The largest gap to the analytical result is computed at $\theta = \pi/4$, where the analytical solution predicts that $||Tn|| = ||Tt||$. Results for the VB model presented in Figure 4-4 (b) show similar characteristics, although the discrepancy between the numerical and analytical results are slightly lower than for the XN model. Results for NP2 $\left(\alpha = \beta = \left(\sqrt{2} - 1\right)\right)$ are depicted in Figure 4-4 (c). This model matches exactly the analytical solution for $\theta = 0$, $\theta = \pi/4$ and $\theta = \pi/2$. However, a clear difference with the analytical model is computed for the intermediate values of θ. Finally, Figure 4-4(d) reveals that the SMC formulation accurately reproduces the analytical solution for all points along the interface.

Figure 4-5 shows the normal(Δ_n) and tangential (Δ_t) displacements computed at 21 equally distributed nodes along the bi-layered arch interface during arch deployment. The lines coincident with the x and y-axis are the computed displacement at the bottom $(\theta = \pi/2)$ and top $(\theta = 0)$ of the arch respectively. Lines indicating proportional separation at $\theta = \pi/8$, $\pi/4$ and $3\pi/8$ are shown in order to compare with computed displacements at these points along the interface. In accordance with the analytical solution, displacements at the interface occur in such a way as to maintain a constant traction ratio(T_n/T_t) until the peak traction magnitude ($|T|_{max} = \max(\sqrt{T_n^2 + T_t^2})$) is reached.

CZM model parameters are chosen so that the peak mode I and mode II tractions are equal (i.e. $|T|_{max}^{\theta=0} = |T|_{max}^{\theta=\pi/2}$) and the separation magnitude at which these peak tractions occur are also equal (i.e. $|\Delta|_{max}^{\theta=0} = |\Delta|_{max}^{\theta=\pi/2}$). However, as discussed in Chapter 3, the form of the traction-separation curves are different for

mode I and mode II separation for NP1, VB and XN models. Considering firstly the XN CZM (Figure 4-5 (a)), in order to maintain a constant traction ratio, the form of the equations dictate that the interface displacements tend toward a mode I type separation for $0 \leq \theta \leq \pi/4$. A reasonable agreement is computed at $\theta = \pi/8$ between the computed displacement ratio and the displacement ratio required for proportional loading. However, it is worth noting that there is a slight tendency towards mode II type separation for $\theta \geq 3\pi/8$. The VB CZM predicts a slight tendency toward mode I separation for all points along the interface (Figure 4-5 (b)). In the case of the NP2 model (Figure 4-5 (c)), separation paths tend toward mode I for $0 \leq \theta < \pi/4$ and towards mode II type separation for $\theta > \pi/4$. Proportional displacement is computed a $\theta = \pi/4$ as expected. Using the SMC CZM (Figure 4-5 (d)), proportional displacement is computed at all points along the interface. Finally, for the NP1 model (Figure 4-5 (e)), mixed-mode separation paths tend towards the mode II axis. The peak traction magnitude is initially reached at $\theta \approx 0.3\pi$, followed by mode II dominated debonding characterised by increasing tangential separation.

The normal traction computed at the top of the arch $(\theta = 0)$ and the tangential traction computed at the base of the arch $(\theta = \pi/2)$ are shown in Figure 4-6 for the XN, VB, NP2 and SMC CZMs. With the exception of the SMC model, the normal traction exceeds the tangential traction as arch displacement is increased, with a peak normal traction being computed at $U/R \approx 2.4 \times 10^{-3}$, followed by interface delamination. In the case of the SMC model, the normal and tangential tractions are equal up to and beyond the peak, which occurs at a higher arch displacement of $U/R \approx 2.6 \times 10^{-3}$. Corresponding interface separations are shown in Figure 4-7 (normal separation at $\theta = 0$ and tangential separation at $\theta = \pi/2$). In the case of the XN and VB models (Figure 4-7(a) and (b)) the normal separation is initially lower than the tangential separation. However, as arch displacement increases the normal separation at the top of the arch exceeds the tangential separation at the bottom of the arch as the peak traction is approached. This results from the different forms of the mode I and mode II traction-separation relationships in the case of the XN and VB CZMs. Following

the peak traction at $U/R \approx 2.4 \times 10^{-3}$, the normal separation at the top of the arch increases rapidly. In the case of the NP2 CZM (Figure 4-7(c)), as the form of the mode I and mode II traction-separation relationships are identical, the normal separation is equal to the tangential separation during initial arch displacement. However, similar to the XN and VB simulations, the normal separation increases rapidly following the peak traction at $U/R \approx 2.4 \times 10^{-3}$, again leading to a mode I delamination of the arch. In the case of the SMC model (Figure 4-7(d)), normal and tangential separations are identical up to and beyond the peak ($U/R \approx 2.6 \times 10^{-3}$). At $U/R \approx 2.8 \times 10^{-3}$ a bifurcation point is reached and tangential separations increase rapidly.

Figure 4-8(a) and (b) show the deformed shape of the arch with contour plots of von Mises stress for SMC and XN models prior to the initiation of debonding ($U/R \approx 2.4 \times 10^{-3}$). Displacement fields are amplified by a factor 100 for better visualization. Similar stress fields are computed in both layers (substrate and coating) of the arch. It should also be noted that the magnitude of mode I separation at the top of the arch and mode II separation at the bottom of the arch are similar (as revealed in Figure 4-7). However, following the initiation of debonding ($U/R \approx 2.8 \times 10^{-3}$) the coating is strained very differently in the case of the XN and SMC CZMs (Figure 4-8 (c) and (d)). Mode I separation at the top of the arch dominates when the XN CZM is used (and indeed when the VB and NP2 CZMs are used, as shown in Figure 4-7). In contrast, the SMC model predicts a gradual transition from mode I at the top of the arch to mode II at the bottom of the arch.

At a glance, the mode I dominance of the XN and VB simulations is somewhat surprising, given that the work of mode I separation ($\emptyset_n$) is greater that the work of mode II separation ($\emptyset_t$) when $\sigma_{max} = \tau_{max}$ for these formulations. However, the analytical solution of Parry and McGarry (2012) demonstrates that the arch interface provides traction controlled mode mixity, with $\theta = Tan^{-1}(T_n/T_t)$. Finite element predictions of separation paths along the arch interface for the XN model are shown in Figure 4-9(a). Following initiation of debonding the stress in

the arch deviates from the analytical elastic solution so that traction controlled mode mixity is no longer enforced. At this point, tangential separations near the bottom of the arch are reversed as normal debonding dominates. A similar pattern is predicted using the NP2 CZM at the arch interface (Figure 4-9(b)).

A final pair of simulations is presented in Figure 4-10 where $\emptyset_t = 4\emptyset_n$ for both the XN (Figure 4-10 (a)) and SMC (Figure 4-10 (b)) models. As expected, mode I delamination at the top of the arch dominates in both cases. However, the mode mixity along the interface is quite different for both models, with the XN predicting separation paths that lie much closer to the pure mode I axis.

4.3.2. Case Study II-Stent Coating Buckling

Using the VB formulation at the stent-coating interface, Figure 4-11(a) shows the computed normal and tangential separation of a point B at the coating-stent interface (see Figure 4-2) during stent deployment. The level of deployment is characterised as the circumferential strain of the stent, simply calculated as $(L - L_o)/L_o$, as shown in Figure 4-2. At the curved section in the region of point B the coating is compressed into the stent surface during deployment. Using the VB model this results in the computation of mixed-mode coating over-closure characterised by negative normal separations and non-zero tangential separations, as shown in Figure 4-11 (a). It can be seen that normal over-closure reaches very unrealistic levels ($\Delta_n/\delta_n \approx 60$) during the simulation. Figure 4-11(b) shows the corresponding tangential traction-separation relationship. Initially, tangential tractions increase during over-closure at the interface. However, a peak value of tangential traction that is lower than τ_{max} is reached, demonstrating the weakened resistance of the interface to tangential separation during mixed-mode over-closure. Following the peak, tangential traction reduces and becomes negative, despite the tangential separation being positive. This means that, instead of penalising the movement of nodes during mixed-mode over-closure, repulsive tangential tractions encourage increasing tangential separation, despite the coating being overclosed into the substrate. Figure 4-11 (c) shows the corresponding normal traction-separation behaviour at point B during stent deployment. Initially,

normal over-closure is correctly penalised. However, the computation of negative (repulsive) tangential tractions (Figure 4-11 (b)) reduces the penalisation of normal over-closure at the interface. Therefore, further over-closure at the stent-coating interface is predicted. This unphysical behaviour occurs because repulsive tangential tractions are computed by the VB model for significant mixed-mode over-closure ($\Delta_n/\delta_n < -1$) as discussed in Chapter 3. Such repulsive tangential tractions lead to excessive tangential separations at the interface, which in turn reduce the penalisation of normal over-closure, leading to excessive mixed-mode over-closure. As demonstrated in Chapter 3, similar problems occur for the XN model during mixed-mode over-closure.

Results computed using the NP1 model at the stent-coating interface are shown in Figure 4-12. During initial stages of stent deployment, mixed-mode over-closure is computed at point B (Figure 4-2) during stent deployment with negative normal separation and non-zero tangential separation (highlighted in the insert of Figure 4-12(a)). However, in contrast to the VB model, significant normal over-closure is prevented due to the ability of the NP1 model to penalise mixed-mode over-closure. The correct penalisation of mixed-mode over-closure in the compressive region of the stent results in buckling of the coating. This buckling initiates to the right of point B. Further stent deployment leads to an increase in the buckling region. When a circumferential strain of 1.25 is reached point B is incorporated into the buckling region, as characterised by a change from normal over-closure to normal separation. The prediction of such buckling is dependent on the correct treatment of tangential traction during over-closure. The tangential traction-separation plot during stent deployment is shown in Figure 4-12(b). As coating over-closure increases during the initial stages of stent deployment, an increase in tangential separation is penalised by a sharp increase in tangential traction. When normal over-closure begins to decrease due to coating buckling a peak in tangential traction of $T_t/\tau_{max} \approx 2.2$ is computed. As point B enters the regime of normal separation following extensive buckling the tangential movement of the node changes direction, with debonding occurring following a peak traction of $T_t/\tau_{max} \approx -0.3$ at a tangential separation of $\Delta_t/\delta_t \approx -0.2$, as illustrated by the

broken line in Figure 4-12(b). The increase in resistance to tangential separation during normal over-closure and the decrease in resistance to tangential separation during normal separation that is provided by the NP1 model is physically realistic and is critical for the prediction of coating buckling. For completeness, the normal traction-separation plot during stent deployment is shown in Figure 4-12(c). Again this illustrates that NP1 correctly penalises mixed-mode over-closure during initial stages of stent deployment and then correctly predicts mixed-mode separation as the coating buckles during higher deployment, with a reduced peak normal traction of $T_n/\sigma_{max} \approx 0.75$ being computed.

A similar pattern of mixed-mode behaviour at point B is predicted when the SMC model is implemented during coating separation$(\Delta_n > 0)$ and the NP2 formulation is utilised during coating compression$(\Delta_n < 0)$ (the SMC formulation is not suitable for use during interface compression as discussed in Chapter 3), as shown in Figure 4-13. Again, mixed-mode over-closure is computed at point B during early stages of stent deployment (Figure 4-13 (a)). Similar to the NP1 model, tangential traction increases during mixed-mode over-closure, increasing the resistance to tangential separation. When normal over-closure reduces with the onset of coating buckling a peak tangential traction of $T_t/\tau_{max} \approx 1.25$ is computed (Figure 4-13 (b)). While this value is lower than the peak tangential traction computed by the NP1 model, mixed-mode over-closure is successfully penalised and coating buckling is predicted at higher stent deployment, as is evident in the normal traction-separation plot of Figure 4-13(c).

Figure 4-14 shows the von Mises stress distribution on the deformed stent-coating geometry at a circumferential strain of 0.6 computed using NP1 and VB formulations (Figure 4-14 (a) and (b) respectively). Figure inserts show details of the deformed stent and coating geometry in the region of point B. Using the NP1 model, mixed-mode over-closure of the coating is correctly penalised in the compressive region of the stent. The prevention of mixed-mode over-closure results in the computation of a highly stressed region in the coating to the right of point B which results in buckling of the coating from the stent surface. As

deployment continues, the buckled region of the coating extends to point B and it separates from the stent surface, as discussed in relation to Figure 4-12. In contrast to the NP1 model, the VB model computes excessive mixed-mode over-closure at point B. As a result stresses in the coating are significantly reduced and buckling of the coating is not correctly predicted by the model as shown in Figure 4-14(b).

As shown in Figure 4-15(a), buckling of the coating from the stent surface becomes very pronounced at high levels of stent deployment (circumferential strain of 7.0) for the NP1 model. Such coating buckling during stent deployment has been observed experimentally (Basalus and von Birgelen, 2010). As demonstrated in Figure 4-11-Figure 4-14, the ability of a CZM to predict such buckling is dependent on correct treatment of mixed-mode over-closure. Figure 4-15(b) demonstrates that a similar pattern of buckling is computed by the SMC model (with the NP2 formulation is utilised during coating compression$(\Delta_n < 0)$). Simulations were also performed using the NP2 formulation to describe coating separation and over-closure with predicted results very similar to those shown in Figure 4-15 (a) and (b).

4.4. Conclusion

This chapter extends on the theoretical analysis presented in Chapter 3 by providing a computational assessment of cohesive zone performance under conditions of mixed-mode separation (case study 1) and mixed-mode over-closure (case study 2). The first case study entails the simulation of the delamination of a bi-layered arch when a horizontal displacement is applied to the arch base. The previously developed analytical solution of Parry and McGarry (2012) demonstrates that in the elastic regime, prior to debonding, the arch interface enforces traction controlled mode mixity, with the ratio of normal to tangential traction depending exclusively on position along the interface. Finite element simulations reveal that the XN, VB and NP2 models provide a significant bias towards mode I delamination when $\sigma_{max} = \tau_{max}$. The NP1 model provides a very weak resistance to mixed-mode delamination, ultimately resulting in mode II delamination of the arch. Only the SMC model provides mode-independent

behaviour up to and beyond the initiation of debonding. This case study demonstrates the importance of normal-tangential coupling terms in CZMs for mode-sensitive traction controlled conditions, as suggested by the theoretical analyses presented in Chapter 3.

In the second case study, the behaviour of a coating on the compressive region of a stent is used as a test case in order to assess of performance of CZMs under conditions of mixed-mode over-closure. The previously proposed VB CZM fails to correctly penalise mixed-mode over-closure at the compressive region of the stent surface, predicting an unphysical penetration of coating into the stent surface. Such over-closure has a pronounced influence on computed stresses in the coating and extensive coating buckling is not predicted. In contrast, the NP1 and NP2 CZMs correctly penalise mixed-mode over-closure, leading to the prediction of coating buckling patterns similar to those observed experimentally (Basalus and von Birgelen, 2010; Regar et al., 2001). This case study clearly demonstrates that a CZM must correctly penalise mixed-mode over-closure in order to predict coating buckling. The two case studies presented in this chapter are used to assess the suitability of CZMs for the highly mode-sensitive application in Chapter 6, where the stress-state at the stent-coating interface is presented as a function of the stent design parameters. Based on the theoretical analyses presented in Chapter 3 and the computational analyses presented in the present chapter, the NP2 formulation is implemented for over-closure ($\Delta_n < 0$) and the SMC formulation is implemented for separation ($\Delta_n > 0$) for the cardiovascular application studies of Chapter 6 (stent coating delamination) and Chapter 7 (aneurysm dissection). For the final cardiovascular application study presented in Chapter 8 (cyclic debonding of an endothelial cell) the potential-based XN and MP models are primarily implemented.

4.5. References

Asaoka, K., Kuwayama, N., Okuno, O.&Miura, I. (1985) Mechanical properties and biomechanical compatibility of porous titanium for dental implants. *Journal of biomedical materials research,* 19**,** 699-713.

Basalus, M. W. Z.&Von Birgelen, C. (2010) Benchside testing of drug-eluting stent surface and geometry. *Interv. Cardiol.,* 2**,** 159-175.

Chandrashekhara, K.&Rao, K. S. N. (1996) Analysis of a long thick orthotropic circular cylindrical shell panel. *Journal of engineering mechanics,* 122**,** 575.

Malekzadeh, P. (2009) A two-dimensional layerwise-differential quadrature static analysis of thick laminated composite circular arches. *Applied Mathematical Modelling,* 33**,** 1850-1861.

Matsunaga, H. (2003) Interlaminar stress analysis of laminated composite and sandwich circular arches subjected to thermal/mechanical loading. *Composite structures,* 60**,** 345-358.

McGarry, J. P., O'Donnell, B. P., McHugh, P. E.&McGarry, J. G. (2004) Analysis of the mechanical performance of a cardiovascular stent design based on micromechanical modelling. *Computational Materials Science,* 31**,** 421-438.

McGarry, J. P., O'Donnell, B. P., McHugh, P. E., O'Cearbhaill, E.&McMeeking, R. M. (2007) Computational Examination of the Effect of Material Inhomogeneity on the Necking of Stent Struts Under Tensile Loading. *Journal of Applied Mechanics,* 74**,** 978.

Parry, G.&McGarry, P. (2012) An analytical solution for the stress state at stent-coating interfaces. *Journal of the Mechanical Behavior of Biomedical Materials,* 10**,** 183-196.

Regar, E., Sianos, G.&Serruys, P. W. (2001) Stent development and local drug delivery. *British medical bulletin,* 59**,** 227.

Tvergaard, V.&Hutchinson, J. W. (1993) The influence of plasticity on mixed mode interface toughness. *Journal of the Mechanics and Physics of Solids,* 41**,** 1119-1135.

van den Bosch, M. J., Schreurs, P. J. G.&Geers, M. G. D. (2006) An improved description of the exponential Xu and Needleman cohesive zone law for mixed-mode decohesion. *Engineering Fracture Mechanics,* 73**,** 1220-1234.

Xu, X. P.&Needleman, A. (1993) Void nucleation by inclusion debonding in a crystal matrix. *Modelling and Simulation in Materials Science and Engineering,* 2**,** 417-418.

4.6. Tables and Figures
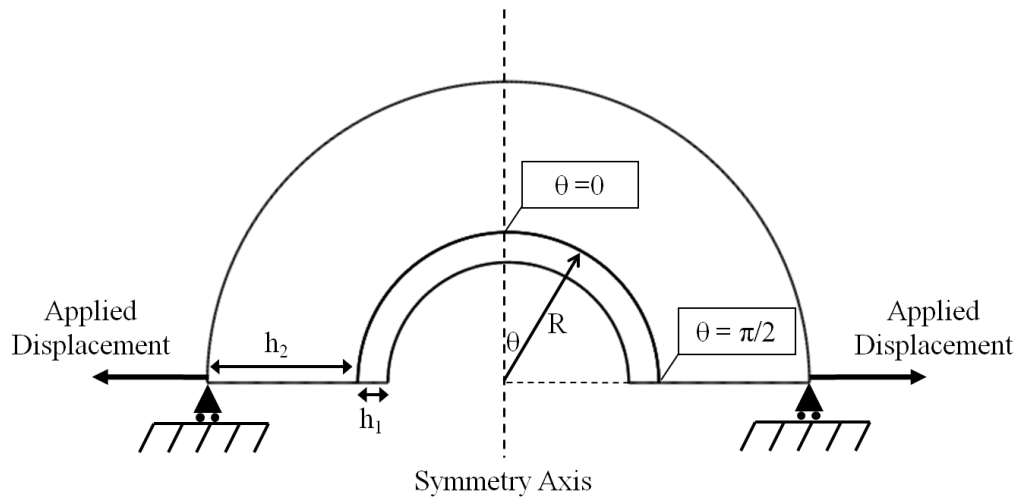
Figure 4-1: Geometry of the arch and coating. Boundary conditions and applied displacements are highlighted. A polar co-ordinate system is used where R is the distance to the interface. Interface tractions and displacements are computed along the interface from $\theta = 0$ to $\theta = \pi/2$.
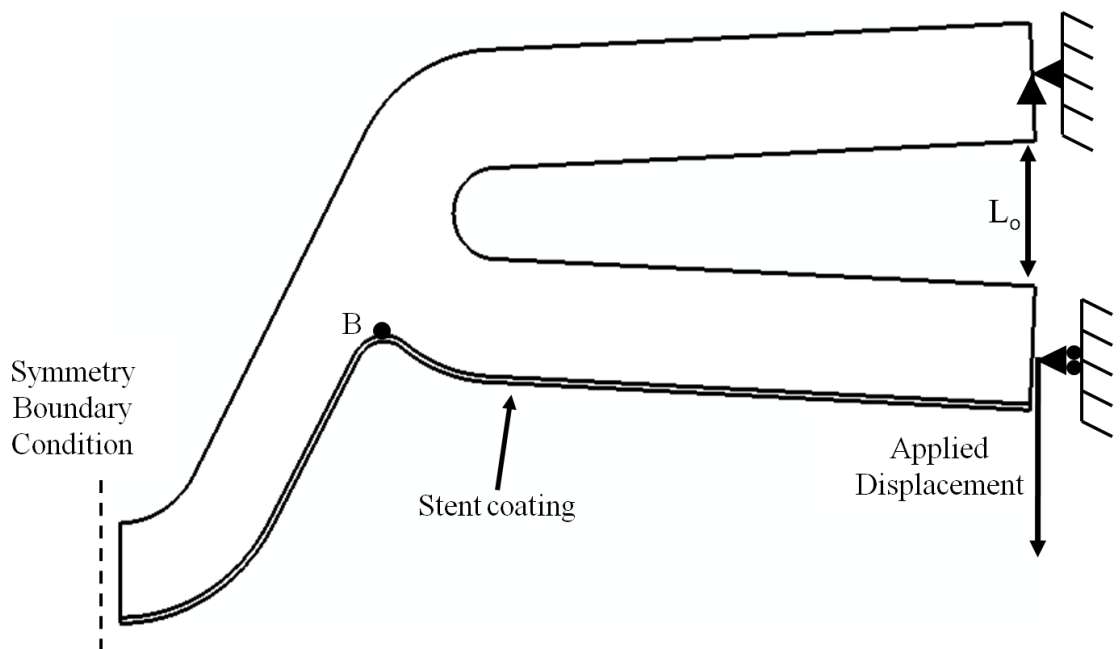
Figure 4-2: Geometry of the stent and stent coating. Boundary conditions and applied displacement are highlighted. Point B indicates a node at the stent-coating interface in the compressive region of the stent. The initial circumferential strain (L_o) is also indicated.

104
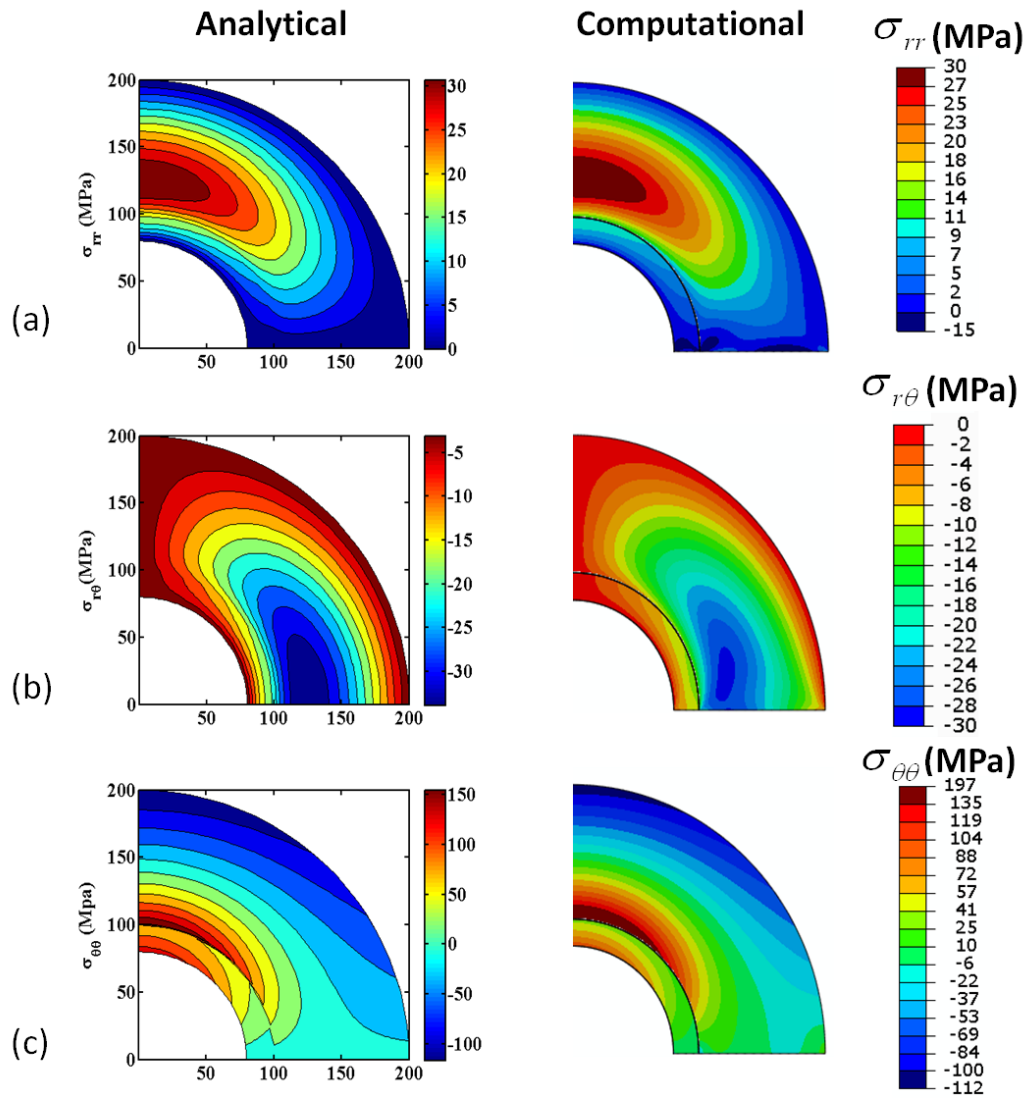
Figure 4-3: Stress distribution plotted on the deformed geometry prior to coating delamination ($U/R = 1.014E - 3$). Comparison is made between analytical (Parry and McGarry, 2012) and finite element predictions for (a) normal stress (σ_{rr}); (b) shear stress ($\sigma_{r\theta}$) and (c) hoop stress ($\sigma_{\theta\theta}$). $h_2/R = 1, \kappa_1 = 1.8, \kappa_2 = 1.8, \mu_2/\mu_1 = 2.5$.
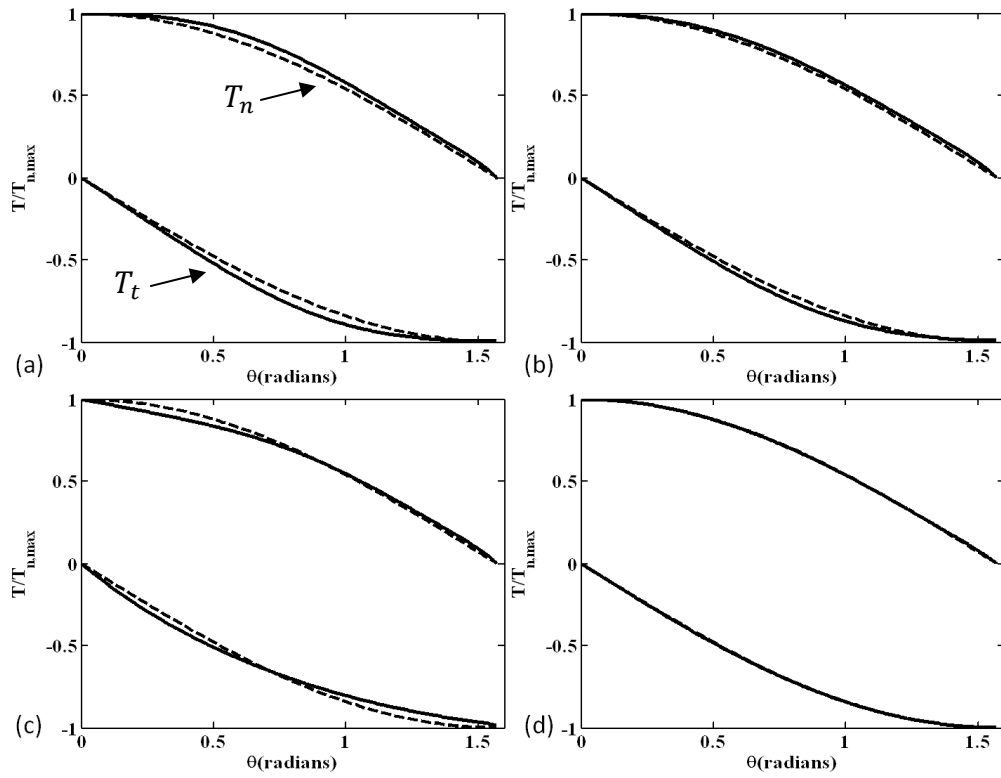
Figure 4-4: Normalised traction $(T/T_{n,max})$ computed at the bi-layered arch interface for (a) XN model; (b) VB model; (c) NP2 model and (d) SMC model at arch deployment where $T_n = T_{n,max}$ at $\theta = 0$. Computational curves are solid lines whereas analytical curves are dotted lines. The normal (T_n) and tangential (T_t) traction responses are indicated in (a).
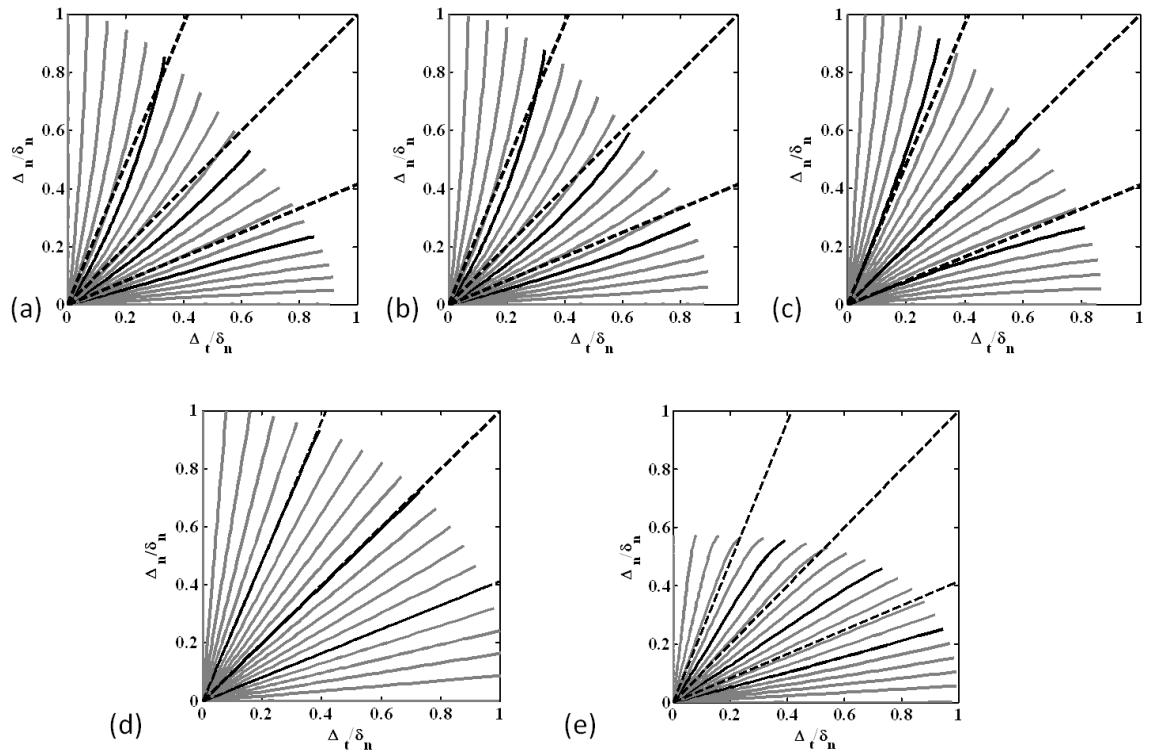
Figure 4-5: Separation paths $[(\Delta_n/\delta_n)$ versus $\Delta_t/\delta_n]$ for 21 equally spaced nodes along the bi-layered arch interface for (a) XN model (b) VB model; (c) NP2 model; (d) SMC model and (e) NP1 model at an arch deployment where the peak traction magnitude $(|T|_{max})$ is reached. Proportional loading paths at $\theta = \pi/8$, $\pi/4$ and $3\pi/8$ are indicated by dotted lines. The lines coincident with the x and y-axis are the computed displacement at the bottom $(\theta = \pi/2$) and top $(\theta = 0$) of the arch respectively.
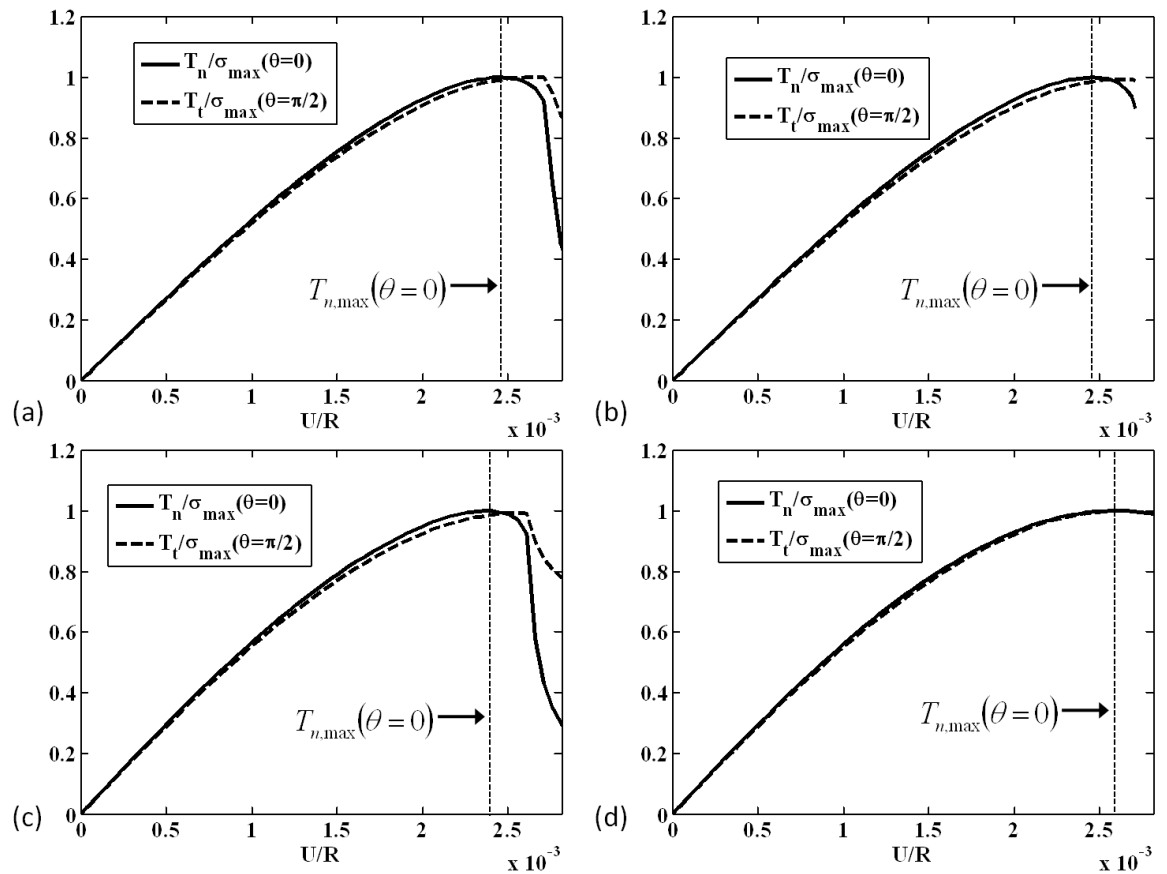
Figure 4-6: Normalised normal traction (T_n/σ_{max}) and normalised tangential traction (T_t/σ_{max}) computed at the bi-layered arch interface as a function of normalised arch deployment (U/R) for (a) XN model; (b) VB model; (c) NP2 model and (d) SMC model. Normal traction is computed at the top of the arch ($\theta = 0$) and tangential traction is computed at the bottom of the arch ($\theta = \pi/2$). The deployment at which maximum normal traction $\left(T_{n,max}\right)$ is computed at the top of the arch ($\theta = 0$) is also indicated.
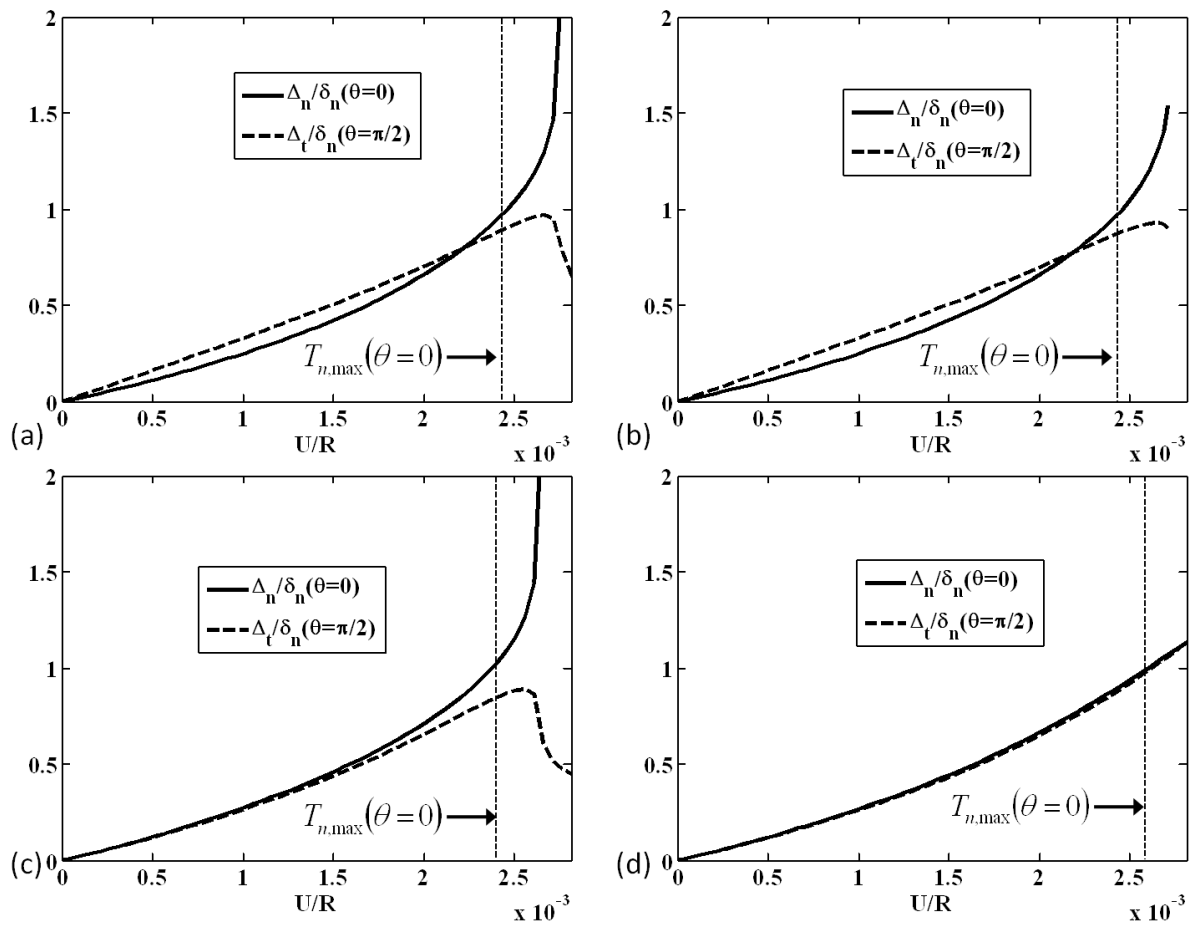
Figure 4-7: Normalised normal displacement (Δ_n/δ_n) and normalised tangential displacement (Δ_t/δ_n) computed at the bi-layered arch interface as a function of normalised arch deployment(U/R) for (a) XN model; (b)VB model; (c) NP2 model and (d) SMC model. Normal displacement is computed at the top of the arch ($\theta = 0$) and tangential displacement is computed at the bottom of the arch ($\theta = \pi/2$). The deployment at which maximum normal traction $(T_{n,max})$ is computed at the top of the arch ($\theta = 0$) is also indicated.
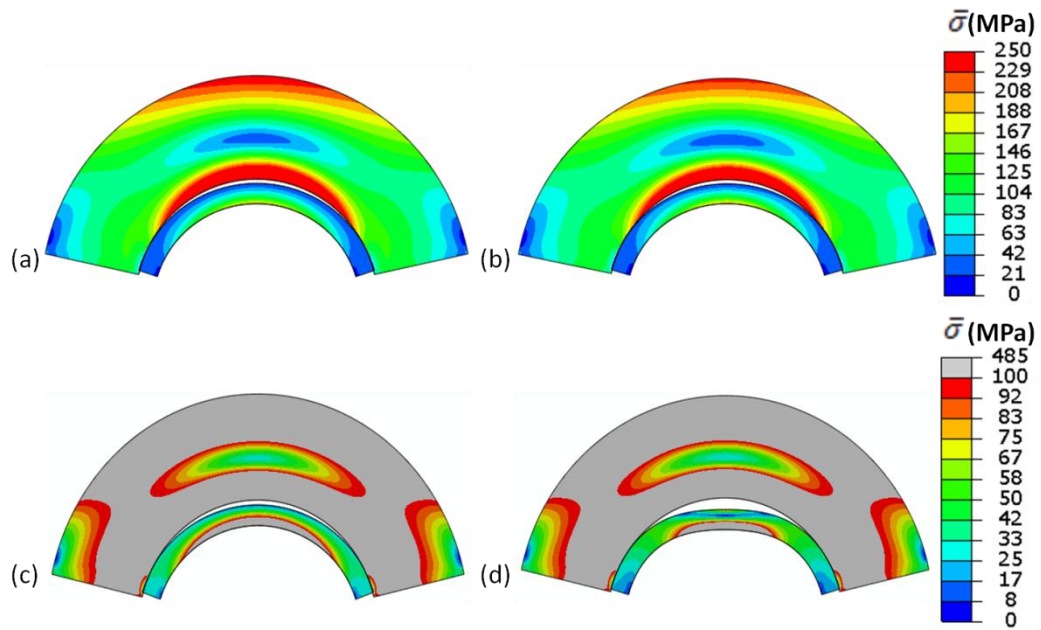
Figure 4-8: von Mises stress distribution ($\bar{\sigma}$) plotted on the deformed geometry at arch deployment where $T_n = T_{n,max}$ at $\theta = 0$ for (a) SMC model and (b) XN model. Computed von Mises stress distribution at arch deployment following the initiation of debonding at $\theta = 0$; $T_n < T_{n,max}$; $(U/R = 2.814E - 3)$ for (c) SMC model and (d) XN model. Scale 1:100.
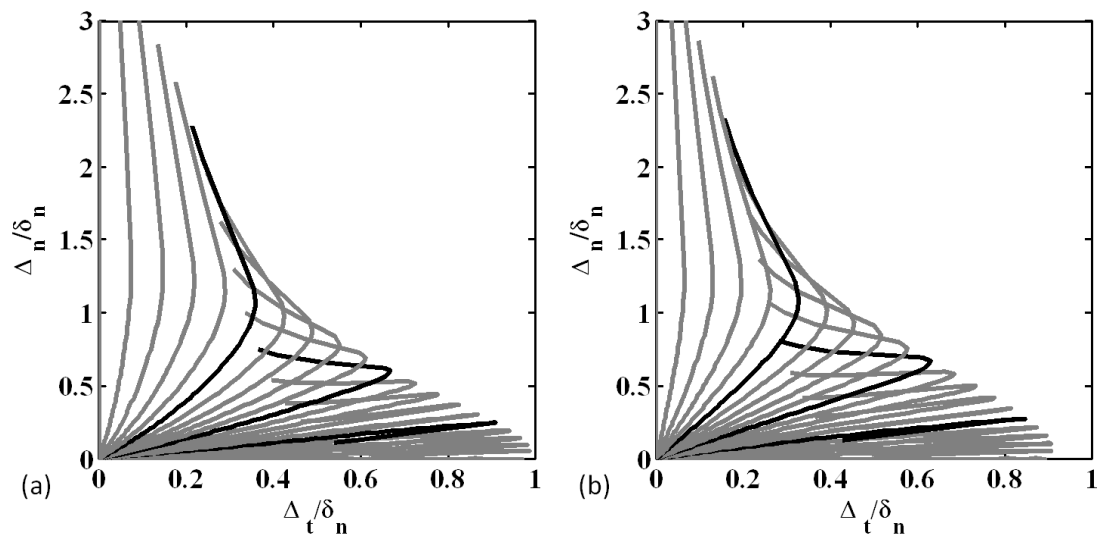
Figure 4-9: Separation paths $[(\Delta_n/\delta_n)$ versus $\Delta_t/\delta_n]$ for 21 equally spaced nodes along the bi-layered arch interface for (a) XN model (b) NP2 model. $(\sigma_{max} = \tau_{max} = 20MPa)$.
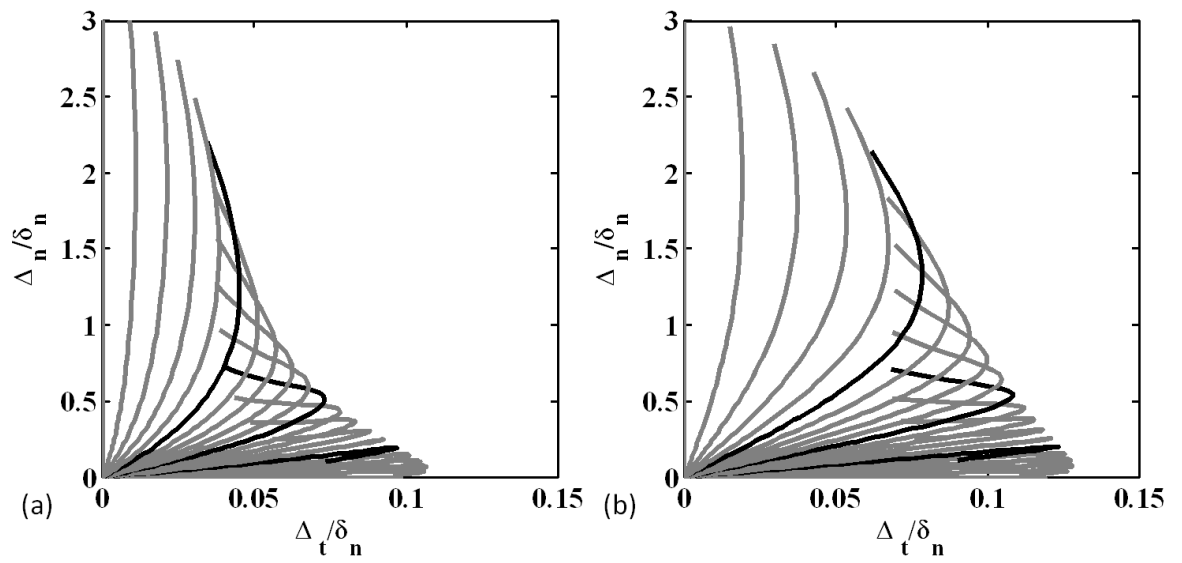
Figure 4-10: Separation paths $[(\Delta_n/\delta_n)$ versus $\Delta_t/\delta_n]$ for 21 equally spaced nodes along the bilayered arch interface for (a) XN model (b) SMC model. $(\emptyset_t = 4\emptyset_n)$.
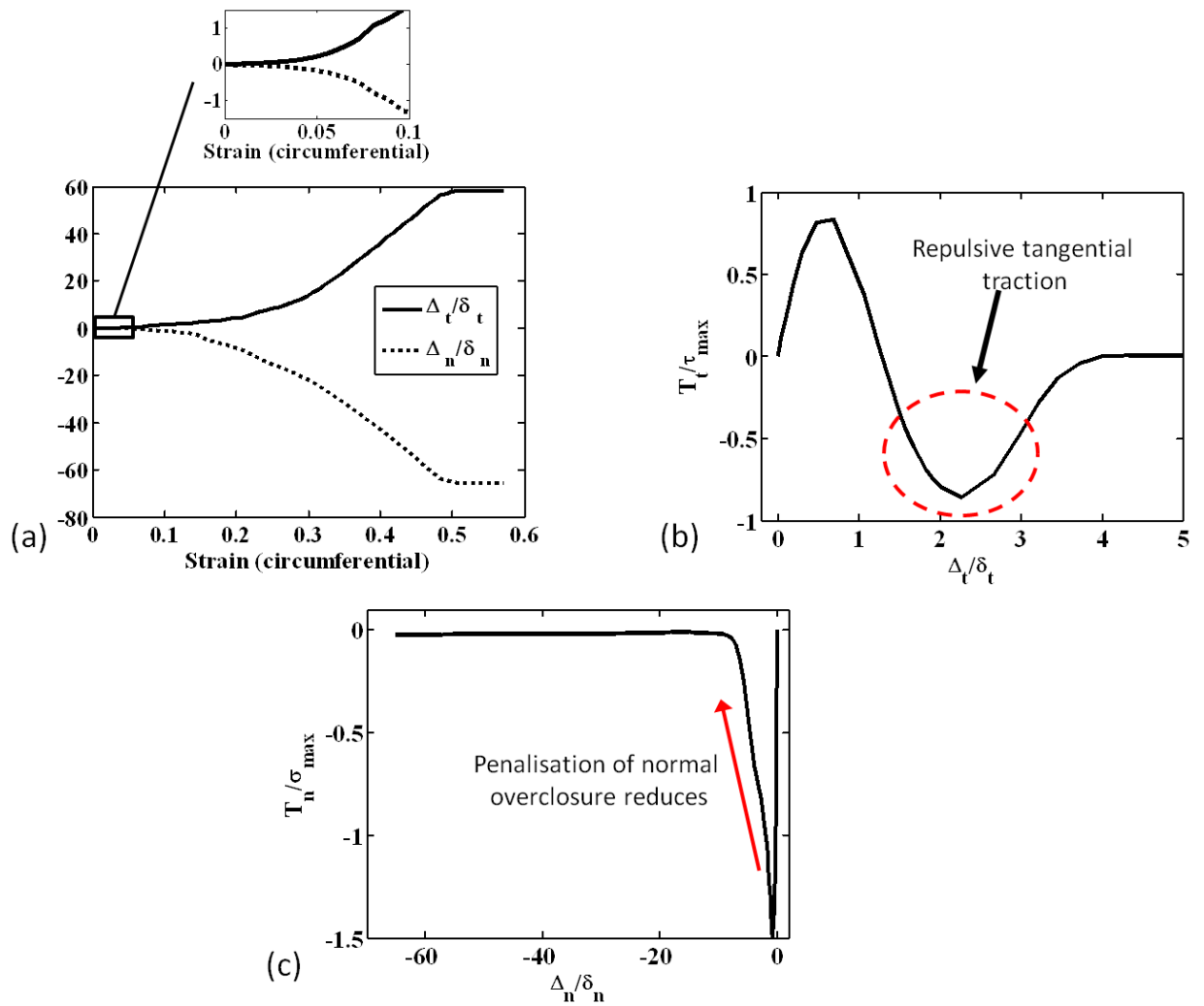
Figure 4-11: Interface behaviour computed at point B during stent deployment using the VB model: (a) Normalised normal (Δ_n/δ_n) and tangential (Δ_t/δ_t) separation as a function of circumferential strain. (b) Normalised tangential traction (T_t/τ_{max}) as a function of normalised tangential separation (Δ_t/δ_t). (c) Normalised normal traction (T_n/σ_{max}) as a function of normalised normal separation (Δ_n/δ_n).
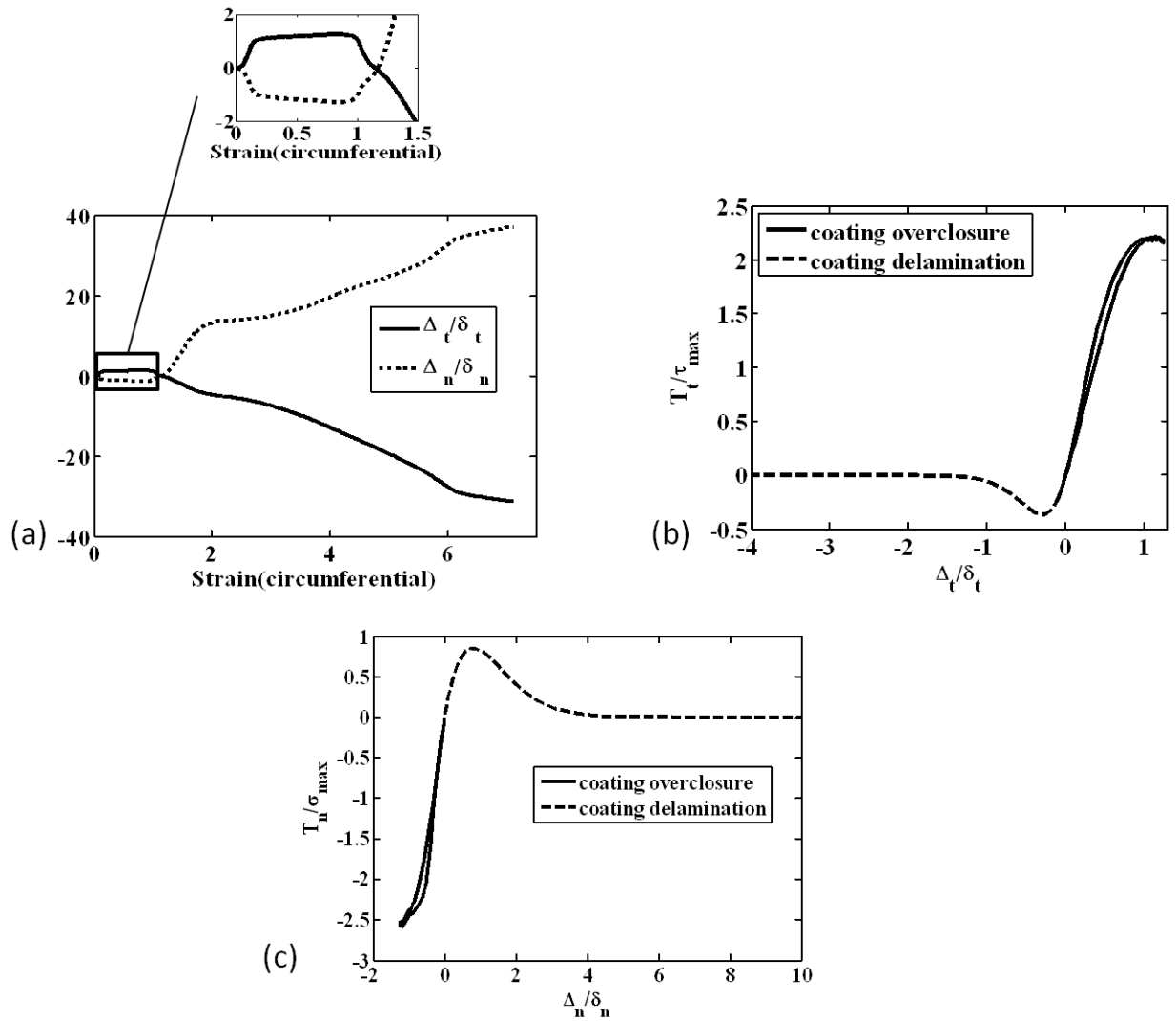
Figure 4-12: Interface behaviour computed at point B during stent deployment using NP1: (a) Normalised normal (Δ_n/δ_n) and tangential (Δ_t/δ_t) separation as a function of circumferential strain. (b) Normalised tangential traction (T_t/τ_{max}) as a function of normalised tangential separation (Δ_t/δ_t). (c) Normalised normal traction (T_n/σ_{max}) as a function of normalised normal separation (Δ_n/δ_n).
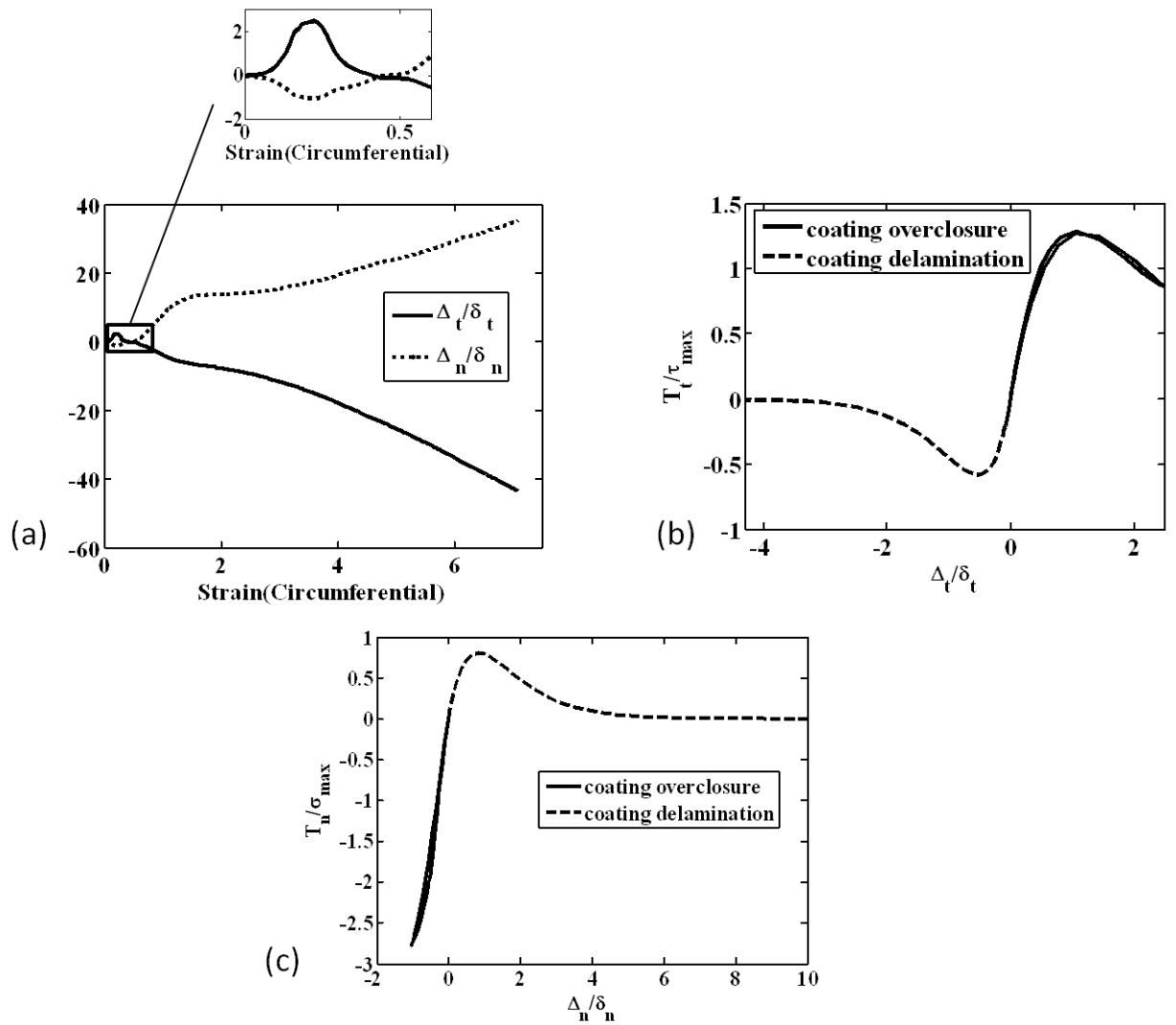
Figure 4-13: Interface behaviour computed at point B during stent deployment using SMC($\Delta_n > 0$) and NP2 ($\Delta_n < 0$): (a) Normalised normal (Δ_n/δ_n) and tangential (Δ_t/δ_t) separation as a function of circumferential strain (b) Normalised tangential traction (T_t/τ_{max}) as a function of normalised tangential separation (Δ_t/δ_t) and (c) Normalised normal traction (T_n/σ_{max}) as a function of normalised normal separation (Δ_n/δ_n).
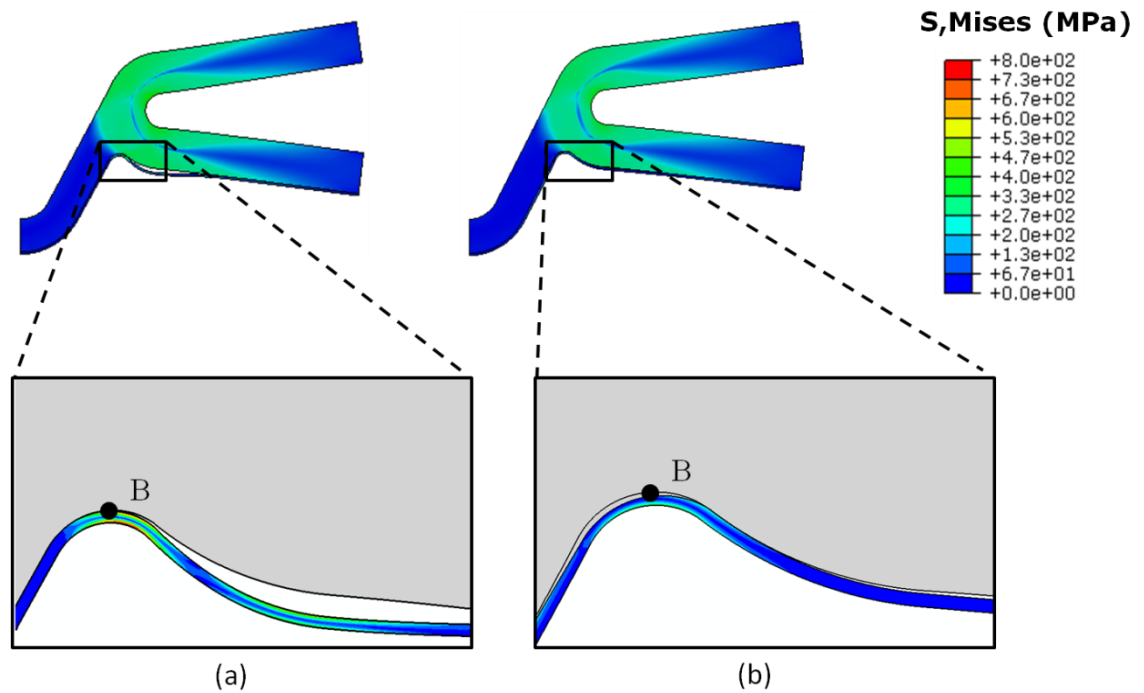
Figure 4-14: Coating stress distribution plotted on the deformed geometry at a stent circumferential strain of 0.6: (a) NP1 model; (b) VB model. Inserts illustrate that significant over-closure is computed by the VB model resulting in decreased coating stress and decreased buckling of the coating.
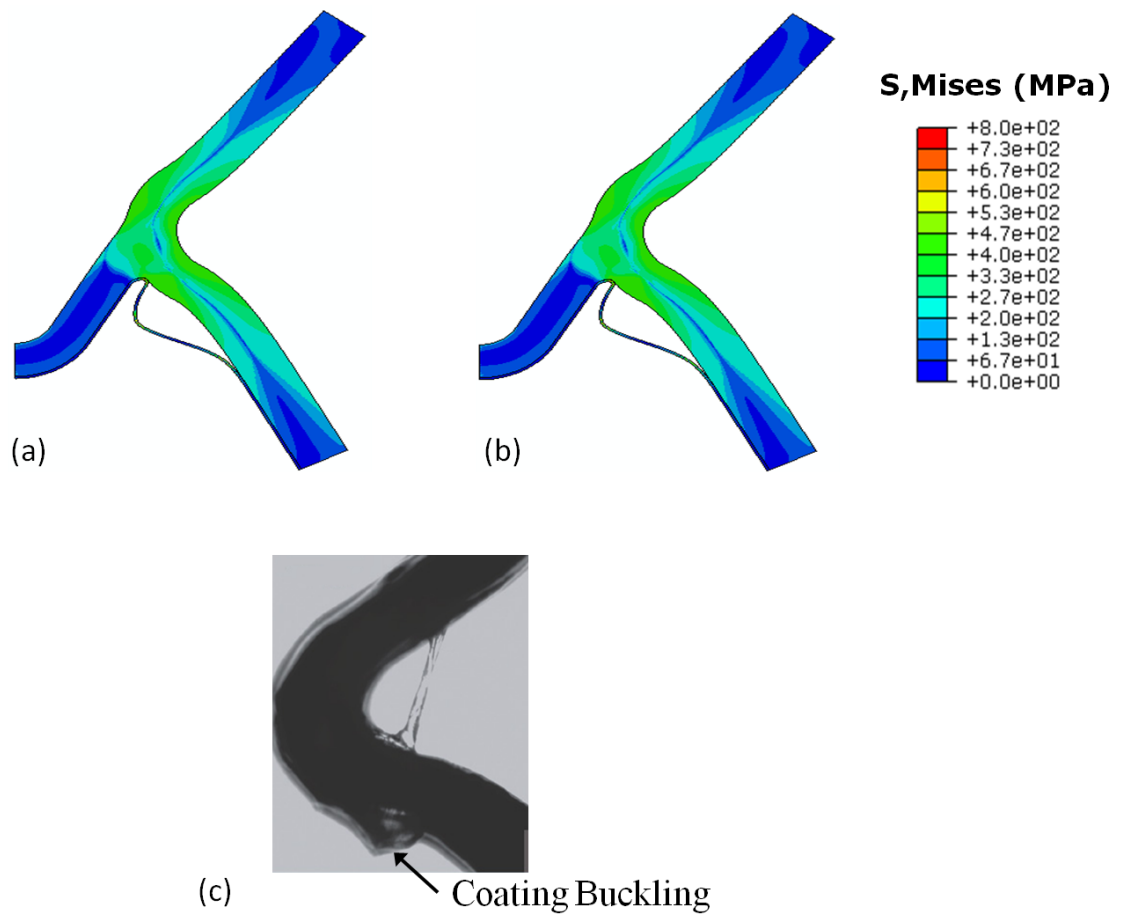
Figure 4-15: Stent stress distribution plotted on the deformed geometry at a stent circumferential strain of 7 for (a) NP1; (b) SMC (NP2 for $\Delta_n < 0$). Significant buckling of the coating from the stent geometry is computed for both models similar to that observed experimentally (Basalus and von Birgelen, 2010).

5 Cardiovascular Stenting Literature Review

5.1 Introduction

Significant progress has been made in the field of interventional cardiology in the past few decades with the development of devices for atherectomy, transluminal angioplasty and stents. However, restenosis, defined as a reduction in vessel patency by 50% or more following surgery, occurs following 30-50% of bare metal stenting procedures within the first six months of stent implantation (Moses et al., 2003; Weintraub, 2007; Newsome et al., 2008). This wound-healing response is characterised by a proliferation of smooth muscle cells into the lumen of an artery following the stenting procedure. Restenosis consists of an inflammatory phase, a granulation phase and a remodelling phase. In the inflammatory phase, platelets and growth factors are activated. Neointimal formation is triggered by arterial injury caused by the stenting procedure which leads to a loss of contractility in the tunica media (Zargham, 2008). This loss of smooth muscle cell contractility facilitates the migration of smooth muscle cells into the lumen. This is defined as the granulation phase. The remodelling phase is characterised by proteoglycan and collagen synthesis. Ultimately, this narrows the previously enlarged lumen. The degree of restenosis depends on a number of patient-specific and lesion-specific factors such as, but not limited to, genetics, general patient health, lesion length and plaque burden (Regar et al., 2001). Procedure-specific factors such as stenting technique and stent design characteristics also have a significant influence on clinical outcome.

Prior to 1990 numerous researchers had experimented with the concept of implementing steel coils and meshes for maintaining vessel patency (Judkins, 1964; Rousseau et al., 1987; Dotter et al., 1983). The concept of balloon mounted stents for use in peripheral arteries was introduced by Palmaz et al. (1985). The first coronary stents were deployed in humans following percutaneous transluminal coronary angioplasty (PTCA) in France by Sigwart et al. (1987). Bare metal stents were approved for use in the United States in 1993 as an

alternative option following failed PTCA (Roubin et al., 1992; Ruygrok and Serruys, 1996). Elective coronary stent implantation was reported to significantly reduce restenosis when compared to PTCA treatment rates in two clinical trials (Serruys et al., 1994; Fischman et al., 1994) which led to the subsequent approval of bare metal stents for elective use by the Food and Drug Administration (FDA, 2012). Despite, these advancements, severe stent thrombosis was still reported following bare metal stent implantation in numerous trials (Ruygrok and Serruys, 1996; Coolong and Mauri, 2006; Serruys et al., 1991). Various anticoagulation treatments were administered to alleviate thrombosis rates including warfarin, heparin, aspirin and dextran (Fischman et al., 1994). Overall rates of stent thrombosis and death were higher following bare metal stent procedures than PTCA alone (Serruys et al., 1994; Fischman et al., 1994). The replacement of anticoagulation treatment with dual antiplatelet therapy (aspirin and Clopidogrel) and the use of high balloon pressures to improve stent apposition led to a significant reduction in bare metal stent thrombosis rates. However, mortality rates as high as 9.5% due to bare metal stent thrombosis have been recently been reported (Chen et al., 2006).

5.2 Surface Treatments

It is understood that bare metal surface properties can trigger the adherence of inflammatory cells which eventually leads to intimal hyperplasia and restenosis (Tepe et al., 2006). A number of manufacturing methods have been developed in order to enhance stent surface quality including electropolishing, sandblasting, photochemical etching, waterjet cutting and radioactivity in an effort to inhibit restenosis (DeScheerder et al., 1997; Thierry et al., 2000; Albiero et al., 2000; Tepe et al., 2006). In the study of DeScheerder et al. (1997), electrochemical polishing was used to enhance the surface characteristics of stainless steel stents. A rat model was implemented and thrombogenicity rates were assessed using Cr-labelled and fibrinogen platelets. Significantly lower thrombogenicity was reported for the polished stents when compared to controls. Decreased neointimal hyperplasia was also reported in a porcine model. The majority of coronary stents are fabricated by laser cutting from tubing (Stoeckel et al., 2002; Mariano and

Sangiorgi, 2009). However, the laser cutting process produces a heat-affected zone at the cutting edge which must be subsequently removed. In contrast, waterjet cutting does not produce a heat-affected zone. Instead, a focused jet of water containing abrasive additives is used to cut the material. Photochemical etching has also been used to produce commercially available stents by machining away specific locations through a corrosion process (Stoeckel et al., 2002). Sterilisation techniques including ethylene oxide, acid and steam treatments have also been used in an effort to enhance the surface finish of nitinol stents (Thierry et al., 2000). Radioactive stents work by continuously delivering ionizing radiation at very low uniform dosages according to the half-life of the specific radioisotopes being implemented. They have been shown to inhibit smooth muscle cell proliferation and neo-intima formation (Fischell and Hehrlein, 1998; Carter Do and Fischell 1998; Rubin et al., 1998). However, clinical trials have shown restenosis occurring at the edge of these stents (Albiero et al., 2000). Surface processing has also been performed on stents to create porous surfaces to accommodate anti-proliferative drugs (Tsujino et al., 2007). This can be done through laser cutting (Serruys et al., 2005), stent sculpturing (Tsujino et al., 2007) and surface modification by sandblasting and (Wessely et al., 2005).

5.3   Stent Manufacturing and Design

A large number of stents are produced by laser-cutting from a tube configuration. Balloon expandable stents are typically cut in the crimped position. Wires can be formed into stents by using a range of techniques including braiding, coiling and knitting (Stoeckel et al., 2002). Closed-cell designs are fabricated by welding at specific points along the stent. Stoeckel et al. (2002) described a closed cell design as one where all internal inflection points are connected by bridging elements. In contrast, in an open cell design not all inflection points are joined by connecting elements. A range of stent designs including helical spiral (Meng et al., 2006) and woven designs (Maetani et al., 2007) are commercially available.

A number of key design properties are required to ensure stent functionality including good radiopacity, low profile, high radial strength, flexibility, strength,

biocompatibility and corrosion resistance (Gunn and Cumberland, 1999; Regar et al., 2001; Stoeckel et al., 2002). One of the key requirements of good stent design is trackability or the ease with which the device can be guided to the target vessel site. The implementation of thinner struts leads to more flexible device with reduced cross-sectional area or low profile. Stent struts impose deep vascular trauma when compared to the more uniform deformation of the arterial wall caused by balloon angioplasty. It was reported in a clinical trial investigation that thinner struts lead to reduced restenosis rates (Kastrati et al., 2001). This finding was also suggested by Briguori et al. (2002). However, some studies have reported no significant differences in restenosis rates for thin or thick strut designs at follow up (Moreno et al., 2004). There are limits to the design criteria however. The use of thinner struts requires the need for high strength materials. However, high elastic recoil is associated with high strength materials as it is more difficult to produce plastic deformation at acceptable balloon expansion pressures (O'Brien and Carroll, 2009). The choice of strut thickness has also been shown to affect the wall shear stress distribution inside a stented coronary artery in a recent computational study (Balossino et al., 2008). The influence of stent coating thickness on delamination was demonstrated in a recent computational study where thicker stiff coatings were shown to debond at lower levels of stent deployment (Hopkins et al., 2010). An analytical study has demonstrated that strut length is an important design parameter in controlling the ratio between peak normal and shear tractions along a stent-coating interface (Parry and McGarry, 2012).

5.4 Stent Materials

Low material yield stress and high elastic moduli are required so that stents are plastically deformed at manageable balloon pressures and produce minimum recoil respectively (Stoeckel et al., 2002). Recoil has been identified as one of the contributory factors of the restenosis response (Lafont et al., 1995). Significantly greater thrombosis rates have been associated with copper stents when compared to steel stents (Wilczek et al., 1996a), leading to the adoption of steel for stenting application. Stainless steel (316L alloy) is the most common material used for

stents due to its low carbon content and good corrosion resistance due to a chromium oxide layer (Hara et al., 2006). It is easily deformable in its fully annealed condition and therefore ideal for balloon expansion (Stoeckel et al., 2002). Due to its high iron content (60-65 wt % pure Fe) and low density, it is a poorly visible fluoroscopic material and is not MRI compatible. The release of nickel, molybdenum and chromate ions from stainless steel has been reported to induce intimal hyperplasia (Koster et al., 2000).

Cobalt chromium (Co-Cr) has also been implemented for stenting applications. It exhibits excellent radial strength due to its high elastic modulus (Stoeckel et al., 2002). The strength of the material is attractive from a design perspective as it is desirable to use thinner stent struts for low profile designs. Co-Cr is also radiopaque and MRI-compatible (Kereiakes et al., 2003; Klocke et al., 2005). A Cobalt-Chromium-Molybdenum alloy, MP35N, has been developed exhibiting increased strength, density and radiopacity in comparison to stainless steel (Sketch et al., 2005). This has allowed for very thin strut design (0.0036 inches).

Nickel-Titanium, also known as Nitinol, is commonly chosen for both coronary and peripheral stenting procedures. It constitutes 49-58% nickel and the remaining portion is titanium (Sumita and Teoh, 2004). Its corrosion resistance and biocompatibility is attributed to a homogenous oxide layer mainly composed of TiO_2 (Thierry et al., 2000). It is the most widely used material for self-expanding stents and can recover elastic deformations of about 10%. This large elastic range of deformation, known as superelasticity is the result of thermo-elastic martensitic transformation (Stoeckel et al., 2002). It exhibits shape memory properties as well as good biocompatibility and radial force. However, the release of nickel ions and their associated toxicity affects have been reported in cardiovascular and orthopaedic applications (Heintz et al., 2001; Berger-Gorbet et al., 1996). Titanium oxide surface treatments have been carried out to inhibit these toxicity affects (Maitz and Shevchenko, 2006). Nitinol visualisation is possible under MRI but most stent deployment is conducted under fluoroscopy. Platinum-iridium (Pt-Ir) alloy is also used for stent applications. This alloy exhibits excellent radiopacity and it is possible to capture 3-D images of the lumen of the stent using

MRI (Trost et al., 2004). Although this material exhibits good corrosion resistance, it has very poor mechanical properties (Park and Kim, 1995) which make it unsuitable for most stenting applications.

Tantalum exhibits good radiopacity due to high density as well as excellent corrosion resistance due to a highly stable surface oxide layer. It is MRI compatible due to its non-ferromagnetic properties. However, it demonstrates inferior radial force and poor yield stress in comparison to other stent materials and is therefore susceptible to fracture (Zitter and Plenk Jr, 1987; Lau et al., 2004). This necessitates the use of lower balloon pressures which can lead to recoil. Tantalum stents are commercially available in Canada, Europe and Japan although they are not approved for use in the United States (Ozaki et al., 1995). Polyethylene terephthalate (PET) has also been proposed as a stent material due to its high radial strength and suitable material properties. In the study of Murphy et al. (1992), PET was implanted in the coronary arteries of a porcine model. However, follow up showed a chronic inflammatory response with intense neointimal hyperplasia that resulted in complete vessel occlusion. Another concern with PET stents is poor radiopacity (Wilczek et al., 1996b). Biodegradable stents have received much attention in recent years. These stents allow for vessel accessibility for further intervention, if required, providing an attractive alternative to permanent stent implantation. Additionally, it is believed that permanent stent implantation could promote long-term complications such as inflammatory reactions and thrombus formation. The first biodegradable stent made from poly-l-lactic acid (PLLA) was implanted in a canine model by Stack et al. (1988). The first generation of biodegradable stents were produced using poly-L-lactate (Tanguay et al., 1994; Colombo and Karvouni, 2000). As well as having sufficient radial strength, animal models suggested that these stents produce less neointimal thickening and less inflammatory responses. In the study of Tamai et al. (2000), a high molecular weight PLLA stent was deployed in 15 human patients with no major cardiac events observed. In the study of Heublein et al. (2003), a magnesium AE21 alloy biodegradable stent was deployed in porcine models. It was reported that struts endothelialised readily, stent corrosion occurred

within the endothelium and neointimal growth significantly abated as strut thickness reduced. A clinical study was conducted by Waksman et al. (2009) to assess the performance of a WE43 alloy magnesium bioabsorbable stent. The stents were deployed in 63 patients with coronary artery disease. The median lumen diameter was increased by 0.3mm at 4 month follow up along with complete stent degradation.

Iron has also been used for biodegradable stent applications. In the study of Peuster et al. (2001), pure iron stents were deployed in rabbit aortas with no major adverse events occurring during 6-8 month follow up. However, major sections of the struts still remained at 18 months due to very slow corrosion rates. In the study of Peuster et al. (2006), corrodible iron stents were implanted into the descending aortas of 29 pigs. One year follow up showed no significant difference in the degree of neointimal proliferation between 316L stainless steel stents and iron stents. There were no signs of local or systemic toxicity but large portions of the stent were still visible after one year. Although, initial investigations are promising, complete control of degradation rates still needs to be demonstrated for these biodegradable stents and is a crucial design requirement in order to control the arterial remodelling response. Furthermore, the degradation rate must not be too quick as this could lead to fragment embolisation (Peuster et al., 2006).

5.5 Stent Coatings and Drug-Eluting Stents

The biocompatibility of metallic stents surfaces in the body remains a serious issue in interventional cardiology since the specific mechanisms underlying the restenosis response are poorly understood. In recent years, stents have been coated with inert metallic or polymeric coatings which serve as biocompatible barriers or delivery vehicles for drug elution into the surrounding arterial tissue in an attempt to alleviate this inflammatory response. It has been demonstrated that coating the stent with a biocompatible material can reduce surface energy, improve surface smoothness and improve the stability of the surface oxide layer (Mani et al., 2007). While coatings were initially employed to improve surface biocompatibility, they are now also utilised as a means of delivering a controlled

dose of anti-proliferative drugs to alleviate restenosis. This approach to local drug-delivery has allowed for drug administration following stent deployment, when vessel wall damage is greatest. Localised drug delivery also minimises toxic affects. A number of methods have been adopted to apply coatings including; plasma-based depositions (Huang et al., 2006), galvanistation (Hehrlein et al., 1995), arc ion plating (Liu et al., 2006), dipping (Nakayama et al., 2001) and spraying (Huang et al., 2002).

5.5.1 Immunosuppressive Drugs

Immunosuppressive drugs such as heparin, sirolimus (also known as rapamycin) and paclitaxel have commonly been used to inhibit restenosis. Heparin has been widely used to reduce thrombosis and neointimal proliferation while sirolimus and paclitaxel are predominantly used to inhibit neointimal hyperplasia. Numerous methods are used to bind heparin to the stent surface such as physical adsorption, copolymerisation, polymer encapsulation and ionic bonding. In order to improve stability, heparin is copolymerised with a range of polymers including poly(vinyl alcohol), polyurethane, poly(methyl-methacrylate), PLGA, PLLGA and PLLA (Labarre et al., 1977; Goosen and Sefton, 1983; Mazid et al., 1991). The copolymerisation techniques must be carefully performed as it can alter the chemical properties of heparin which are essential for its therapeutic functionality. A number of methods have been used to control heparin delivery. PLGA microspheres have been implemented to promote uniform drug delivery. In order to control drug delivery from biodegradable polymers, polyethylene glycol, known as a plasticizer is added to the copolymer coating. Copolymer ratio has also been shown to be significant in controlling the delivery release profile (Mani et al., 2007). Heparin was first coated on a stent for use in canine coronary arteries by Bonan et al. (1991). The absence of in-stent thrombosis and neointimal proliferation has been demonstrated in numerous clinical and animal studies (ShethVishva, 1995; Serruys et al., 1998; Stone et al., 1998; Dzavik et al., 2001; Matsumoto et al., 2002). However, some studies have shown no significant difference between restenosis rates and stent thrombosis between bare metal stents and heparin-coated stents (Haude et al., 2003). Sirolimus works by binding to

intracellular receptor proteins and inducing cell cycle arrest and smooth muscle cell proliferation (Marx et al., 1995). Polyethylene-co-vinyl acetate (PEVA) and poly-n-butyl methacrylate (PMBA) can be applied in a separate coating on top of the sirolimus layer to control drug elution rate (Virmani et al., 2004). Multiple collagen and sirolimus layers were alternately coated on a stainless steel stent in the work of Chen et al. (2005). Collagen was utilised to control the sirolimus elution rate and to ensure that there was no burst effect. The capabilities of sirolimus in reducing smooth muscle cell proliferation and migration has been reported in numerous studies (Schofer et al., 2003; Morice et al., 2004; Schampaert et al., 2004). Paclitaxel binds with proteins in cell microtubules to promote cell death (Liistro and Bolognese, 2003). This drug can be applied to stent surfaces through polymer-based or non polymer-based coatings. Paclitaxel was dip coated onto a stent using ethanolic solution and evaporation by Heldman et al. (2001). The disadvantage with the dip coating process is that a significant amount of drug can be lost during stent deployment. However, using this technique means that there are no possible thrombosis complications induced by polymer-based drug delivery vehicles. Numerous clinical studies have shown that paclitaxel can significantly reduce restenosis rates when compared to bare metal stent designs (Katuza et al., 2004; Gershlick et al., 2004; Lansky et al., 2004). A low profile, thin strut design is usually preferred for successful stent delivery. However, the use of a thin strut design together with the dip coating technique, limits the quantity of drug can be deposited on the stent surface. In contrast, the use of copolymers to deliver the paclitaxel drug enables higher drug dosage. A poly(styrene-b-isobutylene-b-styrene) triblock copolymer was used as a delivery vehicle for paclitaxel in a commercially available stent design (Ranade et al., 2004). However, miscibility was problematic in this delivery approach and the paclitaxel was not properly dissolved in the copolymer matrix which led to a burst effect during drug release (Ranade et al., 2004).

5.5.2 Polymer-Based Coatings

A number of polymer coatings have been applied to the stent surface to inhibit restenosis. Phosphorylcholine-based coatings have been implemented due to their similarity in composition to the phospholipids present on the outer surface of red blood cells (Cumberland et al., 1998). However, it was reported that significant reductions in restenosis were not evident following the application of this material (Babapulle and Eisenberg, 2002). Despite these concerns, phosphorylcholine has been shown to be safe (Garcia-Touchard et al., 2006), stable (Lewis et al., 2002) and capable of drug delivery (Lewis et al., 2001). Some polymer coatings such as polyaprolactone and ethylvinylacetate have been associated with inflammation. More inert polymers such as polytetraflouroethane and polyurethane have also been coated on stent material. The research of Tepe et al. (2006) reported a reduction in thrombogenic markers following the use of a polyurethane coating when compared to heparin coatings in an in-vitro blood flow model.

Much research has been undertaken with respect to coating durability and controlling drug elution profile. Such coatings are often composite structures with each layer providing a specific function (Virmani et al., 2004; Sheiban et al., 2008). For example, some commercially available stents have three separate coating layers. A commercially available composite coating was discussed by Virmani et al. (2004). A parylene tie-layer was first applied to the stent surface. A mixture of polyethylene-co-vinyl acetate (PEVA) and poly-n-butyl methacrylate (PMBA), containing the Sirolimus drug was included in the middle layer. Finally, a top coat consisting of PEVA or PMBA specifically designed to control drug elution rate was applied. Other commercially available devices consist of a single polymer/paclitaxel mixture layer (Ellis et al., 2007). While short term safety of these devices has been reported, the long term effects of using these devices are still unclear. The fact that non-degradable polymer material still remains following full drug elution is still a matter of some concern and it is not certain what influence that this material could have on late stent thrombosis. Therefore, a number of biodegradable polymer drug carriers including polylactic acid (PLA), polyglycolic acid (PGA) and polylactic-co-glycolic acid (PLGA) have been

implemented. Biodegradation of these polymers is dependent on an arbitrary hydrolysis of their ester bonds. These materials usually contain polymer processing substances such as catalysts, solvents and initiators which also must be biocompatible. A number of commercially available devices currently use this technology; biolimus A9 is eluted with PLA degradation in a stainless steel stent while rapamycin is released from PLGA material in a nitinol stent system (Grube and Buellesfeld, 2006; Abizaid et al., 2007).

5.5.3 Metal-Based/Inorganic Coatings

It has been shown in many studies that polymer-based drug-eluting stents significantly reduce restenosis. However, some studies have suggested that the indefinite presence of non-biodegradable polymer matrix following drug elution could initiate inflammation and late stent thrombosis (McFadden et al., 2004; Virmani et al., 2004; Bhargava et al., 2006). Therefore it has been hypothesised that the replacement of non-biodegradable polymer coating matrix with a non-inflammatory vehicle (such as biocompatible metal) which could be used for drug delivery could produce superior long term results (Bhargava et al., 2006). The ability of pyrolytic carbon and diamond-like carbon (DLC) coatings to reduce restenosis rates has been investigated in numerous studies (Antoniucci et al., 2001; Tomai et al., 2003). A significant reduction in platelet activation levels was reported in an in vitro study following application of a DLC coating when compared to an uncoated stent design (Gutensohn et al., 2000). However, improvement in long term vessel patency was not supported by subsequent studies (Airoldi et al., 2004; Meireles et al., 2007). The ability of these coatings to reduce metal ion release when compared to bare metal stents has meant that DLC coated stents were still recently available on the market (O'Brien and Carroll, 2009). A study conducted by Antoniucci et al. (2001) involved the implantation of pyrolytic carbon-coated stents in 112 high risk patients (>75 years old). A restenosis rate of 25% was reported, which compares similarly to restenosis rates reported for bare-metal stents. These studies suggest that carbon coated coatings do not provide significant improvements in restenosis rates.

Coating stents with gold coatings was another option explored to address the issue of stent restenosis due to its attractive properties including high radiopacity and chemical inertness. However, a number of studies have reported higher restenosis rates for gold-coated stents when compared to their bare metal counterparts (Kastrati et al., 2000; Reifart et al., 2004). Silicon carbide has also been proposed as an alternative coating material. It was hypothesised that restenosis could be controlled by utilising the electronic properties of semiconducting, phosphorous-doped silicon carbide to promote a passive blood response (Rzany and Schaldach, 2001). However, numerous studies and randomised trials showed no significant reduction in restenosis rates using silicon carbide surfaces when compared to bare-metal stents (Heublein et al., 1998; Tanajura et al., 2003; Unverdorben et al., 2003).

Titanium renders the stent surface biologically inert, reducing fibrinogen and platelet binding. A randomised trial conducted by Windecker et al. (2005) reported an 18% reduction in restenosis rates for titanium-nitride-oxide coated stents when compared to stainless steel bare metal stents of identical design. In a subsequent clinical study of high risk patients, no stent thrombosis was observed following 270 day follow-up (Karjalainen et al., 2006). Following corrosion of some metals (zinc, nickel, copper, silver, cobalt, chromium), hydrogen peroxide, a strong oxidising agent, is produced on the metal surface (Zhao et al., 1998). Hydrogen peroxide can cause inflammatory reactions in the artery. However, iridium oxide is known to convert hydrogen peroxide into water and oxygen and it was therefore hypothesised that coating stents with iridium oxide could promote endothelialisation and inhibit the inflammatory response. In a clinical trial conducted by Di Mario et al. (2004), it was reported that iridium oxide promoted fast endothelialisation due to its ability to prevent the formation of free oxygen radicals which can affect the activity of endothelial cells. The overall angiographic restenosis rate was reported to be 13.8%. Another study deployed iridium-coated stents in a porcine model (Seliger et al., 2000). A significant reduction in neointimal thickness from 188μm for bare stainless steel stents to 55μm for iridium-coated stents was reported.

Porous metallic coatings have been used as delivery vehicles for immunosuppressive drugs. Nanoporous aluminium oxide has been implemented as a delivery vehicle for drug elution. The application procedure involves the vapour deposition of aluminium onto the stent material followed by anodising the coated stent to create porous aluminium oxide. However, clinical studies involving an aluminium–oxide coated, tacrolimus-eluting stent have reported poor performance (Grube, 2003). Porous carbon-carbon paclitaxel-eluting coatings have also been implemented (Bhargava et al., 2006), showing acceptable performance characteristics in terms of endothelialisation, neointimal hyperplasia, inflammatory response and fibrin deposition. Porosity is controlled by the carbon particle size and degree of pyrolysis (O'Brien and Carroll, 2009). Studies have shown that porous titanium-nitride-oxide (TiNOX) coated on stainless steel stents significantly reduces neointimal hyperplasia (Windecker et al., 2001). In a study involving 1,607 patients, the performance of TiNOX coated stents to paclitaxel and sirolimus (rapamycin)-eluting stents (PES,SES) was compared. Similar clinical outcomes were observed for all groups three years post-operatively in terms of target vessel revascularisation and myocardial infarction (Limacher et al., 2011). However, long term dual antiplatelet therapy is required for patients who receive drug-eluting stents. This type of long term therapy is unsuitable for some patients, suggesting that the TiNOX coated stents could provide a possible alternative for these patients. Porous ceramic coatings such as hydroxyapatite have also been investigated for drug-eluting capability. Electrochemical deposition can be used to produce an outer hydroxyapatite porous layer for drug delivery and some studies have reported promising results (Rajtar et al., 2006; Costa et al., 2008). In the study of Costa et al. (2008), 15 patients with lesions in coronary arteries received hydroxyapatite sirolimus-eluting coated stents. No in-hospital complications were reported and no major cardiac events were observed at 6 month follow-up. Other stent designs involve the storage and elution of drugs from laser cut reservoirs where drug elution is controlled by degradation kinetics of a biodegradable polymer on top of the therapeutic drug (Krucoff et al., 2008).

Another interesting approach has been the direct application of drugs to microtextured stainless steel surfaces. A clinical study has shown that a roughened stent surface is safe for use and can actually lower restenosis rates when compared to smooth stent surfaces (Dibra et al., 2005). The surface can be roughened through a grit-blasting process and recent in vitro and animal studies have shown that the textured stent surface can holds on to and elute drugs over time (Wessely et al., 2005). However, many questions still remain regarding the use of roughened stent surfaces such as possible balloon damage during deployment, long term thrombogenicity affects and accurate control of the degree of surface roughness.

5.5.4   Endothelial Cell Coating

It is known that endothelial cell damage triggers the inflammatory response which promotes restenosis (Kipshidze et al., 2004). It was hypothesised that endothelial cells seeded onto a stent surface before implantation would differentiate and proliferate and subsequently alleviate thrombosis. A stainless steel, self-expandable stent was seeded with human umbilical vein derived endothelial cells in vitro in a study conducted by Van der Giessen et al. (1988). Stent implantations in porcine femoral arteries exhibited complete covering of the stent by endothelium after 1 week. Numerous other attempts have been made to successfully seed endothelial cells onto stent surfaces following implantation but it has proved challenging due to difficulties in maintaining cell adhesion during blood flow and cell damage upon implantation (Consigny, 2000; Kipshidze et al., 2004).

5.6   Coating Delamination and Associated Clinical Implications

A number of studies have highlighted that late stent thrombosis can occur following the use of drug-eluting stents (Wang et al., 2002; Iakovou et al., 2005; Luscher et al., 2007; Daemen et al., 2007). The specific reasons for this are still undetermined. Possible explanations include late endothelialisation (McFadden et al., 2004), inflammatory affects of polymer coatings, discontinuation of dual antiplatelet therapy or a combination of these factors. Neointimal growth in bare metal stents has been reported to reach a peak at approximately 6 months, whereas

neointimal proliferation can continue up to 4 years in drug-eluting stents (Ong et al., 2005; Ong and Serruys, 2005). Several studies have suggested that coating damage plays a significant role in the development of clinical complications such as thrombosis, micro-embolism formation and impaired drug delivery (Hoffmann et al., 2002; Otsuka et al., 2007; Levy et al., 2009; Balakrishnan et al., 2005).

Several recent experimental examinations of drug-eluting stents using scanning electron microscopy have reported delamination of polymer coatings from the stent surface during deployment. The study of Regar et al. (2001) reported significant coating delamination in the hinge region of a commercially available stent (Figure 5-1). The coating morphology of three commercially available polymer-coated stents following balloon expansion and withdrawal were investigated by Otsuka et al. (2007). Polymer delamination following stent expansion was reported for all stent designs. An example of such delamination is shown in Figure 5-2. Numerous studies have reported webbing defects of polymer coatings which can lead to extensive coating delamination (Basalus and von Birgelen, 2010; Wiemer et al., 2010). A study by Levy et al. (2009) reported extensive coating defects including flaking, peeling and cracking in an in vitro coating durability test following 30 day stent incubation in accelerated conditions (Figure 5-3). Drug releases rates, measured by high performance liquid chromatography, were significantly affected following coating damage. A study by Wiemer et al. (2010) investigated the morphology of polymer-coated stents following failed implantation in calcified and tortuous lesions. Scanning electron microscopy was used to assess coating damage for both crimped and expanded stents. Evidence of polymer peeling exposing the underlying stent surface was reported (Figure 5-4). Regions of polymer bridging across stent struts were found for a stent in a crimped morphology. It was reported that these regions were likely to induce polymer damage following stent expansion. Areas of coating spalling and erosion were found in another stent in an expanded state. Localised regions of incomplete re-endothelialisation in drug-eluting stents have been identified in autopsy and optical coherence tomography examinations (Joner et al., 2006). A possible explanation for this clinical outcome is the delamination of the polymer

coating from localised regions of the stent, leading to non-uniform drug delivery to the vessel wall. Webbing, wrinkling, peeling and fragmentation of stent coatings has recently been reported by Basalus and von Birgelen (2010) in a series of rigorous bench-side testing experiments conducted on commercially available drug-eluting stents. Coating irregularities were apparent for thin and thick coating geometries. In vivo evidence of coating damage and associated clinical complications has been reported in numerous animal and human trials. Virmani et al. (2004) reported fragments of polymer surrounded by giant cells and eosinophils within an artery section where late stent thrombosis was the cause of death. It was reported in the study of Kollum et al. (2005) that debris from a nanoporous aluminium oxide coating was surrounded by arterial inflammation post stent placement in a porcine restenosis model. Histomorphometric analysis revealed particle debris in the media and neointima promoting vascular inflammation. In the study of Sydow-Plum and Tabrizian (2008) thrombotic vascular occlusion was attributed to the adhesion of blood constituents governed by the coating surface characteristics including the surface chemical composition, surface morphology, presence of charge, surface wettability and surface roughness.

Accurate drug delivery is essential for controlling neointimal hyperplasia. This was demonstrated in the work of Heldman et al. (2001) where three different dosages of paclitaxel were coated onto a stent before implantation in a porcine model. The degree of intimal hyperplasia was highly sensitive to drug dosage with the highest dosage significantly reducing hyperplasia. In the research of Gershlick et al. (2004), it was reported that a paclitaxel drug dosage density of $2.7\mu g/mm^2$ significantly reduced in-stent restenosis but slightly lower dosage densities of 0.7 and 1.4 $\mu g/mm^2$ exhibited minimal therapeutic effects. Therefore, it is reasonable to suggest that delamination, cracking and fragmentation of the coating have the potential to contribute to thrombus formation. A clinical review of the performance of coated stents was conducted by Hara et al. (2006). It was stressed that toxic levels of drug delivery may occur in an arterial wall if the coated stent is deployed incorrectly. Furthermore, it is pointed out that incorrect coating delivery

could lead to unintended drug delivery into the bloodstream. This further signifies the importance of eliminating coating delamination between the stent and the coating during deployment. A clinical study by Brodie et al. (2008) revealed that polymer coated drug-eluting stents are used in an off-label manner in 59% of cases with higher rates of myocardial infarction and stent thrombosis for the these devices. Stent thrombosis was reported to occur at 9 months for off-label use compared with 2 years for on-label implantation. Off-label use included stenting of bifurcations and chronic total occlusions. It is reasonable to suggest that the occurrence of extensive delamination or webbing, of a polymer coating at a bifurcation could result in a significant disruption of the flow through the stent struts to the unstented branch of the bifurcation. Additionally, the use of polymer coated stents at sites of chronic total occlusion could lead to significant abrasion during the positioning of the stent, increasing the risk of delamination during stent deployment (Wiemer et al., 2010). It was suggested by Basalus and von Birgelen (2010) that drug-eluting stents should be subjected to extreme loading conditions in benchtop testing in order to identify the performance limits of coated stent designs.

5.7   Computational Modelling

A plethora of computational models have been developed to predict stent behaviour with the aim of improving stent design. A brief outline of some of these studies is presented in this section. In the work of Brauer et al. (1999), a test rig was constructed to assess the dilation characteristics and properties of stents of various materials. Numerical simulations of the dilation process were also performed. Agreement between experimental dilation and computational predictions was observed. Interestingly, titanium was found to exhibit superior dilation behaviour when compared to stainless steel stents. A computational investigation into the mechanical behaviour of the Palmaz stent was carried out by Dumoulin and Cochelin (2000). Specifically, the degree of recoil, foreshortening and integrity of the structure following deployment was analysed. The ability of the stent to withstand fatigue loading was also investigated. A perfectly plastic material constitutive theory (Salencon, 1983) was utilised to investigate the

resistance of the structure to collapse under external pressure. Numerical simulations were employed by Etave et al. (2001) to model two commonly implemented stent designs in interventional cardiology- tubular and coil stents. Mathematical modelling was used to determine a number of stent characteristics such as deployment pressure, elastic recoil, radial force, foreshortening, stent coverage, flexibility and stress distribution. The degree of recoil was computed to be significantly higher in tubular stent designs when compared to coiled stents. Localised regions of stress were computed at link points. The influence of geometrical parameters on stent performance was carried out in the computational analysis of Migliavacca et al. (2002). The response of commercially available stent designs to internal pressure was also assessed. Computations revealed that a stent with a low metal to artery surface ratio produced greater recoil but a lower dogboning effect. A 2D crystal plasticity model was used by Savage et al. (2004) to investigate the tensile ductility of individual stent struts. A computational micromechanics approach was taken to represent the grain structure in the struts together with crystal plasticity theory to describe the constitutive behaviour of individual grains. Computations revealed a significant reduction in ductility with a decrease in strut thickness. This pattern was observed experimentally by Murphy et al. (2003).

Computational micromechanics modelling was carried out by McGarry et al. (2004) in order to analyse the mechanical behaviour of a balloon expandable stainless steel stent. Specifically, microscale mechanical phenomena were investigated. Two different descriptions of plastic deformation in the stent material were applied; crystal plasticity theory and classical von Mises plasticity theory (J_2 flow theory). Simulations were carried out using both constitutive theories to determine critical post-deployment behaviours including foreshortening and recoil. Computations using the crystal plasticity model revealed a closer agreement to published performance data. Crystal plasticity theory predicted non-uniform and localised stresses in the stent microstructure as seen experimentally (van Beusekom et al., 1998; Brauer et al., 1999). In contrast, smoothly varying strain fields were predicted by the J_2 flow theory model. In the study of Murphy et al. (2006), a combination of experimental tests and micro-

scale crystal plasticity finite element models was used to investigate the influence of grain structure on ductility in stainless steel stent struts. It was concluded that the ductility of the micro-scale steel struts could be improved by reducing the size of the individual grains. At the microscopic scale, tensile failure strain in stent struts is size dependent. In the study of Harewood and McHugh (2007), polycrystalline computational models incorporating material fracture were used to investigate size effects for stent strut geometries typical of commercially available stent designs. The computational models yielded an excellent quantitative agreement with experimentally observed size effects in tension. Furthermore, additional size effects were revealed when stent struts were subjected to different loading conditions. The findings of this study provide useful insight on the possible origins of strut failure. Useful insights involving the failure risks for a range of stent implantation scenarios were presented in the study of Harewood et al. (2010), where a multiscale modelling approach was used to determine the likelihood of stent fracture. Fully 3D simulations of a stent microstructure were performed by McGarry et al. (2007) where the role of microstructural inhomogeneity on initiation of necking was investigated. Xia et al. (2007) performed a computational assessment of V and S shaped NIR stent link designs. The unit cell method was used to evaluate the stress distributions in these designs. Computations revealed that less pressure was required to expand both NIR stent designs than the Palmaz stent. However, a significant degree of foreshortening was computed for the NIR stents.

Several different strategies to model stent expansion have been reported in the literature. In the work of De Beule et al. (2008), different methodologies were used to model the expansion of a balloon-expandable stent. The free expansion of a stent is governed by the unfolding and expansion of a balloon. In this study, a trifolded balloon methodology was shown to provide very good qualitative and quantitative agreement with both experiments and stent manufacturer data. In the work of Gervaso et al. (2008), three different stent expansion techniques were simulated for a commercially available stent geometry and showed significant differences in overall stent profile and stress distribution depending on expansion technique employed. The changes in stress profile on an arterial wall based on the

expansion technique were also quantified. A widely used constitutive model was used to model the artery (Holzapfel et al., 2005). This paper highlighted the importance of expansion technique and controlled balloon expansion in influencing arterial wall damage. A computational framework in which the commercially available Cypher© Stent was combined with a realistic trifolded balloon geometry was presented by Mortier et al. (2008). The influence of balloon length, balloon folding pattern and the relative position of the stent with respect to the balloon catheter on free stent expansion were investigated. It was demonstrated that small positioning inaccuracies influenced the expansion behaviour of the stent. Various techniques have been applied in the medical field regarding the stenting of bifurcation lesions. In the computational study of Mortier et al. (2009), the influence of implementing different balloon sizes and stent designs on vessel patency was investigated. Specifically, two commercially available stent designs were considered; the Cypher © Stent and the MULTI-LINK Vision© Stent. Simulations revealed interesting changes in the stent cell geometries following balloon dilation at the bifurcated lesion. Restenosis remains a serious issue following the deployment of drug-eluting stents (DESs) in stented coronary bifurcations. The study of Mortier et al. (2010) provided novel insight into changes in the mechanical environment of a patient-specific coronary bifurcation following the implantation of three second generation DESs. The computed wall stress distributions were found to be highly dependent on stent design. Alternative stent design modifications were suggested by the authors to reduce the computed wall stresses.

Higher restenosis rates have been reported in peripheral arteries when compared to coronary arteries (Matsi et al., 1995; Mukherjee and Yadav, 2001). In the research of Early et al. (2009), it was hypothesised that the stresses enforced on the arteries as a result of the mechanical environment such a region of joint flexion could explain high restenosis rates. Numerical simulations of a stent-artery model were performed to investigate this hypothesis. Computations revealed a significant variation in stresses caused by the dynamic loading environment which could be a contributor to vessel wall injury. An insight into critical factors affecting stent coating delamination was conducted in the study of Hopkins et al.

(2010). A cohesive zone model formulation was used to simulate delamination and buckling of compliant polymer coatings during deployment. Critical factors influencing coating delamination included; coating thickness and stiffness, stent-coating interface strength and hinge curvature. One of the major concerns associated with endovascular aneurysm repair (EVAR) is device migration. In the research of Prasad et al. (2011), a coupled computational solid mechanics and fluid dynamics approach was undertaken to predict endograft migration. Device stability was found to be strongly influenced by proximal graft fixation and increased vessel tortuosity. In the study conducted by Auricchio et al. (2011), finite element analysis was used to simulate the deployment of three self-expanding stents in different sizes and configurations (laser-cut open-cell, laser-cut closed-cell and braided closed cell). Patient-specific coronary artery models were implemented. The stress induced on the vessel wall along with vessel straightening and lumen gain were chosen as measures of stenting impact on vessel anatomy. Highest lumen gain was achieved by the laser-cut closed-cell design while simulations also revealed that stent configuration and size had limited impact on vessel straightening. A computational assessment of the influence of three different stent designs on aneurysmal hemodynamics using particle image velocimetry was carried out by Babiker et al. (2012). In vitro experiments were also performed for each stent design and a close agreement was found for flow velocity and distribution between the experimental and computational results. Simulations revealed that alterations in fluid dynamic distributions for the different designs were predominantly due to protruding struts in the bifurcation region. The influence of stent design and vessel geometry on the mechanics of stent deployment in an intracranial aneurysm was recently investigated by De Bock et al. (2012), where three nitinol stent designs were deployed in three patient-specific aneurysmatic vessels. An open cell stent design was reported to provide optimal cover of the aneurysm neck post-deployment.

5.8 Summary and Future Considerations

An overview of the evolution of stent design, latest stent technology, clinical complications and computational predictive frameworks has been provided in this

chapter. Improved clinical outcomes resulting from stenting procedures when compared to alternative cardiovascular interventional approaches has led to the development of a plethora of stent designs each with competing claims of advancement. The need for the quantity of commercially available stents is questionable, as suggested by Regar et al. (2001). It has been suggested that the drive for new stents has largely been motivated by patent and marketing issues rather than scientific considerations (Stoeckel et al., 2002).

Restenosis, defined as a reduction in patency following surgery, remains a significant challenge associated with stenting. A gold standard has not been determined as of yet for preventing this inflammatory response. The elution of immunosuppressive drugs such as heparin, paclitaxel and sirolimus into the damaged arterial wall following stenting, applied either directly to the stent surface or indirectly by means of a coating, have led to significant improvements in restenosis rates (Serruys et al., 1998; Schofer et al., 2003; Stone et al., 1998; Morice et al., 2004; Schampaert et al., 2004; Liistro and Bolognese, 2003; Gershlick et al., 2004; Lansky et al., 2004). These immunosuppressive drugs can be delivered by utilising polymer-based coatings such as phosphorylcholine or polylactic-co-glycolic acid (PLGA) or porous metallic coatings such as TiNOX. However, a number of studies have highlighted that late stent thrombosis can occur following the use of drug-eluting stents (Wang et al., 2002; Iakovou et al., 2005; Luscher et al., 2007; Daemen et al., 2007). The specific mechanisms leading to late stent thrombosis associated with drug-eluting coatings are still unclear. Possible explanations include patient-specific factors such as genetics, general patient health, lesion length and plaque burden (Regar et al., 2001) and procedure-specific factors such as stenting technique, stent design characteristics and off-label stent use, inflammatory affects of polymer coatings, late endothelialisation (McFadden et al., 2004), discontinuation of dual antiplatelet therapy or a combination of these factors. A series of rigorous bench-side testing experiments have recently been conducted on commercially available drug-eluting stent designs (Basalus and von Birgelen, 2010). Coating irregularities such as webbing, wrinkling, peeling and fragmentation were reported. Numerous other studies have reported coating delamination and damage of commercially available

stent designs with numerous studies suggesting that coating damage plays a significant role in the development of clinical complications such as thrombosis, micro-embolism formation and impaired drug delivery (Hoffmann et al., 2002; Otsuka et al., 2007; Levy et al., 2009; Balakrishnan et al., 2005).

New stent technologies must provide more effective long-term treatment and eliminate restenosis. A number of design issues still remain. Patients who receive certain polymer-based drug-eluting stents must receive dual antiplatelet therapy (Clopidogrel and aspirin) with all patients with coronary stents requiring life-long aspirin therapy (McFadden et al., 2004). Clearly, a combination of computational and experimental methods are required to prevent coating delamination in order to ensure uniform drug delivery, avoid toxicity effects and control drug dosage and drug elution profiles (Gershlick et al., 2004; Joner et al., 2006; Hara et al., 2006). Biodegradable stents could provide a suitable alternative to metallic stent designs but degradation rates must be controllable in order to ensure adequate vessel remodelling. The ability to access artery side branches through stent struts has become an important design consideration in certain circumstances (Mariano and Sangiorgi, 2009). Magnesium stents offer some promise with degradation rates getting closer to design requirements (O'Brien and Carroll, 2009). The need for radiopaque materials is reducing with significant technological advances in X-ray fluoroscopy images possible with flat-panel detector technology (Spahn, 2005). Local gene therapy has also been proposed as a method for inhibiting neointimal hyperplasia (Regar et al., 2001; Walter et al., 2004).

5.9   References

Abizaid, A. C., De Ribamar, C. J. J., Whitbourn, R. J.&Chang, J. C. (2007) The CardioMind coronary stent delivery system: stent delivery on a. 014" guidewire platform. *EuroIntervention: journal of EuroPCR in collaboration with the Working Group on Interventional Cardiology of the European Society of Cardiology,* 3**,** 154.

Airoldi, F., Colombo, A., Tavano, D., Stankovic, G., Klugmann, S., Paolillo, V., et al. (2004) Comparison of diamond-like carbon-coated stents versus uncoated stainless steel stents in coronary artery disease. *The American journal of cardiology,* 93**,** 474-477.

Albiero, R., Nishida, T., Adamian, M., Amato, A., Vaghetti, M., Corvaja, N., et al. (2000) Edge Restenosis After Implantation of High Activity 32P Radioactive-Emitting Stents. *Circulation,* 101**,** 2454-2457.

Antoniucci, D., Valenti, R., Migliorini, A., Moschi, G., Trapani, M., Bolognese, L., et al. (2001) Clinical and angiographic outcomes following elective implantation of the Carbostent in patients at high risk of restenosis and target vessel failure. *Catheterization and cardiovascular interventions,* 54**,** 420-426.

Auricchio, F., Conti, M., De Beule, M., De Santis, G.&Verhegghe, B. (2011) Carotid artery stenting simulation: From patient-specific images to finite element analysis. *Medical Engineering & Physics,* 33**,** 281-289.

Babapulle, M. N.&Eisenberg, M. J. (2002) Coated stents for the prevention of restenosis: Part II. *Circulation,* 106**,** 2859-2866.

Babiker, M. H., Gonzalez, L. F., Ryan, J., Albuquerque, F., Collins, D., Elvikis, A., et al. (2012) Influence of stent configuration on cerebral aneurysm fluid dynamics. *Journal of Biomechanics*.

Balakrishnan, B., Tzafriri, A. R., Seifert, P., Groothuis, A., Rogers, C.&Edelman, E. R. (2005) Strut position, blood flow, and drug deposition. *Circulation,* 111**,** 2958-2965.

Balossino, R., Gervaso, F., Migliavacca, F.&Dubini, G. (2008) Effects of different stent designs on local hemodynamics in stented arteries. *Journal of Biomechanics,* 41**,** 1053-1061.

Basalus, M. W. Z.&Von Birgelen, C. (2010) Benchside testing of drug-eluting stent surface and geometry. *Interv. Cardiol.,* 2**,** 159-175.

Berger-Gorbet, M., Broxup, B., Rivard, C.&Yahia, L. H. (1996) Biocompatibility testing of NiTi screws using immunohistochemistry on sections containing metallic implants. *Journal of biomedical materials research,* 32**,** 243-248.

Bhargava, B., Reddy, N. K., Karthikeyan, G., Raju, R., Mishra, S., Singh, S., et al. (2006) A novel paclitaxel-eluting porous carbon-carbon nanoparticle coated, nonpolymeric cobalt-chromium stent: Evaluation in a porcine model. *Catheterization and cardiovascular interventions,* 67**,** 698-702.

Bonan, R., Bhat, K., Lefã¨Vre, T., Lemarbre, L., Paiement, P., Wolff, R., et al. (1991) Coronary artery stenting after angioplasty with self-expanding parallel wire metallic stents. *American heart journal,* 121**,** 1522-1530.

Brauer, H., Stolpmann, J., Hallmann, H., Erbel, R.&Fischer, A. (1999) Measurement and numerical simulation of the dilatation behaviour of coronary stents. *Materialwissenschaft und Werkstofftechnik,* 30**,** 876-885.

Briguori, C., Sarais, C., Pagnotta, P., Liistro, F., Montorfano, M., Chieffo, A., et al. (2002) In-stent restenosis in small coronary arteries: Impact of strut thickness. *Journal of the American College of Cardiology,* 40**,** 403-409.

Brodie, B. R., Stuckey, T., Downey, W., Humphrey, A., Bradshaw, B., Metzger, C., et al. (2008) Outcomes and complications with off-label use of drug-eluting stents: Results from the STENT (Strategic Transcatheter Evaluation of New Therapies) Group. *JACC: Cardiovascular Interventions,* 1**,** 405-414.

Carter Do, A. J.&Fischell , T. A. (1998) Current status of radioactive stents for the prevention of in-stent restenosis. *International Journal of Radiation Oncology* Biology* Physics,* 41**,** 127-133.

Chen, M. C., Liang, H. F., Chiu, Y. L., Chang, Y., Wei, H. J.&Sung, H. W. (2005) A novel drug-eluting stent spray-coated with multi-layers of collagen and sirolimus. *Journal of controlled release,* 108**,** 178-189.

Chen, M. S., John, J. M., Chew, D. P., Lee, D. S., Ellis, S. G.&Bhatt, D. L. (2006) Bare metal stent restenosis is not a benign clinical entity. *American heart journal,* 151**,** 1260-1264.

Colombo, A.&Karvouni, E. (2000) Biodegradable stents:" Fulfilling the mission and stepping away". *Circulation,* 102**,** 371-373.

Consigny, P. M. (2000) Endothelial cell seeding on prosthetic surfaces. *Journal of long-term effects of medical implants,* 10**,** 79.

Coolong, A.&Mauri, L. (2006) Clopidogrel treatment surrounding percutaneous coronary intervention: when should it be started and stopped? *Current cardiology reports,* 8**,** 267-271.

Costa, J. R., Abizaid, A., Costa, R., Feres, F., Tanajura, L. F., Mattos, L. A., et al. (2008) Preliminary results of the hydroxyapatite nonpolymer-based sirolimus-eluting stent for the treatment of single de novo coronary lesions: a first-in-human analysis of a third-generation drug-eluting stent system. *JACC: Cardiovascular Interventions,* 1**,** 545-551.

Cumberland, D. C., Gunn, J., Malik, N.&Holt, C. M. (1998) Biomimicry 1: PC.

Daemen, J., Wenaweser, P., Tsuchida, K., Abrecht, L., Vaina, S., Morger, C., et al. (2007) Early and late coronary stent thrombosis of sirolimus-eluting and paclitaxel-eluting stents in routine clinical practice: data from a large two-institutional cohort study. *The Lancet,* 369**,** 667-678.

De Beule, M., Mortier, P., Carlier, S. G., Verhegghe, B., Van Impe, R.&Verdonck, P. (2008) Realistic finite element-based stent design: The impact of balloon folding. *Journal of Biomechanics,* 41**,** 383-389.

De Bock, S., Iannaccone, F., De Santis, G., De Beule, M., Mortier, P., Verhegghe, B., et al. (2012) Our capricious vessels: The influence of stent design and vessel geometry on the mechanics of intracranial aneurysm stent deployment. *Journal of Biomechanics*.

Descheerder, I., Wang, K., Sohier, J., Verbeken, E., Zhou, X. R., Frooyen, L., et al. (1997) Metallic surface treatment using electrochemical polishing decreases thrombogenicity and neointimal hyperplasia after coronary stent implantation in a porcine model. *American journal of cardiology,* 80**,** TC133-TC133.

Di Mario, C., Grube, E., Nisanci, Y., Reifart, N., Colombo, A., Rodermann, J., et al. (2004) MOONLIGHT: a controlled registry of an iridium oxide-coated

stent with angiographic follow-up. *International journal of cardiology,* 95**,** 329-331.

Dibra, A., Kastrati, A., Mehilli, J., Pache, J., Von Oepen, R., Dirschinger, J., et al. (2005) Influence of stent surface topography on the outcomes of patients undergoing coronary stenting: A randomized double-blind controlled trial. *Catheterization and cardiovascular interventions,* 65**,** 374-380.

Dotter, C. T., Buschmann, R. W., Mckinney, M. K.&Rosch, J. (1983) Transluminal expandable nitinol coil stent grafting: preliminary report. *Radiology,* 147**,** 259-260.

Dumoulin, C.&Cochelin, B. (2000) Mechanical behaviour modelling of balloon-expandable stents. *Journal of Biomechanics,* 33**,** 1461-1470.

Dzavik, V., Carere, R. G., Mancini, G. B., Cohen, E. A., Catellier, D., Anderson, T. E., et al. (2001) Predictors of improvement in left ventricular function after percutaneous revascularization of occluded coronary arteries: a report from the Total Occlusion Study of Canada (TOSCA). *American heart journal,* 142**,** 301-308.

Early, M., Lally, C., Prendergast, P. J.&Kelly, D. J. (2009) Stresses in peripheral arteries following stent placement: a finite element analysis. *Computer methods in biomechanics and biomedical engineering,* 12**,** 25-33.

Ellis, S. G., Colombo, A., Grube, E., Popma, J., Koglin, J., Dawkins, K. D., et al. (2007) Incidence, timing, and correlates of stent thrombosis with the polymeric paclitaxel drug-eluting stent: a TAXUS II, IV, V, and VI meta-analysis of 3,445 patients followed for up to 3 years. *Journal of the American College of Cardiology,* 49**,** 1043-1051.

Etave, F., Finet, G., Boivin, M., Boyer, J. C., Rioufol, G.&Thollet, G. (2001) Mechanical properties of coronary stents determined by using finite element analysis. *Journal of Biomechanics,* 34**,** 1065-1075.

FDA (2012) U.S. Food and Drug Administration, date accessed 06/09/2012.

Fischell, T. A.&Hehrlein, C. (1998) The radioisotope stent for the prevention of restenosis. *Herz,* 23**,** 373-379.

Fischman, D. L., Leon, M. B., Baim, D. S., Schatz, R. A., Savage, M. P., Penn, I., et al. (1994) for the Stent Restenosis Study Investigators. A randomized comparison of coronary-stent placement and balloon angioplasty in the treatment of coronary artery disease. *N Engl j Med,* 331**,** 496-501.

Garcia-Touchard, A., Burke, S. E., Toner, J. L., Cromack, K.&Schwartz, R. S. (2006) Zotarolimus-eluting stents reduce experimental coronary artery neointimal hyperplasia after 4 weeks. *European Heart Journal,* 27**,** 988-993.

Gershlick, A., De Scheerder, I., Chevalier, B., Stephens-Lloyd, A., Camenzind, E., Vrints, C., et al. (2004) Inhibition of restenosis with a paclitaxel-eluting, polymer-free coronary stent. *Circulation,* 109**,** 487-493.

Gervaso, F., Capelli, C., Petrini, L., Lattanzio, S., Di Virgilio, L.&Migliavacca, F. (2008) On the effects of different strategies in modelling balloon-expandable stenting by means of finite element method. *Journal of Biomechanics,* 41**,** 1206-1212.

Goosen, M. F. A.&Sefton, M. V. (1983) Properties of a heparin-poly (vinyl alcohol) hydrogel coating. *Journal of biomedical materials research,* 17**,** 359-373.

Grube, E. (2003) Final tacrolimus outcomes in native coronaries and saphenous vein grafts: present & evident.

Grube, E.&Buellesfeld, L. (2006) BioMatrix Biolimus A9-eluting coronary stent: a next-generation drug-eluting stent for coronary artery disease. *Expert review of medical devices,* 3**,** 731-741.

Gunn, J.&Cumberland, D. (1999) Does stent design influence restenosis? *European Heart Journal,* 20**,** 1009-1013.

Gutensohn, K., Beythien, C., Bau, J., Fenner, T., Grewe, P., Koester, R., et al. (2000) In vitro analyses of diamond-like carbon coated stents: reduction of metal ion release, platelet activation, and thrombogenicity. *Thrombosis research,* 99**,** 577-585.

Hara, H., Nakamura, M., Palmaz, J. C.&Schwartz, R. S. (2006) Role of stent design and coatings on restenosis and thrombosis. *Advanced drug delivery reviews,* 58**,** 377-386.

Harewood, F., Grogan, J.&McHugh, P. (2010) A Multiscale Approach To Failure Assessment In Deployment For Cardiovascular Stents. *Journal of Multiscale Modelling,* 2**,** 1-22.

Harewood, F. J.&McHugh, P. E. (2007) Modeling of size dependent failure in cardiovascular stent struts under tension and bending. *Annals of Biomedical Engineering,* 35**,** 1539-1553.

Haude, M., Konorza, T. F. M., Kalnins, U., Erglis, A., Saunamaki, K., Glogar, H. D., et al. (2003) Heparin-coated stent placement for the treatment of stenoses in small coronary arteries of symptomatic patients. *Circulation,* 107**,** 1265-1270.

Hehrlein, C., Zimmermann, M., Metz, J., Ensinger, W.&Kubler, W. (1995) Influence of surface texture and charge on the biocompatibility of endovascular stents. *Coronary artery disease,* 6**,** 581.

Heintz, C., Riepe, G., Birken, L., Kaiser, E., Chakfe, N., Morlock, M., et al. (2001) Corroded nitinol wires in explanted aortic endografts: an important mechanism of failure? *Journal Information,* 8.

Heldman, A. W., Cheng, L., Jenkins, G. M., Heller, P. F., Kim, D. W., Ware, M., et al. (2001) Paclitaxel stent coating inhibits neointimal hyperplasia at 4 weeks in a porcine model of coronary restenosis. *Circulation,* 103**,** 2289-2295.

Heublein, B., Pethig, K., Ozbek, C., Elsayed, M., Bolz, A.&Schaldach, M. (1998) Silicon carbide coating-a new hybrid design of coronary stents. *Prog Biomed Res,* 1**,** 33-9.

Heublein, B., Rohde, R., Kaese, V., Niemeyer, M., Hartung, W.&Haverich, A. (2003) Biocorrosion of magnesium alloys: a new principle in cardiovascular implant technology? *Heart,* 89**,** 651-656.

Hoffmann, R., Mintz, G. S., Haager, P. K., Bozoglu, T., Grube, E., Gross, M., et al. (2002) Relation of stent design and stent surface material to subsequent in-stent intimal hyperplasia in coronary arteries determined by intravascular ultrasound. *The American journal of cardiology,* 89**,** 1360-1364.

Holzapfel, G. A., Sommer, G., Gasser, C. T.&Regitnig, P. (2005) Determination of layer-specific mechanical properties of human coronary arteries with nonatherosclerotic intimal thickening and related constitutive modeling.

American Journal of Physiology-Heart and Circulatory Physiology, 289**,** H2048.

Hopkins, C. G., McHugh, P. E.&McGarry, J. P. (2010) Computational Investigation of the Delamination of Polymer Coatings During Stent Deployment. *Annals of Biomedical Engineering,* 38**,** 2263-2273.

Huang, N., Leng, Y. X., Yang, P., Chen, J. Y., Sun, H., Wang, J., et al. (2006) Surface modification of coronary artery stent by Ti O/Ti N complex film coating prepared with plasma immersion ion implantation and deposition. *Nuclear Instruments and Methods in Physics Research Section B: Beam Interactions with Materials and Atoms,* 242**,** 18-21.

Huang, Y., Wang, L., Verweire, I., Qiang, B., Liu, X., Verbeken, E., et al. (2002) Optimization of local methylprednisolone delivery to inhibit inflammatory reaction and neointimal hyperplasia of coated coronary stents. *The Journal of invasive cardiology,* 14**,** 505-513.

Iakovou, I., Schmidt, T., Bonizzoni, E., Ge, L., Sangiorgi, G. M., Stankovic, G., et al. (2005) Incidence, predictors, and outcome of thrombosis after successful implantation of drug-eluting stents. *JAMA: the journal of the American Medical Association,* 293**,** 2126-2130.

Joner, M., Finn, A. V., Farb, A., Mont, E. K., Kolodgie, F. D., Ladich, E., et al. (2006) Pathology of Drug-Eluting Stents in Humans:: Delayed Healing and Late Thrombotic Risk. *Journal of the American College of Cardiology,* 48**,** 193-202.

Judkins, M. P. (1964) Transluminal treatment of arteriosclerotic obstruction. Description of a new technique and a preliminary report of its application. *Circulation,* 30**,** 654-670.

Karjalainen, P. P., Ylitalo, A. S.&Juhani Airaksinen, K. E. (2006) Real world experience with the TITAN (R) stent: a 9-month follow-up report from the Titan PORI Registry. *EuroIntervention,* 2**,** 187-191.

Kastrati, A., Mehilli, J., Dirschinger, J., Dotzer, F., Schuhlen, H., Neumann, F. J., et al. (2001) Intracoronary stenting and angiographic results: strut thickness effect on restenosis outcome (ISAR-STEREO) trial. *Circulation,* 103**,** 2816-2821.

Kastrati, A., Schomig, A., Dirschinger, J., Mehilli, J., Von Welser, N., Pache, J., et al. (2000) Increased risk of restenosis after placement of gold-coated stents: results of a randomized trial comparing gold-coated with uncoated steel stents in patients with coronary artery disease. *Circulation,* 101**,** 2478-2483.

Katuza, G. L., Gershlick, A. H., Park, S. J., De Scheerder, I., Chevalier, B., Camenzind, E., et al. (2004) Comparison of neointimal formation in polymer-free paclitaxel stents versus stainless stents (from the ASPECT and ELUTES randomized clinical trials). *The American journal of cardiology,* 94**,** 199-201.

Kereiakes, D. J., Cox, D. A., Hermiller, J. B., Midei, M. G., Bachinsky, W. B., Nukta, E. D., et al. (2003) Usefulness of a cobalt chromium coronary stent alloy. *The American journal of cardiology,* 92**,** 463-466.

Kipshidze, N., Dangas, G., Tsapenko, M., Moses, J., Leon, M. B., Kutryk, M., et al. (2004) Role of the endothelium in modulating neointimal formation: vasculoprotective approaches to attenuate restenosis after percutaneous

coronary interventions. *Journal of the American College of Cardiology,* 44, 733.

Klocke, A., Kemper, J., Schulze, D., Adam, G.&Kahl-Nieke, B. (2005) Magnetic field interactions of orthodontic wires during magnetic resonance imaging (MRI) at 1.5 Tesla. *Journal of Orofacial Orthopedics,* 66, 279-287.

Kollum, M., Farb, A., Schreiber, R., Terfera, K., Arab, A., Geist, A., et al. (2005) Particle debris from a nanoporous stent coating obscures potential antiproliferative effects of tacrolimus-eluting stents in a porcine model of restenosis. *Catheterization and cardiovascular interventions,* 64, 85-90.

Koster, R., Vieluf, D., Kiehn, M., Sommerauer, M., Kahler, J., Baldus, S., et al. (2000) Nickel and molybdenum contact allergies in patients with coronary in-stent restenosis. *The Lancet,* 356, 1895-1897.

Krucoff, M. W., Kereiakes, D. J., Petersen, J. L., Mehran, R., Hasselblad, V., Lansky, A. J., et al. (2008) A novel bioresorbable polymer paclitaxel-eluting stent for the treatment of single and multivessel coronary disease: primary results of the COSTAR (Cobalt Chromium Stent With Antiproliferative for Restenosis) II study. *Journal of the American College of Cardiology,* 51, 1543-1552.

Labarre, D., Jozefowicz, M.&Boffa, M. C. (1977) Properties of heparin-poly (methyl methacrylate) copolymers. II. *Journal of biomedical materials research,* 11, 283-295.

Lafont, A., Guzman, L. A., Whitlow, P. L., Goormastic, M., Cornhill, J. F.&Chisolm, G. M. (1995) Restenosis after experimental angioplasty: intimal, medial, and adventitial changes associated with constrictive remodeling. *Circulation Research,* 76, 996-1002.

Lansky, A. J., Costa, R. A., Mintz, G. S., Tsuchiya, Y., Midei, M., Cox, D. A., et al. (2004) Non Polymer-Based Paclitaxel-Coated Coronary Stents for the Treatment of Patients With De Novo Coronary Lesions. *Circulation,* 109, 1948-1954.

Lau, K. W., Mak, K. H., Hung, J. S.&Sigwart, U. (2004) Clinical impact of stent construction and design in percutaneous coronary intervention. *American heart journal,* 147, 764-773.

Levy, Y., Mandler, D., Weinberger, J.&Domb, A. J. (2009) Evaluation of drug-eluting stents' coating durability-"Clinical and regulatory implications. *Journal of Biomedical Materials Research Part B: Applied Biomaterials,* 91, 441-451.

Lewis, A. L., Furze, J. D., Small, S., Robertson, J. D., Higgins, B. J., Taylor, S., et al. (2002) Long-term stability of a coronary stent coating post-implantation. *Journal of biomedical materials research,* 63, 699-705.

Lewis, A. L., Vick, T. A., Collias, A. C. M., Hughes, L. G., Palmer, R. R., Leppard, S. W., et al. (2001) Phosphorylcholine-based polymer coatings for stent drug delivery. *Journal of Materials Science: Materials in Medicine,* 12, 865-870.

Liistro, F.&Bolognese, L. (2003) Drug-eluting stents. *Heart Drug,* 3, 203-213.

Limacher, A., Raber, L., Laube, E., Lauterburg, A., Lotscher, S., Hess, N., et al. (2011) Clinical long-term outcome after implantation of titanium nitride-oxide coated stents compared with paclitaxel-or sirolimus-eluting stents: propensity-score matched analysis. *EuroIntervention: journal of EuroPCR*

in collaboration with the Working Group on Interventional Cardiology of the European Society of Cardiology.

Liu, C. L., Chu, P. K., Lin, G. Q.&Qi, M. (2006) Anti-corrosion characteristics of nitride-coated AISI 316L stainless steel coronary stents. *Surface and Coatings Technology,* 201**,** 2802-2806.

Luscher, T. F., Steffel, J., Eberli, F. R., Joner, M., Nakazawa, G., Tanner, F. C., et al. (2007) Drug-Eluting Stent and Coronary Thrombosis Biological Mechanisms and Clinical Implications. *Circulation,* 115**,** 1051-1058.

Maetani, I., Isayama, H.&Mizumoto, Y. (2007) Palliation in patients with malignant gastric outlet obstruction with a newly designed enteral stent: a multicenter study. *Gastrointestinal Endoscopy,* 66**,** 355-360.

Maitz, M. F.&Shevchenko, N. (2006) Plasma-immersion ion-implanted nitinol surface with depressed nickel concentration for implants in blood. *Journal of Biomedical Materials Research Part A,* 76**,** 356-365.

Mani, G., Feldman, M. D., Patel, D.&Agrawal, C. (2007) Coronary stents: a materials perspective. *Biomaterials,* 28**,** 1689-1710.

Mariano, E.&Sangiorgi, G. M. (2009) Coronary Stents. *CT Evaluation of Coronary Artery Disease***,** 113-128.

Marx, S. O., Jayaraman, T., Go, L. O.&Marks, A. R. (1995) Rapamycin-FKBP inhibits cell cycle regulators of proliferation in vascular smooth muscle cells. *Circulation Research,* 76**,** 412-417.

Matsi, P. J., Manninen, H. I., Soder, H. K., Mustonen, P.&Kouri, J. (1995) Percutaneous transluminal angioplasty in femoral artery occlusions: primary and long-term results in 107 claudicant patients using femoral and popliteal catheterization techniques. *Clinical radiology,* 50**,** 237-244.

Matsumoto, Y., Shimokawa, H., Morishige, K., Eto, Y.&Takeshita, A. (2002) Reduction in neointimal formation with a stent coated with multiple layers of releasable heparin in porcine coronary arteries. *Journal of cardiovascular pharmacology,* 39**,** 513.

Mazid, M. A., Scott, E.&Li, N. H. (1991) New biocompatible polyurethane-type copolymer with low molecular weight heparin. *Clinical Materials,* 8**,** 71-80.

Mcfadden, E. P., Stabile, E., Regar, E., Cheneau, E., Ong, A. T. L., Kinnaird, T., et al. (2004) Late thrombosis in drug-eluting coronary stents after discontinuation of antiplatelet therapy. *The Lancet,* 364**,** 1519-1521.

McGarry, J. P., O'Donnell, B. P., McHugh, P. E.&McGarry, J. G. (2004) Analysis of the mechanical performance of a cardiovascular stent design based on micromechanical modelling. *Computational Materials Science,* 31**,** 421-438.

McGarry, J. P., O'Donnell, B. P., McHugh, P. E., O'Cearbhaill, E.&McMeeking, R. M. (2007) Computational Examination of the Effect of Material Inhomogeneity on the Necking of Stent Struts Under Tensile Loading. *Journal of Applied Mechanics,* 74**,** 978.

Meireles, G. C. X., Abreu, L. M., Forte, A. A. C., Sumita, M. K., Sumita, J. H.&Aliaga, J. D. C. S. (2007) Randomized comparative study of diamond-like carbon coated stainless steel stent versus uncoated stent implantation in patients with coronary artery disease. *Arquivos Brasileiros de Cardiologia,* 88**,** 390-395.

Meng, B., Wang, J., Zhu, N., Meng, Q. Y., Cui, F. Z.&Xu, Y. X. (2006) Study of biodegradable and self-expandable PLLA helical biliary stent in vivo and in vitro. *Journal of Materials Science: Materials in Medicine,* 17**,** 611-617.

Migliavacca, F., Petrini, L., Colombo, M., Auricchio, F.&Pietrabissa, R. (2002) Mechanical behavior of coronary stents investigated through the finite element method. *Journal of Biomechanics,* 35**,** 803-811.

Moreno, R., Fernandez, C., Alfonso, F., Hernandez, R., Perez-Vizcayno, M. J., Escaned, J., et al. (2004) Coronary stenting versus balloon angioplasty in small vessels: a meta-analysis from 11 randomized studies. *Journal of the American College of Cardiology,* 43**,** 1964-1972.

Morice, M. C., Serruys, P.&Costantini, C. O. (2004) and the RAVEL investigators. Three-year follow-up of the RAVEL study: A randomized study with the sirolimus-eluting Bx VELOCITYTM stent in the treatment of patients with de novo native coronary artery lesions. *J Am Coll Cardiol,* 43**,** 87A.

Mortier, P., De Beule, M., Carlier, S. G., Van Impe, R., Verhegghe, B.&Verdonck, P. (2008) Numerical study of the uniformity of balloon-expandable stent deployment. *Journal of Biomechanical Engineering,* 130**,** 021018.

Mortier, P., De Beule, M., Van Loo, D., Verhegghe, B.&Verdonck, P. (2009) Finite element analysis of side branch access during bifurcation stenting. *Medical Engineering & Physics,* 31**,** 434-440.

Mortier, P., Holzapfel, G. A., De Beule, M., Van Loo, D., Taeymans, Y., Segers, P., et al. (2010) A novel simulation strategy for stent insertion and deployment in curved coronary bifurcations: comparison of three drug-eluting stents. *Annals of Biomedical Engineering,* 38**,** 88-99.

Moses, J. W., Leon, M. B., Popma, J. J., Fitzgerald, P. J., Holmes, D. R., O'shaughnessy, C., et al. (2003) Sirolimus-eluting stents versus standard stents in patients with stenosis in a native coronary artery. *New England Journal of Medicine,* 349**,** 1315-1323.

Mukherjee, D.&Yadav, J. S. (2001) Update on peripheral vascular diseases: from smoking cessation to stenting. *Cleveland Clinic Journal of Medicine,* 68**,** 723-733.

Murphy, B. P., Cuddy, H., Harewood, F. J., Connolley, T.&McHugh, P. E. (2006) The influence of grain size on the ductility of micro-scale stainless steel stent struts. *Journal of Materials Science: Materials in Medicine,* 17**,** 1-6.

Murphy, B. P., Savage, P., McHugh, P. E.&Quinn, D. F. (2003) The stress-strain behavior of coronary stent struts is size dependent. *Annals of Biomedical Engineering,* 31**,** 686-691.

Murphy, J. G., Schwartz, R. S., Edwards, W. D., Camrud, A. R., Vlietstra, R. E.&Holmes Jr, D. R. (1992) Percutaneous polymeric stents in porcine coronary arteries. Initial experience with polyethylene terephthalate stents. *Circulation,* 86**,** 1596-1604.

Nakayama, Y., Ji-Youn, K., Nishi, S., Ueno, H.&Matsuda, T. (2001) Development of high-performance stent: Gelatinous photogel-coated stent that permits drug delivery and gene transfer. *Journal of biomedical materials research,* 57**,** 559-566.

Newsome, L. T., Kutcher, M. A.&Royster, R. L. (2008) Coronary artery stents: Part I. Evolution of percutaneous coronary intervention. *Anesthesia & Analgesia,* 107**,** 552-569.

O'Brien, B.&Carroll, W. (2009) The evolution of cardiovascular stent materials and surfaces in response to clinical drivers: A review. *Acta biomaterialia,* 5**,** 945-958.

Ong, A. T. L., McFadden, E. P., Regar, E., De Jaegere, P., Van Domburg, R. T.&Serruys, P. W. (2005) Late angiographic stent thrombosis (LAST) events with drug-eluting stents. *Journal of the American College of Cardiology,* 45**,** 2088-2092.

Ong, A. T. L.&Serruys, P. W. (2005) Keynote Address: Drug-Eluting Stents: Current Issues. *Texas Heart Institute Journal,* 32**,** 372.

Otsuka, Y., Chronos, N. A. F., Apkarian, R. P.&Robinson, K. A. (2007) Scanning electron microscopic analysis of defects in polymer coatings of three commercially available stents: comparison of BiodivYsio, Taxus and Cypher stents. *Journal of Invasive Cardiology,* 19**,** 71.

Ozaki, Y., Keane, D., Nobuyoshi, M., Hamasaki, N., Popma, J. J.&Serruys, P. W. (1995) Coronary lumen at six-month follow-up of a new radiopaque Cordis tantalum stent using quantitative angiography and intracoronary ultrasound. *The American journal of cardiology,* 76**,** 1135-1142.

Palmaz, J. C., Sibbitt, R. R., Reuter, S. R., Tio, F. O.&Rice, W. J. (1985) Expandable intraluminal graft: a preliminary study. Work in progress. *Radiology,* 156**,** 73-77.

Park, J. B.&Kim, Y. K. (1995) Metallic biomaterials. *JD Bronzino, ed***,** 529-723.

Parry, G.&McGarry, P. (2012) An analytical solution for the stress state at stent-coating interfaces. *Journal of the Mechanical Behavior of Biomedical Materials,* 10**,** 183-196.

Peuster, M., Hesse, C., Schloo, T., Fink, C., Beerbaum, P.&Von Schnakenburg, C. (2006) Long-term biocompatibility of a corrodible peripheral iron stent in the porcine descending aorta. *Biomaterials,* 27**,** 4955-4962.

Peuster, M., Wohlsein, P., Brugmann, M., Ehlerding, M., Seidler, K., Fink, C., et al. (2001) A novel approach to temporary stenting: degradable cardiovascular stents produced from corrodible metal-results 6-18 months after implantation into New Zealand white rabbits. *Heart,* 86**,** 563-569.

Prasad, A., Zarins, C. K.&Figueroa, C. A. (2011) A finite element approach for evaluating the risk of endograft migration. *Proceedings of ASME 2011, Irvine California, USA.*

Rajtar, A., Kaluza, G. L., Yang, Q., Hakimi, D., Liu, D., Tsui, M., et al. (2006) Hydroxyapatite-coated cardiovascular stents. *EuroIntervention,* 2**,** 113-115.

Ranade, S. V., Miller, K. M., Richard, R. E., Chan, A. K., Allen, M. J.&Helmus, M. N. (2004) Physical characterization of controlled release of paclitaxel from the TAXUS Express2 drug-eluting stent. *Journal of Biomedical Materials Research Part A,* 71**,** 625-634.

Regar, E., Sianos, G.&Serruys, P. W. (2001) Stent development and local drug delivery. *British medical bulletin,* 59**,** 227.

Reifart, N., Morice, M. C., Silber, S., Benit, E., Hauptmann, K. E., De Sousa, E., et al. (2004) The NUGGET study: NIR ultra gold-gilded equivalency trial. *Catheterization and cardiovascular interventions,* 62**,** 18-25.

Roubin, G. S., Cannon, A. D., Agrawal, S. K., Macander, P. J., Dean, L. S., Baxley, W. A., et al. (1992) Intracoronary stenting for acute and threatened closure complicating percutaneous transluminal coronary angioplasty. *Circulation,* 85**,** 916-927.

Rousseau, H., Puel, J., Joffre, F., Sigwart, U., Duboucher, C., Imbert, C., et al. (1987) Self-expanding endovascular prosthesis: an experimental study. *Radiology,* 164**,** 709-714.

Rubin, P., Williams, J. P., Riggs, P. N., Bartos, S., Sarac, T., Pomerantz, R., et al. (1998) Cellular and molecular mechanisms of radiation inhibition of restenosis. Part I: role of the macrophage and platelet-derived growth factor. *International Journal of Radiation Oncology* Biology* Physics,* 40**,** 929-941.

Ruygrok, P. N.&Serruys, P. W. (1996) Intracoronary stenting: from concept to custom. *Circulation,* 94**,** 882-890.

Rzany, A.&Schaldach, M. (2001) Smart material silicon carbide: reduced activation of cells and proteins on a-SiC: H-coated stainless steel. *Progress in Biomedical Research,* 6**,** 182-194.

Salencon, J. (1983) *Calcul a la rupture et analyse limite.*

Savage, P., O'Donnell, B. P., McHugh, P. E., Murphy, B. P.&Quinn, D. F. (2004) Coronary stent strut size dependent stress-strain response investigated using micromechanical finite element models. *Annals of Biomedical Engineering,* 32**,** 202-211.

Schampaert, E., Cohen, E. A., Schluter, M., Reeves, F., Traboulsi, M., Kuntz, R. E., et al. (2004) The Canadian study of the sirolimus-eluting stent in the treatment of patients with long de novo lesions in small native coronary arteries (C-SIRIUS). *Journal of the American College of Cardiology,* 43**,** 1110-1115.

Schofer, J., Schluter, M., Gershlick, A. H., Wijns, W., Garcia, E., Schampaert, E., et al. (2003) Sirolimus-eluting stents for treatment of patients with long atherosclerotic lesions in small coronary arteries: double-blind, randomised controlled trial (E-SIRIUS). *The Lancet,* 362**,** 1093-1099.

Seliger, C., Schwennicke, K., Schaffer, C., Wolf, W. P.&Alt, E. (2000) Influence of a rough, ceramic-like stent surface made of iridium oxide on neointimal structure and thickening. *Eur Heart J,* 21**,** 286.

Serruys, P. W., De Jaegere, P., Kiemeneij, F., Macaya, C., Rutsch, W., Heyndrickx, G., et al. (1994) A comparison of balloon-expandable-stent implantation with balloon angioplasty in patients with coronary artery disease. *New England Journal of Medicine,* 331**,** 489-495.

Serruys, P. W., Sianos, G., Abizaid, A., Aoki, J., Den Heijer, P., Bonnier, H., et al. (2005) The effect of variable dose and release kinetics on neointimal hyperplasia using a novel paclitaxel-eluting stent platform: the Paclitaxel In-Stent Controlled Elution Study (PISCES). *Journal of the American College of Cardiology,* 46**,** 253-260.

Serruys, P. W., Strauss, B. H., Beatt, K. J., Bertrand, M. E., Puel, J., Rickards, A. F., et al. (1991) Angiographic follow-up after placement of a self-

expanding coronary-artery stent. *New England Journal of Medicine,* 324**,** 13-17.

Serruys, P. W., Van Hout, B., Bonnier, H., Legrand, V., Garcia, E., Macaya, C., et al. (1998) Randomised comparison of implantation of heparin-coated stents with balloon angioplasty in selected patients with coronary artery disease (Benestent II). *The Lancet,* 352**,** 673-681.

Sheiban, I., Villata, G., Bollati, M., Sillano, D., Lotrionte, M.&Biondi-Zoccai, G. (2008) Next-generation drug-eluting stents in coronary artery disease: focus on everolimus-eluting stent (Xience V®). *Vascular Health and Risk Management,* 4**,** 31.

Shethvishva, S. (1995) Prevention of subacute stent thrombosis by polymer-polyethylene oxide-heparin coating in the rabbit carotid artery. *Journal of the American College of Cardiology,* 25**,** 348A-349A.

Sigwart, U., Puel, J., Mirkovitch, V., Joffre, F.&Kappenberger, L. (1987) Intravascular stents to prevent occlusion and re-stenosis after transluminal angioplasty. *New England Journal of Medicine,* 316**,** 701-706.

Sketch, M. H., Ball, M., Rutherford, B., Popma, J. J., Russell, C.&Kereiakes, D. J. (2005) Evaluation of the Medtronic (Driver) cobalt-chromium alloy coronary stent system. *The American journal of cardiology,* 95**,** 8-12.

Spahn, M. (2005) Flat detectors and their clinical applications. *European radiology,* 15**,** 1934-1947.

Stack, R. S., Califf, R. M., Phillips, H. R., Pryor, D. B., Quigley, P. J., Bauman, R. P., et al. (1988) Interventional cardiac catheterization at Duke Medical Center. *The American journal of cardiology,* 62**,** 3F.

Stoeckel, D., Bonsignore, C.&Duda, S. (2002) A survey of stent designs. *Minimally Invasive Therapy & Allied Technologies,* 11**,** 137-147.

Stone, G. W., Brodie, B. R., Griffin, J. J., Morice, M. C., Costantini, C., St Goar, F. G., et al. (1998) Prospective, multicenter study of the safety and feasibility of primary stenting in acute myocardial infarction: in-hospital and 30-day results of the PAMI stent pilot trial. *Journal of the American College of Cardiology,* 31**,** 23-30.

Sumita, M.&Teoh, S. H. (2004) Durability of metallic implant materials. *Engineering materials for biomedical applications,* 1.

Sydow-Plum, G.&Tabrizian, M. (2008) Review of stent coating strategies: clinical insights. *Materials Science and Technology,* 24**,** 1127-1143.

Tamai, H., Igaki, K., Kyo, E., Kosuga, K., Kawashima, A., Matsui, S., et al. (2000) Initial and 6-month results of biodegradable poly-l-lactic acid coronary stents in humans. *Circulation,* 102**,** 399-404.

Tanajura, L. F., Abizaid, A. A., Feres, F., Pinto, I., Mattos, L., Staico, R., et al. (2003) Randomized intravascular ultrasound comparison between patients that underwent amorphous hydrogenated silicon-carbide coated stent deployment versus uncoated stents. *Journal of the American College of Cardiology,* 41**,** 58-58.

Tanguay, J. F., Zidar, J. P., Phillips 3rd, H. R.&Stack, R. S. (1994) Current status of biodegradable stents. *Cardiology clinics,* 12**,** 699.

Tepe, G., Schmehl, J., P Wendel, H., Schaffner, S., Heller, S., Gianotti, M., et al. (2006) Reduced thrombogenicity of nitinol stents-In vitro evaluation of different surface modifications and coatings. *Biomaterials,* 27**,** 643-650.

Thierry, B., Tabrizian, M., Trepanier, C., Savadogo, O.&Yahia, L. H. (2000) Effect of surface treatment and sterilization processes on the corrosion behavior of NiTi shape memory alloy. *Journal of biomedical materials research,* 51**,** 685-693.

Tomai, F., Ghini, A. S., Ferri, C., Desideri, G., Versaci, F., Gaspardone, A., et al. (2003) Effects of carbon-coated coronary stents on the markers of inflammation, thrombin generation and platelet and endothelial activation. *Italian heart journal: official journal of the Italian Federation of Cardiology,* 4**,** 23.

Trost, D. W., Zhang, H. L., Prince, M. R., Winchester, P. A., Wang, Y., Watts, R., et al. (2004) Three-dimensional MR angiography in imaging platinum alloy stents. *Journal of Magnetic Resonance Imaging,* 20**,** 975-980.

Tsujino, I., Ako, J., Honda, Y.&Fitzgerald, P. J. (2007) Drug delivery via nano-, micro and macroporous coronary stent surfaces.

Unverdorben, M., Sippel, B., Degenhardt, R., Sattler, K., Fries, R., Abt, B., et al. (2003) Comparison of a silicon carbide-coated stent versus a noncoated stent in human beings: the Tenax versus Nir Stent Study's long-term outcome. *American heart journal,* 145**,** E17-E17.

Van Beusekom, H. M. M., Tuin, J.&Kutryk, M. J. B. (1998) Stents up-close: electron micrographic appearance. *Handbook of Coronary Stents. London, UK: Martin Dunitz***,** 317-343.

Van Der Giessen, W. J., Serruys, P. W., Visser, W. J., Verdouw, P. D., Van Schalkwijk, W. P.&Jongkind, J. F. (1988) Endothelialization of intravascular stents. *Journal of interventional cardiology,* 1**,** 109-120.

Virmani, R., Guagliumi, G., Farb, A., Musumeci, G., Grieco, N., Motta, T., et al. (2004) Localized hypersensitivity and late coronary thrombosis secondary to a sirolimus-eluting stent. *Circulation,* 109**,** 701-705.

Waksman, R., Erbel, R., Di Mario, C., Bartunek, J., De Bruyne, B., Eberli, F. R., et al. (2009) Early-and long-term intravascular ultrasound and angiographic findings after bioabsorbable magnesium stent implantation in human coronary arteries. *JACC: Cardiovascular Interventions,* 2**,** 312-320.

Walter, D. H., Cejna, M., Diaz-Sandoval, L., Willis, S., Kirkwood, L., Stratford, P. W., et al. (2004) Local gene transfer of phVEGF-2 plasmid by gene-eluting stents. *Circulation,* 110**,** 36-45.

Wang, F., Stouffer, G. A., Waxman, S.&Uretsky, B. F. (2002) Late coronary stent thrombosis: early vs. late stent thrombosis in the stent era. *Catheterization and cardiovascular interventions,* 55**,** 142-147.

Weintraub, W. S. (2007) The pathophysiology and burden of restenosis. *The American journal of cardiology,* 100**,** S3-S9.

Wessely, R., Hausleiter, J., Michaelis, C., Jaschke, B., Vogeser, M., Milz, S., et al. (2005) Inhibition of neointima formation by a novel drug-eluting stent system that allows for dose-adjustable, multiple, and on-site stent coating. *Arteriosclerosis, Thrombosis, and Vascular Biology,* 25**,** 748-753.

Wiemer, M., Butz, T., Schmidt, W., Schmitz, K. P., Horstkotte, D.&Langer, C. (2010) Scanning electron microscopic analysis of different drug eluting stents after failed implantation: from nearly undamaged to major damaged polymers. *Catheterization and cardiovascular interventions,* 75**,** 905-911.

Wilczek, K., De Scheerder, I., Wang, K., Tam, L., Lan, P., Verbeken, E., et al. (1996a) Implantation of balloon expandable copper stents in porcine coronary arteries. A model for testing the efficacy of stent coating in decreasing stent thrombogenicity. *European Heart Journal,* 17**,** 455.

Wilczek, K., De Scheerder, I., Wang, K., Verbeken, E.&Piessens, J. (1996b) Comparison of self-expanding polyethylene terephthalate and metallic stents implanted in porcine iliac arteries. *Cardiovascular and interventional radiology,* 19**,** 176-180.

Windecker, S., Mayer, I., De Pasquale, G., Maier, W., Dirsch, O., De Groot, P., et al. (2001) Stent coating with titanium-nitride-oxide for reduction of neointimal hyperplasia. *Circulation,* 104**,** 928-933.

Windecker, S., Simon, R., Lins, M., Klauss, V., Eberli, F. R., Roffi, M., et al. (2005) Randomized Comparison of a Titanium-Nitride-Oxide Coated Stent With a Stainless Steel Stent for Coronary Revascularization. *Circulation,* 111**,** 2617-2622.

Xia, Z., Ju, F.&Sasaki, K. (2007) A general finite element analysis method for balloon expandable stents based on repeated unit cell (RUC) model. *Finite elements in analysis and design,* 43**,** 649-658.

Zargham, R. (2008) Preventing restenosis after angioplasty: a multistage approach. *Clinical Science,* 114**,** 257-264.

Zhao, Z. H., Sakagami, Y.&Osaka, T. (1998) Toxicity of hydrogen peroxide produced by electroplated coatings to pathogenic bacteria. *Canadian journal of microbiology,* 44**,** 441-447.

Zitter, H.&Plenk Jr, H. (1987) The electrochemical behavior of metallic implant materials as an indicator of their biocompatibility. *Journal of biomedical materials research,* 21**,** 881-896.

5.10 Tables and Figures
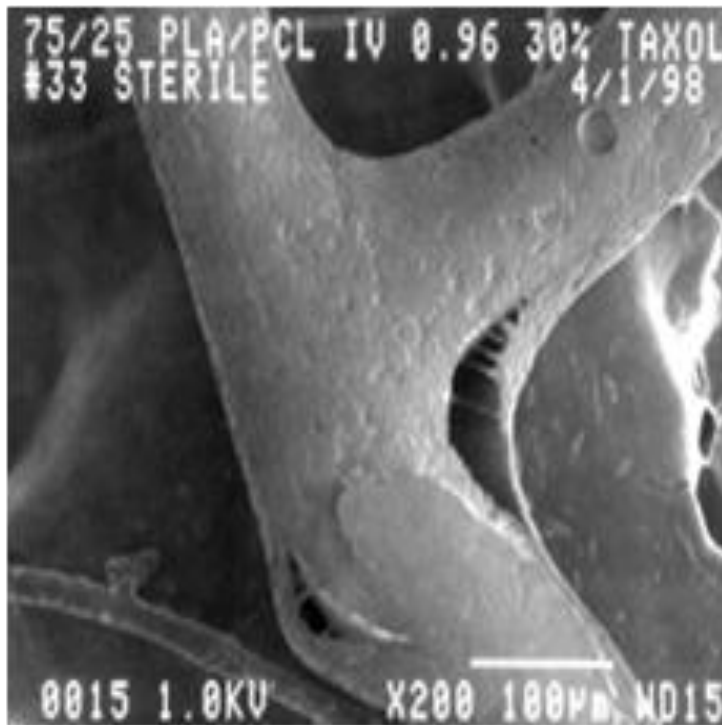
Figure 5-1: SEM image of stent coating delamination in the region of the hinge (Regar et al., 2001).

Removed due to copyright

Figure 5-2: SEM evidence of stent coating delamination in the region of the hinge in the commercially available Cypher$^{©}$ stent (Otsuka et al., 2007).
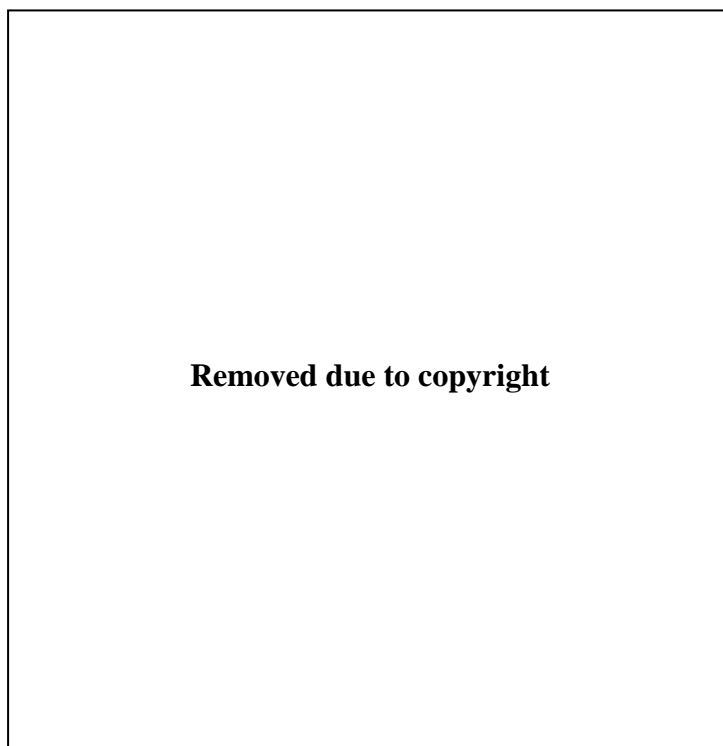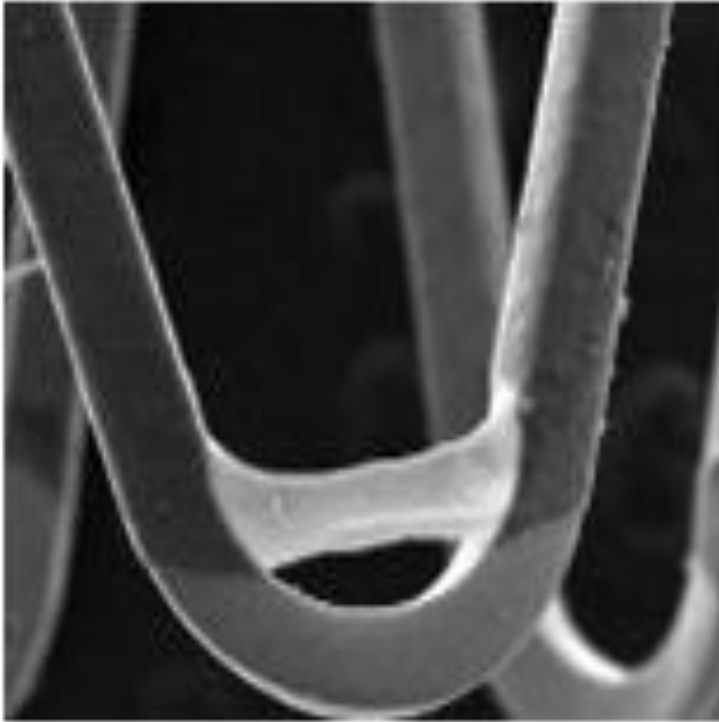
153

Figure 5-3: SEM image of stent coating peeling in the region of the stent hinge (Levy et al., 2009).
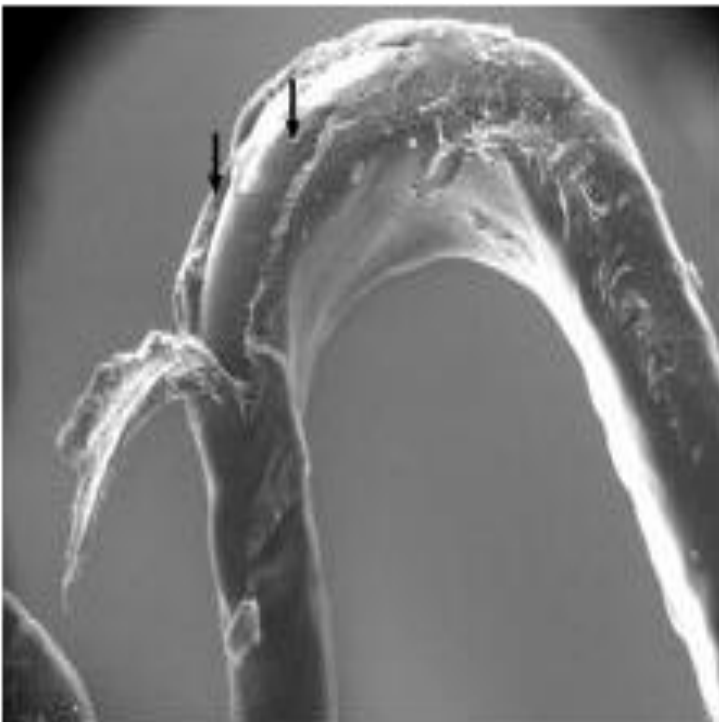

Figure 5-4: SEM image of polymer coating peeling in the region of the stent hinge of the Cypher© stent (Wiemer et al., 2010)

6. Computational Investigation of Stent Coating Debonding

6.1. Introduction

An in depth discussion concerning coating delamination and associated clinical implications has been provided in Chapter 5, Section 5.6. Despite enormous global investment in new generation coated stents, with an annual market volume of approximately \$15 billion for vascular stents (Uurto et al., 2011), and the importance of the clinical implications of coating delamination, currently the Food and Drug Administration does not provide guidelines on computational analysis and design techniques for coated stents (FDA, 2012).

Numerous studies have reported that the use of a thinner strut leads to a significant reduction in restenosis post operatively (Kastrati et al., 2001; Hara et al., 2006; Turco et al., 2008). The choice of strut thickness has been shown to affect the wall shear stress distribution inside a stented coronary artery in a recent computational study (Balossino et al., 2008). The influence of coating thickness on delamination was reported in a recent computational study where thicker stiff coatings were shown to debond at lower levels of stent deployment (Hopkins et al., 2010). Additionally, it has been demonstrated that strut length is an important design parameter in controlling the ratio between peak normal and shear tractions along the stent-coating interface (Parry and McGarry, 2012). However, no comprehensive computational analysis has been conducted concerning the influence of stent geometry and material properties on the distribution of shear and normal tractions at the stent-coating interface. While the study of Hopkins et al. (2010) simulated delamination and buckling of compliant polymer coatings from a metallic stent, only mode I delamination was considered and the full range of mixed-mode delamination patterns at the stent-coating interface were not uncovered. Additionally, finite element analyses have not previously been provided for coatings that are of a comparable stiffness to the stent substrate,

despite the use of metallic and ceramic coatings on stents (Babapulle and Eisenberg, 2002; Edelman et al., 2001; Windecker et al., 2001; Karjalainen et al., 2010).

In this chapter, a novel and in depth study of the mechanisms of stent-coating delamination is presented. Firstly, in order to gain an in-depth understanding of the mechanics of coating delamination, elastic coatings on elastic stent substrates are simulated in Section 6.3.1. Specifically, the influence of stent geometry (strut length, strut thickness and coating thickness) on interface tractions and coating delamination is analysed. Additionally, the influence of prescribed stent-coating interaction strength on the mechanism of coating debonding is demonstrated. The influence of stent plasticity on interface tractions and coating delamination is investigated in Section 6.3.2. The findings of this chapter provide valuable insight into the stress-state at the stent-coating interface as a function of the stent design parameters, allowing for a more reliable assessment of the limits relating to safe implantation of coated stents.

6.2. Methods

6.2.1. Finite Element Model

Many stent architectures are roughly based on the same design concept. The stent geometry consists of a series of interconnected repeating units, as shown in Figure 6-1, with each repeating unit consisting of an arch connected to straight struts (Parry and McGarry, 2012). The reference configuration of the stent and coating geometry utilised in the present study is depicted in Figure 6-2(a). A 2D unit cell idealisation is utilised and stent and coating dimensions are chosen based on commercially available stent designs (Regar et al., 2001). Similar to the presented finite element model for a bi-layered arch in Section 4.2.2, a polar coordinate system (r, θ) is utilised with the stent-coating interface located at $r = R$. A displacement boundary condition is applied on the bottom edge of the strut to simulate stent deployment. The coating material and the stent materials are identified as layers 1 and 2, of thickness h_1 and h_2 respectively. The arch and strut sections are also clearly indicated in Figure 6-2(a) along with the strut length, L.

The distance along the stent-coating interface, x, originating at the top of the arch ($x/R = 0$) is also indicated.

As the arch deformation is the critical determinant of the interface tractions (Parry and McGarry, 2012), non-dimensional arch deformation is defined as;

$$\Sigma_a = (D - D_0)/D_0 \qquad (6.1)$$

where D_0 and D are the initial and final arch deployments respectively, as depicted in Figure 6-2. Σ_a is referred to as the *deployment level* for the remainder of this chapter.

The circumferential strain $\left(\varepsilon_{circumf}\right)$ is also defined in Figure 6-2(b) as;

$$\varepsilon_{circumf} = (\varepsilon - \varepsilon_0)/\varepsilon_0 \qquad (6.2)$$

Based on the earlier theoretical (Chapter 3) and computational (Chapter 4) analyses of mixed-mode CZM behaviour, the NP2 formulation is implemented during coating compression ($\Delta_n < 0$) and the SMC formulation is applied during coating separation ($\Delta_n > 0$). The cohesive zone models are implemented in Abaqus/Standard software (V.6.8-1, Abaqus Inc., RI, USA) via a user-defined interface subroutine (UINTER).

6.3. Results

6.3.1. Elastic Stent

In this section, elastic material properties are utilised to describe both the coating and stent materials. The stent stiffness (Young's modulus), E_s, and the coating stiffness, E_c, are chosen so that $E_s/E_c = 2.5$ ($E_s = 500GPa, E_c = 200GPa$), unless otherwise stated. The choice of a relatively stiff coating is supported by the fact that diamond like carbon coatings (Kim et al., 2007) and aluminium coatings (Kollum et al., 2005) have frequently been coated on stents. In this section the influence of strut length (L), coating thickness (h_1) and stent thickness (h_2) on computed interface tractions is considered. Unless otherwise stated, cohesive zone

parameters are chosen so that peak mode I traction and peak mode II tractions are equal ($\sigma_{max}/E_c = \tau_{max}/E_c = 2$) with the peak occurring at the same effective separation in mode I and mode II separation ($|T|_{max}^{\theta=0} = |T|_{max}^{\theta=\pi/2}$; $|\Delta|_{max}^{\theta=0} = |\Delta|_{max}^{\theta=\pi/2}$). A characteristic distance of $\delta_n = \delta_t = 0.04\mu m$ was chosen based on the parameter sensitivity and mesh sensitivity analyses (see Appendix B for details). A Poisson's ratio of 0.3 is assumed for both the stent and coating materials.

6.3.1.1. *Effect of Strut Length*

In this section the effect of strut length on stent-coating interface tractions is investigated, assuming a constant stent thickness, coating thickness and stent-coating stiffness ratio for all simulations. Assuming parameters of $h_1/R = 0.2$, $h_2/R = 1$ and $E_s/E_c = 2.5$, three strut length are considered; $L/R = 0.5$, $L/R = 2$, and $L/R = 10$, representing stent designs with very short, typical and very long struts respectively.

Figure 6-3 shows the computed normal (T_n) and tangential (T_t) tractions at the stent-coating interface for a range of strut lengths. A line indicating the location of the bottom of the arch ($x/R = \pi/2$) is clearly shown in Figure 6-3. It is important to note that tractions computed at $x/R > \pi/2$ are referred to as tractions computed along the stent strut for all results presented in this chapter. A high interface strength is assumed for all simulations presented in Figure 6-3 so that the distribution of tangential and normal tractions can be examined in the absence of interface debonding. Additionally, a high interface stiffness is assumed so that the infinitesimal strain analytical elastic solution of Parry and McGarry (2012) is reproduced when the strut is removed from the geometry (as discussed in Chapter 4). Results are presented at three stent deployment levels: Low deployment ($\Sigma_a = 0.024$) results are shown in Figure 6-3(a), where the solution is in the infinitesimal strain regime; Medium deployment ($\Sigma_a = 0.134$) is shown in Figure 6-3(b), where the solution is in the finite strain regime; High deployment ($\Sigma_a = 0.608$) is shown in Figure 6-3(c), again with the solution in the finite strain regime. It should be noted that tractions are presented for a specified arch

deformation (Σ_a) defined in Figure 6-2(b). For this specified value of Σ_a, the radial expansion of the stent will depend also on the strut length. This is clearly evident from Figure 6-4 where stress distributions and deformed geometries for the three deployment levels ($\Sigma_a = 0.024, 0.134, 0.608$) are shown for a strut length of $L/R = 2$ in Figure 6-4(a-c) and for a strut length of $L/R = 10$ in Figure 6-4(d-f). For example, for the high deployment level ($\Sigma_a = 0.608$) a strut length of $L/R = 2$ provides an 87% increase in stent radius, representing a moderate radial expansion (as shown in Figure 6-4(c)) whereas a strut length of $L/R = 10$ provides a 466% increase in stent radius, representing a significant radial overexpansion (as shown in Figure 6-4(f)).

An examination of the computed tractions for the shortest strut length ($L/R = 0.5$) at a low deployment ($\Sigma_a = 0.024$) in Figure 6-3(a) reveals that the peak normal traction at the top of the arch ($x/R = 0$) is greater than the peak tangential traction at the bottom of the arch ($x/R = \pi/2$). A sinusoidal distribution of normal and shear traction can be observed at the interface along the arch ($0 \leq x/R \leq \pi/2$), whereby the tangential traction reduces to 0 at the top of the arch (as required by symmetry) and the normal traction reduces to a non-zero value at the bottom of the arch ($x/R = \pi/2$). It is worth noting that the range of tangential and normal tractions is approximately equal over the arch interface ($T_n(x/R = 0)$-$T_n(x/R = \pi/2) \approx T_t(x/R = \pi/2)$). These observations are closely aligned with the traction distribution determined by the pseudo-analytical approach of Parry and McGarry (2012), where the incorporation of a strut simply effects an increased rotation of the base of the arch, reducing the tangential traction and increasing the normal traction.

A sinusoidal traction distribution is not computed along the arch interface ($0 \leq x/R \leq \pi/2$) for longer strut lengths at infinitesimal deformations ($\Sigma_a = 0.024$). As shown in Figure 6-3(a), for a strut of length $L/R = 10$ the computed normal traction exhibits a flatter profile for $x/R < 1$. Tangential tractions are extremely low for $x/R < 1$, but increase significantly in the bottom part of the arch, reaching a peak at ($x/R = \pi/2$), where the curvature of the stent interface

changes between the arch and the strut. While results are presented for $x/R < 3$ in Figure 6-3 (omitting computed tractions towards the bottom of the longer struts $(L/R = 2, 10)$, it is clear that normal tractions reduce to zero in the strut, whereas tangential tractions reduce to a non-zero near constant value along the strut, with shorter struts providing higher tangential traction in the strut. The key observations for low deployment (infinitesimal strain) are as follows: (i) Peak normal traction occurs at the top of the arch; (ii) Peak tangential traction occurs at the bottom of the arch and is lower than the peak normal traction at the top of the arch for the range of strut lengths considered $(L/R \leq 10)$; (iii) Sinusoidal distributions are computed in the arch only for a very short strut length $(L/R \leq 0.5)$; (iv) Tractions in the strut are lower than those in the arch, with normal tractions reducing to zero and tangential tractions reducing to a constant non-zero value that depends on strut length.

The patterns of computed traction for a medium deployment level $((\Sigma_a = 0.134)$, Figure 6-3(b)) are reasonably similar to those presented for a low deployment level. However, for the highest deployment level $(\Sigma_a = 0.608)$, (Figure 6-3(c)) significantly different trends can be observed. The peak tangential traction at the bottom of the arch is greater in magnitude than the peak normal traction for all strut lengths. Shorter struts lead to the greatest increase in tangential traction. Additionally, a further increase in tangential traction (and reduction in normal traction) is computed when the strut is omitted $(L/R = 0)$. The normal traction is constant for all points on the interface where $x/R < 0.5$ for all strut lengths. Additionally, it can be observed that compressive normal tractions are computed along the strut, highlighting the importance of the cohesive zone behaviour under conditions of mixed-mode over-closure, as previously investigated in Chapters 3 and 4.

Finally, it should be noted that rotational constraints are not imposed on the strut ends for all simulations presented in this chapter, as this is representative of the majority of commercially available stent designs (McGarry et al., 2004; Hopkins et al., 2010). However, certain stent designs may result in a rotational constraint at

the bottom of the struts, e.g. a repeating diamond arrangement of struts (see Figure C-1 in the Appendix). This constraint essentially results in a significant increase in tangential traction for all deployment levels and also results in a normal compression at the stent–coating interface at the bottom of the arch (see Appendix C for details).

6.3.1.2. Influence of Prescribed Interface Strength on the Initial Debonding

Mechanism

The interface strength dramatically influences the initial delamination mechanism at the stent-coating interface. Figure 6-5-Figure 6-7 show the initial coating delamination patterns for a strut length of $L/R = 2$ when differing interaction strengths are chosen. When a low interface strength of $\sigma_{max}/E_c = \tau_{max}/E_c = 0.0019$ is prescribed (Figure 6-5), mode I coating delamination initiates at the top of the arch ($x/R = 0$) at a moderate stent deployment ($\Sigma_a = 0.025$). Following delamination, a significant reduction in coating stress is computed, whereas an increase in tensile stress is computed on the stent surface in the delamination region (Figure 6-5 (b)).

A markedly different pattern of coating delamination is observed if a stronger interface strength ($\sigma_{max}/E_c = \tau_{max}/E_c = 0.026$) is prescribed. As the interface strength is high, delamination does not occur until a high level of stent deployment is reached ($\Sigma_a = 0.47$)(Figure 6-6(b)). As demonstrated in Figure 6-6(a), prior to the initiation of debonding ($\Sigma_a = 0.43$) tangential tractions at the bottom of the arch become greater in magnitude than normal tractions at the top of the arch when high stent deployment levels are imposed. Again, it should be noted that this effect is particularly dominant for stents with shorter struts. Hence, predominantly mode II coating delamination initiates in the region of the bottom of the arch ($x/R = \pi/2$). Following initiation of predominantly mode II debonding, a reduction of both tangential and normal tractions is observed at the bottom of the arch in Figure 6-6(b), demonstrating the importance of correct coupling in the cohesive zone formulations. The predominantly tangential separation of the interface at the bottom of the arch ($x/R = \pi/2$) is shown in

Figure 6-7(b). Following mode II initiation, mixed-mode delamination propagates from the bottom of the arch towards the top of the arch, as shown in Figure 6-7(c). The coating remains attached to the stent at the top of the arch as mode I delamination is not achieved until further deployment.

In summary, these debonding simulations demonstrate that the location and mode of debonding at the stent-coating interface is highly dependent on the interface strength. Assuming that the normal and tangential strength of the interface are equal, if the interface is very weak, mode I debonding will initiate at the top of the arch. However, if the interface strength is very high, debonding will initiate at the bottom of the arch and will be predominantly mode II in nature. As a successful stent design requires high deployment levels, mode II initiation at the bottom of the arch should be carefully considered.

6.3.1.3. *Effect of Stent-Coating Stiffness Ratio*

The effect of stent-coating stiffness ratio on stent-coating interface tractions is investigated in this section for the reference stent geometry $(h_1/R = 0.2 , h_2/R = 1, L/R = 2)$. Three stent-coating stiffness ratios are considered $(E_s/E_c = 1.5, 2.5$ and $10000)$, noting that the stent is stiffer than the coating in all simulations. The lower stiffness ratios are representative of a polymer coating on a polymer stent whereas the highest stiffness ratio is representative of a polymer coating on a metallic stent. The Interface strength is sufficiently high so that debonding is not computed and the interface stiffness is several orders of magnitude higher than the stent stiffness in all simulations. The interface is assumed to be equally strong and stiff in the tangential and normal direction.

Figure 6-8 reveals that for a typical stent geometry $(h_1/R = 0.2 , h_2/R = 1, L/R = 2)$, the stent-coating stiffness ratio has a relatively weak influence on computed interface tractions, particularly at a high level of stent deployment $(\Sigma_a = 1.27)$. For example, comparing $E_s/E_c = 1.5$ and $E_s/E_c = 10000$, a very significant increase (four orders of magnitude) in stent-

162

coating stiffness ratio results in only a 25% increase in peak normal traction at the top of the arch ($x/R = 0$) at a low level of deployment ($\Sigma_a = 0.0065$) and only an 11% increase in peak normal traction at high deployment ($\Sigma_a = 1.27$). While the stent-coating stiffness ratio has a weak influence on the curves presented in Figure 6-8, it is important to note that reported tractions are normalised by the coating stiffness. Hence, for the stent geometry considered in Figure 6-8, at high levels of stent deployment, tractions approximately scale with coating stiffness and are relatively insensitive to the stent-coating stiffness ratio.

Therefore, from a design perspective, for a typical balloon deployed metallic stent design with a polymer coating, the elastic modulus of the metallic substrate (stainless steel, cobalt chromium, biodegradable magnesium etc.) will have negligible effect on interface traction, which will be determined primarily by the polymer stiffness. Indeed Figure 6-8 suggests that in the case of a next-generation polymer coating on a biodegradable polymer stent, again the stiffness of the coating will primarily determine the interface tractions, provided that the stent is significantly stiffer than the coating ($E_s/E_c = 2.5$).

Once again, it should be stressed that the trends reported in Figure 6-8 can be generally interpreted for typical stent geometry where $h_2/h_1 \geq 5$. However, for an unusually thin stent geometry (for example if $h_2/h_1 \approx 1$) the stiffness of the stent would have a more pronounced effect on interface tractions.

6.3.1.4. Effect of Coating Thickness

In this section the effect of coating thickness on stent-coating interface tractions is investigated, assuming a constant stent thickness, strut length and stent-coating stiffness ratio for all simulations.

Figure 6-9 shows the computed normal (T_n) and tangential (T_t) tractions at the stent-coating interface for a range of coating thicknesses. Again normal and tangential tractions are first assessed in the absence of interface debonding. Interface tractions increase with coating thickness with higher normal and tangential interface tractions being computed for thicker coating at all stent

deployment levels. This suggests that the use of a thinner coating could prevent coating debonding.

At a low level of stent deployment ($\Sigma_a = 0.0063$) (Figure 6-9(a)), the peak normal traction at the top of the arch (x/R = 0) is greater than the peak tangential traction at the bottom of the arch (x/R = π/2) for the thicker coatings ($h_1/R = 0.2; h_1/R = 0.5$). However, the peak tangential traction at the bottom of the arch is similar in magnitude to the peak normal traction at the top of the arch for the thinner coating ($h_1/R = 0.05$) with $|T/E_c| \approx 1.25$ x 10^{-4}.

At medium stent deployment ($\Sigma_a = 0.236$) (Figure 6-9(b)), the peak normal traction computed at the top of the arch (x/R = 0) again exceeds the peak tangential traction at the bottom of the arch (x/R = π/2) except for the case of the thinner coating ($h_1/R = 0.05$), where the computed peak tangential tractions are marginally greater.

At high stent deployment ($\Sigma_a = 0.737$) (Figure 6-9(c)), the peak tangential traction computed at the bottom of the arch exceeds the peak normal traction at the top of the arch for all coating thicknesses. At this level of stent deployment, instead of normal traction reducing monotonically from the top of the arch towards the bottom of the arch along the arch interface ($0 \leq$ x/R $\leq \pi$/2), as seen in Figure 6-9(a) and (b), an increase in normal traction is computed along the interface from the top of the arch (x/R = 0) to x/R = 1.05 and x/R = 0.82 for coating thicknesses of $h_1/R = 0.05$, and 0.2 respectively. A marginal increase in normal traction is also computed for the thickest coating ($h_1/R = 0.5$) from the top of the arch (x/R = 0) to x/R = 0.28 before reducing towards the bottom of the arch. Therefore, at a high level of stent deployment, the location of maximum normal traction is computed further from the top of the arch as coating thickness reduces. Additionally, tangential traction along the strut also increases with coating thickness.

A small degree of coating compression is computed for coating thicknesses of $h_1/R = 0.05$ and $h_1/R = 0.2$ at a low level of stent deployment (Figure 6-9(a)) along the stent strut ($x/R > \pi/2$) with no compression computed for the thickest coating. Minor coating compression is computed along the stent strut for all coating thicknesses at medium stent deployment (Figure 6-9(b)). At a high level of deployment, in the case of the thinnest coating ($h_1/R = 0.05$), maximum normal compression ($T/E_c \approx -4.8\,E-4$) is computed in the region of the bottom of the arch at $x/R = 1.9$. Maximum normal compression is computed further along the stent strut, at $x/R = 2.2$ and 2.5 for the thicker coatings of $h_1/R = 0.2$ and 0.5 respectively. Again, it is worth noting that the cohesive zone formulation correctly penalises mixed-mode coating over-closure along the stent struts.

6.3.1.5. *Influence of Mode I to Mode II Interface Strength Ratio on Coating Delamination at Finite Deformation*

In Section 6.3.1.2, it was demonstrated that the magnitude of interface strength can significantly influence the location and mode of initial coating debonding and subsequent coating delamination pattern, where the normal and tangential interface strength are assumed to be equal ($\sigma_{max} = \tau_{max}$). It is next demonstrated, for the same stent geometry ($L/R = 2\,, h_1/R = 0.2\,, h_2/R = 1$), that the ratio of tangential to normal interface strength also dramatically influences the initial delamination location at the stent-coating interface. Specifically, it is assumed that the interface is significantly stronger in the tangential direction than in the normal direction ($\tau_{max} = 5\sigma_{max}$) so that mode II initiation is prevented at the bottom of the arch. Additionally, a high interface strength of $\sigma_{max}/E_c = 0.019$ is assumed so that delamination initiates at a reasonably high stent deployment level ($\Sigma_a = 0.358$). Figure 6-10(b) shows the computed normal traction along the arch interface at the point of debonding initiation. Clearly, the peak normal interface traction does not occur at the top of the arch. Rather, it occurs at $x/R = 0.19$. Consequently, coating delamination

initiates at $x/R = 0.19$. The mode of debonding is close to mode I, as highlighted by the arrows in Figure 6-10(c), as tangential tractions are extremely low at this point. Following initiation at $x/R = 0.19$, debonding propagates along the interface. It should be noted that the location of debonding initiation depends on the stent deployment level at the point of initiation, which is determined by the interface strength. For example, if the interface strength was increased to $\sigma_{max}/E_c = 0.02$, it is suggested by Figure 6-9(c) that debonding would initiate at a deployment level of $\Sigma_a \approx 0.737$ at a point farther from the top of the arch ($x/R \approx 0.82$).

Figure 6-10 illustrates that the magnitude of σ_{max} dictates the deployment level and hence the location of delamination, when τ_{max} is sufficiently high to prevent mode II initiation at the bottom of the arch. From the non-debonding tractions presented in Figure 6-9, it can be seen that coating thickness also dictates the deployment level and location of debonding initiation. Figure 6-10(d) demonstrates that for a coating thickness of $h_1/R = 0.05$ and an interface strength of σ_{max}/E_c=0.00455 debonding initiates quite far from the top of the arch ($x/R = 0.4$) (once again, $\tau_{max} = 5\sigma_{max}$ so that mode II initiation is prevented at the bottom of the arch). Comparison of the debonding initiation for the thin coating shown in Figure 6-10(d) to the debonding initiation for the thick coating shown in Figure 6-10(c) highlights the following important point: When the mode I interface strength (σ_{max}) is sufficiently high so that debonding initiates at a high level of stent deployment, the thickness of the coating will strongly influence the location of debonding initiation. This finding is relevant when the mode II interface strength is sufficiently high so that mode II initiation is prevented at the bottom of the arch. The relevance of this finding is underlined by several experimental studies that report mode II interface strengths that are significantly higher that the mode I interface strength (Cao and Evans, 1989; Thouless, 1990; Chai and Liechti, 1992; O'Dowd et al., 1992).

6.3.1.6. *Effect of Stent Thickness*

In this section the effect of stent thickness on stent-coating interface tractions is investigated, assuming a constant coating thickness, strut length and stent-coating

stiffness ratio for all simulations. Analyses presented in previous sections assume a stent thickness of $h_2/R = 1$, based on typical dimensions of commercially available stents. In Figure 6-11, three additional stent thicknesses are considered: $h_2/R = 5$ (significantly thicker than typical commercially available stent designs); $h_2/R = 0.5$ (significantly thinner than typical commercially available stent designs; $h_2/R = 0.1$ (unconventionally thin stent: In this case, the coating is twice as thick as the stent). The investigation of stent thickness on stent-coating interface traction is particularly relevant given recent clinical studies that suggest that thinner stent struts lead to reduced rates of restenosis (Kastrati et al., 2001; Turco et al., 2008).

Figure 6-11 shows the computed normal (T_n) and tangential(T_t) tractions at the stent-coating interface for the three aforementioned stent thicknesses. At a low level of stent deployment $(\Sigma_a = 0.017)$ (Figure 6-11(a)) interface tractions generally increase with stent thickness. However, a 10 fold increase in stent thickness from $h_2/R = 0.5$ to $h_2/R = 5$ results in only a ~2 fold increase in peak normal traction at the top of the arch. Peak normal tractions at the top of the arch $(x/R = 0)$ are greater than the peak tangential tractions at the bottom of the arch $(x/R = \pi/2)$ for all stent thicknesses. Most notably, tangential tractions are negligible for the thinnest stent geometry $(h_2/R = 0.1)$ at a low level of deployment. Similar trends can also be observed at a medium level of stent deployment $(\Sigma_a = 0.327)$, as shown in Figure 6-11(b).

In contrast to lower stent deployment (Figure 6-11(a) and (b)), at a high level of stent deployment $(\Sigma_a = 0.831)$ (Figure 6-11(c)) peak tangential tractions are greater than peak normal tractions for all strut thicknesses, in particular for thinner struts $(h_2/R = 0.1, 0.5)$. Normal(T_n/E_c) and tangential (T_t/E_c) tractions are depicted in two separate figures in part (c) to enhance the visualisation of the tractions. Interestingly, for the two thinnest stents, the normal tractions decrease from the values computed for the lower deployment level considered in Figure 6-11(b). In fact, negligible normal tractions are computed for the thinnest stent design $(h_2/R = 0.1)$. Additionally, coating compression is computed in the

region of maximum tangential traction (the bottom of the arch) for the thinnest stent. Tangential tractions are significantly higher than normal tractions at the high deployment level for all stent thicknesses. The significant increase in computed tangential traction at high deployment for a thin stent ($h_2/R = 0.1$) can be attributed to its highly deformed stent configuration at this deployment magnitude, as shown in Figure 6-12(a). The excessive straightening of the stent unit cell essentially mimics a tensile test of a composite beam with normal interface stress being negligible. Such straightening is not computed for the thicker stent geometry (Figure 6-12(b)), such that normal interface tractions remain significant at high levels of deployment ($\Sigma_a = 0.831$).

6.3.1.7. *The Influence of Geometrical Parameters on Peak Tangential to Peak Normal Interface Traction Ratio*

Extending on the data presented in Figure 6-3,Figure 6-9 and Figure 6-11, Figure 6-13 shows the ratio of peak tangential to peak normal traction at the stent coating interface as a function of deployment, Σ_a. Figure 6-13(a) demonstrates that the peak normal traction exceeds the tangential traction for all strut lengths at a low level of deployment. It may be recalled from Chapter 4 that peak normal and tangential tractions are equal only for the deployment of an arch with no strut. At higher deployment levels ($\Sigma_a > 0.55$) tangential tractions exceed normal tractions for all strut lengths considered. Shorter struts result in a higher ratio of tangential to normal traction at such high deployment levels. However, only in the case of a very short strut ($L/R < 0.5$) does the tangential traction exceed the normal traction by a factor of two or greater.

The effect of stent thickness on peak tangential to peak normal traction ratio is shown in Figure 6-13(b). At an initial stent deployment level ($0 \le \Sigma_a \le 0.34$), peak normal tractions exceed peak tangential tractions $(T_{t,max}/T_{n,max} < 1)$ for all stent thicknesses. However, at high stent deployment ($\Sigma_a \ge 0.375$), peak tangential tractions exceed peak normal tractions $(T_{t,max}/T_{n,max} > 1)$ for all strut

thicknesses. In particular, the peak tangential traction magnitude increases very significantly relative to the peak normal traction for the thinner strut ($h_2/R = 0.1$) at finite deformation. This can be explained by the results presented in Section 6.3.1.6 where increased tangential tractions and negligible normal tractions are computed for a thin stent ($h_2/R = 0.1$) at finite deformation. From a design perspective, the results suggest that mode II delamination should be a primary concern for very thin stents. However, only for unconventionally thin struts ($h_2/R \leq 0.2$) does the tangential traction exceed the normal traction by a factor greater than four for an extremely high deployment level ($\Sigma_a \geq 0.8$).

The effect of coating thickness on peak tangential to peak normal traction ratio is shown in Figure 6-13(c). Again, normal traction exceeds tangential tractions at low levels of deployment, with tangential tractions becoming dominant at high deployment levels ($\Sigma_a \geq 0.47$) for the range of coating thicknesses considered. While higher ratios of peak tangential to peak normal traction are computed for thinner coatings, overall, this ratio is not highly sensitive to coating thickness at high deployment levels: At $\Sigma_a \approx 0.7$ a ratio of $T_{t,max}/T_{n,max} \approx 1.6$ is computed for the thickest coating ($h_1/R = 0.5$) whereas a 50 fold decrease in coating thickness to $h_1/R = 0.01$ merely increases the ratio to $T_{t,max}/T_{n,max} \approx 1.85$.

Overall, Figure 6-13 demonstrates that at medium to high levels of stent deployment the ratio of peak tangential to peak normal interface traction is increased for shorter stent struts, thinner stents and thinner coatings. However, only for stent geometries with extremely short struts, or for extremely thin stents does the peak tangential traction exceed the peak normal traction by a factor greater than three. The importance of this factor from a stent design viewpoint is highly dependent on the ratio of mode II to mode I fracture toughness. Experimental studies have reported mode II fracture toughness values that are significantly higher that the mode I values for epoxy-plexiglass interfaces (Hutchinson and Suo, 1992) and polymer-steel interfaces (Cao and Evans, 1989; Thouless, 1990; Chai and Liechti, 1992; O'Dowd et al., 1992). Mixed-mode experimentation should be performed on stent-coating interfaces to determine the

ratio of mode II to mode I fracture toughness. If this ratio exceeds the ratios of peak tractions reported in Figure 6-13 then mode I delamination at high deployment levels should be a primary design consideration. If, on the other hand, mode II fracture toughness is found to be similar to or less than the mode I fracture toughness for a stent-coating interface, then mode II initiation at the bottom of the arch at high deployment levels should be a primary design consideration. SEM images of coating delamination suggest that mode I delamination in the region of a stent arch is a common mechanism of coating debonding for several commercially available stents (Otsuka et al., 2007; Levy et al., 2009; Basalus and von Birgelen, 2010). However, it should be noted that mode II initiation is more difficult to detect using visual/SEM inspection.

6.3.2. Elastic-Plastic Stent

In this section, the influence of stent plasticity on computed interface tractions is investigated. Plastic deformation is required for the correct functionality of a metallic balloon expandable stent. Plastic strains of 30-50% are developed in the region of the arch while the diameter of the stent increases by a factor of 3-5 during balloon deployment (McGarry et al., 2004). Typically, elastic recoil results in a 2-5% reduction in deployed diameter following balloon removal.

6.3.2.1. Analysis of Interface Tractions Without Coating Debonding

A high interface strength is assumed for all simulations presented in this section so that the distribution of tangential and normal tractions can be examined in the absence of interface debonding. Interface tractions are analysed for the reference stent thickness ($h_2/R = 1$) in Sections 6.3.2.1.1-6.3.2.1.3. An initial analysis of stent plasticity is provided in Section 6.3.2.1.1. In Section 6.3.2.1.2, computed interface tractions are presented for a range of yield stresses. Interface tractions are presented for a range of stent strain hardening moduli ($E_h = 2, 20$ and 200 MPa) and coating stiffnesses in Section 6.3.2.1.3. Additionally, interface tractions are presented for range of stent strain hardening moduli and coating stiffnesses for a thin stent ($h_2/R = 0.1$) and a thick stent ($h_2/R = 2$) in Section 6.3.2.1.4 and Section 6.3.2.1.5 respectively.

Coatings are modelled as elastic materials with two Young's moduli being considered $(E_c = 20MPa, 200MPa)$, based on the stiffness range of commercially available polymer coatings (Antony et al., 2003; Yung and Cooper, 1998). In all cases, coating thickness $(h_1/R = 0.2)$ and strut length $(L/R = 2)$ are based on the reference stent geometry. A Young's modulus (E_s) of 200GPa, yield stress (σ_y) of 200MPa and Poisson's ratio (ν) of 0.3 is chosen for the elastic-plastic stent material (representative of 316L stainless steel) unless otherwise stated.

6.3.2.1.1. *Initial Analysis of Stent Plasticity (Reference Stent Geometry, $h_2/R = 1$)*

In Figure 6-14(a) the computed stress distribution for a plastically deforming stent is plotted on the deformed geometry at a medium level of stent deployment ($\Sigma_a = 0.245$). Results for a corresponding elastic stent, in which yielding of the stent material does not occur, are shown in Figure 6-14(b) for comparison. The stress state in the plastically deforming stent is dramatically different to that for the elastic stent, as expected. Plasticity results in significant deformation of the arch, with very low stresses computed in the struts. Significantly higher stresses are computed for the elastic stent throughout the entire stent geometry, and not just in the arch region. The equivalent plastic strain distribution is shown in Figure 6-14(c), illustrating a significant plastic zone in the arch with a peak equivalent plastic strain of ~0.2 being computed at the top of the arch.

Stress and equivalent plastic strain distributions are shown in Figure 6-15 when the stent deployment is increased to $\Sigma_a = 0.759$. At this level of deployment significant differences in the deformed geometry between the plastically deforming stent and the elastic stent are evident. Stent plasticity dramatically influences the computed stress distribution, not just in the stent but also in the coating. A localised region of high coating stress at the top of the arch is computed for the plastically deforming stent. Additionally, the arch region undergoes significant plastic deformation, with the region at the top of the arch becoming very straight with a peak equivalent plastic strain of ~0.46 being

computed. Such highly localised deformation in the arch region results in reduced rotation and stretching of the stent struts in comparison to the elastic stent.

Figure 6-16 shows the normal and tangential interface tractions for the elastic-plastic stent (shown in Figure 6-14) at a deployment level of $\Sigma_a = 0.245$. Tractions computed for the elastic stent (also shown in Figure 6-14) are also reproduced for comparison. For the elastic-plastic stent, the onset of plastic yielding in the arch occurs at a deployment level of $\Sigma_a = 0.007$, hence, as illustrated in Figure 6-14(c), significant plastic deformation has already occurred in the arch at the deployment levels considered in Figure 6-16(a).

Clearly plastic deformation of the stent material has a significant influence on computed interface tractions. In Figure 6-16(a) at a deployment of level of $\Sigma_a = 0.245$ the peak tangential traction is computed at $x/R = 0.49$ and is significantly higher than computed peak normal tractions. Local maxima are computed for normal traction at the top of the arch ($x/R = 0$) and at $x/R = 0.72$, both of which exceed the corresponding elastic solution. Additionally, a local minimum in normal traction is computed at $x/R = 0.37$. The computed tractions for the elastic-plastic stent are very different to the computed tractions for an elastic stent (also shown in Figure 6-16 for comparison) where a monotonic sinusoidal decrease in normal traction is computed from the top to the bottom of the arch, with similar magnitudes of peak normal and tangential traction computed.

Further deployment of the plastically deforming stent to $\Sigma_a = 0.759$ results in a reduction of normal traction at the top of the arch ($x/R = 0$) to a negligible value ($|T/E_s| \approx 1 \text{x} 10^{-6}$) as shown in Figure 6-16(b). In fact, negative normal tractions (indicating compression of the coating into the stent surface) are computed from $0.075 \leq x/R \leq 0.26$. This reduction in normal traction at the top of the arch results from a straightening of the arch in this region due to significant plastic deformation, as shown in Figure 6-15(c). Complex normal traction distribution is

again computed along the arch interface with a local minimum in normal traction computed at $x/R = 0.94$ and two local maxima in normal traction computed at $x/R = 0.5$ and 1.135 near the bottom of the arch. Again, peak tangential traction is computed away from the bottom of the arch $(x/R = \pi/2)$ at $x/R = 0.94$. Clearly, this pattern of normal and tangential traction is very different to the elastic solution, also shown for comparison.

6.3.2.1.2. *Influence of Yield Stress (Reference Stent Geometry, $h_2/R = 1$)*

Figure 6-17 reveals the influence of yield stress on the computed normal (T_n) and tangential (T_t) tractions at the stent-coating interface. It is shown that yield stress (σ_y) dramatically influences the computed interface tractions, particularly at high levels of stent deployment. Three yield stresses are considered, $\sigma_y = 80\ MPa, 200MPa,$ and $600MPa,$ representative of the yield stress of biodegradable magnesium, 316L stainless steel, and cobalt chromium, respectively.

At a low level of stent deployment $(\Sigma_a = 0.056)$, peak tangential traction exceeds peak normal traction for each yield stress considered (Figure 6-17(a)). Even at this low deployment level, yielding has occurred in all three cases and the patterns of normal and tangential tractions differ significantly to those reported for elastic stents in previous sections of this chapter. Peak tangential tractions are computed close to the top of the arch at $x/R = 0.4$ with greatest tangential traction computed for $\sigma_y = 200MPa$. A minimum in normal traction is computed in all cases at $x/R = 0.36$ with coating compression (characterised by negative normal traction) computed for $\sigma_y = 200MPa$. In all cases two local maxima are computed for normal traction, one at the top of the arch $(x/R = 0)$ and one at $x/R \approx 0.6$.

At a medium level of stent deployment $(\Sigma_a = 0.303)$, the largest normal and tangential tractions are computed at the top of the arch $(x/R = 0)$ and at $x/R = 0.375$ respectively for $\sigma_y = 600MPa$ (Figure 6-17(b)). Furthermore, significant coating compression is computed for $\sigma_y = 600MPa$, from $0.26 \leq x/R \leq 0.43$.

In the case of the lower yield stresses ($\sigma_y = 80MPa$ and $200MPa$) the peak normal traction is not computed at the top of the arch and does not fluctuate very significantly along the arch interface. Yield stress has a significant influence on the location and magnitude of maximum tangential traction at this deployment level with peak tangential traction computed at $x/R = 0.85$ and $x/R = 0.57$ for $\sigma_y = 80MPa$ and $200MPa$ respectively.

At a high stent deployment ($\Sigma_a = 0.627$) similar trends in tangential traction are computed (Figure 6-17(c)). Significant coating compression is again computed for $\sigma_y = 600\ MPa$ from $0.16 \leq x/R \leq 0.47$. Interestingly, relative to Figure 6-17(b), a significant decrease in normal traction is computed at the top of the arch ($x/R = 0$), for $\sigma_y = 200\ MPa$, with negligible normal traction computed ($T/E_s \sim 1.7x10^{-6}$). Similar to Figure 6-17(b), largest normal and tangential tractions traction are still computed for $\sigma_y = 600\ MPa$ at the top of the arch ($x/R = 0$) and at $x/R = 0.37$ respectively.

6.3.2.1.3. *Influence of Stent Strain Hardening and Coating Stiffness on Interface Tractions (Reference Stent Geometry,$h_2/R = 1$)*

The computed normal (T_n) and tangential (T_t) tractions for a range of stent strain hardening moduli and coating stiffnesses (E_c) of $200MPa$ and 20MPa are shown in Figure 6-18 and Figure 6-19 respectively. Three strain hardening moduli are considered ($E_h = 2,20$ and $200MPa$).

At a low stent deployment, the influence of coating stiffness on interface traction distributions is not significant (Figure 6-18(a) and Figure 6-19(a)). At medium stent deployment ($\Sigma_a = 0.255$), it is evident that both the coating stiffness and strain hardening moduli significantly affect the computed traction distributions (Figure 6-18(b) and Figure 6-19(b)). The greatest normal and tangential tractions are computed for $E_h = 2MPa$ at this level of stent deployment for both coating stiffnesses. Significant coating compression is computed in the case of the more compliant coating for $E_h = 2MPa$ and $20MPa$ at $x/R \approx 0.35$ (Figure 6-19(b))

while only a small degree of coating compression is predicted for $E_h = 2MPa$ for the stiffer coating. For $E_h = 2MPa$ and $20MPa$, peak tangential tractions are computed in the same location along the stent-coating interface as minimum normal tractions at $x/R \approx 0.4$.

At a high level of stent deployment $(\Sigma_a = 0.5)$, the greatest normal and tangential tractions are again computed for $E_h = 2MPa$ for both coating stiffnesses. However, it should be noted that the location of peak normal traction is computed at $x/R \approx 0.9$ in the case of the stiffer coating while a significant reduction in normal traction is computed at the top of the arch for $E_h = 2MPa$ and $20MPa$. This reduction in normal traction can be attributed to the high concentration of plastic deformation in the region of the top of the arch at high stent deployment as discussed in Section 6.3.2.1. While significant coating compression is computed for $E_h = 2MPa$ and $20MPa$ in the case of the more compliant coating, no coating compression is predicted for a stiffer coating at this deployment magnitude. Lowest tangential tractions are computed for the stiffer strain hardening modulus $(E_h = 200MPa)$ for $x/R < 0.7$.

In summary the following should be noted: (i) At high deployment, strain hardening moduli have a significant influence on computed interface tractions for both coating stiffnesses considered $(E_c = 20$ and $200MPa)$. (ii) Coating stiffness has a significant influence on the computed patterns of interface traction at high stent deployment. For a more compliant coating, peak normal tractions are computed at the top of the arch $(x/R = 0)$ for $E_h = 2MPa$ and $20MPa$, whereas negligible normal tractions are computed for $E_h = 2MPa$ and $20MPa$ at $x/R = 0$ when a stiff coating $(E_c = 200MPa)$ is considered; (iii) No coating compression is computed for the stiffer coating at high stent deployment whereas significant coating compression is computed at high deployment for $E_c = 20MPa$ $(E_h = 2MPa$ and $20MPa)$.

6.3.2.1.4. *Influence of Stent Strain Hardening and Coating Stiffness on Interface Tractions (Thin Stent Geometry, $h_2/R = 0.1$)*

Normal (T_n) and tangential (T_t) tractions computed for a thin stent geometry $(h_2/R = 0.1)$ for a range of stent strain hardening moduli are shown in Figure 6-20 for a coating of stiffness, $E_c = 200MPa$, and in Figure 6-21 for a coating of stiffness, $E_c = 20MPa$.

Coating stiffness has a significant influence on the computed distribution of interface tractions for a thin stent geometry at low stent deployment. This is in contrast to the computed results for the reference stent at low deployment, where the distribution of interface traction is largely unaffected by coating stiffness, traction magnitudes merely scaling with coating stiffness (Figure 6-18 (a), Figure 6-19(a)). As shown in Figure 6-20(a), in the case of the stiffer coating ($E_c = 200MPa$) maximum normal tractions are computed at the top of the arch $(x/R = 0)$ at low stent deployment $(\Sigma_a = 0.139)$ with normal tractions reducing towards the bottom of the arch $(x/R = \pi/2)$. Peak tangential tractions are computed away from the bottom of the arch at $x/R = 0.9$. Peak interface normal tractions are slightly higher than tangential tractions at this level of stent deployment. In contrast, for a more compliant coating ($E_c = 20MPa$), for the same level of deployment, peak normal tractions are computed away from the top of the arch at $x/R = 0.5$ (Figure 6-21(a)). Additionally, peak tangential tractions are computed much closer to the top of the arch at $x/R = 0.3$ for the more compliant coating.

The patterns of computed traction for a medium deployment level $(\Sigma_a = 0.371)$ are reasonably similar to those computed for a low deployment level (Figure 6-20(b)) for a stiffer coating ($E_c = 200MPa$). However, in the case of a more compliant coating ($E_c = 20MPa$), a normal traction local minimum is computed at $x/R = 0.6$ while maximum normal tractions are computed at $x/R = 0.9$ for all strain hardening moduli considered. Additionally, little variation in normal traction is computed along the interface where $x/R < 0.4$.

At high stent deployment ($\Sigma_a = 0.558$), for $E_c = 200MPa$ (Figure 6-20(c)), peak tangential tractions are computed close to the bottom of the arch ($x/R = 1.7$). In contrast to computed normal interface tractions at lower levels of stent deployment (Figure 6-20(a) and (b)), peak normal tractions are also computed towards the bottom of the arch ($x/R = 1.4$). Additionally, coating compression is computed in the region of the bottom of the arch ($x/R = 1.7$) for all strain hardening moduli considered. A second normal traction maximum is computed along the strut at $x/R = 2.1$. For a more compliant coating ($E_c = 20MPa$), maximum tangential tractions are computed at $x/R = 1.2$ (Figure 6-21(c)). Similar normal traction behaviour is computed to that observed at lower deployment (Figure 6-21(b)). A maximum in normal traction is computed towards the bottom of the arch at $x/R \approx 1.3$. In contrast to the stiffer coating ($E_c = 200MPa$), no coating compression is computed along the interface.

In summary the following should be noted for a thin stent geometry: (i) Strain hardening moduli do not influence computed interface tractions when a stiff coating ($E_c = 200MPa$) is considered, and weakly influence computed tractions in the case of a more compliant coating ($E_c = 20MPa$) when $E_h = 200MPa$ (ii) Coating stiffness has a significant influence on the computed patterns of interface traction with coating compression computed only in the case of the stiffer coating ($E_c = 200MPa$) at high stent deployment.

6.3.2.1.5. *Influence of Stent Strain Hardening and Coating Stiffness on Interface Tractions (Thick Stent Geometry, $h_2/R = 2$)*

The computed normal (T_n) and tangential (T_t) tractions for a thick stent geometry ($h_2/R = 2$) for a range of stent strain hardening moduli are shown in Figure 6-22 for a coating of stiffness $E_c = 200MPa$, and in Figure 6-23 for a coating of stiffness $E_c = 20MPa$. Firstly it should be noted that, for a given strain hardening modulus and for a given deployment level, very similar distributions of normal and tangential tractions are computed for the stiff ($E_c = 200MPa$) and the compliant ($E_c = 20MPa$)coatings, with the traction magnitudes scaling with

coating stiffness. Additionally, similar traction distributions are computed for stent hardening moduli of 2MPa and 20MPa, with a significantly different distribution being computed for the highest hardening modulus$(E_h = 200MPa)$. Comparison of Figure 6-22(a) with Figure 6-18(a) reveals that at a low deployment level the normal and tangential traction distributions are similar for the thick stent geometry $(h_2/R = 2)$ and for reference stent thickness $(h_2/R = 1)$. However, Figure 6-22(c) reveals that at a high deployment level normal tractions at the top of the arch $(x/R = 0)$ do not vanish for the thicker stent, in contrast to the reference stent geometry (Figure 6-18 (c)). This results from the fact that for the thicker stent $(h_2/R = 2)$, the top of the arch remains curved at high deployment levels.

6.3.2.2. *Analysis of Coating Debonding Mechanisms*

Section 6.3.2.1 illustrates that complex distributions of normal and tangential traction are computed along the stent-coating interface when plastic deformation of the stent is considered. The ratio of normal to tangential traction at any point on the interface is shown to be highly dependent on the deployment level in addition to the stent-coating geometry and material properties. While delamination is not considered in the previously presented analyses of plastically deforming stents, with a very strong stiff interface being assumed, the complex traction distributions suggest that if a lower interface strength is considered the location and mode mixity of debonding will be highly dependent on several factors, including deployment level at debonding initiation, ratio of normal to tangential interface strength, in addition to stent geometric and material parameters. In this section, three examples of diverse coating debonding patterns during deployment of a plastically deforming stent are presented. The first two examples entail debonding of a coating from a thin stent geometry $(h_2/R = 0.1)$ (Section 6.3.2.2.1-6.3.2.2.2) and the third example entails the debonding of a coating from a thick stent geometry $(h_2/R = 2)$ (Section 6.3.2.2.3). These debonding simulations do not represent an exhaustive collection of all possible debonding patterns. They merely serve to illustrate some possible debonding patterns that emerge as a result of the

complex distributions of normal and tangential tractions at the stent–coating interface in the case of a plastically deforming stent.

6.3.2.2.1. Coating Debonding Behaviour for a Thin Stent $(h_2/R = 0.1)$

For the thin stent geometry $(h_2/R = 0.1)$ it can be seen in Figure 6-21(b) that tangential tractions are dominant at an arch deployment of $\Sigma_a = 0.371$ for $E_c = 20MPa$ and $E_h = 200MPa$ with peak tangential tractions computed at $x/R = 0.75$. In the first sample simulation of coating debonding, presented in Figure 6-24, interface strengths are chosen so that coating debonding initiates at this level of deployment. Furthermore, it is assumed that mode I and mode II interface strengths are equal $(\sigma_{max}/E_s = \tau_{max}/E_s = 2\text{x}10^{-6})$. The coating node located at $x/R = 0.75$ is highlighted in Figure 6-24(b). Corresponding interface tractions are depicted in Figure 6-24(c) and (d). Mixed-mode delamination is initially computed at the interface at $x/R = 0.75$ as shown in Figure 6-24(b). As stent deployment increases, a predominantly mode II delamination is computed at the interface with $T_t/\tau_{max} \approx 0.914$ (Figure 6-24(c)). Due to the dominant mode II type delamination, the resistance to normal separation is significantly reduced with computed peak normal traction of $T_n/\sigma_{max} \approx 0.46$ (Figure 6-24 (d)). No coating compression is computed at the stent-coating interface. Following full coating delamination at $x/R = 0.75$, mixed-mode delamination progresses along the interface with pure mode I coating delamination eventually occurring at the top of the arch $(x/R = 0)$. Further progression of coating delamination at higher stent deployment is shown in Figure 6-24(e). However, at the level of stent deployment shown in Figure 6-24(e), pure mode I delamination has not yet occurred.

In the second sample simulation of coating debonding from a plastically deforming stent, presented in Figure 6-25, geometric and material parameters are identical to those used for Figure 6-24.   In this case, however, the prescribed mode II interaction strength is increased relative to the mode I interaction strength $(\tau_{max} = 5\sigma_{max})$.   A normal interface strength of $\sigma_{max}/E_s = 1.045\text{x}10^{-6}$ is used so that coating debonding again initiates at an arch

deployment of $\Sigma_a = 0.371$. The computed normal and tangential tractions for the highlighted coating node (Figure 6-25(b)) located at $x/R = 0.9$ (location of initial coating debonding) are shown in Figure 6-25(c) and (d). Similar to the previous example, no coating compression is computed at the stent-coating interface during stent deployment. However, as stent deployment increases predominantly mode I coating delamination is computed at the highlighted coating node. This predominantly mode I delamination is shown in Figure 6-25(c) with a peak normal traction of $T_n/\sigma_{max} \approx 0.96$ being computed at the point of debonding initiation. Resistance to tangential separation is reduced with $T_t/\tau_{max} \approx 0.42$, due to the predominantly normal separation at this point. Further progression of coating delamination following increased stent deployment is shown in Figure 6-25(e) where coating delamination is computed all along the arch, including pure mode I delamination at the top of the arch.

6.3.2.2.2. *Coating Debonding Behaviour for a Thick Stent* $(h_2/R = 2)$

The complex interface traction distributions shown in Figure 6-22, at an arch deployment of $\Sigma_a = 0.101$, for a thick elastic-plastic stent $(h_2/R = 2, E_c = 200MPa, E_h = 2MPa)$ can lead to complex patterns of coating delamination. Peak tangential traction and maximum coating compression are computed in the same location along the interface $(x/R = 0.6)$.

In the final sample simulation of coating debonding from a plastically deforming stent a thick stent geometry $(h_2/R = 2)$ is considered, with $E_c = 200MPa, E_h = 2MPa$. The interface strengths are reduced so that debonding initiates at a deployment level of $\Sigma_a = 0.101$, assuming that the normal and tangential interface strengths are equal $(\sigma_{max}/E_s = \tau_{max}/E_s = 4.8 \times 10^{-5})$. The peak tangential traction is computed at $x/R \approx 0.6$ at this low level of deployment as indicated by the non-debonding simulation of Figure 6-22. Additionally, in this region the coating is compressed normally into the stent surface, hence nodes in this region undergo mixed-mode over-closure. The node at $x/R = 0.6$ is highlighted in Figure 6-26(a). The insert shown in Figure 6-26(b) illustrates the mixed-mode over-closure of the node. It can be noted that while the

coating is compressed into the stent surface the magnitude of over-closure is very small, as the cohesive zone framework penalises such mixed-mode over-closure (characterised by the computation of a rapid increase in negative normal tractions highlighted by red arrow in Figure 6-26(e)). The displacement vector of the node is predominantly in the tangential direction. The tangential traction is sufficiently large to cause a predominantly mode II delamination at the interface. At the point of debonding initiation the peak tangential traction is higher than τ_{max} due to compression at the interface ($T_t/\tau_{max} \approx 1.04$) (Figure 6-26(c)). Full debonding then occurs as tangential tractions reduce to zero. During the debonding of the node highlighted in Figure 6-26, the compression of the node into the stent surface is reversed and the node separates from the stent in a mixed-mode fashion. Resistance to normal separation is significantly reduced due to the earlier initiation of tangential debonding, with peak normal traction of $T_n/\sigma_{max} \approx 0.17$ being computed (Figure 6-26(e)). The insert in Figure 6-26(d) illustrates the final mixed-mode separation of the node from the stent surface. Further progression of coating delamination at higher stent deployment is shown in Figure 6-26(f) where coating delamination is computed all along the arch, including pure mode I debonding at the top of the arch ($x/R = 0$). The insert in Figure 6-26(f) shows that the stent surface at the interface becomes highly non-uniform at finite deformation. Such non-uniform undulations on the surface of a plastically deforming stent surface underlie the complex patterns of interface traction and mixed-mode delamination illustrated in this study.

6.4. Concluding Remarks

In this study the influence of geometrical parameters (strut length, coating stiffness, stent thickness) and material properties and on the stress state at a stent-coating interface is investigated. The influence of finite deformation on interface tractions is examined, significantly advancing on the analytical analyses of Parry and McGarry (2012) which were limited to infinitesimal elastic deformation with an idealised coupling between the arch and the strut via linear and torsional springs. Most importantly, the present chapter also considers the affect of stent plasticity on interface tractions and provides simulations of coating debonding.

This study represents a significant advancement on the study of Hopkins et al. (2010) where interface traction distributions were not examined and only mode I debonding initiation at the top of the arch was considered. The current study demonstrates that the mechanisms of coating debonding are complex and depend on numerous stent, coating and interface design criteria. The full complexity of coating debonding for elastic and elastic-plastic stents is uncovered. Several recent experimental studies using scanning electron microscopy have reported extensive delamination of polymer coatings from the stent surface during deployment (Otsuka et al., 2007; Levy et al., 2009; Basalus and von Birgelen, 2010; Wiemer et al., 2010). Numerous studies have suggested that coating damage may play a significant role in late stent thrombosis, following the use of drug-eluting stents (Hoffmann et al., 2002; Wang et al., 2002; Balakrishnan et al., 2005; Iakovou et al., 2005; Otsuka et al., 2007; Luscher et al., 2007; Daemen et al., 2007; Levy et al., 2009). It is reasonable to suggest that some of the other clinical implications associated with coating damage may include micro-embolism formation, impaired drug delivery and obstruction of blood flow. Therefore, computational analyses and reliable design techniques are required in order to determine the limits relating to the safe implantation of coated stents. The analyses presented in this chapter provide valuable insight into the stress-state at the stent-coating interface as a function of the stent design parameters. Such analyses allow for a more reliable assessment of the limits relating to safe implantation of coated stents.

Key implications for the improved design of coated stents uncovered in this chapter are summarised below.

An **elastic stent** is first considered in order to develop an initial fundamental understanding of interface traction behaviour. A number of important findings are revealed for an elastic stent:

- Firstly, it is important to note that peak normal tractions exceed peak tangential tractions at low stent deployment whereas peak tangential tractions exceed peak normal tractions at high stent deployment (finite deformation) when interface tractions are assessed for a range of strut lengths, stent thicknesses and coating thicknesses. Since stents typically undergo high deployment levels, mode II coating debonding initiation at the bottom of the arch should be carefully considered.

- The implementation of a longer stent strut effects an increased rotation at the base of the stent arch which reduces the tangential tractions and increases the normal tractions along the stent-coating interface. This effect can be counteracted by using a shorter strut design.

- For a typical stent geometry, where the stent thickness is significantly greater than the coating thickness $(h_2/h_1 = 5)$, the stent-coating stiffness ratio has a relatively weak influence on the distribution of normal and tangential tractions along the interface, particularly at a high level of stent deployment. Interface tractions approximately scale with the coating stiffness, with the ratio of normal to tangential traction at a given point along on the interface being insensitive to the stent-coating stiffness ratio when $h_2/h_1 = 5$. This suggests that, for a given geometry, a more compliant Chronoflex® coating is less likely to delaminate during stent deployment than stiffer coatings such as PU-GPC (Hopkins et al., 2010).

- As expected, it is shown that interface tractions increase with coating thickness suggesting that antiproliferative drugs should be delivered via a thinner coating in order to reduce the risk of coating debonding. Commercially available stent coatings range in thickness from $10-20\mu m$ (Hopkins et al., 2010). Since interface tractions increase with increasing coating thickness, a higher bond strength must be achieved when thicker coatings are utilised.

- The influence of stent thickness on interface tractions is particularly relevant given that recent clinical studies suggest that thinner stent struts lead to reduced rates of restenosis (Kastrati et al., 2001; Turco et al., 2008). Interface tractions increase with increasing stent thickness suggesting that thinner stents should be utilised to reduce the risk of coating delamination. Increased tangential tractions and negligible normal tractions are computed for a thin stent at high stent deployment due to excessive straightening of the thin stent geometry.

- The location and mechanism of coating debonding is shown to be highly dependent on the interface strength as the ratio of peak tangential to peak normal traction is highly dependent on deployment level. The location of debonding initiation is also shown to be highly dependent on geometrical parameters with initial debonding computed further away from the top of the arch when a thinner coating is utilised and the mode II interface strength is increased relative to the mode I interface strength.

In the second section of this study, an **elastic-plastic stent** is considered:

- Firstly, the stress distributions in the stent and coating materials and the tractions computed at the stent-coating interface are compared for an elastic and elastic-plastic stent. In contrast to an elastic stent where there is a gradual increase in normal and tangential tractions towards the top $(x/R = 0)$ and bottom $(x/R = \pi/2)$ of the arch respectively, when an

elastic-plastic stent is utilised, significant plastic deformation in the region of the arch results in the computation of significantly altered traction distributions. Specifically, at a high level of stent deployment, multiple peaks and minimums in normal traction are computed for an elastic-plastic stent with coating compression computed in the region of the top of the arch. Additionally, in contrast to the elastic stent, the peak tangential traction is computed away from the bottom of the arch with tangential tractions significantly increased when an elastic-plastic stent is utilised.

- Yield stress is shown to significantly influence the location and magnitude of peak normal and tangential interface tractions. Additionally, a high yield stress $(\sigma_y = 600\ MPa)$ is shown to promote significant coating compression at high deployment.

- Interface tractions are also presented for a range of stent strain hardening moduli and coating stiffnesses. For a typical stent thickness $(h_2/h_1 = 5)$, both coating stiffness and strain hardening moduli have a significant influence on the computed interface tractions at high stent deployment. In contrast, for a very thin stent, where the stent is half the thickness of the coating $(h_2/h_1 = 0.5)$, interface tractions are not significantly influenced by strain hardening moduli. For a thick stent $(h_2/h_1 = 10)$, for a given strain hardening modulus and for a given deployment level, very similar distributions of normal and tangential tractions are computed for the stiff $(E_c = 200MPa)$ and the compliant $(E_c = 20MPa)$ coatings, with the traction magnitudes scaling with coating stiffness.

- For a thin elastic-plastic stent $(h_2/h_1 = 0.5)$, it is demonstrated that the prescribed ratio of peak tangential to peak normal traction significantly alters the mechanism and location of initial coating debonding. A highly non-uniform stent surface is computed at the stent-coating interface for a thick elastic-plastic stent. In this case, mixed-mode coating over-closure is

computed prior to mixed-mode coating delamination, highlighting the importance of implementing a cohesive zone formulation which can appropriately penalise mixed-mode compression.

- In summary, in contrast to an elastic stent, the inclusion of an elastic-plastic stent influences both the location of peak interface tractions together with the magnitude of computed tractions. Furthermore, the location and magnitude of coating compression is significantly altered when an elastic-plastic stent is used. All of these factors significantly influence the location and mode of coating debonding and can lead to complex coating debonding mechanisms such as those shown in Section 6.3.2.2.

6.5. References

Antony, P., Puskas, J. E.&Kontopoulou, M. (2003) Investigation of the rheological and mechanical properties of a polystyrene-polyisobutylene-polystyrene triblock copolymer and its blends with polystyrene. *Polymer Engineering & Science,* 43**,** 243-253.

Babapulle, M. N.&Eisenberg, M. J. (2002) Coated stents for the prevention of restenosis: Part I. *Circulation,* 106**,** 2734-2740.

Balakrishnan, B., Tzafriri, A. R., Seifert, P., Groothuis, A., Rogers, C.&Edelman, E. R. (2005) Strut position, blood flow, and drug deposition. *Circulation,* 111**,** 2958-2965.

Balossino, R., Gervaso, F., Migliavacca, F.&Dubini, G. (2008) Effects of different stent designs on local hemodynamics in stented arteries. *Journal of Biomechanics,* 41**,** 1053-1061.

Basalus, M. W. Z.&Von Birgelen, C. (2010) Benchside testing of drug-eluting stent surface and geometry. *Interv. Cardiol.,* 2**,** 159-175.

Cao, H. C.&Evans, A. G. (1989) An experimental study of the fracture resistance of bimaterial interfaces. *Mechanics of Materials,* 7**,** 295-304.

Chai, Y. S.&Liechti, K. M. (1992) Asymmetric Shielding in lnterfacial Fracture Under/n-Plane Shear. *Journal of Applied Mechanics,* 59**,** 295-304.

Daemen, J., Wenaweser, P., Tsuchida, K., Abrecht, L., Vaina, S., Morger, C., et al. (2007) Early and late coronary stent thrombosis of sirolimus-eluting and paclitaxel-eluting stents in routine clinical practice: data from a large two-institutional cohort study. *The Lancet,* 369**,** 667-678.

Edelman, E. R., Seifert, P., Groothuis, A., Morss, A., Bornstein, D.&Rogers, C. (2001) Gold-coated NIR stents in porcine coronary arteries. *Circulation,* 103**,** 429.

FDA (2012) U.S. Food and Drug Administration, date accessed 06/09/2012.

Hara, H., Nakamura, M., Palmaz, J. C.&Schwartz, R. S. (2006) Role of stent design and coatings on restenosis and thrombosis. *Advanced drug delivery reviews,* 58**,** 377-386.

Hoffmann, R., Mintz, G. S., Haager, P. K., Bozoglu, T., Grube, E., Gross, M., et al. (2002) Relation of stent design and stent surface material to subsequent in-stent intimal hyperplasia in coronary arteries determined by intravascular ultrasound. *The American journal of cardiology,* 89**,** 1360-1364.

Hopkins, C. G., McHugh, P. E.&McGarry, J. P. (2010) Computational Investigation of the Delamination of Polymer Coatings During Stent Deployment. *Annals of Biomedical Engineering,* 38**,** 2263-2273.

Hutchinson, J. W.&Suo, Z. (1992) Mixed mode cracking in layered materials. *Advances in applied mechanics,* 29**,** 191.

Iakovou, I., Schmidt, T., Bonizzoni, E., Ge, L., Sangiorgi, G. M., Stankovic, G., et al. (2005) Incidence, predictors, and outcome of thrombosis after successful implantation of drug-eluting stents. *JAMA: the journal of the American Medical Association,* 293**,** 2126-2130.

Karjalainen, P. P., Annala, A. P., Ylitalo, A., Vahlberg, T.&Airaksinen, K. E. (2010) Long-term clinical outcome with titanium-nitride-oxide-coated

stents and paclitaxel-eluting stents for coronary revascularization in an unselected population. *International journal of cardiology,* 144**,** 42-46.

Kastrati, A., Mehilli, J., Dirschinger, J., Dotzer, F., Schuhlen, H., Neumann, F. J., et al. (2001) Intracoronary stenting and angiographic results: strut thickness effect on restenosis outcome (ISAR-STEREO) trial. *Circulation,* 103**,** 2816-2821.

Kim, H. J., Moon, M. W., Kim, D. I., Lee, K. R.&Oh, K. H. (2007) Observation of the failure mechanism for diamond-like carbon film on stainless steel under tensile loading. *Scripta materialia,* 57**,** 1016-1019.

Kollum, M., Farb, A., Schreiber, R., Terfera, K., Arab, A., Geist, A., et al. (2005) Particle debris from a nanoporous stent coating obscures potential antiproliferative effects of tacrolimus-eluting stents in a porcine model of restenosis. *Catheterization and cardiovascular interventions,* 64**,** 85-90.

Levy, Y., Mandler, D., Weinberger, J.&Domb, A. J. (2009) Evaluation of drug-eluting stents' coating durability-"Clinical and regulatory implications. *Journal of Biomedical Materials Research Part B: Applied Biomaterials,* 91**,** 441-451.

Luscher, T. F., Steffel, J., Eberli, F. R., Joner, M., Nakazawa, G., Tanner, F. C., et al. (2007) Drug-Eluting Stent and Coronary Thrombosis Biological Mechanisms and Clinical Implications. *Circulation,* 115**,** 1051-1058.

McGarry, J. P., O'Donnell, B. P., McHugh, P. E.&McGarry, J. G. (2004) Analysis of the mechanical performance of a cardiovascular stent design based on micromechanical modelling. *Computational Materials Science,* 31**,** 421-438.

O'Dowd, N. P., Stout, M. G.&Shih, C. F. (1992) Fracture toughness of alumina-niobium interfaces: experiments and analyses. *Philosophical Magazine A,* 66**,** 1037-1064.

Otsuka, Y., Chronos, N. A. F., Apkarian, R. P.&Robinson, K. A. (2007) Scanning electron microscopic analysis of defects in polymer coatings of three commercially available stents: comparison of BiodivYsio, Taxus and Cypher stents. *Journal of Invasive Cardiology,* 19**,** 71.

Parry, G.&McGarry, P. (2012) An analytical solution for the stress state at stent-coating interfaces. *Journal of the Mechanical Behavior of Biomedical Materials,* 10**,** 183-196.

Regar, E., Sianos, G.&Serruys, P. W. (2001) Stent development and local drug delivery. *British medical bulletin,* 59**,** 227.

Thouless, M. D. (1990) Fracture of a model interface under mixed-mode loading. *Acta metallurgica et materialia,* 38**,** 1135-1140.

Turco, M. A., Ormiston, J. A., Popma, J. J., Hall, J. J., Mann, T., Cannon, L. A., et al. (2008) Reduced Risk of Restenosis in Small Vessels and Reduced Risk of Myocardial Infarction in Long Lesions With the New Thin-Strut TAXUS Liberté Stent: 1-Year Results From the TAXUS ATLAS Program. *JACC: Cardiovascular Interventions,* 1**,** 699-709.

Uurto, I., Mikkonen, J., Kotsar, A., Juuti, H., Leppiniemi, J., Isotalo, T., et al. (2011) Preclinical Evaluation of New Drug-Eluting Biodegradable Poly-D/L-lactic Acid Vascular Stent.

Wang, F., Stouffer, G. A., Waxman, S.&Uretsky, B. F. (2002) Late coronary stent thrombosis: early vs. late stent thrombosis in the stent era. *Catheterization and cardiovascular interventions,* 55**,** 142-147.

Wiemer, M., Butz, T., Schmidt, W., Schmitz, K. P., Horstkotte, D.&Langer, C. (2010) Scanning electron microscopic analysis of different drug eluting stents after failed implantation: from nearly undamaged to major damaged polymers. *Catheterization and cardiovascular interventions,* 75**,** 905-911.

Windecker, S., Mayer, I., De Pasquale, G., Maier, W., Dirsch, O., De Groot, P., et al. (2001) Stent coating with titanium-nitride-oxide for reduction of neointimal hyperplasia. *Circulation,* 104**,** 928-933.

Yung, L. Y. L.&Cooper, S. L. (1998) Neutrophil adhesion on phosphorylcholine-containing polyurethanes. *Biomaterials,* 19**,** 31-40.

6.6. Tables and Figures

Figure 6-1: An example of a cardiovascular stent architecture consisting of a series of repeating interconnected unit cells (highlighted), where each unit cell consists of an arch connected to straight struts (Parry and McGarry, 2012).
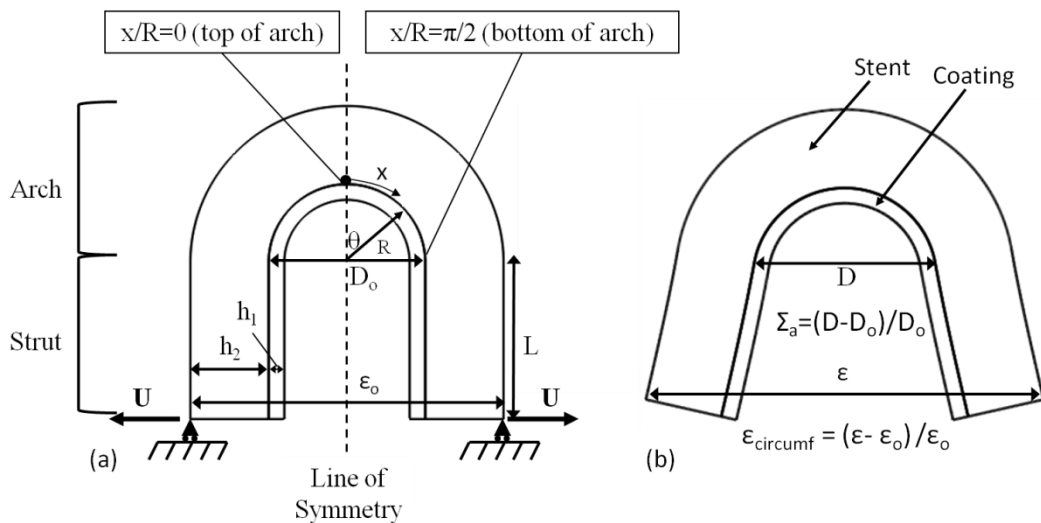

Figure 6-2: (a) Geometry of the stent and stent coating in the initial configuration. Boundary conditions at the base of the stent struts and applied displacements, U, are highlighted at the strut ends. The radial distance to the stent-coating interface, R, and the distance along the stent-coating interface from the top of the arch, x, is also indicated. The arch and strut sections are also highlighted. The coating thickness, h_1, stent thickness, h_2 and strut length, L, are also shown. (b) Geometry of a deployed stent configuration with the stent and coating materials highlighted. The arch deployment (Σ_a) and circumferential strain ($\varepsilon_{circumf}$) are also defined, with ε_o and D_o defined in (a).
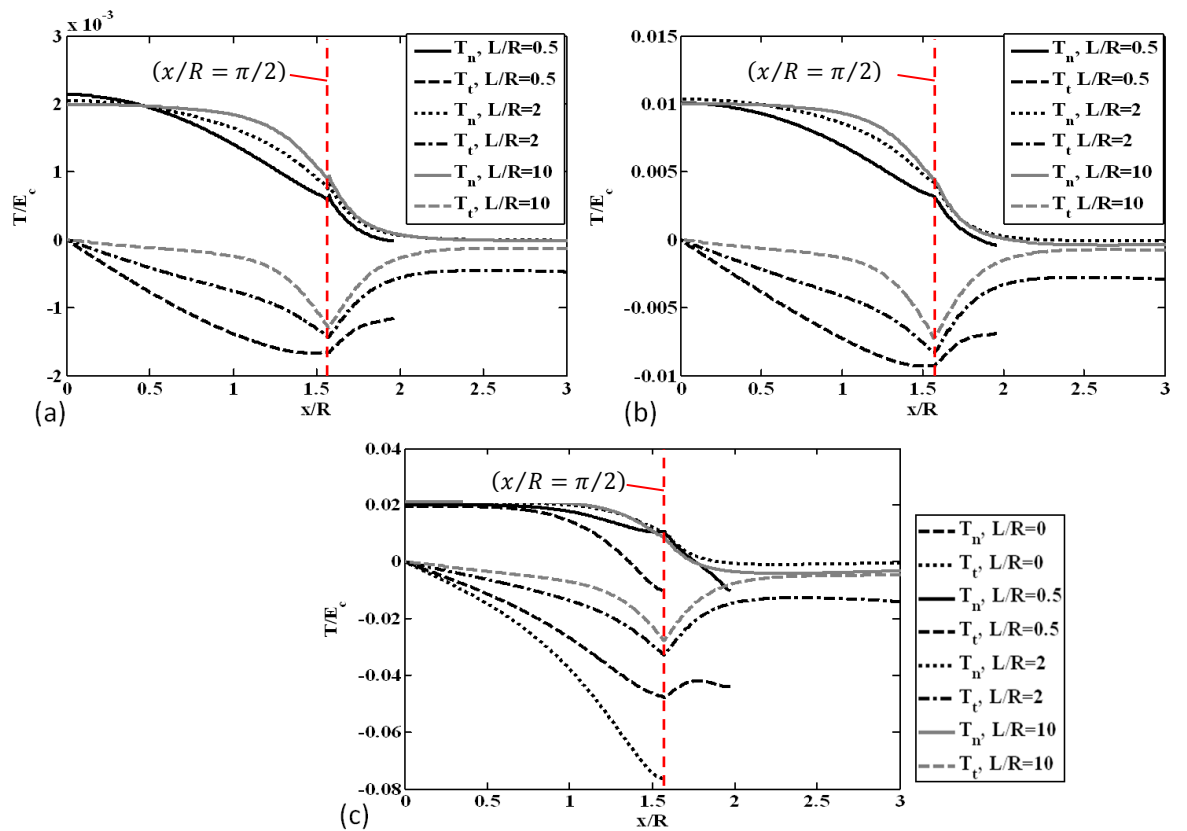
Figure 6-3: Computed normal (T_n) and tangential (T_t) tractions along the stent-coating interface for a range of strut lengths for (a) low deployment $(\Sigma_a = 0.024)$ (b) medium deployment $(\Sigma_a = 0.134)$ and (c) high deployment $(\Sigma_a = 0.608)$. At low deployment, normal tractions increase from the bottom of the arch $(x/R = \pi/2)$ to the top of the arch $(x/R = 0)$ while tangential tractions increase from the top of the arch $(x/R = 0)$ to the bottom of the arch $(x/R = \pi/2)$. $E_c = 200$GPa, $E_s = 500$GPa, $\sigma_{max}/E_c = \tau_{max}/E_c = 2$, $h_1/R = 0.2$, $h_2/R = 1$.
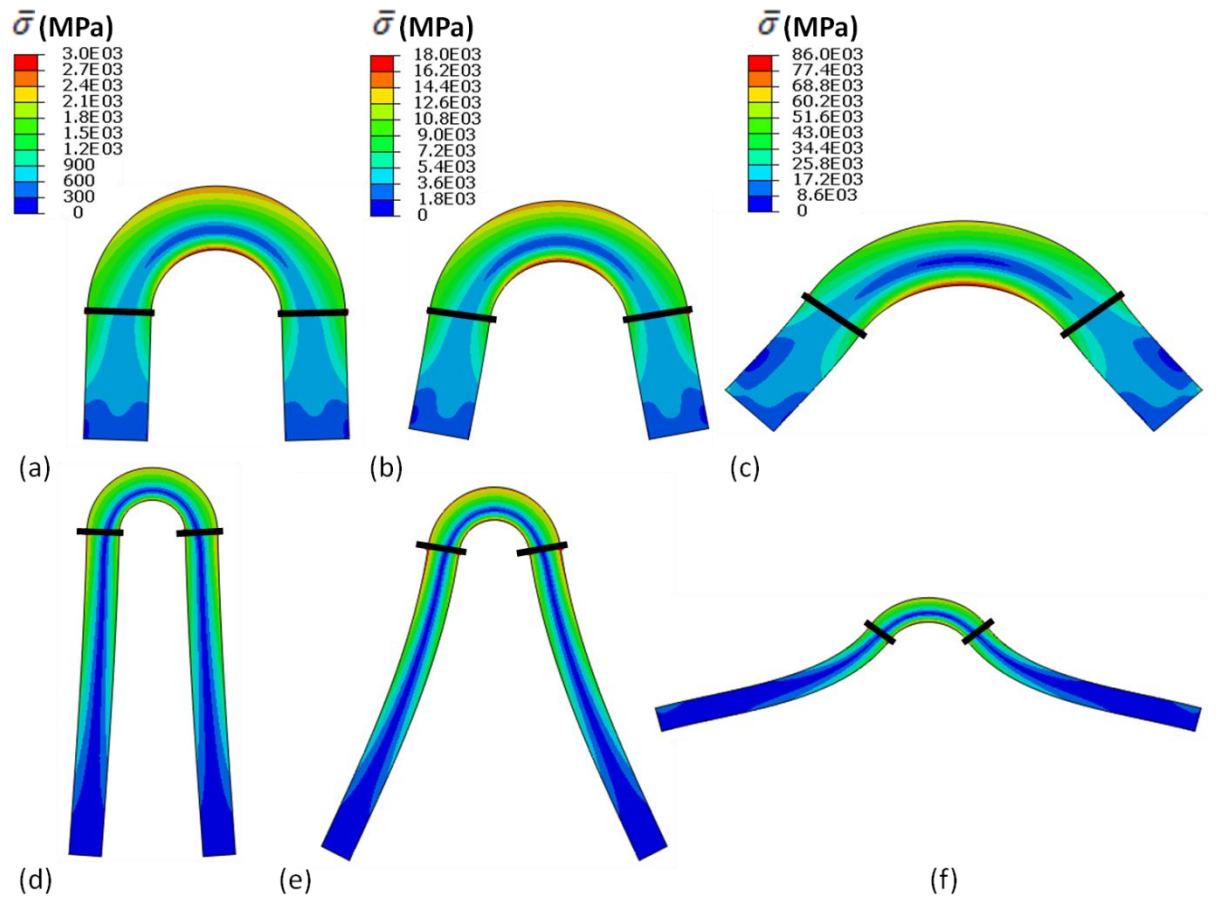
Figure 6-4: von Mises stress ($\bar{\bar{\sigma}}$) distribution for deformed stent geometries at low ($\Sigma_a = 0.024$), medium ($\Sigma_a = 0.134$) and high ($\Sigma_a = 0.608$) deployment for (a)-(c) $L/R = 2$ and (d)-(f) $L/R = 10$. The black line at base of the arch is included to highlight the increase in arch rotation with increasing stent deployment.
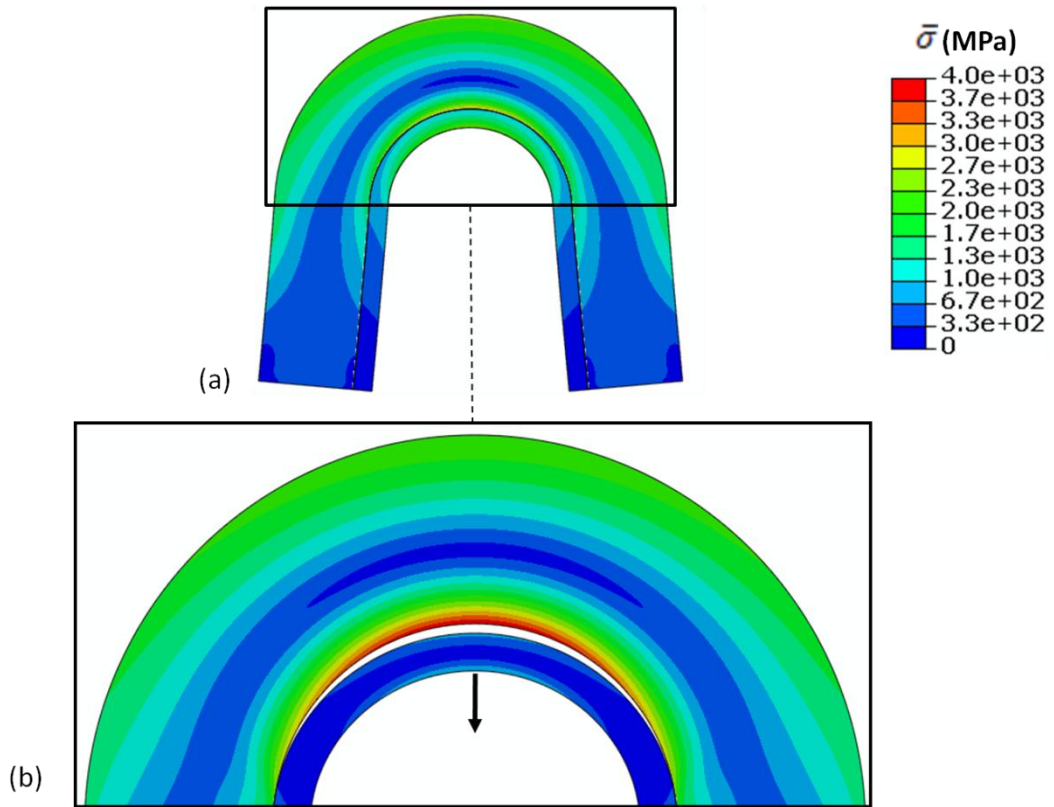
Figure 6-5: Stent and coating von Mises stress $(\bar{\sigma})$ distribution plotted on the deformed geometry for an arch deployment, Σ_a, of (a) 0.023 and (b) 0.025. Mode I coating delamination initiates at the top of the arch $(x/R = 0)$ as shown in (b). $E_c = 200\text{GPa}$, $E_s = 500\text{GPa}$, $\sigma_{max}/E_c = \tau_{max}/E_c = 0.0019$, $h_1/R = 0.2$, $h_2/R = 1$, L/R = 2. Deformation factor =3 in (b).
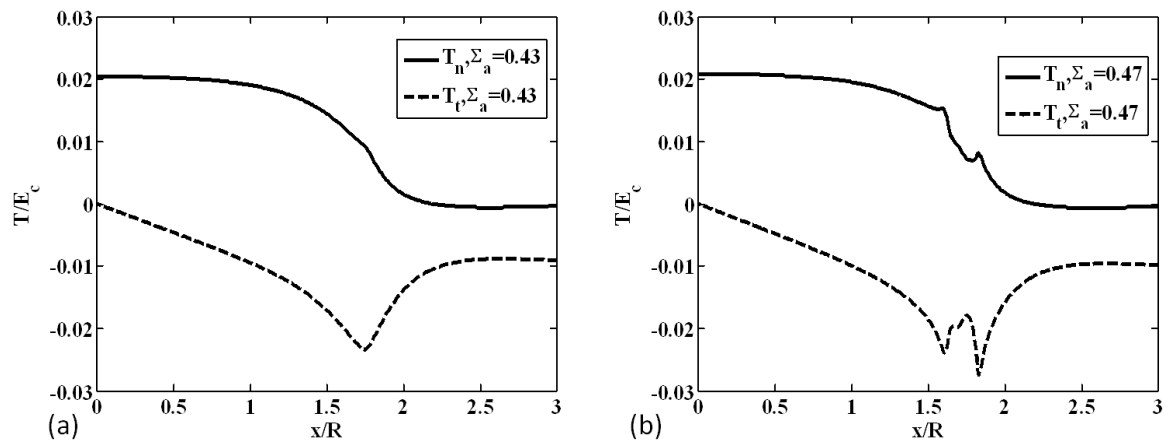
Figure 6-6: Computed interface traction (T/E_c) as a function of the distance along the stent-coating interface (x/R) for an arch deployment, Σ_a, of (a) 0.43 and (b) 0.47. Predominantly mode II coating delamination initiates at the bottom of the arch $(x/R = \pi/2)$ as indicated by the reduction in traction in (b). $E_c = 200\text{GPa}$, $E_s = 500\text{GPa}$, $\sigma_{max}/E_c = \tau_{max}/E_c = 0.026$, $h_1/R = 0.2$, $h_2/R = 1$, $L/R = 2$.
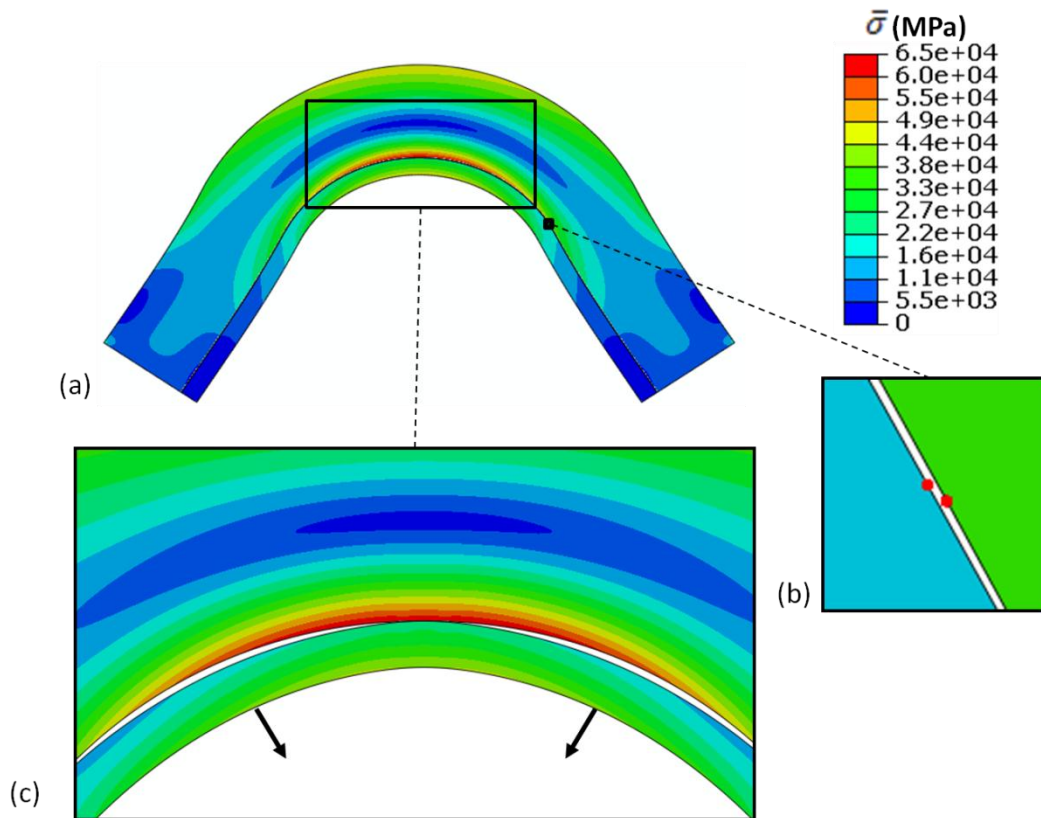
Figure 6-7: Stent and coating von Mises stress ($\bar{\sigma}$) distribution plotted on the deformed geometry for an arch deployment, Σ_a, of (a)-(b) 0.47 and (c) 0.475. Predominantly mode II coating delamination initiates at the bottom of the arch ($x/R = \pi/2$) as shown in (b). Mixed-mode coating delamination computed at higher stent deployment is shown in (c). $E_c = 200\text{GPa}$, $E_s = 500\text{GPa}$, $\sigma_{max}/E_c = \tau_{max}/E_c = 0.026$, $h_1/R = 0.2$, $h_2/R = 1$, $L/R = 2$. Deformation factor =3 for (c).
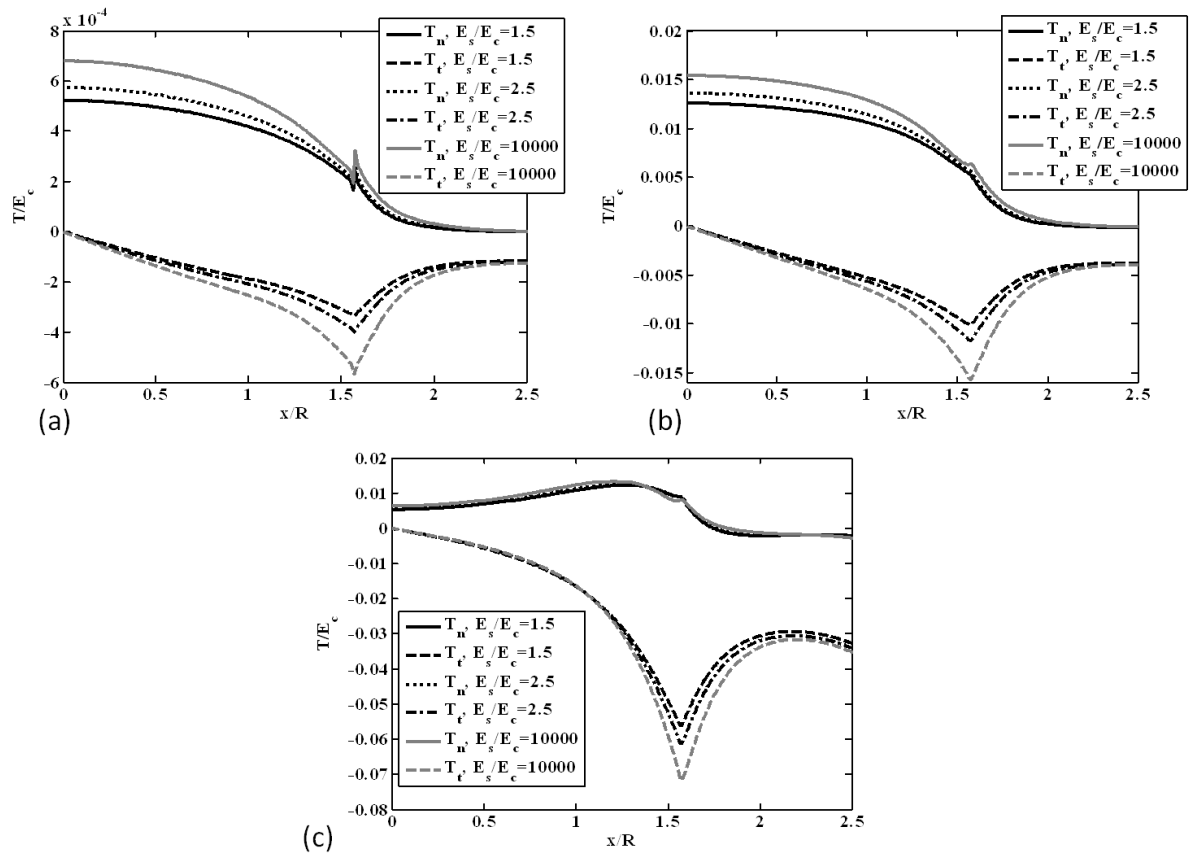
Figure 6-8: Computed normal (T_n) and tangential (T_t) tractions along the stent-coating interface for a range of stent to coating stiffness ratios (E_s/E_c) for (a) low deployment $(\Sigma_a = 0.0065)$ (b) medium deployment $(\Sigma_a = 0.202)$ and (c) high deployment $(\Sigma_a = 1.27)$. $E_c = 200\text{GPa}$, $\sigma_{max}/E_c = \tau_{max}/E_c = 2$, $h_1/R = 0.2$, $h_2/R = 1$, $L/R = 2$.
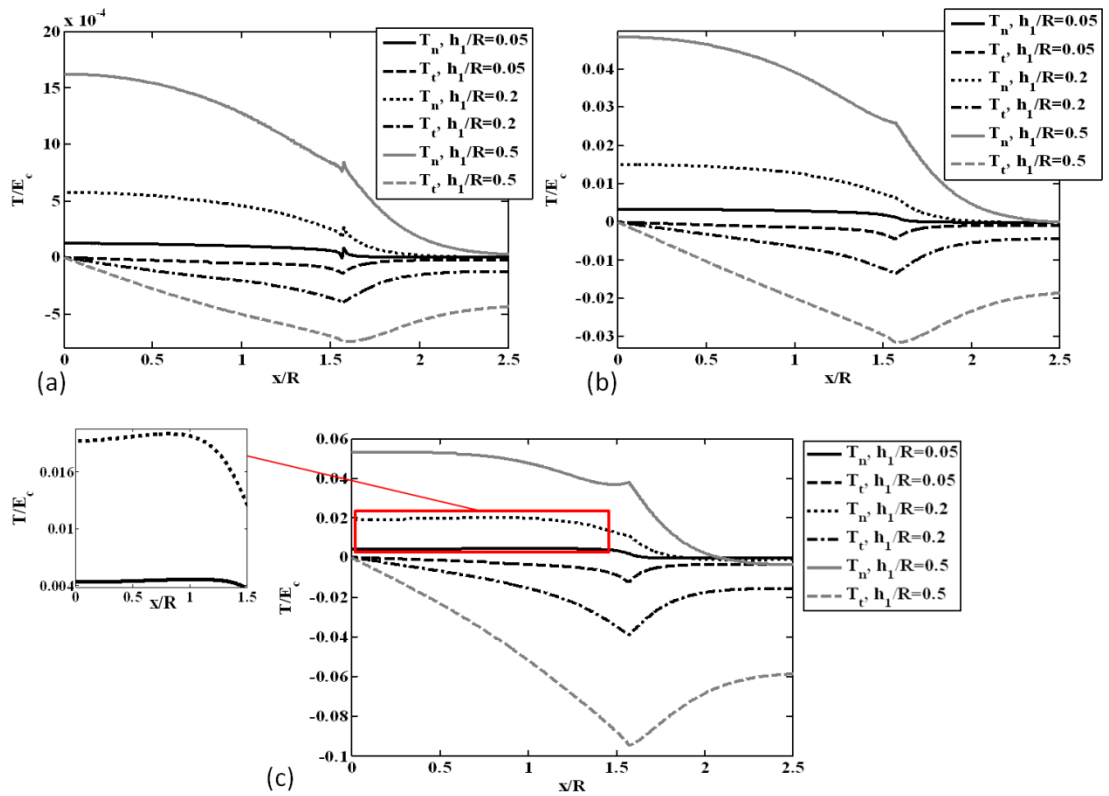
Figure 6-9: Computed normal (T_n) and tangential (T_t) tractions along the stent-coating interface for a range of coating thicknesses for (a) low deployment $(\Sigma_a = 0.0063)$ (b) medium deployment $(\Sigma_a = 0.236)$ and (c) high deployment $(\Sigma_a = 0.737)$. The insert in (c) shows increasing normal tractions away from the top of the arch $(x/R = 0)$ for $h_1/R = 0.05$ and 0.2. $E_c = 200\text{GPa}$, $E_s = 500\text{GPa}$, $\sigma_{max}/E_c = \tau_{max}/E_c = 2$, $h_2/R = 1$, $\text{L}/R = 2$.
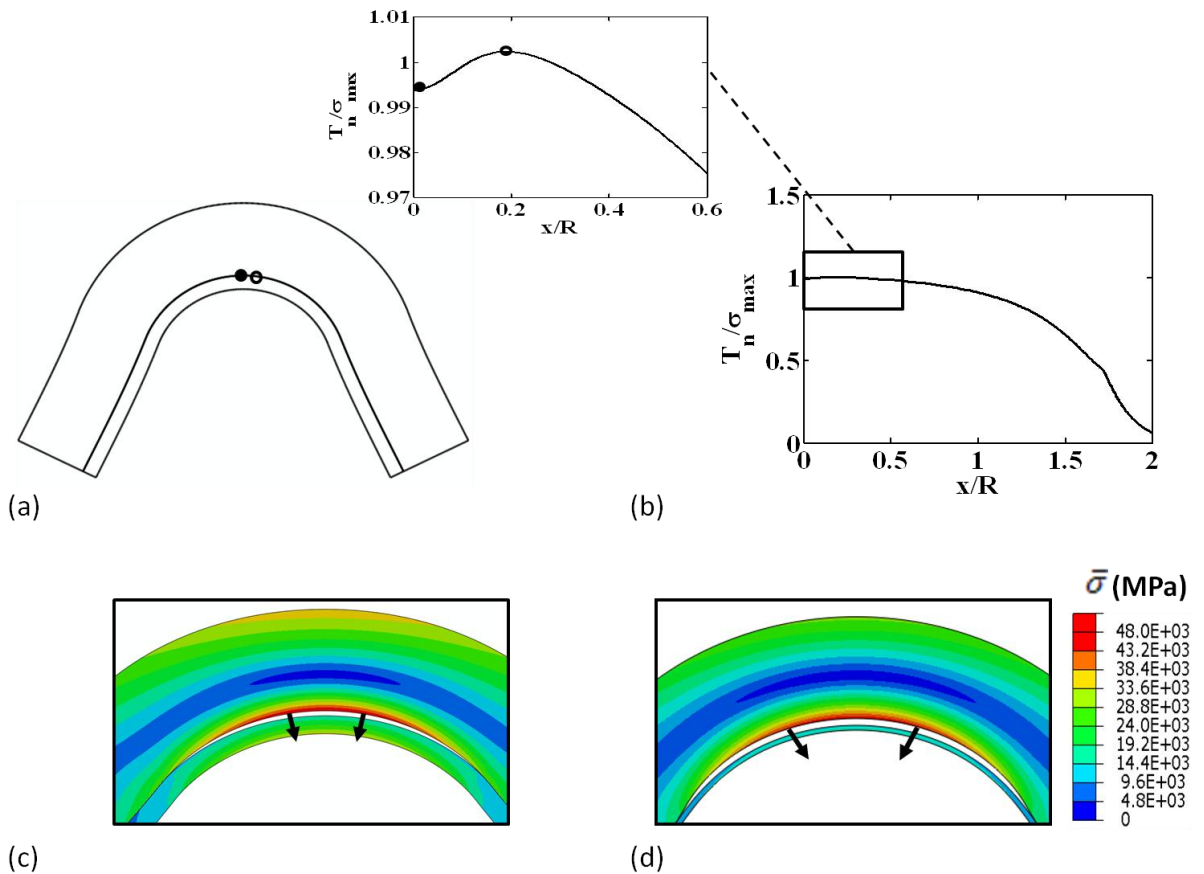
Figure 6-10: (a) Stent and coating geometry highlighting two points along the stent-coating interface for an arch deployment, $\Sigma_a = 0.358$ (b) Normalised normal traction T_n/σ_{max} computed along the stent-coating interface as a function of the distance along the stent-coating interface (x/R). Insert highlights the computed increase in normal traction from $0 \leq x/R \leq 0.19$. (c) von Mises $(\bar{\sigma})$ stress distribution plotted on the deformed geometry. Predominantly mode I coating delamination initiates at $x/R \approx 0.19$ for $h_1/R = 0.2$ $(\sigma_{max}/E_c = 0.019)$. (d) Predominantly mode I coating delamination initiates at $x/R \approx 0.4$ for $h_1/R = 0.05$ $(\sigma_{max}/E_c = 0.00455)$. $E_c = 200\text{GPa}, E_s = 500\text{GPa}, \tau_{max} = 5\sigma_{max}, h_2/R = 1, \text{L}/R = 2$.
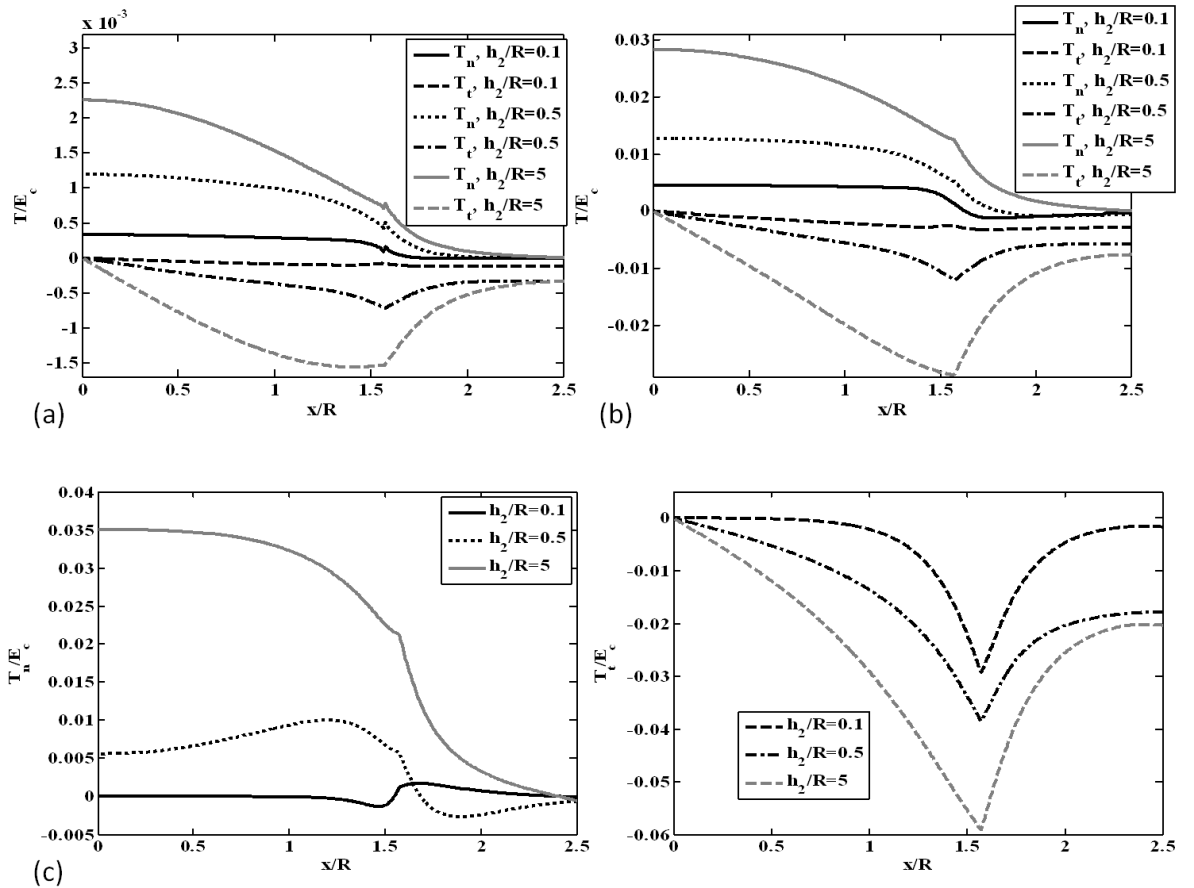
Figure 6-11: Computed normal (T_n) and tangential (T_t) tractions along the stent-coating interface for a range of strut thicknesses for (a) low deployment $(\Sigma_a = 0.017)$ (b) medium deployment $(\Sigma_a = 0.327)$ and (c) high deployment $(\Sigma_a = 0.831)$. Computed normal (T_n/E_c) and tangential (T_t/E_c) tractions are shown separately in (c) to enhance the visualisation. $E_c = 200\text{GPa}$, $E_s = 500\text{GPa}$, $\sigma_{max}/E_c = \tau_{max}/E_c = 2$, $h_1/R = 0.2$, $L/R = 2$.
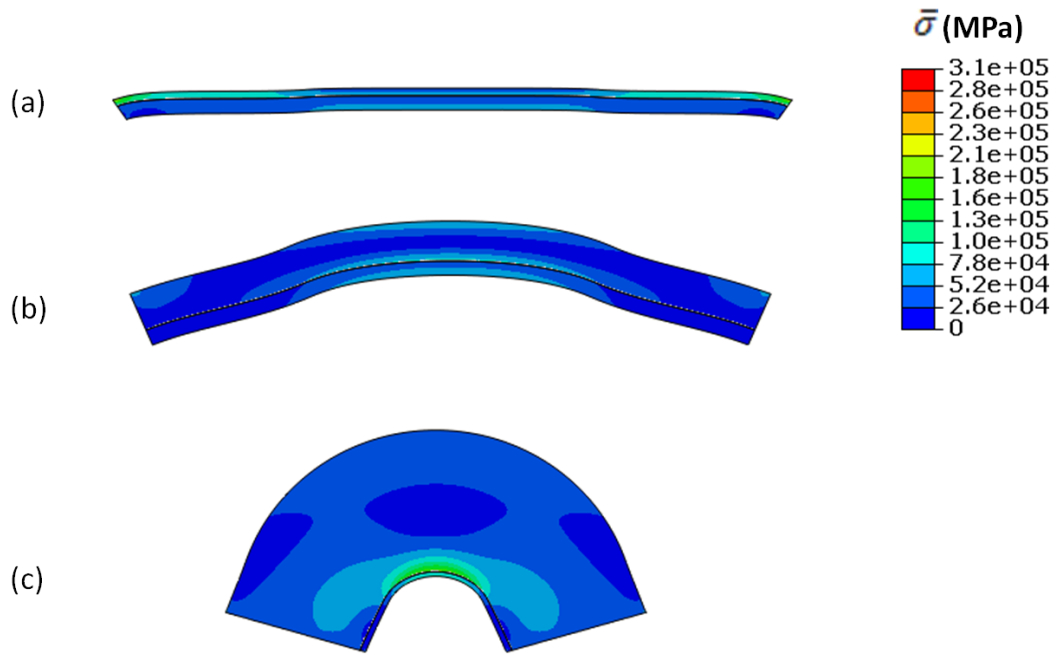
Figure 6-12: von Mises stress$(\bar{\sigma})$ distribution plotted on the deformed stent geometries at high deployment $(\Sigma_a = 0.831)$ for (a) $h_2/R = 0.1$, (b) $h_2/R = 0.5$ and (c) $h_2/R = 5$. $E_c = 200$GPa, $E_s = 500$GPa, $\sigma_{max}/E_c = \tau_{max}/E_c = 2$, $h_1/R = 0.2$, L/R = 2.
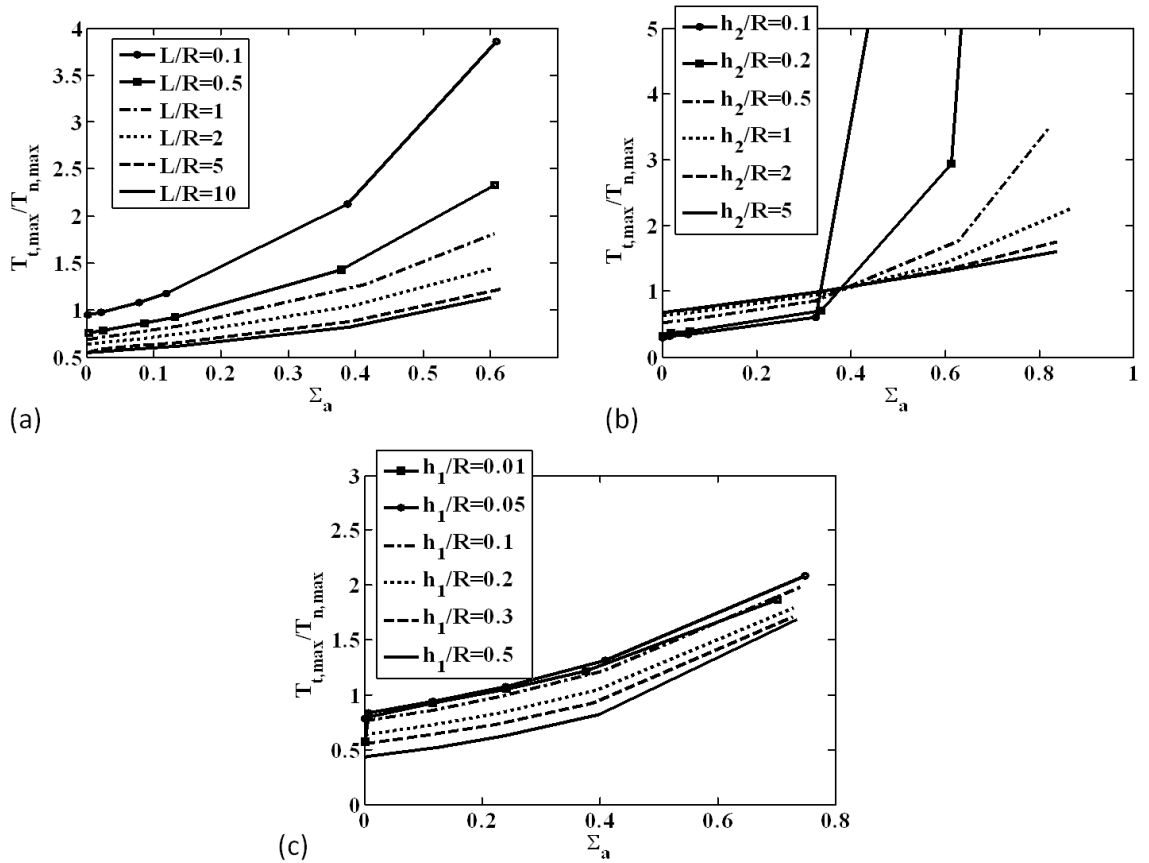
Figure 6-13: Ratio of maximum tangential to normal traction $\left(T_{t,max}/T_{n,max}\right)$ as a function of arch deployment (Σ_a) for (a) a range of strut lengths $\left(h_1/R = 0.2\,, h_2/R = 1\right)$ (b) a range of substrate thicknesses $\left(L/R = 2, h_1/R = 0.2\right)$ and (c) a range of coating thicknesses $\left(L/R = 2, h_2/R = 1\right)$. $E_c = 200GPa, E_s = 500GPa\ \sigma_{max}/E_c = \tau_{max}/E_c = 2$.

Figure 6-14: von Mises stress distribution($\bar{\sigma}$) plotted on the deformed geometry for (a) elastic-plastic stent and elastic coating and (b) elastic stent and elastic coating. (c) Equivalent plastic strain (PEEQ) distribution for elastic-plastic stent and elastic coating. In all cases the arch deployment, Σ_a, = 0.245. For the elastic stent, $E_s = 200GPa$. For the elastic-plastic stent, $E_s = 200GPa$, the strain hardening modulus, E_h, = 20MPa, and yield stress, σ_y, = 200MPa. In all cases, an elastic coating ($E_c = 200MPa$) is considered. $L/R = 2$, $h_1/R = 0.2$, $h_2/R = 1$. $\sigma_{max}/E_s = \tau_{max}/E_s = 2$.
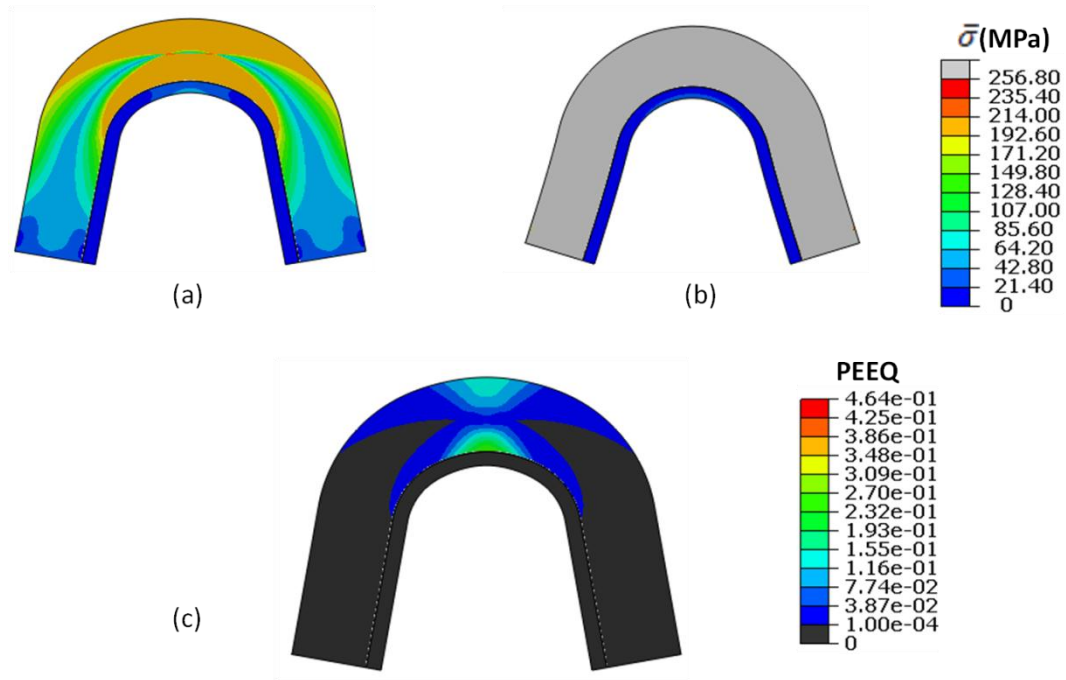
Figure 6-15: von Mises stress distribution($\bar{\sigma}$) plotted on the deformed geometry for (a) elastic-plastic stent and elastic coating and (b) elastic stent and elastic coating. (c) Equivalent plastic strain (PEEQ) distribution for elastic-plastic stent and elastic coating. In all cases the arch deployment, Σ_a, $= 0.759$. For the elastic stent, $E_s = 200GPa$. For the elastic-plastic stent, $E_s = 200GPa$, the strain hardening modulus, E_h, $= 20MPa$, and yield stress, σ_y, $= 200MPa$. In all cases, an elastic coating ($E_c = 200MPa$) is considered. $L/R = 2$, $h_1/R = 0.2$, $h_2/R = 1$. $\sigma_{max}/E_s = \tau_{max}/E_s = 2$.

(a)

(b)

Figure 6-16: Computed normal (T_n) and tangential (T_t) tractions along the stent-coating interface for an elastic stent and an elastic-plastic stent for (a) medium deployment $(\Sigma_a = 0.245)$ and (b) high deployment $(\Sigma_a = 0.759)$. For the elastic stent, $E_s = 200GPa$. For the elastic-plastic stent, $E_s = 200GPa$, the strain hardening modulus, $E_h = 20MPa$, and yield stress, $\sigma_y = 200MPa$. In all cases, an elastic coating $(E_c = 200MPa)$ is considered. $L/R = 2$, $h_1/R = 0.2$, $h_2/R = 1$. $\sigma_{max}/E_s = \tau_{max}/E_s = 2$.
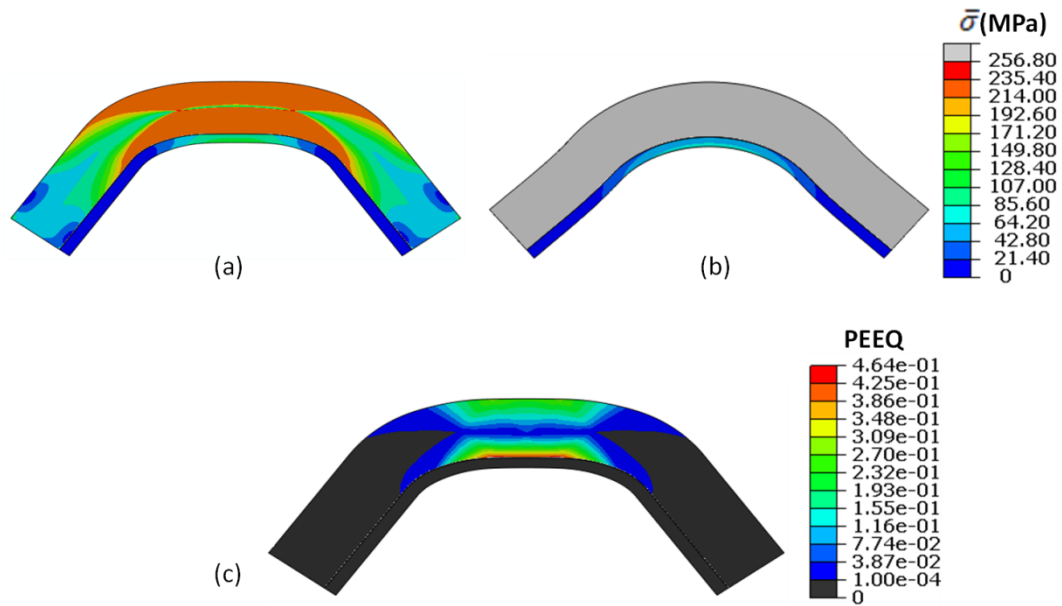
Figure 6-17: Computed normal (T_n) and tangential (T_t) tractions along the stent-coating interface for a range of yield stresses $(\sigma_y = 80MPa, 200MPa, 600MPa)$, for (a) low deployment $(\Sigma_a = 0.056)$ (b) medium deployment $(\Sigma_a = 0.303)$ and (c) high deployment $(\Sigma_a = 0.627)$. In all cases, an elastic coating $(E_c = 200MPa)$ is considered. For the elastic-plastic stent, $E_s = 200GPa$, the strain hardening modulus, $E_h = 20$MPa, and yield stress, $\sigma_y = 200$MPa. $L/R = 2$, $h_1/R = 0.2$, $h_2/R = 1$. $\sigma_{max}/E_s = \tau_{max}/E_s = 2$.

Figure 6-18: Computed normal (T_n) and tangential (T_t) tractions along the stent-coating interface for (a) low deployment ($\Sigma_a = 0.03$) (b) medium deployment ($\Sigma_a = 0.255$) and (c) high deployment ($\Sigma_a = 0.5$) for an elastic-plastic stent with the substrate thickness, $h_2/R = 1$. Three strain hardening moduli are considered for the strut ($E_h = 2, 20$ and $200 MPa$). In all cases, an elastic coating ($E_c = 200 MPa$) is considered. $h_1/R = 0.2, E_s = 200 GPa$, $L/R = 2$, $\sigma_{max}/E_s = \tau_{max}/E_s = 2$. The strut yield stress $(\sigma_y) = 200 MPa$.
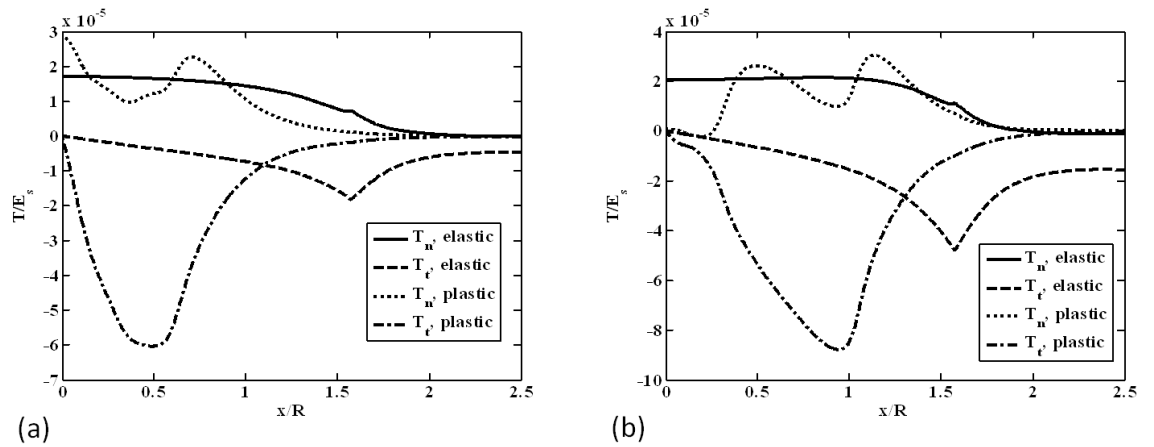
Figure 6-19: Computed normal (T_n) and tangential (T_t) tractions along the stent-coating interface for (a) low deployment $(\Sigma_a = 0.03)$ (b) medium deployment $(\Sigma_a = 0.255)$ and (c) high deployment $(\Sigma_a = 0.5)$ for an elastic-plastic stent with the substrate thickness, $h_2/R = 1$. Three strain hardening moduli are considered for the strut $(E_h = 2, 20$ and $200 MPa)$. In all cases, an elastic coating $(E_c = 20 MPa)$ is considered. $h_1/R = 0.2, E_s = 200 GPa$, $L/R = 2$, $\sigma_{max}/E_s = \tau_{max}/E_s = 2$. The strut yield stress $(\sigma_y) = 200 MPa$.
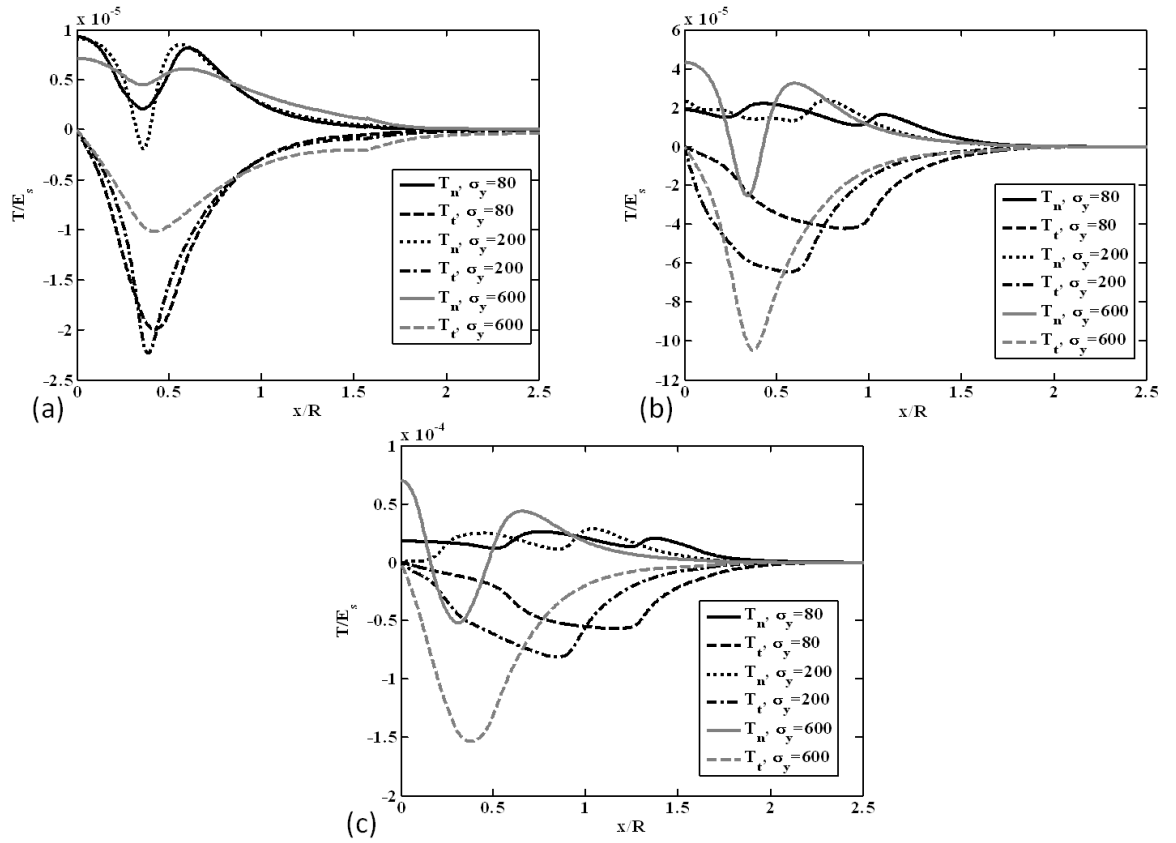
Figure 6-20: Computed normal (T_n) and tangential (T_t) tractions along the stent-coating interface for (a) low deployment $(\Sigma_a = 0.139)$ (b) medium deployment $(\Sigma_a = 0.371)$ and (c) high deployment $(\Sigma_a = 0.558)$ for an elastic-plastic stent with the substrate thickness, $h_2/R = 0.1$. Three strain hardening moduli are considered for the strut $(E_h = 2, 20 \text{ and } 200 MPa)$. In all cases, an elastic coating $(E_c = 200 MPa)$ is considered. $h_1/R = 0.2, E_s = 200 GPa, L/R = 2, \sigma_{max}/E_s = \tau_{max}/E_s = 2$. The strut yield stress $(\sigma_y) = 200 MPa$.
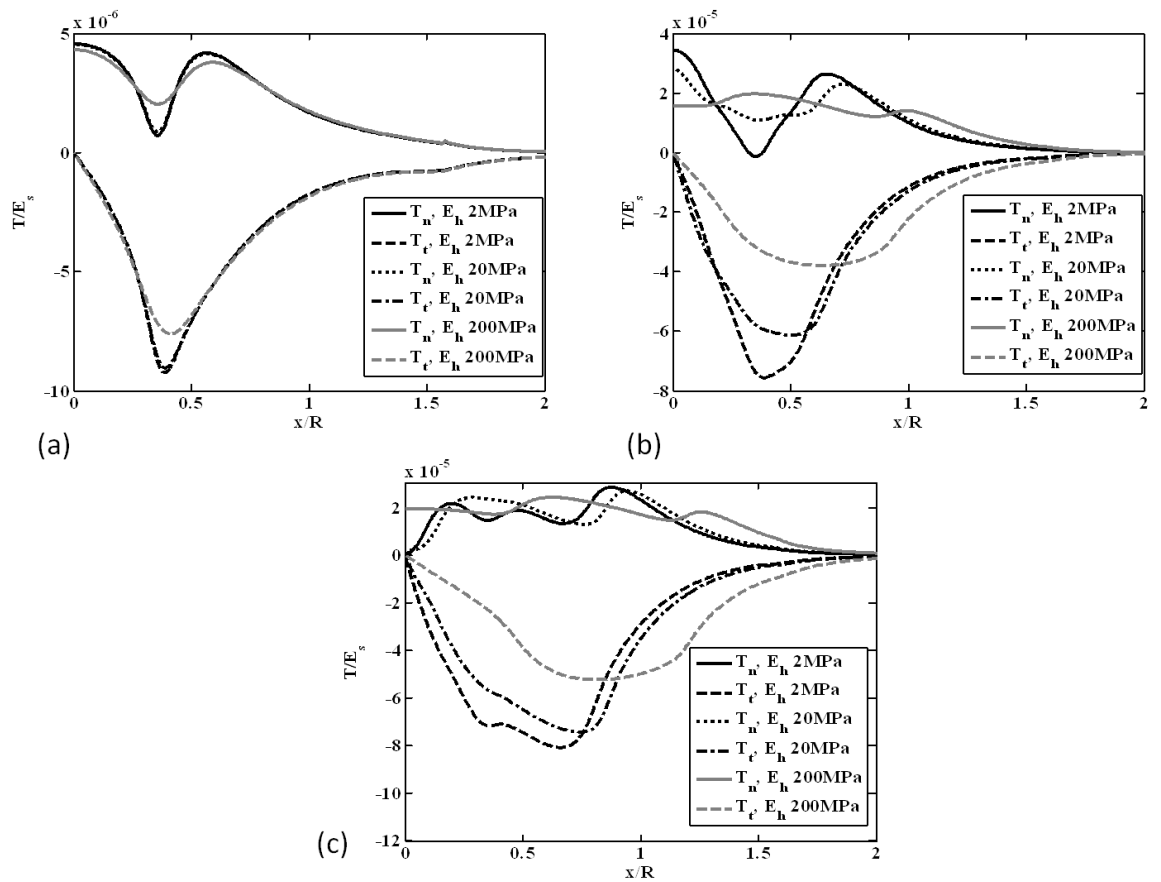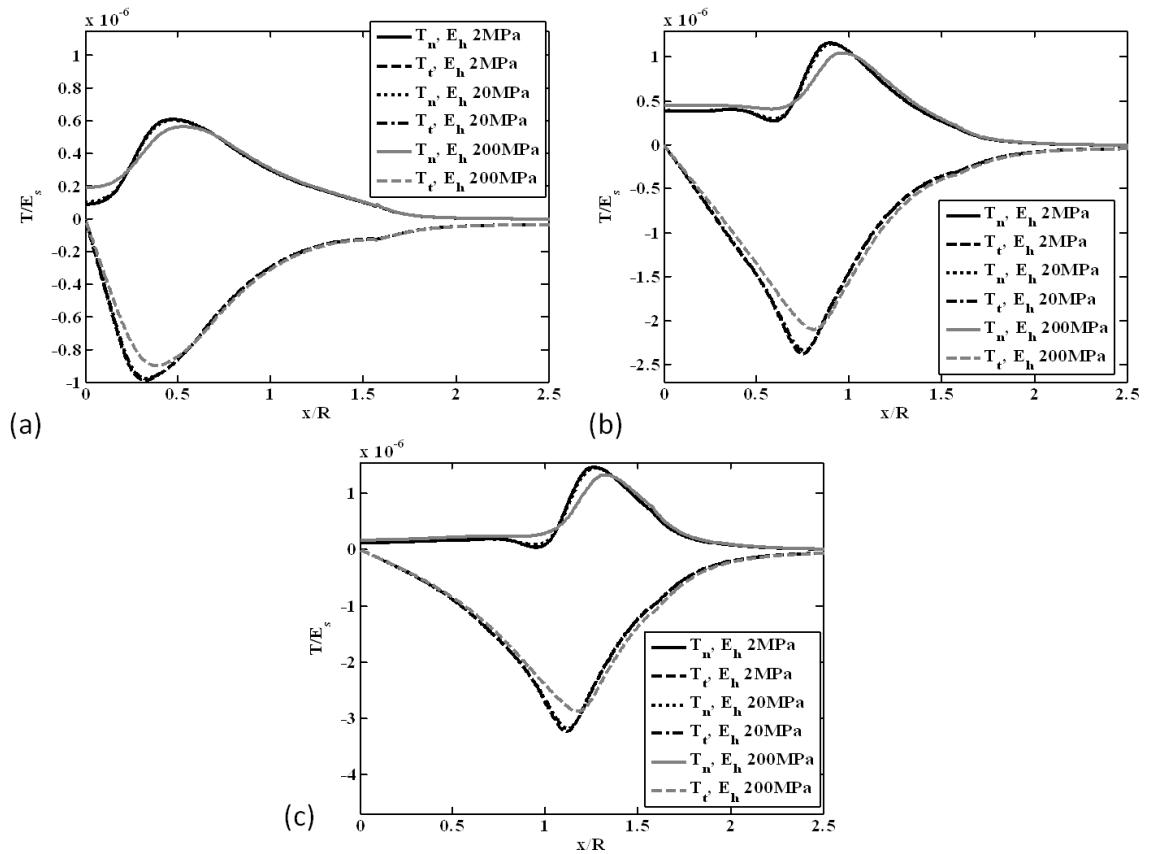
Figure 6-21: Computed normal (T_n) and tangential (T_t) tractions along the stent-coating interface for (a) low deployment $(\Sigma_a = 0.139)$ (b) medium deployment $(\Sigma_a = 0.371)$ and (c) high deployment $(\Sigma_a = 0.558)$ for an elastic-plastic stent with the substrate thickness, $h_2/R = 0.1$. Three strain hardening moduli are considered for the strut $(E_h = 2, 20$ and $200 MPa)$. In all cases, an elastic coating $(E_c = 20 MPa)$ is considered. $h_1/R = 0.2, E_s = 200 GPa, L/R = 2, \sigma_{max}/E_s = \tau_{max}/E_s = 2$. The strut yield stress $(\sigma_y) = 200 MPa$.
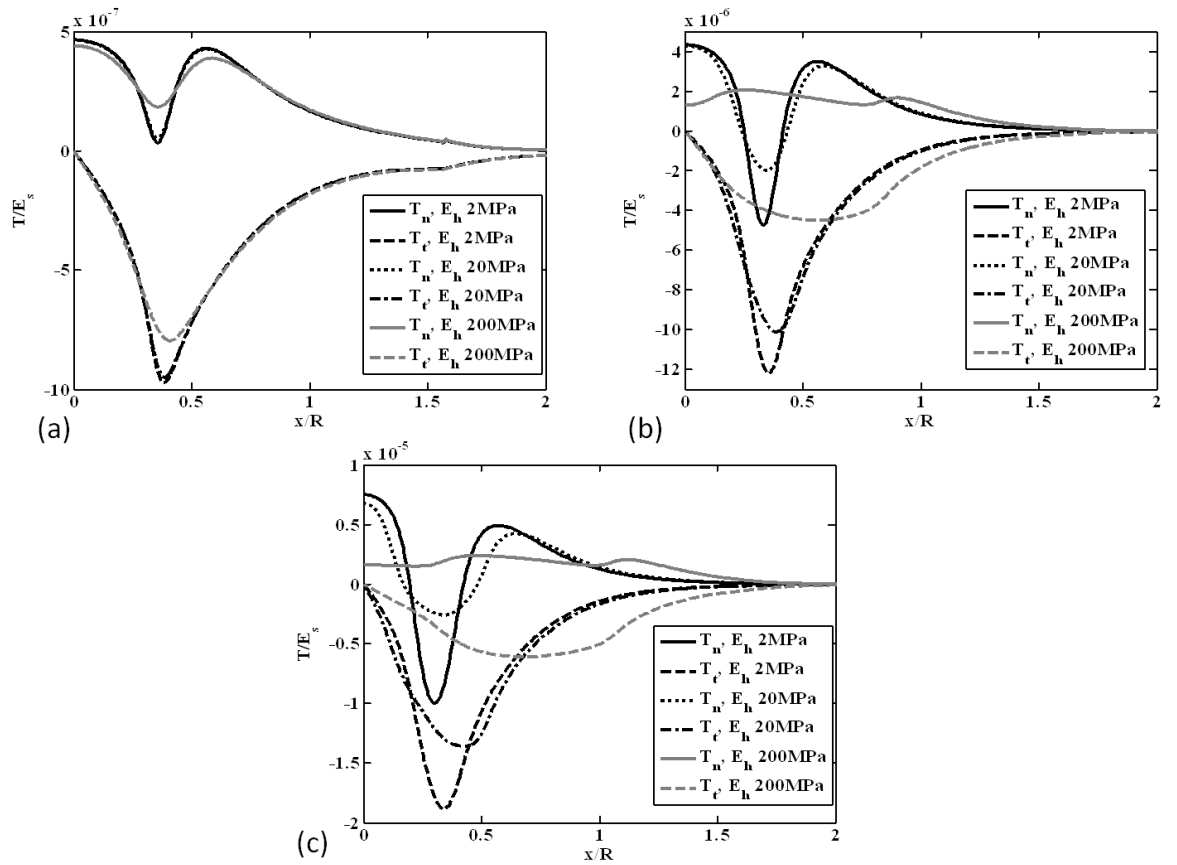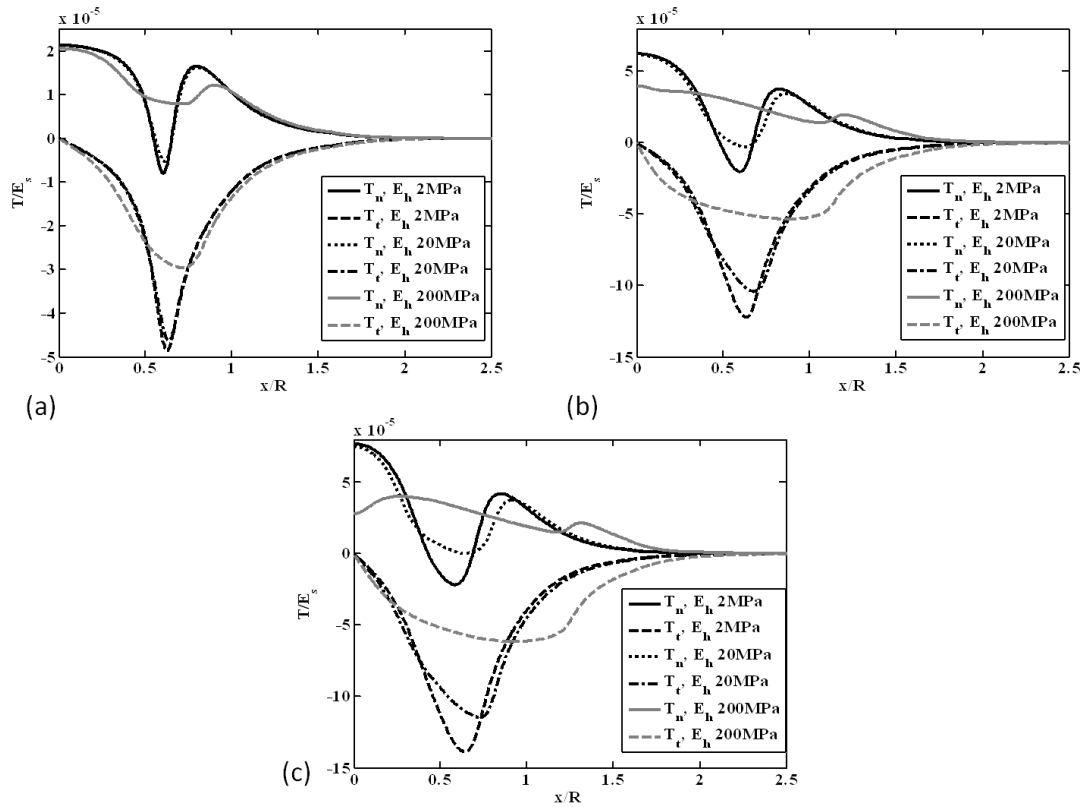
Figure 6-22: Computed normal (T_n) and tangential (T_t) tractions along the stent-coating interface for (a) low deployment $(\Sigma_a = 0.101)$ (b) medium deployment $(\Sigma_a = 0.37)$ and (c) high deployment $(\Sigma_a = 0.54)$ for an elastic-plastic stent with the substrate thickness, $h_2/R = 2$. Three strain hardening moduli are considered for the strut $(E_h = 2,20 \text{ and } 200MPa)$. In all cases, an elastic coating $(E_c = 200MPa)$ is considered. $h_1/R = 0.2, E_s = 200GPa, L/R = 2, \sigma_{max}/E_s = \tau_{max}/E_s = 2$. The strut yield stress $(\sigma_y) = 200MPa$.
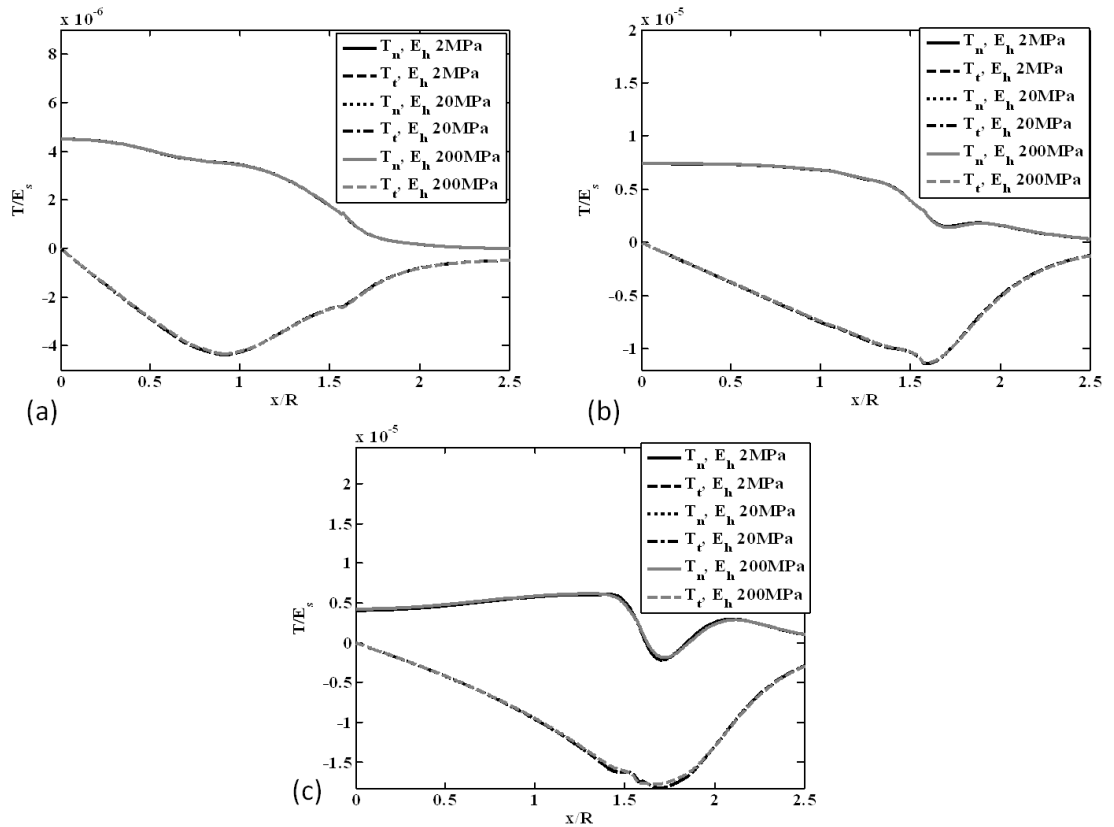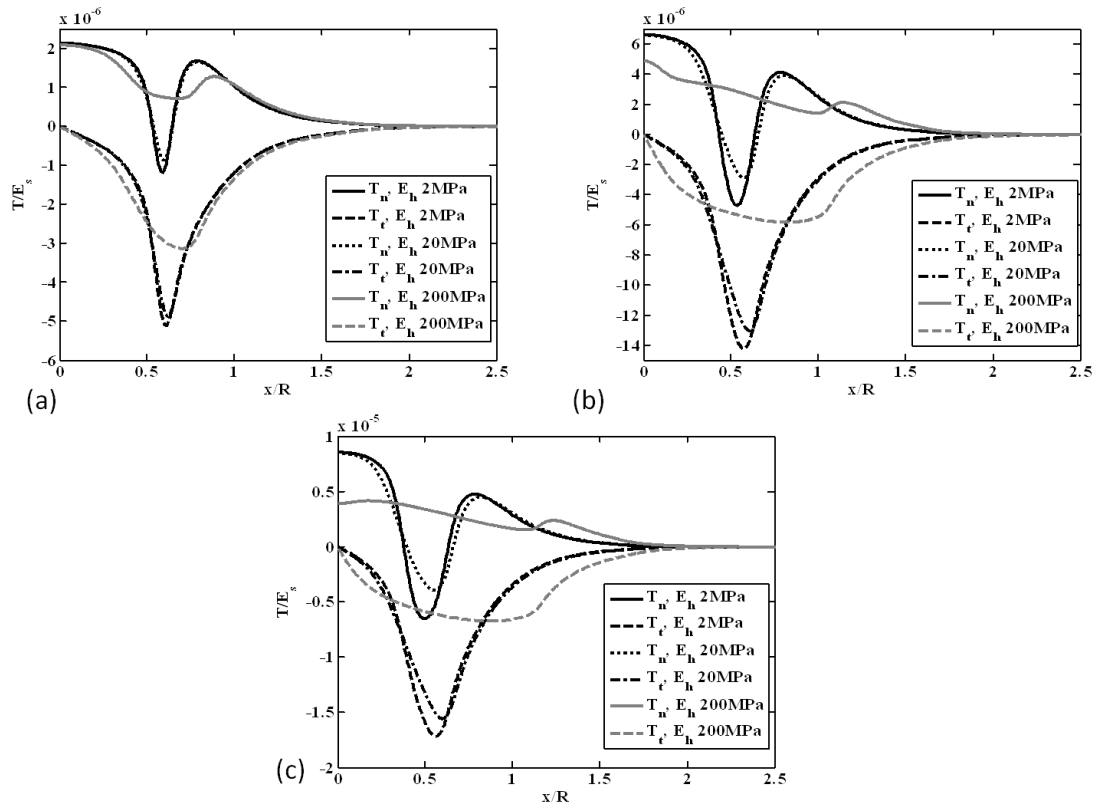
Figure 6-23: Computed normal (T_n) and tangential (T_t) tractions along the stent-coating interface for (a) low deployment $(\Sigma_a = 0.101)$ (b) medium deployment $(\Sigma_a = 0.37)$ and (c) high deployment $(\Sigma_a = 0.54)$ for an elastic-plastic stent with the substrate thickness, $h_2/R = 2$. Three strain hardening moduli are considered for the strut $(E_h = 2,20$ and $200 MPa)$. In all cases, an elastic coating $(E_c = 20 MPa)$ is considered. $h_1/R = 0.2, E_s = 200 GPa,$ $L/R = 2,$ $\sigma_{max}/E_s = \tau_{max}/E_s = 2$. The strut yield stress $(\sigma_y) = 200 MPa$.

Figure 6-24: (a) Stent and coating von Mises ($\overline{\sigma}$) stress distribution plotted on the deformed geometry at an arch deployment of $\Sigma_a = 0.371$ (b) Mixed-mode coating delamination computed at $x/R = 0.75$ (c) Normalised tangential traction (T_t/τ_{max}) as a function of normalised tangential separation (Δ_t/δ_t) computed at coating node ($x/R = 0.75$). (d) Normalised normal traction (T_n/σ_{max}) as a function of normalised normal separation (Δ_n/δ_n) computed at coating node ($x/R = 0.75$). (e) von Mises ($\overline{\sigma}$) stress distribution plotted on the deformed stent geometry at an arch deployment of $\Sigma_a = 0.42$. An elastic coating ($E_c = 20MPa$) is considered. Elastic-plastic properties are assigned for the stent strut with $E_s = 200GPa$, strain hardening modulus, $E_h = 200MPa$ and yield stress, $\sigma_y = 200MPa$. $h_1/R = 0.2, h_2/R = 0.1, L/R = 2$, $\sigma_{max}/E_s = \tau_{max}/E_s = 2x10^{-6}$.
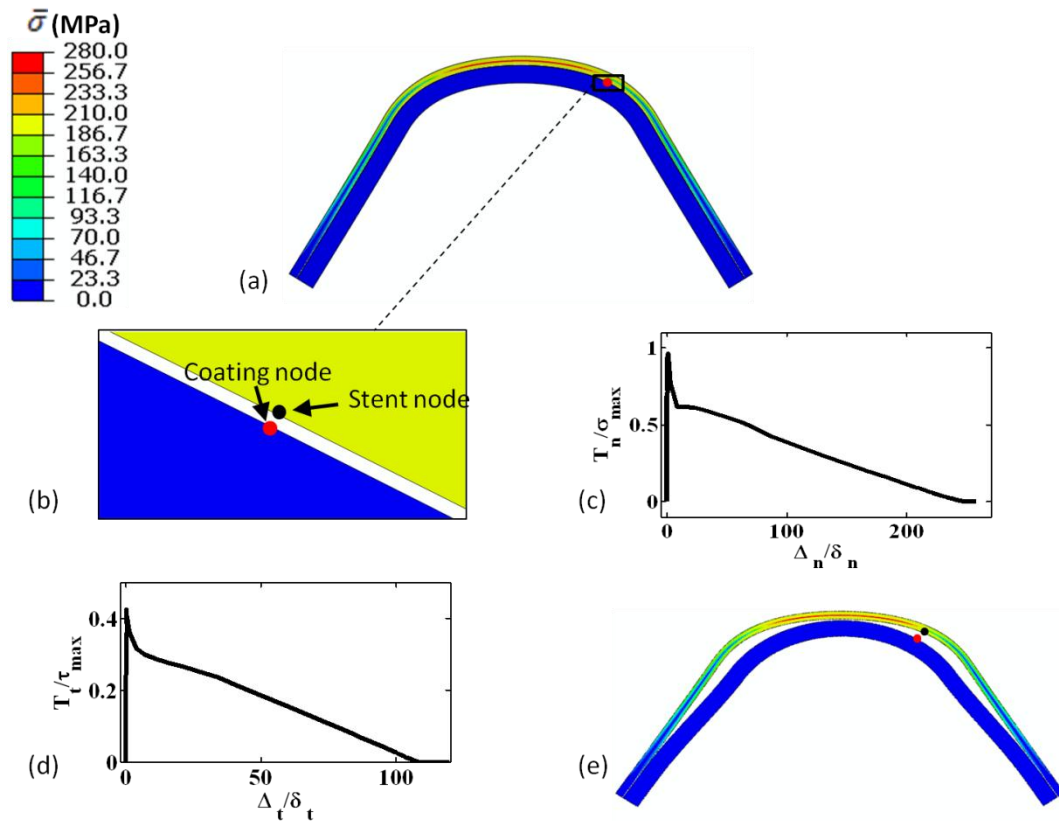
Figure 6-25: (a) Stent and coating von Mises ($\overline{\sigma}$) stress distribution plotted on the deformed geometry at an arch deployment of $\Sigma_a = 0.371$ (b) Predominantly mode I coating delamination at $x/R = 0.9$ (c) Normalised normal traction (T_n/σ_{max}) as a function of normalised normal separation (Δ_n/δ_n) computed at coating node ($x/R = 0.9$) (d) Normalised tangential traction (T_t/τ_{max}) as a function of normalised tangential separation (Δ_t/δ_t) computed at coating node ($x/R = 0.9$) (e) von Mises ($\overline{\sigma}$) stress distribution plotted on the deformed stent geometry at an arch deployment, $\Sigma_a = 0.42$. An elastic coating ($E_c = 20MPa$) is considered. Elastic-plastic properties are assigned for the stent strut with $E_s = 200GPa$, strain hardening modulus, $E_h = 200MPa$ and yield stress, $\sigma_y = 200MPa$. $h_1/R = 0.2, h_2/R = 0.1, L/R = 2$. $\sigma_{max}/E_s = 1.045\text{x}10^{-6}, \tau_{max} = 5\sigma_{max}$.
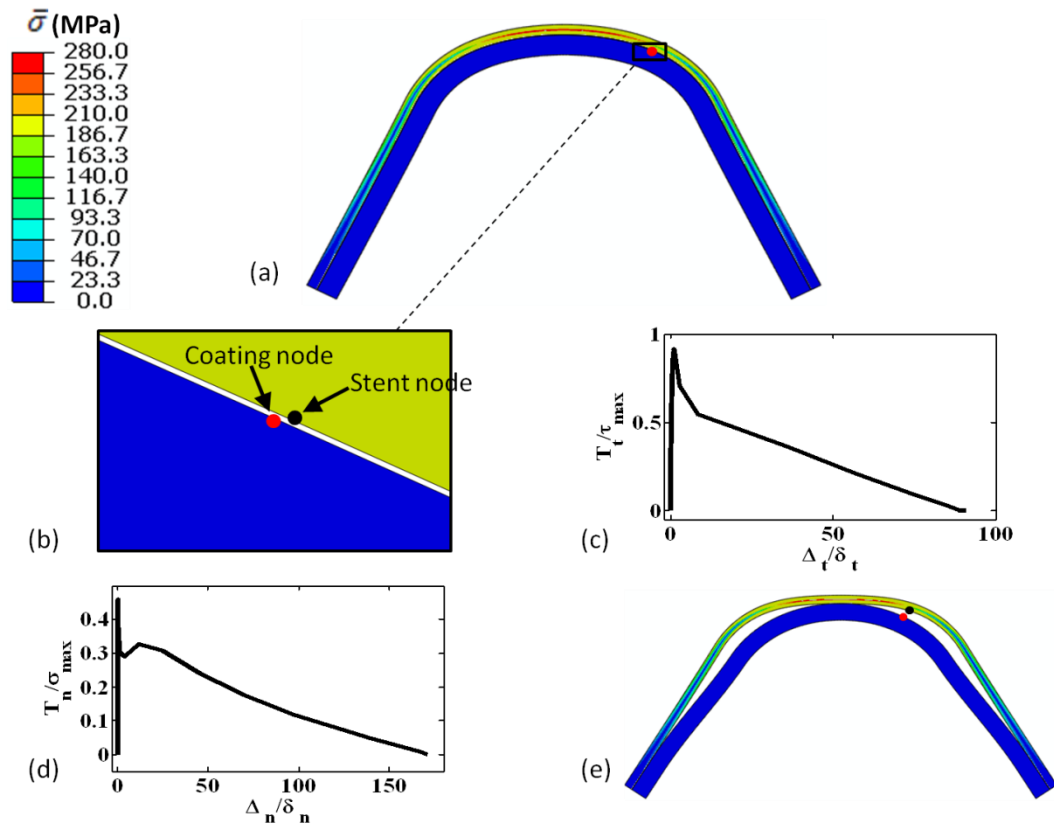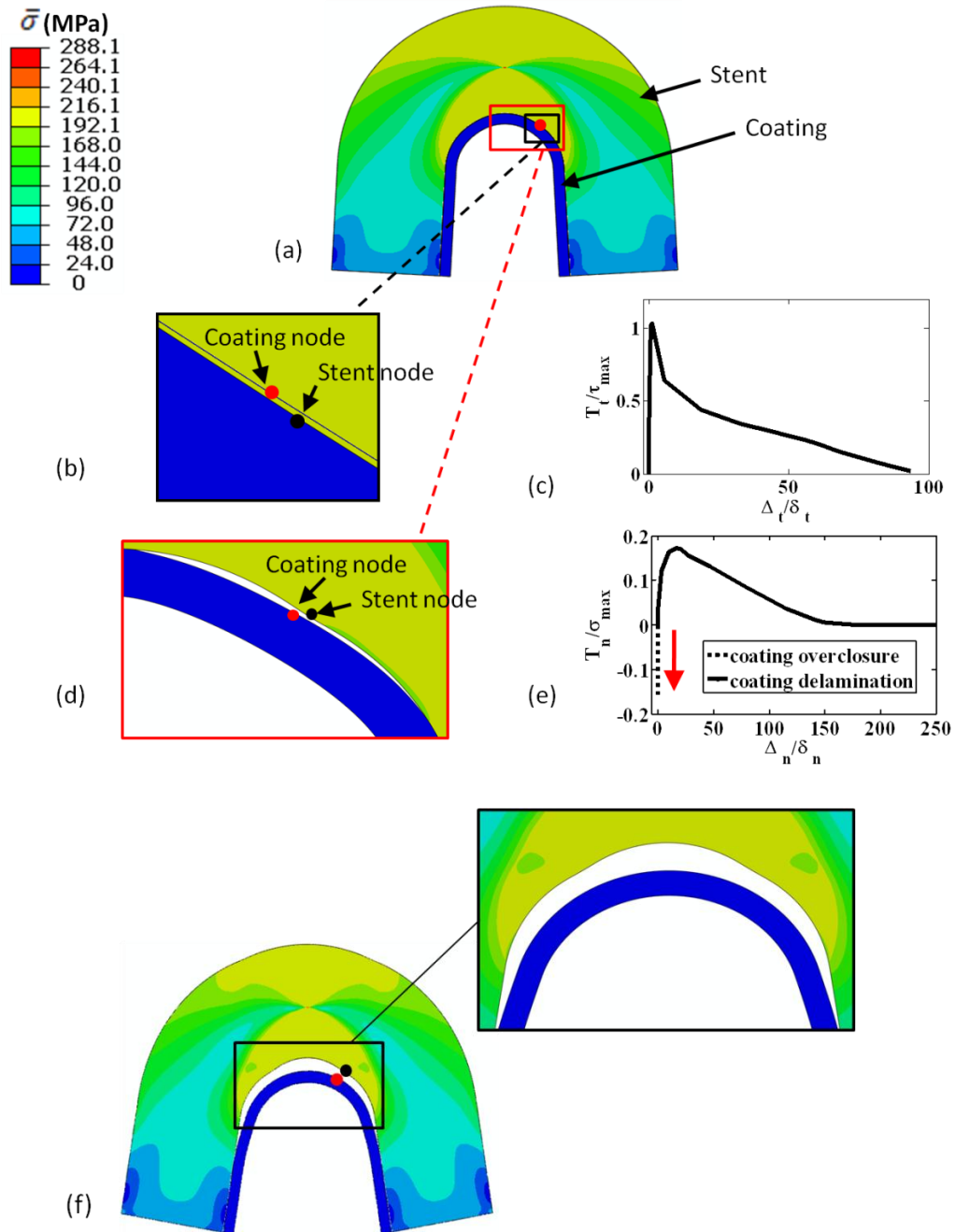
Figure 6-26: (a) Stent and coating von Mises ($\overline{\sigma}$) stress distribution plotted on the deformed geometry at an arch deployment of $\Sigma_a = 0.098$ (b) Mixed-mode coating compression computed at $x/R = 0.6$ (c) Normalised tangential traction (T_t/τ_{max}) as a function of normalised tangential separation (Δ_t/δ_t) computed at coating node ($x/R = 0.6$) (d) Mixed-mode coating delamination computed at $x/R = 0.6$ and $\Sigma_a = 0.112$ (e) Normalised normal traction (T_n/σ_{max}) as a function of normalised normal separation (Δ_n/δ_n) computed at coating node ($x/R = 0.6$). (f) von Mises ($\overline{\sigma}$) stress distribution plotted on the deformed stent geometry at an arch deployment, $\Sigma_a = 0.305$. Insert highlights non-uniform strut surface. An elastic coating ($E_c = 200MPa$) is considered. Elastic-plastic properties are assigned for the stent strut with $E_s = 200GPa$, strain hardening modulus, $E_h = 2MPa$ and yield stress, $\sigma_y = 200MPa$. $h_1/R = 0.2, L/R = 2, h_2/R = 2$. $\sigma_{max}/E_c = \tau_{max}/E_c = 4.8 \times 10^{-5}$. Deformation factor=3 for (b) and (d).

7 Computational Investigation of Aneurysm Dissection

7.1 Introduction

An abdominal aortic aneurysm (AAA) is defined as a permanent and irreversible dilation of the aorta. Most AAAs form in the area just below the renal arteries and above the iliac arteries (Standring, 2008). The rupture of a AAA is a significant clinical event, having a mortality rate of 90% and was ranked by Vorp and Geest (2005b) as the 13th highest cause of death in the western world. Approximately 150,000 new cases are diagnosed every year (Vorp, 2007). A recent study has reported that aneurysms are at least 9 times more prevalent in the abdominal section of the aorta than in the thoracic section (Kuivaniemi and Elmore, 2012). AAA formation is more common in the elderly (>65years) and approximately four times more likely in males (Hultgren et al., 2012). Numerous studies have reported a significant drop in AAA-associated mortality as a consequence of regular ultrasonography screening programs (Scott, 1999; Chaikof et al., 2009; Moll et al., 2011). Nevertheless, an accurate predictive framework is crucial in order to reduce the risk of future mortality due to AAA rupture.

The reliable evaluation of the rupture risk of a specific AAA does not currently exist. Nearly all of the criteria which are used by clinicians to indicate the need for surgical intervention are been base on empirical data (Vorp, 2007). The maximum AAA diameter has widely been used to justify the need for surgical intervention with AAAs greater than 5cm in diameter deemed to require elective surgery (Dryjski et al., 1994). However, clinical studies conducted by Darling et al. (1977), and Hall et al. (2000) determined that rupture rates of between 12% and 23% have been reported for AAAs less than 5cm in diameter and rupture rates of 40% have been reported for AAAs greater than 5cm. A number of non-specific factors for AAA formation include male gender, hypertension, smoking, Marfan syndrome, Ehlers–Danlos syndrome and family history of AAAs (Alexander, 2004; Kuivaniemi and Elmore, 2012). Other factors have been proposed as

possible predictors of AAA rupture including; increase in wall stiffness (Sonesson et al., 1999), increase in intraluminal thrombus (ILT) thickness (Stenbaek et al., 2000), expansion rate (Lederle et al., 2002) and peak wall stress (Fillinger et al., 2002). Therefore, without an accepted technique to assess rupture risk, the surgeon is left with a dilemma: a reparative operation with its inherent risk of complications, or careful monitoring of the growth of the aneurysm, possibly exacerbating the risk of AAA rupture. Clearly, a more accurate predictive framework is required to improve the clinical management of these patients.

A number of computational frameworks have been proposed to predict AAA rupture. Most of these computational models have involved predicting the magnitude and location of peak von Mises stress in the AAA wall and using this as a predictor for AAA rupture. Early research conducted by Stringfellow et al. (1987) idealised the AAA geometry as a cylinder or sphere and employed the Law of Laplace, which defines wall stress to be proportional to inverse of the mean curvature, to predict locations of peak wall stress. A plethora of additional computational models employing idealised geometries and linear-elastic constitutive models were subsequently proposed to investigate peak AAA wall stress (Stringfellow et al., 1987; Inzoli et al., 1993; Mower et al., 1993; Elger et al., 1996). The AAA geometry is usually asymmetric as the vertebral column prevents posterior expansion and therefore leads, predominantly, to anterior bulging. It was understood that the use of idealised AAA geometries yielded erroneous stress distribution predictions and therefore over the past decade researchers have focused on analysing the walls stress distributions in patient-specific geometries constructed through a combination of computer tomographic (CT) scans and reconstruction software (Vorp et al., 1998; Raghavan et al., 2000; Raghavan and Vorp, 2000; Doyle et al., 2007).

Furthermore, numerous studies neglected the inclusion of an intraluminal thrombus (ILT) in the patient-specific geometries. It was reported by Vande Geest et al. (2006c) that ILT's are present in approximately 75% of AAAs. The concept that the ILT may affect the stresses in the AAA wall was first investigated by Inzoli et al. (1993). The incorporation of the ILT in patient-specific geometries

was shown to have a significant influence on the predicted stress distribution by Wang et al. (2002) where peak systolic blood pressure was applied to the inner surface of the AAA geometry to simulate conditions that would generate highest stresses in the wall. Both the AAA wall and the ILT were modelled as hyperelastic, homogenous, incompressible and isotropic materials. Doyle et al. (2007) showed that AAA models incorporating the ILT resulted in significant changes in both the magnitude and location of peak von Mises stresses in the AAA wall compared to simpler models where the ILT was omitted.

Uniaxial tests were conducted on both aneurysmal and non-aneurymal tissue by Raghavan et al. (1996) where it was suggested that AAA tissue is isotopic. The uniaxial test data of Raghavan et al. (1996) together with uniaxial tests conducted on 69 new AAA samples were utilised by Raghavan and Vorp 2000 to develop a hyperelastic, isotropic constitutive formulation to describe a AAA wall. The constitutive formulation for the AAA wall accounted for variations in the mechanical properties of the tested AAA samples within a sample population. Finite element simulations revealed that the computed AAA wall stresses varied by only 4% or less when AAA material parameters were varied within a 95% confidence interval for the patient population studied. However, this generalised approach to predict patient-specific rupture is not necessarily ideal as researchers have indicated that the wall strength can vary significantly in the same aneurysm as well as from patient to patient (J. Thubrikar, 2001; Wang et al., 2002; Vallabhaneni et al., 2004; Vande Geest et al., 2006b). Very few biaxial tests were conducted on AAA tissue until 2006 (Vorp and Geest, 2005a). In contrast to the suggestion that AAA tissue exhibits isotropic behaviour (Raghavan et al., 1996), the study of Vande Geest et al. (2006b), where AAA samples were subjected to biaxial tests, revealed that AAA tissue exhibits anisotropic behaviour. In this study, an anisotropic exponential form of constitutive model, based on the strain energy density function of Tong and Fung (1976) was utilised to describe the AAA wall, exhibiting typical strain stiffening effects associated with aortic tissue. Additionally, the uniaxial and biaxial tests conducted by Wang et al. (2001) and

Vande Geest et al. (2006c) suggest that the intraluminal thrombus behaves as an isotropic material.

A rupture potential index (RPI) has been proposed based on the ratio of computed wall stress to an estimate of wall strength (based on factors such as family history, gender, AAA diameter and intraluminal thrombus (ILT) thickness) (Vande Geest et al., 2006a). An equation for the prediction of rupture which takes into account the ratio of the ILT to the AAA geometry, the asymmetry of the AAA, the maximum diameter of the AAA, wall thickness and systolic blood pressure has recently been proposed by Li and Kleinstreuer (2005). Such semi-empirical approaches to rupture prediction incorporating finite element computation of von Mises stresss in a homogeneous AAA wall provide litte insight into the damage mechanism in the arterial tissue. Indeed, the underlying mechanisms of AAA rupture are poorly understood. It has been suggested by Phillippi et al. (2011) and Pasta et al. (2011) that aortic shear dissection, characterised as a separation of the arterial wall layers, plays a key role in AAA rupture. Additionally, a previous experimental study has suggested that increasing lumen pressure in healthy cardiovascualr tissue leads to shear failure within the arterial walls (Haslach et al., 2011). Aortic pseudoaneurysms or the creation of a false lumen, defined as a dilation of the aorta between two layers of the arterial wall, also suggest that shear dissection between the layers of the aneurysmal wall could play a key role in AAA development (Ring, 2000). This highlights the need for a more indepth understanding of the mechanisms involved in damage initiation, damage propagation, and eventual rupture of AAA tissue. In particular, as motivated by the aforementioned experimental findings, the mechanism of interlayer dissection of the AAA should be investigated. The need for such a mechanistic approach to the damage of AAA tissue is further highlighted by the study of Georgakarakos et al., 2010 in which it is demonstrated that bleb locations do not coincide with locations of peak von Mises stress in the AAA wall.

In this chapter, dissection between the individual wall layers of the AAA is investigated using CZMs. It is hypothesised that peak von Mises stress in the

AAA wall is not a reliable indicator for AAA dissection. Cohesive zone formulations have previously been implemented to model the propagation of arterial dissection and plaque rupture during balloon angioplasty intervention (Gasser and Holzapfel, 2007; Ferrara and Pandolfi, 2008). However, cohesive zone modelling has not previously been used to predict interlayer dissection in AAAs. In the present study, the NP2 $(\Delta_n < 0)$ and the SMC $(\Delta_n > 0)$ CZM formulations are used to simulate delamination between the adventitia-media and intima-media layers of an aneurysm wall. The influence of the ILT on overall stress distribution patterns and dissection locations is also investigated. It is demonstrated that regions of interlayer dissection do not coincide with regions of computed peak wall stress. Previous studies have modelled the AAA wall as a single homogenous entity (Stringfellow et al., 1987; Inzoli et al., 1993; Mower et al., 1993; Elger et al., 1996; Vorp et al., 1998; Raghavan and Vorp, 2000; Raghavan et al., 2000; Doyle et al., 2007). Additionally in this chapter, for the first time, the importance of modelling an inhomogeneous trilayered AAA wall is demonstrated. The reconstruction method utilised to create three patient-specific AAA geometries along with the finite element model is presented in Section 7.2 of this chapter. In Section 7.3, the influence of material and geometric properties on interface traction distributions is investigated. Additionally, predicted interlayer dissection locations are presented for each AAA model and compared to maximum von Mises stress locations. The influence of the intima thickness layer on the initial dissection location is also investigated, motivated by previous studies that report a thickening of the intima layer in diseased arteries (Holzapfel et al., 2005; Holzapfel et al., 2007).

7.2 Methods

Patient-specific CT scans (1.25mm slice thickness) are obtained with permission from the Western Vascular Institute, University College Hospital, Galway. DICOM (Digital Imaging and Communication in Medicine) files containing the CT data are imported into Mimics$^{©}$ (v14.11, Materialise, Belgium), a specialised image processing software, for segmentation and reconstruction. Firstly, a Hounsfield unit thresholding technique is applied to the CT scans to obtain the initial geometry of the intraluminal thrombus (ILT). Hounsfield units are measures of the radiointensity of each pixel (Materialise, 2002). For example, a lower Hounsfield thresholding range is used to isolate regions in the vasculature such as cardiovascular tissue which has a pixel intensity which is closer to that of fat rather that bone (Doyle et al., 2007). A special contrast agent (dye) is administered intravenously during CT examinations in order to enhance the visualisation of internal tissue structures such as organs and blood vessels. As a result, the lumen of the aneurysms was easily identifiable from the surrounding internal bodily structures. However, the segmentation of the ILT from the surrounding internal structures is not trivially achieved. An illustration summarising the reconstruction process, from CT scans to final geometry, is shown in Figure 7-1. A thresholding range is first chosen to ensure the incorporation of the entire ILT (a CT slice of the original geometry is shown in Figure 7-1(c)). After the creation of the initial geometry, each CT slice is carefully examined and edited to establish a more accurate model of the ILT geometry (Figure 7-1(d)). Additionally, a number of smoothing iterations are performed to remove sharp edges and other surface artefacts. The integrity of the final AAA geometry is ensured by creating a polyline representation of the AAA geometry. Any discontinuity in a polyline indicates that additional reconstruction iterations are required (Figure 7-1(e)). The polyline growing tool is utilised to ensure that there are no holes present in the geometry. Fifteen control points (a measure of the number of smoothing iterations performed) per slice, are chosen based on previous work which established the optimum number of control points required without losing geometry accuracy (Doyle et al., 2007). The final reconstructed 3D geometry of the ILT (for geometry 1), including the vertebral column, is shown in

Figure 7-1(f). In total, three AAA geometries, shown in Figure 7-2, are analysed. For the remainder of this chapter these AAA geometries will be referred to as geometry 1, geometry 2 and geometry 3, as indicated in Figure 7-2.

A tetrahedral mesh was firstly created on the ILT geometries using 3-matic© editing software. However, difficulties in obtaining a uniform distribution of nodes on the surface of the ILT were encountered using this meshing methodology. The irregular distribution of nodes on the surface of the thrombus was found to result in numerical difficulties during the prediction of interlayer crack front propagation. Hence, a structured mesh with a uniform distribution of nodes and elements was required to avoid such numerical difficulties. Since neither Mimics© nor Abaqus software offer the capability of generating a hexahedral structured mesh of optimal quality on the ILT geometries, it was decided to avail of an alternative meshing methodology, recently developed at Ghent University. The ILT geometries were sent to Dr. Gianluca de Santis where they were subsequently discretized into high quality hexahedral meshes. The meshing methodology used consisted of three main steps: topographical partition, geometrical surface reconstruction and meshing, as reported in De Santis et al. (2010). These ILT hexahedral meshes were then returned to the author of this thesis, whereupon meshed AAA wall geometries were constructed. Specifically, meshed ILT geometries were imported into Abaqus/Standard, where intima, media and adventitia layers were generated by offsetting the geometry from the abluminal surface of the ILT. Cohesive zone surfaces were then created between the AAA wall layers with coincident nodes on opposing cohesive surfaces. The thickness of each layer of the AAA wall is estimated from reported data for aged iliac arteries (Schulze-Bauer and Mörth, 2003). Unless otherwise stated, intima, media and adventita layer thicknesses of 0.17mm, 0.73mm and 0.43mm, respectively, are assumed. A schematic indicating the AAA wall layers for Geometry 1 is shown in Figure 7-3. The interface between each artery wall layer is modelled using the non-potential-based SMC and NP2 CZMs presented in Chapter 3 (SMC model is used in separation and NP2 model is used in compression/over-closure). Values of maximum interface strengths in the

normal (σ_{max}) and tangential (τ_{max}) directions are based on dissection experiments of healthy arterial tissue (Sommer et al., 2008). Specifically, an interaction strength of $\sigma_{max} = \tau_{max} = 16kPa$ and a critical cohesive interface length of $10\mu m$ is chosen. A neo hookean hyperelastic constitutive formulation is utilised to describe the AAA wall layers and intraluminal thrombus. The properties for each wall layer are estimated from published properties of stenotic iliac arteries (Holzapfel et al., 2004), as the properties for aortic aneurysmal wall layers are not currently available. Unless otherwise stated, the stiffness of the intima, media and adventitia layers are 2.9MPa, 1.8MPa and 10.8MPa respectively. The properties of the intraluminal thrombus (ILT) are based on the study of Wang et al. (2001) with a stiffness of 0.428MPa assigned to the ILT in this study. A Poisson's ratio of 0.45 is assumed for all AAA materials. An internal pressure of 200mmHg is applied to simulate blood pressure acting on the AAA wall. The AAA geometry is partially constrained in the proximal and distal regions. A tie constraint is applied between the aneurysm and the vertebral column surfaces. An increase in finite element mesh density from approximately 5000 to 50000 elements results in only a ~2% increase in the computed wall stress (see Appendix B). Therefore, a mesh density of approximately 5000 elements is used for all analyses presented in this chapter.

7.3   Results

7.3.1   Influence of Geometrical and Material Considerations on Interface Tractions

In this section preliminary simulations are presented using geometry 1. A lumen pressure of 100mmHg is applied. This relatively low lumen pressure is not sufficient to cause interlayer dissection. Rather the focus of this section is the assessment of the effect of modelling an inhomogeneous arterial wall (and ILT) in terms of computed locations and magnitudes of interlayer shear tractions. Specifically, interlayer shear traction distributions are compared for three cases:
Case 1: AAA wall layer properties are based on published properties of stenotic iliac artery layers (Holzapfel et al., 2004) with different properties assigned to the

intima, media and adventitia layers. In this case the intraluminal thrombus (ILT) is also accounted for; <u>Case 2:</u> Media layer properties, also based on the work of Holzapfel et al., 2004, are assigned to each AAA wall layer. The ILT is also included; <u>Case 3:</u> The same AAA wall layer properties as those used in Case 1 are utilised again. However, in this case the ILT is omitted. In all simulations performed in this chapter, computed normal interface tractions are negligible, indicating that interlayer dissection is primarily mode II in nature. Hence, only shear tractions and shear separations are presented in this study.

7.3.1.1 Case 1- Inhomogeneous AAA Wall with ILT

The computed distribution of shear traction at the adventitia-media and intima-media interface following an applied lumen pressure of 100mmHg is shown in Figure 7-, where different material properties are assigned to each AAA wall layer (Holzapfel et al., 2004) and an ILT is also incorporated. Regions of maximum interlayer traction are highlighted. The position of the vertebral column (VC) is also indicated as a frame of reference. It is worth noting that AAA expansion is constrained by the presence of the vertebral column leading to anterior expansion.

Focusing firstly on the adventitia-media interface (Figure 7-(a) and (b)), a significant region of shear traction is computed laterally to the right in the region of the aneurysm neck (Figure 7-(a)). Additionally, a band of increased shear tractions are also computed at the anterior bulge (ANT). A significant region of shear traction is also computed at the aneurysm neck, laterally to the left (Figure 7-(b)).

Considering the intima-media interface (Figure 7-(c) and (d)), a similar shear traction distribution is computed relative to the adventitia-media interface. A region of high shear traction is computed near the aneurysm neck, laterally to the right, while the predicted shear tractions at the anterior bulge are also marginally increased (Figure 7-(c)) when compared to computed separation at the adventitia-media interface (Figure 7-(a)). Focusing on the lateral left region of the AAA (Figure 7-(d)), again shear tractions computed at the aneurysm neck are

marginally increased relative to the adventitia-media interface. Additionally, a band of increased shear tractions are computed towards the anterior bulge in the region of the aneurysm neck.

7.3.1.2   Case 2- Homogeneous AAA Wall with ILT

In Figure 7-, for the same lumen pressure (100mmHg), the distribution of computed shear tractions at the adventitia-media and intima-media interface are presented, where identical hyperelastic properties (corresponding to the media layer properties) are assumed for each AAA wall layer. The ILT is included in the simulation, with the aforementioned ILT hyperelastic properties being assumed. Considering the intima-media interface, a region of high shear traction is computed in the region of the aneurysm neck in the lateral right location (Figure 7-(c)). Additionally, in the lateral left aneurysm region (Figure 7-(d)), two distinct regions of significant traction are computed in the region of the aneurysm neck. This is significantly different to the computed traction pattern for an inhomogeneous trilayered wall (Figure 7-(d)) where only one localised region of increased interlayer traction is predicted. It can also be observed that shear traction magnitudes are significantly different at the adventitia-media interface (Figure 7- (a) and (b)) than when an inhomogeneous arterial wall is simulated (Figure 7-). In summary these simulations highlight the importance of modelling the AAA wall as an inhomogeneous trilayered structure in terms of prediction of the distribution of interface traction and stress in the AAA wall.

7.3.1.3   Case 3- Inhomogeneous AAA Wall without ILT

The computed interlayer traction distribution when the ILT is excluded (Figure 7-6) differs significantly from that computed when the ILT is included in the model (Figure 7-4). The band of increased shear tractions computed from the aneurysm neck to the anterior bulge laterally to the right (Figure 7-) is not computed at either the adventitia-media interface or intima-media interface when the ILT is excluded (Figure 7-6). Focusing on the adventitia-media interface, a significant region of interlayer traction is computed directly above the vertebral column (VC) (Figure 7-(a)). This is in contrast to predicted tractions when an ILT is accounted for, where increased shear tractions are computed closer to the anterior region

(Figure 7-(a)). Furthermore, negligible interlayer tractions are computed in the anterior region (Figure 7-(a)) compared to Figure 7-(a) when an ILT is accounted for. Additionally, it is worth noting that increased interlayer traction is computed in the region of the aneurysm neck (Figure 7-(b)) relative to models incorporating the ILT. A significant concentration of interlayer traction is computed at the intima-media interface when the ILT is accounted for (Figure 7- (c) and (d)). However, when the ILT is omitted, negligible interface tractions are computed at the intima-media interface in both the lateral right and lateral left orientations (Figure 7-(c) and (d)). In summary, this section clearly demonstrates the importance of modelling a trilayered inhomogeneous AAA wall in addition to an intraluminal thrombus (ILT) for the prediction of interlayer traction distributions.

7.3.2 Comparison of Interlayer Dissection Locations with Peak von Mises Stress Locations

In this section computed regions of interlayer dissection are presented for three AAA geometries (Figure 7-2). Dissection initiation (when the maximum interface traction is exceeded) and dissection propagation are computed. It is demonstrated, in most cases, that locations of interlayer dissection do not coincide with regions of peak von Mises stress. The magnitude and location of peak von Mises stress in the AAA wall (computed for the lumen pressure at which interlayer dissection initiates) is presented in Table 7-1. Additionally, the distance from the point of initial dissection to the point of peak von Mises stress is included in Table 7-1 to highlight the significant differences in location of interlayer dissection and peak von Mises stress.

7.3.2.1 AAA Geometry 1

The evolution of interface shear traction at six selected nodes (only six nodes are highlighted for illustrative purposes, but several additional nodes exist between these nodes) in a region of predicted dissection (where the critical interface characteristic separation is exceeded) at the adventitia-media interface is depicted

in Figure 7- for geometry 1. As internal lumen pressure is increased, an inhomogeneous increase in interlayer shear tractions is predicted (traction increases at a different rate for each node in the region). A linear increase in shear traction with increasing lumen pressure is computed at each node up to the point of dissection initiation. Following initiation, a rapid reduction in interface traction is computed, characterising dissection. It should be noted that the computed value of peak shear traction exceeds the prescribed interface strength of $\tau_{max} = 16kPa$ for all nodes which undergo complete interlayer dissection. For example, a peak shear traction of approximately 19.5kPa is computed at the point of dissection initiation in Figure 7-. This is due to the fact that mixed-mode over-closure (compression) of the AAA wall layers occurs due to the applied lumen pressure. This compression at the interface between the AAA layers results in an increased resistance to tangential separation as part of the physically realistic penalisation of mixed-mode over-closure provided by the NP2 CZM (see Chapter 3). A systolic blood pressure measurement of 142mmHg was reported by Fillinger et al. (2002) for ruptured AAAs. In the simulation presented in Figure 7-, interlayer dissection is initiated at a lumen pressure of 132mmHg when the critical interface traction ($\tau_{max} = 16kPa$) is exceeded at a node in the bottom of the region that subsequently undergoes dissection (referred to hereafter as a *dissection patch.* Dissection patches are readily identifiable as the red regions in contour plots, where the critical interface separation has been exceeded). A rapid decrease in traction to zero is then computed for this node. The rate of increase of shear traction then increases along the path of dissection as the crack front propagates. Many nodes exhibit an extremely rapid increase in traction to the critical value, followed by a reduction to zero traction as the crack front propagates towards the neck of the aneurysm. The predicted dissection propagates upwards from the bottom right quadrant of the dissection patch to the upper left quadrant at which point the luminal pressure has reached a value of 165mmHg.

Dissection is also computed at the intima-media interface as shown in Figure 7-. In this case, initial dissection is computed at a lumen pressure of 138mmHg in the region of the aneurysm neck. The critical cohesive interface strength ($\tau_{max} = $

$16kPa$) is also exceeded in the anterior region at a lumen pressure of 168mmHg. Two nodes adjacent to the initiation nodes are highlighted in Figure 7-. Again, it can be seen that a rapid increase in interlayer shear traction is computed as the crack front propagates along the interface.

The computed dissection patch at the adventitia-media interface when the ILT is neglected is shown in Figure 7-. In contrast to the predicted dissection region computed at the adventitia-media interface when the ILT is included (laterally to the right-Figure 7-), it is evident that omission of the ILT results in a significant dissection region above the vertebral column. It is worth noting that interlayer dissection is computed at a much lower lumen pressure in this case, in comparison to simulations where the ILT is included (Figure 7-). Fast crack propagation is computed along a line of nodes in the longitudinal direction (highlighted in Figure 7-) at 70mmHg. However, the crack does not continue its upwards trajectory into the non-dilated region, but rather propagates laterally, as indicated by four highlighted nodes that undergo dissection at a lumen pressure of ~85mmHg. No dissection is computed at the intima-media interface.

The computed von Mises stress distribution for geometry 1, where individual AAA wall layer properties are assigned and an ILT is included, is shown in Figure 7- in order to compare locations of von Mises stress concentrations in the AAA wall with computed dissection locations presented in Figure 7- and Figure 7-. In Figure 7- contour plots of the von Mises stress distribution in the adventitia (Figure 7-(a)) and media layer (Figure 7-(b)) are presented, with a selection of nodes in the computed dissection patches highlighted for comparison of location. It is evident that the predicted location of interlayer dissection at the adventitia-media interface does not coincide directly with the location of maximum von Mises stress in the adventitia layer (Figure 7-(a)). Furthermore, predicted interlayer dissections at the intima-media interface (Figure 7-(b)) do not coincide with the peak von Mises stress location in the media layer. In particular, the computed dissection location in the anterior region (circled) at the intima-media interface coincides with a region in which the computed magnitude of von Mises

stress in the media layer is relatively low. It is important to note that initiation of delamination does not appreciably alter the distribution of von Mises stress throughout the AAA wall.

In contrast, when the ILT is neglected (Figure 7-3), predicted interlayer dissection locations at the adventitia-media interface roughly coincide with the peak von Mises stress region in the adventitia layer. This can be attributed to the fact that omission of the ILT leads to significant bending of the AAA geometry above the aneurysm neck, thereby inducing both high interlayer shear tractions and high von Mises stresses in this location.

7.3.2.2   AAA Geometry 2

Next, computed dissection regions for geometry 2 (shown in Figure 7-2(b)) are analysed when individual wall layer properties are assigned and the ILT is accounted for. A significant region of dissection is predicted at the intima-media interface to the right of the vertebral column (VC) as shown in Figure 7-4(a). The associated interface shear traction evolution for a selection of nodes in the dissection patch are also depicted in Figure 7-4(a). Following initial interface dissection, computed at 142mmHg in the bottom left quadrant of the dissection patch, the interlayer crack front propagates towards the top right quadrant of the dissection patch following an increase in lumen pressure to 195mmHg. The progression of the interlayer crack front is shown in Figure 7-4(b)-(f) as the lumen pressure is increased from 142mmHg to 195mmHg. The computed region of intima-media dissection is very different to that computed for geometry 1, where dissections of the intima-media interface occurs in the region of the aneurysm neck and in the anterior region. Additionally a lower rate of crack front propagation is predicted with increasing lumen pressure for geometry 1. The computed von Mises stress distribution in the media layer (when the ILT is included) is presented in Figure 7-5. A selection of nodes in the dissection patch are superimposed for comparison. The initial dissection region, highlighted by circle 'B', does not correlate with a significant von Mises stress concentration. In

fact the computed von Mises stress in this region is relatively low (≈ 0.06MPa). Further increase in lumen pressure causes propagation of the dissection patch longitudinally upwards, eventually reaching a region of high von Mises stress (highlighted by circle 'A'). Crucially, however, dissection initiation does not occur in a region of high von Mises stress. Interlayer dissection is also computed at the adventitia-media interface, initiating at approximately 150mmHg as shown in Table 7-1. Again, the location of initial interlayer dissection does not coincide with the peak von Mises stress location with initial dissection computed approximately 26mm away from the peak von Mises stress location.

The critical interface cohesive strength $(\tau_{max} = 16kPa)$ is exceeded at the adventitia-media interface in two regions on the posterior side of the AAA at approximately 135mmHg when the ILT is neglected as shown in Figure 7-6. This is in contrast to the computed dissection region (directly above the vertebral column) when the ILT is omitted for geometry 1. No interlayer dissection is computed at the intima-media interface. The predicted von Mises stress distribution in the adventitia layer, when the ILT is neglected, is shown in Figure 7-7. Again, it is evident that the nodes in which the critical cohesive interface strength is exceeded at the adventitia-media interface do not coincide with the maximum von Mises stress locations in the adventitia layer.

7.3.2.3   AAA Geometry 3

Dissection regions for geometry 3 (shown in Figure 7-2(c)) are analysed next, when inhomogeneous wall layer properties are assigned and the ILT is included in the model. A region of dissection is predicted at the adventitia-media interface just above the position of the vertebral column (VC) as shown in Figure 7-8. The associated shear traction evolution for two nodes in the dissection patch is also depicted. Initial interface dissection is computed at 188mmHg. Following complete interlayer dissection at this node, characterised by a rapid decrease in interface traction, dissection is computed in an adjacent node in the dissection patch at 190mmHg. No interlayer dissection is computed at the intima-media

interface. The computed von Mises stress distribution in the adventitia layer is presented in Figure 7-9(a) and Figure 7-9(b) for the posterior and anterior AAA sides respectively with the nodes in the dissection patch superimposed for comparison. It is evident that von Mises stress concentrations do not coincide with predicted computed dissection locations. Furthermore, no interlayer dissection is computed on the anterior side where two regions of high von Mises stress are computed.

Computed dissection regions for geometry 3 when an ILT is neglected are shown in Figure 7-10 with interlayer dissection computed at the adventitia-media interface in the region above the vertebral column (VC). Again, interlayer dissection is computed at a much lower lumen pressure in this case, in comparison to simulations where the ILT is included, with initial dissection computed at 105mmHg. Subsequent interlayer dissection is computed in a second dissection patch at approximately 190mmHg. No interlayer dissection is computed at the intima-media layer. The computed von Mises stress distribution in the adventitia layer is shown in Figure 7-11 for the posterior (Figure 7-11(a)) and anterior (Figure 7-11(b)) AAA sides with nodes in the dissection patch superimposed for comparison of location. Again, it is clear that there is no direct correlation between the computed regions of interlayer dissection and peak von Mises stress locations. Additionally, it is worth noting that a localised region of increased von Mises stress is computed on the anterior AAA side (Figure 7-11(b)). However, no interlayer dissection is computed in this region.

7.3.3 Conditions Required to Cause Intima-Media Dissection Prior to Media-Adventitia Dissection (Geometry 1)

For geometry 1, adventitia-media dissection is computed prior to intima-media dissection (initial dissection is computed at 132mmHg in the adventitia-media interface as opposed to 138mmHg at the intima-media interface). However, it has been observed through CT imaging that dissections primarily occur at the intima-media interface in aneurysms (Hyodoh et al., 1996). Additionally, it has been

reported that the intima is a mechanically significant layer of considerable thickness and stiffness for human aged iliac arteries, in contrast to healthy cardiovascular tissue where the intima is relatively thin (Holzapfel et al., 2005; Holzapfel et al., 2007).

Therefore, considering geometry 1, an investigation into the conditions which lead to intima-media dissection prior to adventitia-media dissection is carried out. Specifically, both the intima thickness and stiffness are doubled. Results are summarised in Table 7-2. As reported in Figure 7- above, initial dissection occurs at the lateral right (LR) location of the adventitia-media interface prior to intima-media dissection at a lumen pressure of 132mmHg for an intima thickness of 0.17mm and E_{intima}=2.9MPa. Intima-media dissection is computed at a higher pressure at the lateral right (LR) and anterior bulge (ANT) locations at 138mmHg and 168mmHg respectively. An increase in intima stiffness to E_{intima}=5.8MPa also results in an initial adventitia-media tear computed at 131mmHg in the lateral right aneurysm location. Interestingly, the increase in intima stiffness also increases the pressure at which intima-media dissection is computed in the lateral right location (146mmHg), relative to the less stiff intima. Additionally, for the increased intima stiffness, no dissection is computed in the anterior region of the aneurysm. It is evident in Table 7-2 that an increase in intima thickness (0.34mm) significantly reduces the pressure at which intima-media dissections are computed, regardless of intima stiffness. Specifically, intima-media dissection is computed prior to adventitia-media dissection for E_{intima}=2.9MPa while interlayer dissections are computed at approximately the same pressure for E_{intima}=5.8MPa. Therefore, it is evident that accurate intima stiffness and thickness measurements are crucial in order to accurately predict initial AAA dissection locations. An additional summary of the influence of intima thickness on rupturing pressures at the adventitia-media and intima-media interface is also presented in Figure 7- for the reference intima stiffness ($E_{intima} = 2.9MPa$). This figure simply illustrates again that interlayer dissection, at both the intima-media and adventitia-media interface, is computed at lower pressures with increasing intima thickness and that intima-media dissection is computed prior to adventitia-media dissection for a thicker intima ($E_{intima} = 2.9MPa$). Finally, it should be

noted that all simulations assume an identical interface strength for both the intima-media and adventitia-media interfaces ($\sigma_{max} = \tau_{max} = 16kPa$). Accurate experimental characterisation of the interlayer interface strengths for AAA tissue has not yet been reported in the literature. Clearly, a higher adventitia-media interface strength would promote initiation of dissection in the intima-media layer.

7.4   Discussion

A key finding of the present study is that the location of dissection initiation does not coincide with locations of peak von Mises stress in the artery wall. Previous studies have modelled the AAA wall as a single homogenous entity, using the peak computed von Mises stress as a predictor for rupture (Stringfellow et al., 1987; Inzoli et al., 1993; Mower et al., 1993; Elger et al., 1996; Vorp et al., 1998; Raghavan and Vorp, 2000; Raghavan et al., 2000; Doyle et al., 2007). However, the specific rupturing mechanism has not been considered in these studies. The prediction of interlayer dissection presented in this chapter may represent a critical first step in the rupture process of AAA tissue. Dissection may lead to bleb and false lumen formation, ultimately resulting in full rupture of the wall. The finding of the present study which shows that dissection locations do not coincide with locations of von Mises stress concentrations is broadly supported by the study of Georgakarakos et al. (2010) in which it has been reported that aortic blebs, associated with increased risk of rupture, do not correlate with peak von Mises stress computed for a homogeneous AAA wall. Intima flaps and false lumens have been reported in the clinical literature for aneurysms, again suggesting that interlayer dissection is an important mode of damage, potentially contributing to total rupture (Hyodoh et al., 1996; Ring, 2000). Additionally, a study by Raghavan et al. (2011), where the microstructural content of ruptured and unruptured AAAs was investigated, reported a dissection of a AAA wall. The present chapter represents an important first step towards understanding the mechanical role of interlayer dissection in the process of AAA rupture.

It is also demonstrated in this chapter that modelling the AAA wall as an inhomogeneous trilayered structure has a significant effect on the computed distribution of interlayer shear tractions. Both the location and magnitude of interlayer shear traction concentrations are altered if the AAA wall is modelled as a homogeneous structure. Despite this important finding, the author is not aware of a previous finite element study in which the AAA wall is modelled as an inhomogeneous layered structure. Experimental characterisation of AAA tissue has focused on mechanical testing of the entire wall thickness, without examination of the properties of the individual layers of the tissue. Due to the paucity of data in the literature in relation to the thickness and mechanical properties of AAA tissue, this study has relied on published data for the intima, media and adventitia of aged iliac arteries (Schulze-Bauer and Mörth, 2003) and stenotic iliac arteries (Holzapfel et al., 2004).

Interlayer dissection is simulated for three AAA geometries reconstructed from patient-specific CT scans. In geometry 1 dissection initiates at the adventitia-media interface with initial dissection computed at lumen pressure of 132mmHg. Dissection at the intima-media interface initiates at a lumen pressure of 138mmHg. These predictions of dissection initiation are supported by the study of Fillinger et al. (2002) where AAA rupture is reported at a lumen pressure of 142mmHg, indicating that the assumed properties of the individual wall layers and the assumed values of interface strength are in the correct range for AAA tissue. However, as stated above, accurate characterisation of the mechanical properties and interface strengths of AAA tissue should be performed in a follow-on experimental study. The finding of the present study that interlayer dissection is primarily a mode II process, accompanied by interlayer over-closure (compression), indicates that experimental lap-shear experiments would be most appropriate for AAA tissue. Simulations for geometry 2 predict dissection initiation at a lumen pressure of 142mmHg, again similar to the rupture pressure reported by Fillinger et al. (2002). However, the dissection location very different to that computed for geometry 1. In the case of geometry 2, dissection initiates in the intima-media layer, on the lateral right side of the aneurysm far from the neck

region. While dissection initiates at a higher lumen pressure for geometry 2, the crack front propagates a much higher rate than that computed for geometry 1, so that a very large dissection patch is at a lumen pressure of 200mmHg. Finally, initial interlayer dissection is computed at the adventitia-media interface for geometry 3 at an increased lumen pressure of 188mmHg, with no dissection computed at the intima-media interface. The pronounced differences between the dissection predictions, in terms of initiation pressure, location and crack front propagation highlight the critical importance of geometric variation of AAA. These findings provide very strong motivation for the use patient-specific finite element cohesive zone simulations to inform clinical intervention strategies, as opposed to an exclusive reliance on empirical data derived from clinical studies. Ultimate tensile strengths of 0.942MPa and 1.5MPa have been reported for AAA tissue by Raghavan et al. (1996) and Raghavan et al. (2006) respectively. The computed peak von Mises stresses in each AAA wall layer at the lumen pressure at which dissection initiates is lower than these reported values in this study, with the sole exception of the computed peak von Mises stress for geometry 2 in the adventitia layer (1.06MPa) which is slightly above the failure stress reported by Raghavan et al. (1996).

The influence of the thickness of the intima layer on dissection location is also investigated in the present study. A doubling of intima thickness is predicted to reduce the lumen pressure at dissection initiation from 132mmHg to 111mmHg, while also altering the location of dissection initiation with intima-media dissection occurring prior to adventitia-media dissection. Intima-media dissection has been observed in the CT imaging of aneurysms (Hyodoh et al., 1996). This finding that intima thickness has a strong influence on dissection may have clinial implications in light of studies that report a thickening of the intima layer in diseased arteries (Holzapfel et al., 2005; Holzapfel et al., 2007). Again, this highlights the requirement for further experimental characterisation and enhanced imaging techniques in order to accurately determine AAA wall layer geometries.

The presence of an intraluminal thrombus (ILT) has been reported in approximately 75% of AAAs (Vande Geest et al., 2006c). In addition to the importance of modelling the AAA wall as an inhomogeneous structure, this study also demonstrates the pronounced effect of the ILT on interlayer shear tractions. The presence of the ILT significantly alters the location of interlayer shear traction concentrations in comparison to simulations in which the ILT is included. In all cases the removal of the ILT resulted in the prediction of interlayer dissection near the vertebral column. This highlights the importance of the constraining effect of the vertebrae, which results in high concentrations of interlayer tractions if a AAA does not have an ILT. It is therefore suggested that the vertebral column should be represented in all AAA models. Interestingly, when the ILT was removed from the three patient-specific geometries used in this study, rupture initiated at a lower lumen pressure in all cases relative to simulations in which the ILT was included. The effect of the ILT on AAA wall stress has previously been reported by (Wang et al., 2002; Doyle et al., 2007). The present study furthers emphasises the importance of the ILT in terms of interlayer tractions and dissection prediction in an inhomogeneous wall.

Mixed-mode over-closure (compression) at the interface between AAA wall layers is computed due to the applied lumen pressure, demonstrating the importance of CZM over-closure behaviour in the simulation of AAA dissection. The theoretical analyses and computational assessment presented in Chapters 3 and 4, respectively, demonstrate the ability of the NP2 formulation to penalise mixed-mode over-closure, with interface compression leading to a physically realistic increase in resistance to shear (tangential) interface separation. The analyses presented in Chapters 3 and 4 suggest that the XN (Xu and Needleman, 1993) and VB (van den Bosch et al., 2006) CZMs will not provide reliable predictions of AAA dissection due to their failure to correctly penalise mixed-mode over-closure.

This study has a number of limitations. First of all, passive, hyperelastic materials are assigned the AAA wall layers and ILT. In reality the remodelling process involved in AAA evolution is a complex one involving the degradation of elastin

fibres, increase in collagen crosslinking and a reduction in the contractility of the AAA wall (Rizzo et al., 1989; Sakalihasan et al., 1993; Lopez-Candales et al., 1997; Henderson et al., 1999; Wilson et al., 2001; Carmo et al., 2002). A review of AAA histology is provided in the Appendix D. Important initial steps have been taken to develop an active remodelling constitutive framework to describe the evolution of a AAA (Watton et al., 2004; Watton and Hill, 2009). More biaxial tensile tests must also be conducted on AAA tissue in order to develop improved constitutive material formulations. Additionally, experimental dissection tests are required in order to characterise the interlayer dissection properties of the AAA wall. In this study, in the absence of AAA interlayer strength reported in the literature, AAA interlayer strength was estimated based on dissection experiments of healthy arterial tissue (Sommer et al., 2008). Some initial work in this area has been conducted by Pasta et al. (2011) for ascending thoracic aortic aneurysms. Residual stresses, which may exist in the AAA wall in vivo (Holzapfel et al., 2000), and wall shear stress induced by blood flow (Peattie et al., 1996) were also neglected in this study.

In conclusion, this study provides, for the first time, predictions of interlayer dissection in inhomogeneous trilayered AAA walls. Dissection locations are not found to correlate with locations of von Mises stress concentrations. Furthermore, initial interlayer dissection pressures and locations, in addition to the rate of dissection propagation are found to be highly influenced by the geometric variations between the three patient-specific CT reconstructed aneurysms. Finally, the inclusion of an ILT and the deformation constraint provided by the vertebral column were found to significantly influence the lumen pressures at which dissection initiates, and also strongly influences the location of dissection. This study highlights the potential of CZMs to predict interlayer dissection in CT derived geometries to guide the clinical management of AAAs.

7.5 References

Alexander, J. J. (2004) The pathobiology of aortic aneurysms. *Journal of Surgical Research,* 117**,** 163-175.

Carmo, M., Colombo, L., Bruno, A., Corsi, F. R. M., Roncoroni, L., Cuttin, M. S., et al. (2002) Alteration of elastin, collagen and their cross-links in abdominal aortic aneurysms. *European Journal of Vascular & Endovascular Surgery,* 23**,** 543-549.

Chaikof, E. L., Brewster, D. C., Dalman, R. L., Makaroun, M. S., Illig, K. A., Sicard, G. A., et al. (2009) SVS practice guidelines for the care of patients with an abdominal aortic aneurysm: Executive summary. *Journal of vascular surgery,* 50**,** 880.

Darling, R. C., Messina, C. R., Brewster, D. C.&Ottinger, L. W. (1977) Autopsy study of unoperated abdominal aortic aneurysms. *Circulation,* 56**,** 161-164.

De Santis, G., Mortier, P., De Beule, M., Segers, P., Verdonck, P.&Verhegghe, B. (2010) Patient-specific computational fluid dynamics: structured mesh generation from coronary angiography. *Medical and Biological Engineering and Computing,* 48**,** 371-380.

Doyle, B. J., Callanan, A.&Mcgloughlin, T. M. (2007) A comparison of modelling techniques for computing wall stress in abdominal aortic aneurysms. *BioMedical Engineering OnLine,* 6**,** 38.

Dryjski, M., Driscoll, J. L., Blair, R. C., Mcgurrin, M. A., Dagher, F. J., Ceraolo, M. J., et al. (1994) The small abdominal aortic aneurysm: the eternal dilemma. *The Journal of cardiovascular surgery,* 35**,** 95.

Elger, D. F., Blackketter, D. M., Budwig, R. S.&Johansen, K. H. (1996) The influence of shape on the stresses in model abdominal aortic aneurysms. *Journal of Biomechanical Engineering,* 118**,** 326.

Ferrara, A.&Pandolfi, A. (2008) Numerical modelling of fracture in human arteries. *Computer methods in biomechanics and biomedical engineering,* 11**,** 553-567.

Fillinger, M. F., Raghavan, M. L., Marra, S. P., Cronenwett, J. L.&Kennedy, F. E. (2002) In vivo analysis of mechanical wall stress and abdominal aortic aneurysm rupture risk. *Journal of vascular surgery,* 36**,** 589-597.

Gasser, T. C.&Holzapfel, G. A. (2007) Modeling plaque fissuring and dissection during balloon angioplasty intervention. *Annals of Biomedical Engineering,* 35**,** 711-723.

Georgakarakos, E., Ioannou, C. V., Papaharilaou, Y., Kostas, T., Tsetis, D.&Katsamouris, A. N. (2010) Peak wall stress does not necessarily predict the location of rupture in abdominal aortic aneurysms. *European Journal of Vascular and Endovascular Surgery,* 39**,** 302-304.

Hall, A. J., Busse, E. F. G., Mccarville, D. J.&Burgess, J. J. (2000) Aortic wall tension as a predictive factor for abdominal aortic aneurysm rupture: improving the selection of patients for abdominal aortic aneurysm repair. *Annals of Vascular Surgery,* 14**,** 152-157.

Haslach, H. W., Riley, P.&Molotsky, A. (2011) The Influence of Medial Substructures on Rupture in Bovine Aortas. *Cardiovascular Engineering and Technology***,** 1-16.

Henderson, E. L., Geng, Y. J., Sukhova, G. K., Whittemore, A. D., Knox, J.&Libby, P. (1999) Death of smooth muscle cells and expression of mediators of apoptosis by T lymphocytes in human abdominal aortic aneurysms. *Circulation,* 99**,** 96.

Holzapfel, G. A., Gasser, T. C.&Ogden, R. W. (2000) A new constitutive framework for arterial wall mechanics and a comparative study of material models. *Journal of elasticity,* 61**,** 1-48.

Holzapfel, G. A., Sommer, G., Auer, M., Regitnig, P.&Ogden, R. W. (2007) Layer-specific 3D residual deformations of human aortas with non-atherosclerotic intimal thickening. *Annals of Biomedical Engineering,* 35**,** 530-545.

Holzapfel, G. A., Sommer, G., Gasser, C. T.&Regitnig, P. (2005) Determination of layer-specific mechanical properties of human coronary arteries with nonatherosclerotic intimal thickening and related constitutive modeling. *American Journal of Physiology-Heart and Circulatory Physiology,* 289**,** H2048.

Holzapfel, G. A., Sommer, G.&Regitnig, P. (2004) Anisotropic mechanical properties of tissue components in human atherosclerotic plaques. *Transactions of the ASME-K-Journal of Biomechanical Engineering,* 126**,** 657-665.

Hultgren, R., Forsberg, J., Alfredsson, L., Swedenborg, J.&Leander, K. (2012) Regional variation in the incidence of abdominal aortic aneurysm in Sweden. *British Journal of Surgery,* 99**,** 647-653.

Hyodoh, H., Hyodoh, K., Takahashi, K., Yamagata, M.&Kanazawa, K. (1996) Three-dimensional CT imaging of an isolated dissecting aneurysm of the superior mesenteric artery. *Abdominal imaging,* 21**,** 515-516.

Inzoli, F., Boschetti, F., Zappa, M., Longo, T.&Fumero, R. (1993) Biomechanical factors in abdominal aortic aneurysm rupture. *European journal of vascular surgery,* 7**,** 667.

J. Thubrikar, M. L., F. Robicsek, J. Al-Soudi, B. Fowler M. (2001) Mechanical properties of abdominal aortic aneurysm wall. *Journal of medical engineering & technology,* 25**,** 133-142.

Kuivaniemi, H.&Elmore, J. R. (2012) Opportunities in Abdominal Aortic Aneurysm Research: Epidemiology, Genetics, and Pathophysiology. *Annals of Vascular Surgery,* 26**,** 862-870.

Lederle, F. A., Johnson, G. R., Wilson, S. E., Ballard, D. J., Jordan, W. D., Jr., Blebea, J., et al. (2002) Rupture Rate of Large Abdominal Aortic Aneurysms in Patients Refusing or Unfit for Elective Repair. *JAMA,* 287**,** 2968-2972.

Li, Z.&Kleinstreuer, C. (2005) A new wall stress equation for aneurysm-rupture prediction. *Annals of Biomedical Engineering,* 33**,** 209-213.

Lopez-Candales, A., Holmes, D. R., Liao, S., Scott, M. J., Wickline, S. A.&Thompson, R. W. (1997) Decreased vascular smooth muscle cell density in medial degeneration of human abdominal aortic aneurysms. *The American journal of pathology,* 150**,** 993.

Materialise (2002) MIMICS User Manual. Materialise Leuven.

Moll, F. L., Powell, J. T., Fraedrich, G., Verzini, F., Haulon, S., Waltham, M., et al. (2011) Management of abdominal aortic aneurysms clinical practice guidelines of the European society for vascular surgery. *European Journal of Vascular and Endovascular Surgery,* 41**,** 1.

Mower, W. R., Baraff, L. J.&Sneyd, J. (1993) Stress distributions in vascular aneurysms: factors affecting risk of aneurysm rupture. *The Journal of surgical research,* 55**,** 155.

Pasta, S., Phillippi, J. A., Gleason, T. G.&Vorp, D. A. (2011) Effect of aneurysm on the mechanical dissection properties of the human ascending thoracic aorta. *The Journal of Thoracic and Cardiovascular Surgery,* 143**,** 460-467.

Peattie, R. A., Asbury, C. L., Bluth, E. I.&Riehle, T. J. (1996) Steady flow in models of abdominal aortic aneurysms. Part II: Wall stresses and their implication for in vivo thrombosis and rupture. *Journal of ultrasound in medicine,* 15**,** 689-696.

Phillippi, J. A., Pasta, S.&Vorp, D. A. (2011) Biomechanics and Pathobiology of Aortic Aneurysms. *Biomechanics and Mechanobiology of Aneurysms***,** 67-118.

Raghavan, M. L., Hanaoka, M. M., Kratzberg, J. A., Higuchi, M. D. L.&Da Silva, E. S. (2011) Biomechanical failure properties and microstructural content of ruptured and unruptured abdominal aortic aneurysms. *Journal of Biomechanics,* 44**,** 2501-2507.

Raghavan, M. L., Kratzberg, J., Castro De Tolosa, E. M., Hanaoka, M. M., Walker, P.&Da Silva, E. S. (2006) Regional distribution of wall thickness and failure properties of human abdominal aortic aneurysm. *Journal of Biomechanics,* 39**,** 3010-3016.

Raghavan, M. L.&Vorp, D. A. (2000) Toward a biomechanical tool to evaluate rupture potential of abdominal aortic aneurysm: identification of a finite strain constitutive model and evaluation of its applicability. *Journal of Biomechanics,* 33**,** 475-482.

Raghavan, M. L., Vorp, D. A., Federle, M. P., Makaroun, M. S.&Webster, M. W. (2000) Wall stress distribution on three-dimensionally reconstructed models of human abdominal aortic aneurysm. *Journal of vascular surgery,* 31**,** 760-769.

Raghavan, M. L., Webster, M. W.&Vorp, D. A. (1996) Ex vivo biomechanical behavior of abdominal aortic aneurysm: assessment using a new mathematical model. *Annals of Biomedical Engineering,* 24**,** 573-582.

Ring, W. S. (2000) Congenital Heart Surgery Nomenclature and Database Project: aortic aneurysm, sinus of Valsalva aneurysm, and aortic dissection. *The Annals of thoracic surgery,* 69**,** 147-163.

Rizzo, R. J., Mccarthy, W. J., Dixit, S. N., Lilly, M. P., Shively, V. P., Flinn, W. R., et al. (1989) Collagen types and matrix protein content in human abdominal aortic aneurysms. *Journal of vascular surgery: official publication, the Society for Vascular Surgery [and] International Society for Cardiovascular Surgery, North American Chapter,* 10**,** 365.

Sakalihasan, N., Heyeres, A., Nusgens, B. V., Limet, R.&Lapiere, C. M. (1993) Modifications of the extracellular matrix of aneurysmal abdominal aortas as a function of their size. *European journal of vascular surgery,* 7**,** 633.

Schulze-Bauer, C. A. J.&Mörth, C. (2003) Passive biaxial mechanical response of aged human iliac arteries. *Journal of Biomechanical Engineering,* 125**,** 395.

Scott, R. A. P. (1999) UK small aneurysms trial. *The Lancet,* 353**,** 408.

Sommer, G., Gasser, T. C., Regitnig, P., Auer, M.&Holzapfel, G. A. (2008) Dissection Properties of the Human Aortic Media: An Experimental Study. *Journal of Biomechanical Engineering,* 130**,** 021007.

Sonesson, B., Sandgren, T.&Länne, T. (1999) Abdominal aortic aneurysm wall mechanics and their relation to risk of rupture. *European Journal of Vascular & Endovascular Surgery,* 18**,** 487-493.

Standring, S. (2008) *Gray's anatomy*, Churchill Livingstone, Elsevier.

Stenbaek, J., Kalin, B.&Swedenborg, J. (2000) Growth of thrombus may be a better predictor of rupture than diameter in patients with abdominal aortic aneurysms. *European Journal of Vascular & Endovascular Surgery,* 20**,** 466-469.

Stringfellow, M. M., Lawrence, P. F.&Stringfellow, R. G. (1987) The influence of aorta-aneurysm geometry upon stress in the aneurysm wall. *J Surg Res,* 42**,** 425-33.

Tong, P.&Fung, Y. C. (1976) The stress-strain relationship for the skin. *Journal of Biomechanics,* 9**,** 649-657.

Vallabhaneni, S. R., Gilling-Smith, G. L., How, T. V., Carter, S. D., Brennan, J. A.&Harris, P. L. (2004) Heterogeneity of tensile strength and matrix metalloproteinase activity in the wall of abdominal aortic aneurysms. *Journal of Endovascular Therapy,* 11**,** 494-502.

van den Bosch, M. J., Schreurs, P. J. G.&Geers, M. G. D. (2006) An improved description of the exponential Xu and Needleman cohesive zone law for mixed-mode decohesion. *Engineering Fracture Mechanics,* 73**,** 1220-1234.

Vande Geest, J. P., Di Martino, E. S., Bohra, A., Makaroun, M. S.&Vorp, D. A. (2006a) A Biomechanics-Based Rupture Potential Index for Abdominal Aortic Aneurysm Risk Assessment. *Annals of the New York Academy of Sciences,* 1085**,** 11-21.

Vande Geest, J. P., Sacks, M. S.&Vorp, D. A. (2006b) The effects of aneurysm on the biaxial mechanical behavior of human abdominal aorta. *Journal of Biomechanics,* 39**,** 1324-1334.

Vande Geest, J. P., Sacks, M. S.&Vorp, D. A. (2006c) A planar biaxial constitutive relation for the luminal layer of intra-luminal thrombus in abdominal aortic aneurysms. *Journal of Biomechanics,* 39**,** 2347-2354.

Vorp, D. A. (2007) Biomechanics of abdominal aortic aneurysm. *Journal of Biomechanics,* 40**,** 1887-1902.

Vorp, D. A.&Geest, J. P. V. (2005a) Biomechanical determinants of abdominal aortic aneurysm rupture. *Arteriosclerosis, Thrombosis, and Vascular Biology,* 25**,** 1558-1566.

Vorp, D. A.&Geest, J. P. V. (2005b) Biomechanical determinants of abdominal aortic aneurysm rupture. *Arteriosclerosis, Thrombosis, and Vascular Biology,* 25**,** 1558.

Vorp, D. A., Raghavan, M. L.&Webster, M. W. (1998) Mechanical wall stress in abdominal aortic aneurysm: influence of diameter and asymmetry. *Journal of vascular surgery,* 27**,** 632-639.

Wang, D. H. J., Makaroun, M., Webster, M. W.&Vorp, D. A. (2001) Mechanical properties and microstructure of intraluminal thrombus from abdominal aortic aneurysm. *Journal of Biomechanical Engineering,* 123**,** 536.

Wang, D. H. J., Makaroun, M. S., Webster, M. W.&Vorp, D. A. (2002) Effect of intraluminal thrombus on wall stress in patient-specific models of abdominal aortic aneurysm. *Journal of vascular surgery,* 36**,** 598-604.

Watton, P. N.&Hill, N. A. (2009) Evolving mechanical properties of a model of abdominal aortic aneurysm. *Biomechanics and Modeling in Mechanobiology,* 8**,** 25-42.

Watton, P. N., Hill, N. A.&Heil, M. (2004) A mathematical model for the growth of the abdominal aortic aneurysm. *Biomechanics and Modeling in Mechanobiology,* 3**,** 98-113.

Wilson, K. A., Lindholt, J. S., Hoskins, P. R., Heickendorff, L., Vammen, S.&Bradbury, A. W. (2001) The Relationship Between Abdominal Aortic Aneurysm Distensibility and Serum Markers of Elastin and Collagen Metabolism. *European Journal of Vascular and Endovascular Surgery,* 21**,** 175-178.

Xu, X. P.&Needleman, A. (1993) Void nucleation by inclusion debonding in a crystal matrix. *Modelling and Simulation in Materials Science and Engineering,* 2**,** 417-418.

7.6   Tables and Figures
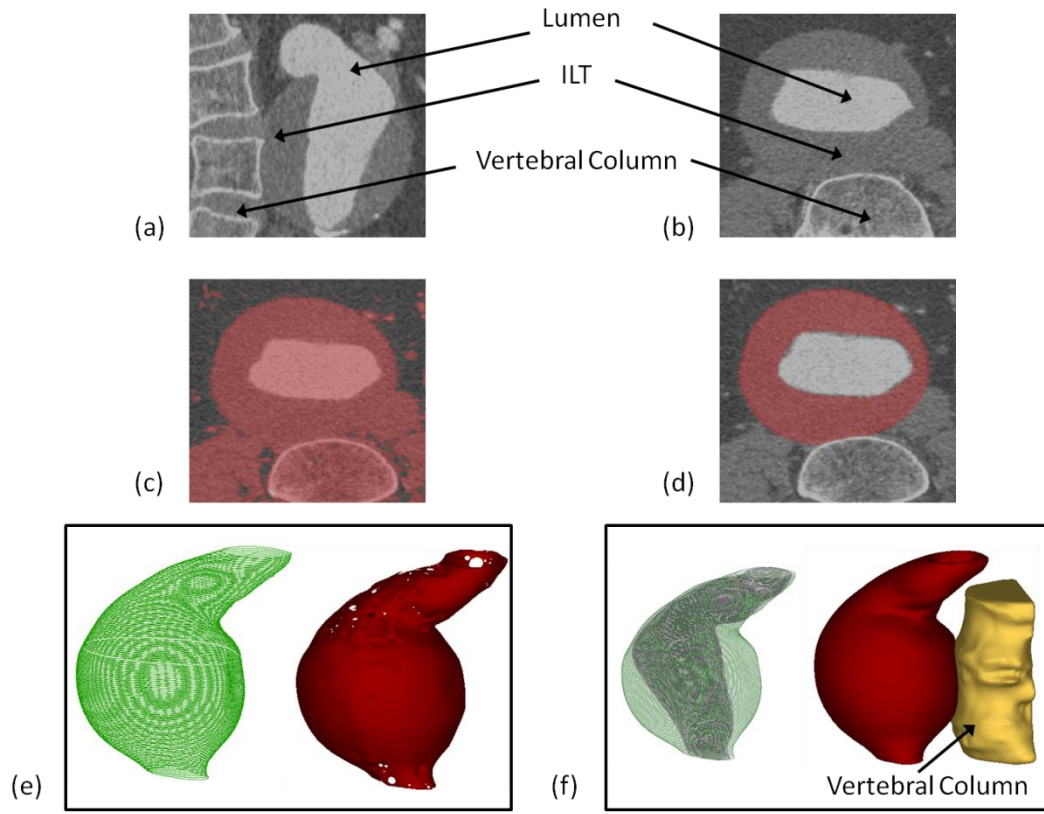
Figure 7-1: Outline of the reconstruction steps taken to create final AAA geometry. CT scans of the aneurysm (geometry 1) in the sagittal and transverse planes are shown in (a) and (b) respectively. The initial and final aneurysm 'mask' in the transverse plane is shown in (c) and (d) respectively. The initial and final 3D AAA geometry together with surface polylines is shown in (e) in (f) respectively with the position of the vertebral column also indicated.
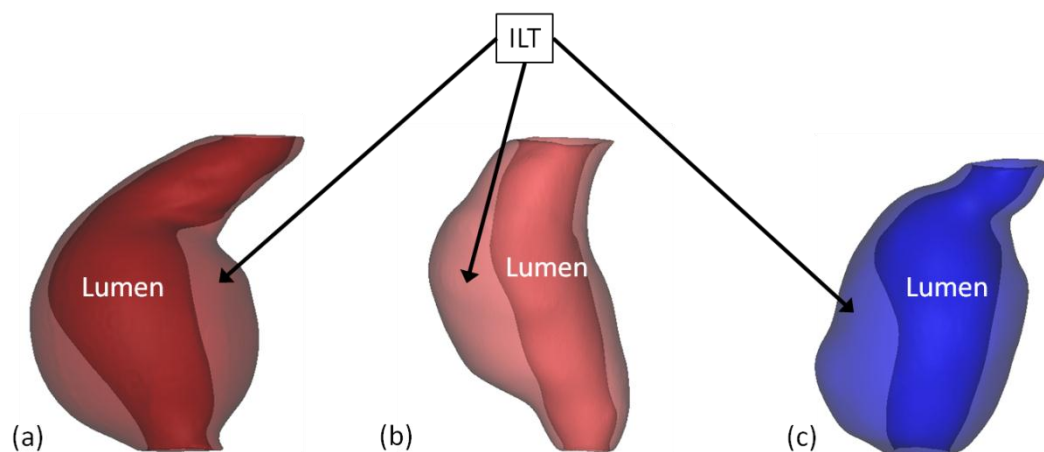
Figure 7-2: Three AAA geometries utilised: (a) geometry 1(b) geometry 2 and (c) geometry3. The intraluminal thrombus (ILT) and lumen is indicated for each AAA geometry.
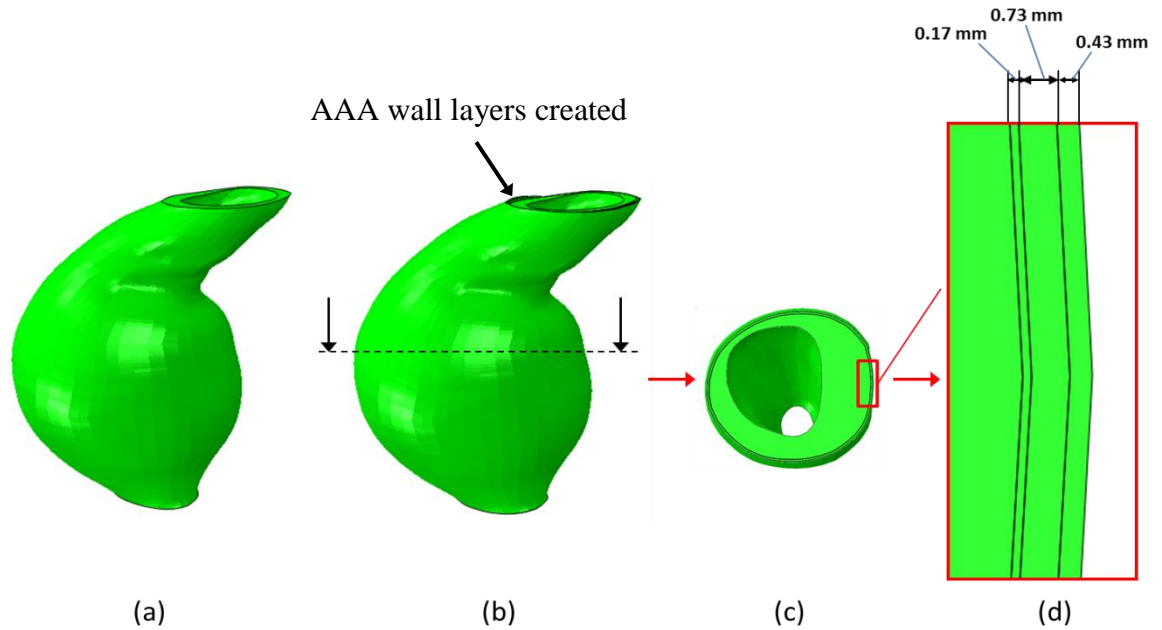
Figure 7-3: (a) Geometry of the reconstructed thrombus for AAA Geometry 1; (b) AAA wall layers are created by offsetting the wall of the thrombus three times; (c) Section view of the AAA geometry as indicated by the section line in (b); Zoomed in image of the individual AAA wall layers- intima, media and adventitia layer thicknesses of 0.17mm, 0.73mm and 0.43mm respectively are assigned (Holzapfel et al, 2004).
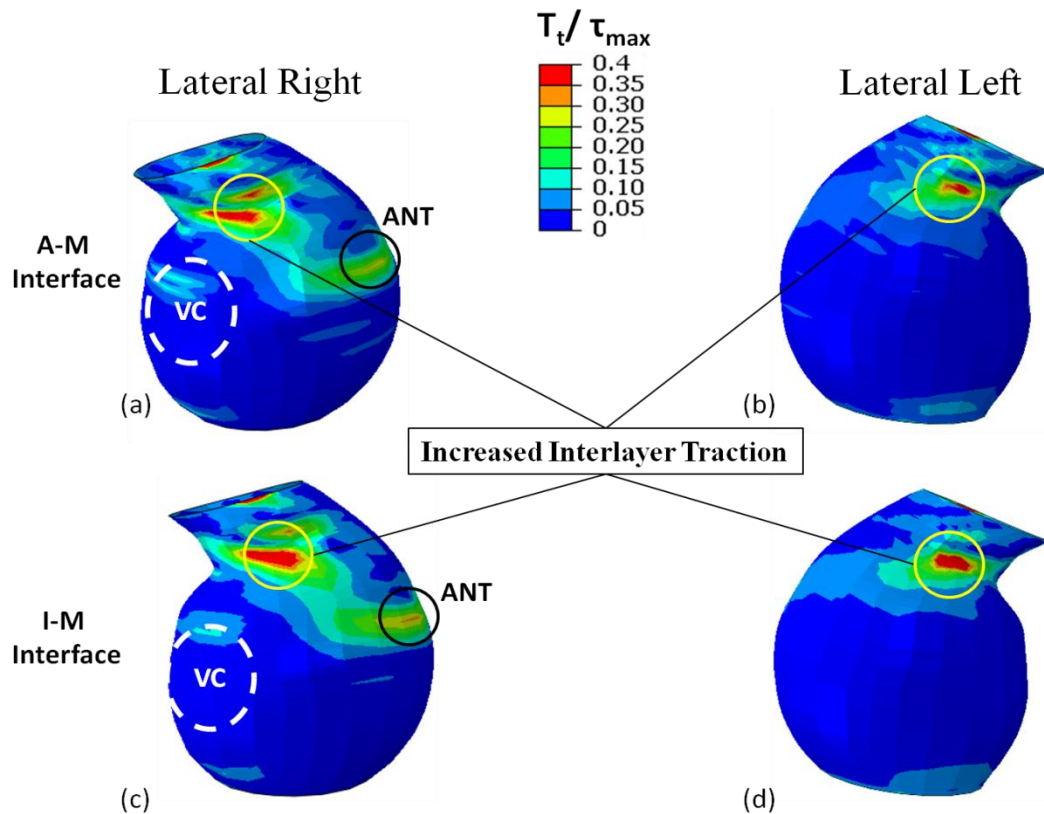
Figure 7-4: Normalised interlayer shear traction (T_t/τ_{max}) following 100mmHg of applied lumen pressure when individual material properties are assigned to each AAA wall layer and an intraluminal thrombus (ILT) is included.

243

Figure 7-5: Normalised interlayer shear traction (T_t/τ_{max}) following 100mmHg of applied lumen pressure when media layer properties are assigned to each AAA wall layer and an intraluminal thrombus (ILT) is included.
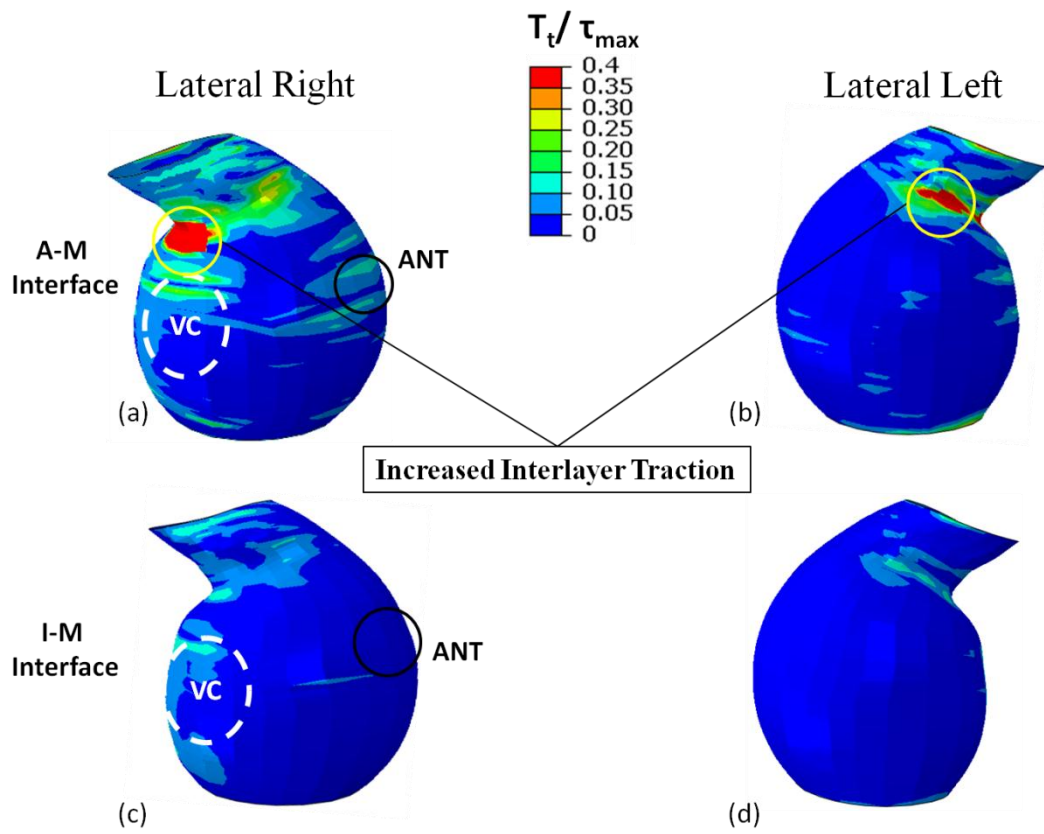
Figure 7-6: Normalised interlayer shear traction (T_t/τ_{max}) following 100mmHg of applied lumen pressure when individual material properties are assigned to each AAA wall layer but an intraluminal thrombus (ILT) is neglected.
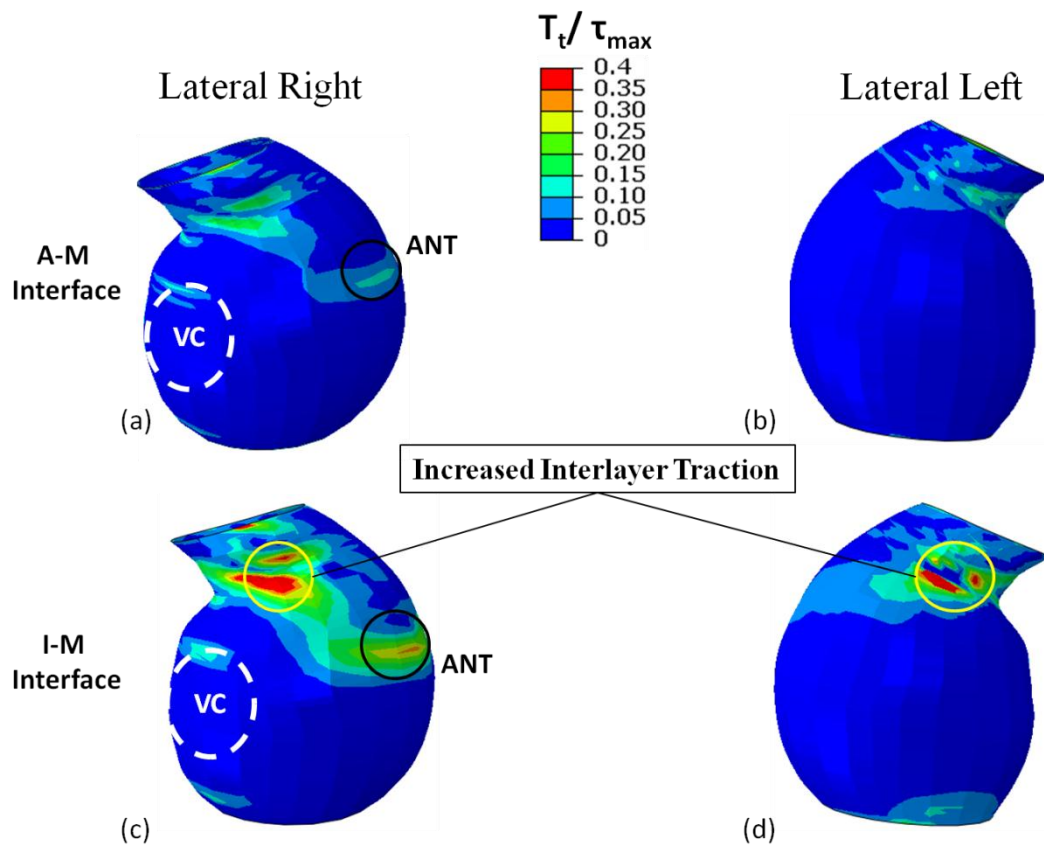
Figure 7-7: Computed interface shear traction as a function of applied lumen pressure for 6 nodes at the adventitia-media interface for geometry 1. A region where the critical cohesive characteristic distance is exceeded ($\Delta_s/\Delta_c > 1$) is shown on the right together with the position of the vertebral column (VC). Individual wall layer properties are used for the intima, media and adventitia layers and the intraluminal thrombus (ILT) is included.
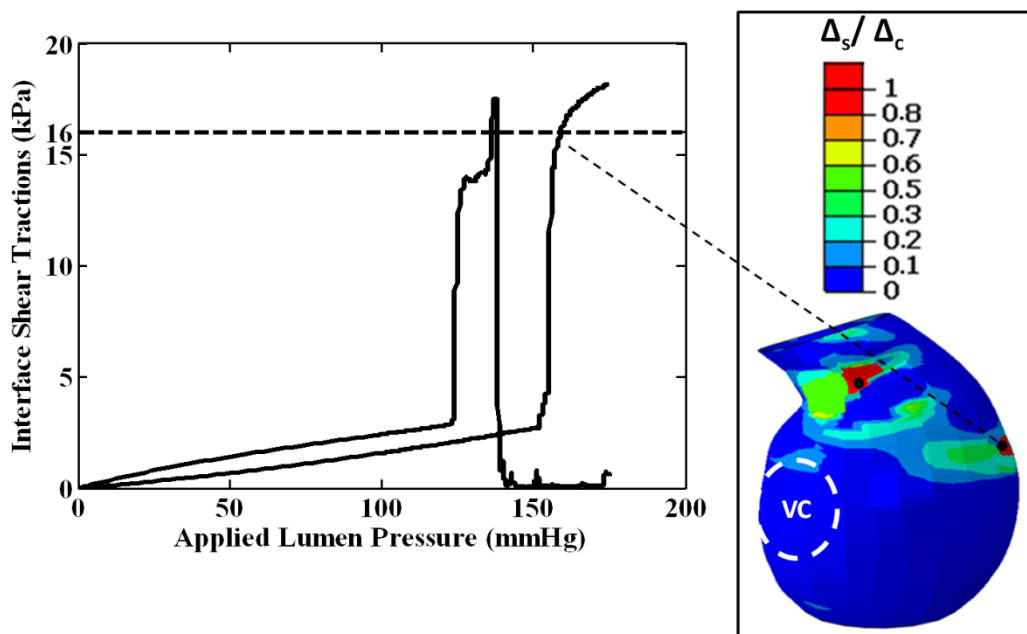
Figure 7-8: Computed interface shear traction as a function of applied lumen pressure for 2 nodes at the intima-media interface for geometry 1. Two regions where the critical cohesive characteristic distance is exceeded ($\Delta_s/\Delta_c > 1$) are shown on the right together with the position of the vertebral column (VC). Individual wall layer properties are chosen for the intima, media and adventitia layers and the intraluminal thrombus (ILT) is included.

Figure 7-9: Computed interface shear traction as a function of applied lumen pressure for 8 nodes at the adventitia-media interface for geometry 1 when the intraluminal thrombus (ILT) is omitted. A region in which the critical cohesive characteristic distance is exceeded ($\Delta_s/\Delta_c > 1$) is shown on the right together with the position of the vertebral column (VC). The initial dissection region is also highlighted. Individual wall layer properties are chosen for the intima, media and adventitia layers.

Figure 7-10: Distribution of computed von Mises stress in (a) the adventitia layer and (b) the media layer at an applied lumen pressure of 150mmHg for geometry 1. Computed regions of interlayer dissection do not coincide with areas of peak von Mises stress. Individual wall layer properties are chosen for the intima, media and adventitia layers. The position of the vertebral column (VC) is also indicated.

Figure 7-3: Distribution of computed von Mises stress in the adventitia layer at an applied lumen pressure of 93mmHg for geometry 1 where the intraluminal thrombus (ILT) is omitted. Individual wall layer properties are chosen for the intima, media and adventitia layers. The position of the vertebral column (VC) is also indicated.
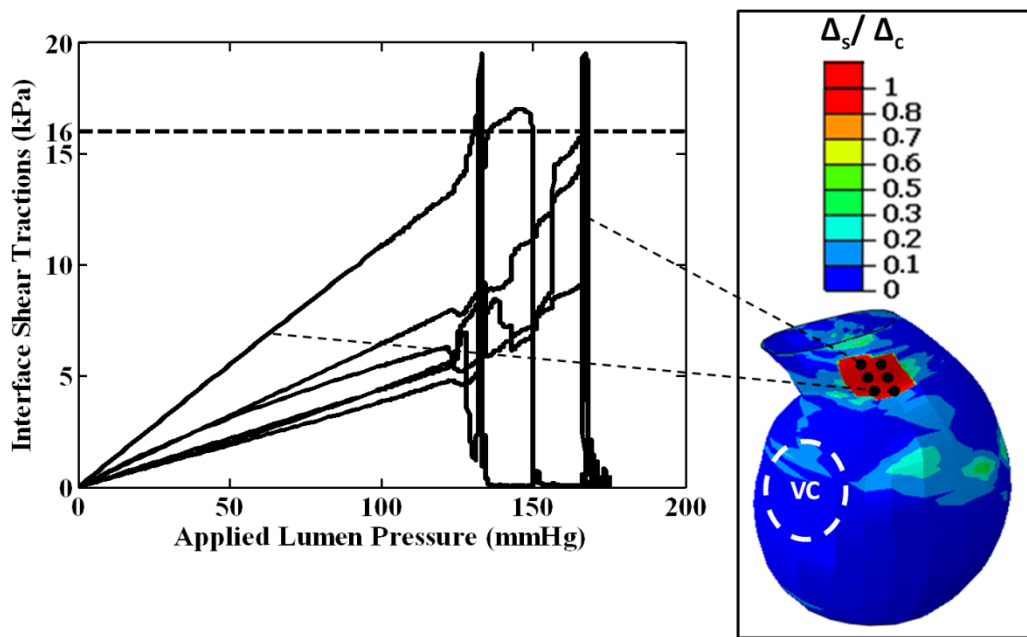
Figure 7-4: (a) Computed interface shear traction as a function of applied lumen pressure at the intima-media interface for geometry 2. A significant region in which the critical cohesive characteristic distance is exceeded ($\Delta_s/\Delta_c > 1$) is shown on the right together with the position of the vertebral column (VC). The initial computed dissection region is also indicated. The dissection patch is also shown for a lumen pressure of: (b) 142mmHg; (c) 160mmHg; (d) 170mmHg; (e) 180mmHg and (f) 195mmHg. Individual wall layer properties are chosen for the intima, media and adventitia layers and the intraluminal thrombus (ILT) is included.
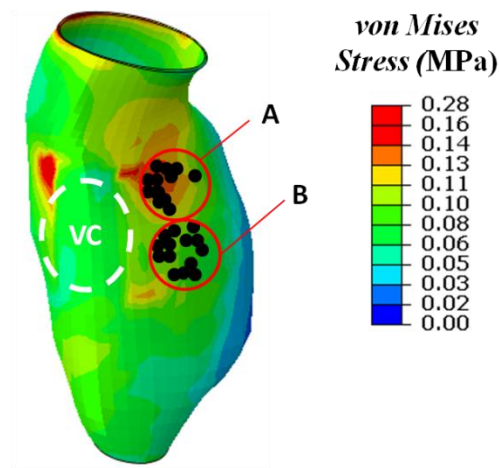
Figure 7-5: Distribution of computed von Mises stress in the media layer at an applied lumen pressure of 142mmHg for geometry 2. While a region of interlayer dissection (dissection patch A) coincides with peak von Mises stress, the computed region of initial interlayer dissection at the intima-media interface (dissection patch B) does not coincide with region of peak von Mises stress. Individual wall layer properties are chosen for the intima, media and adventitia layers. The position of the vertebral column (VC) is also indicated.
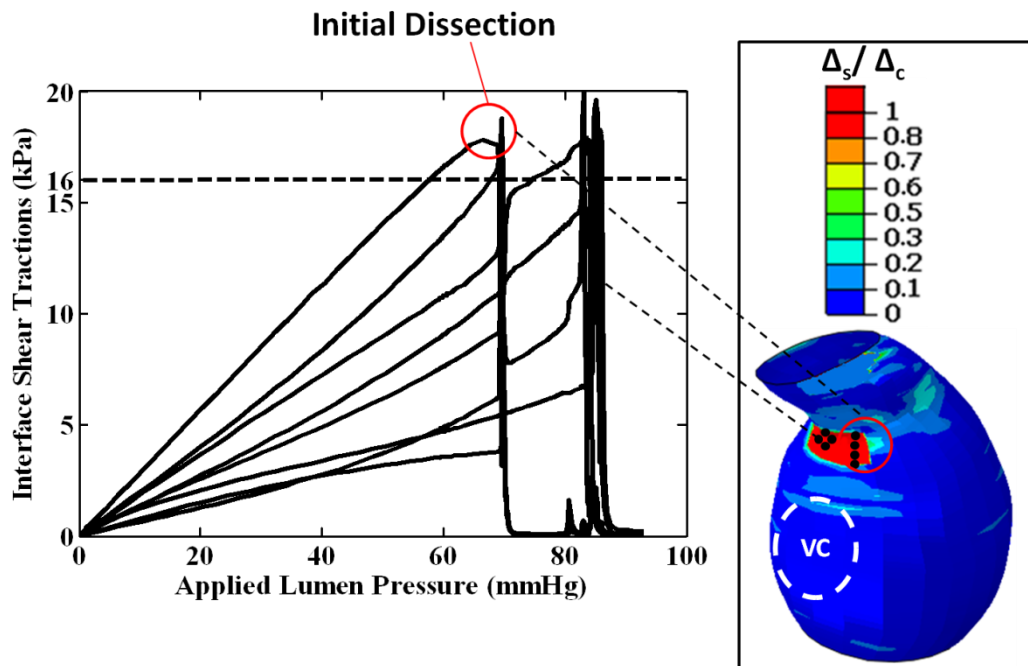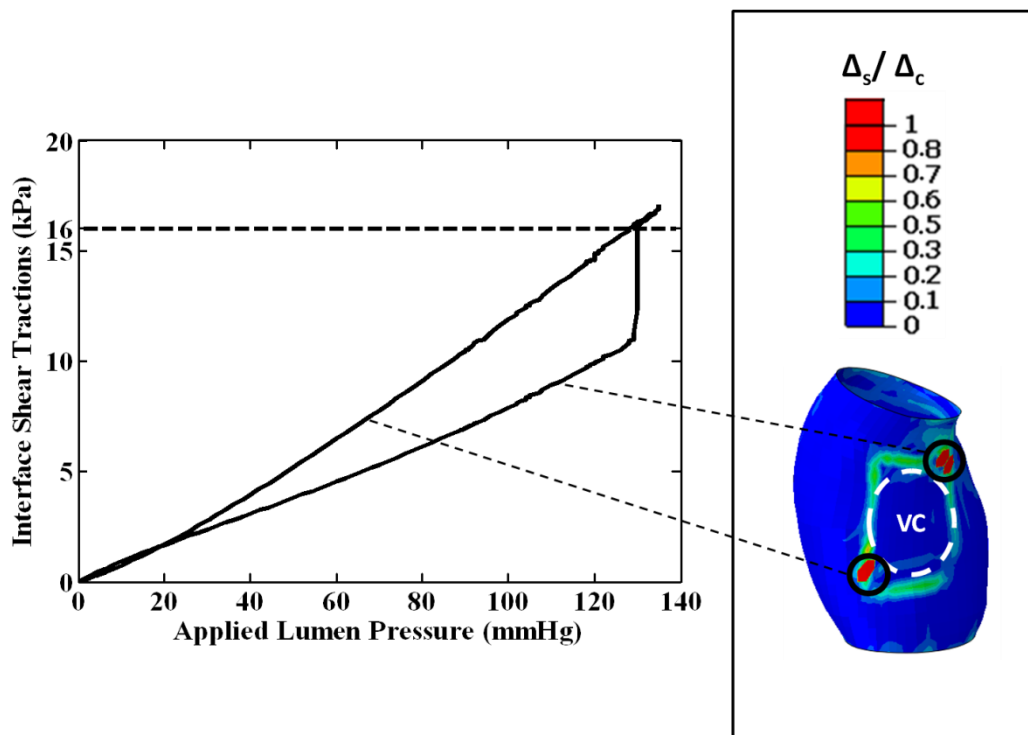

Figure 7-6: Computed interface shear traction as a function of applied lumen pressure at 2 nodes at the adventitia-media interface for geometry 2 when the intraluminal thrombus (ILT) is omitted. Two regions in which the critical cohesive characteristic distance is exceeded ($\Delta_s/\Delta_c > 1$) are shown on the right together with the position of the vertebral column (VC). Individual wall layer properties are chosen for the intima, media and adventitia layers.
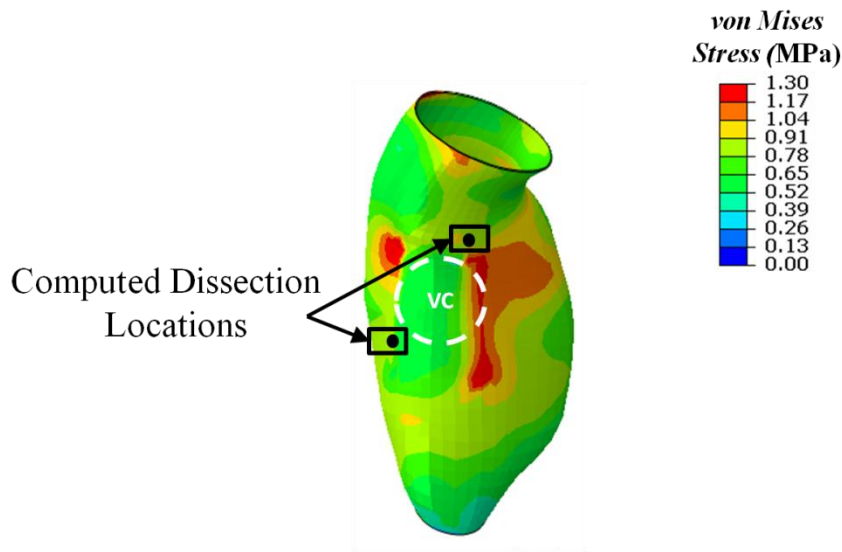
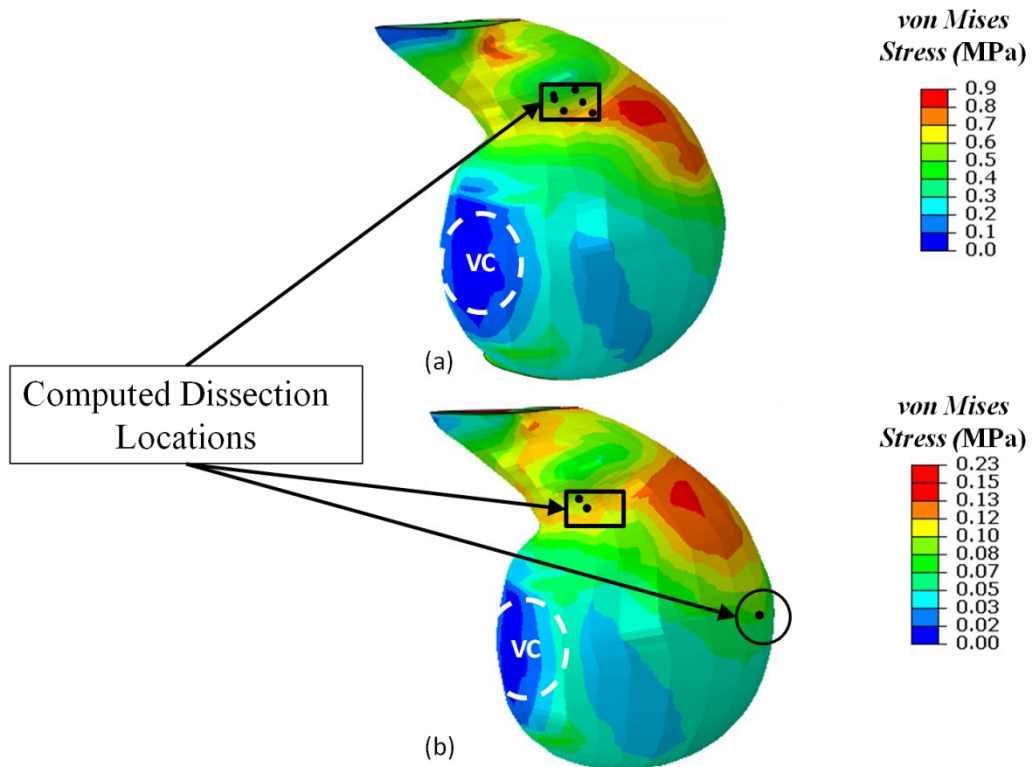Figure 7-7: Distribution of computed von Mises stress in the adventitia layer at an applied lumen pressure of 135mmHg for geometry 2 where the intraluminal thrombus (ILT) is omitted. Computed regions of initial interlayer dissection at the adventitia-media do not coincide with region of peak von Mises stress. Individual wall layer properties are chosen for the intima, media and adventitia layers. The position of the vertebral column (VC) is also indicated.
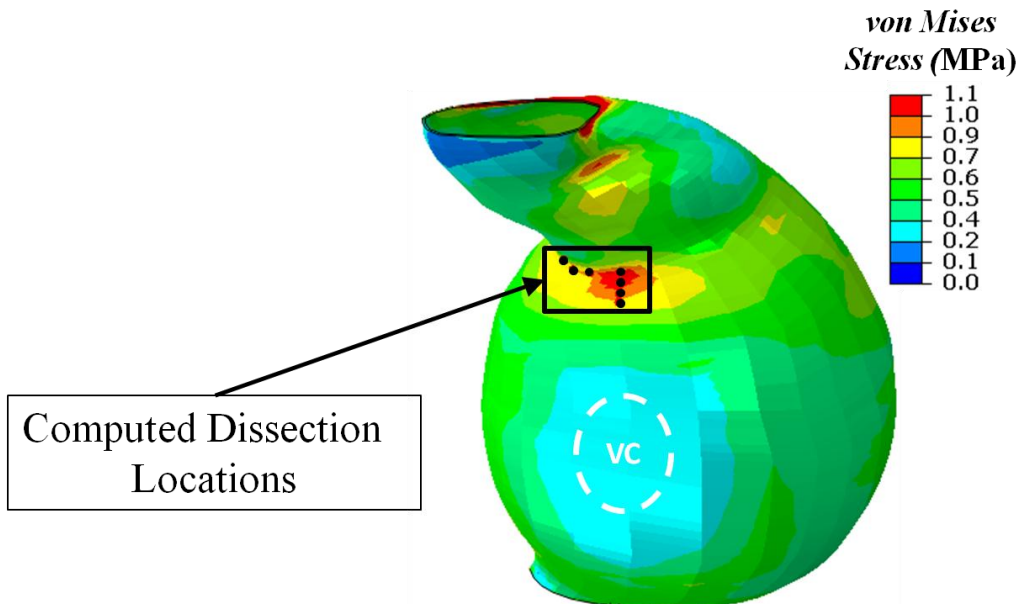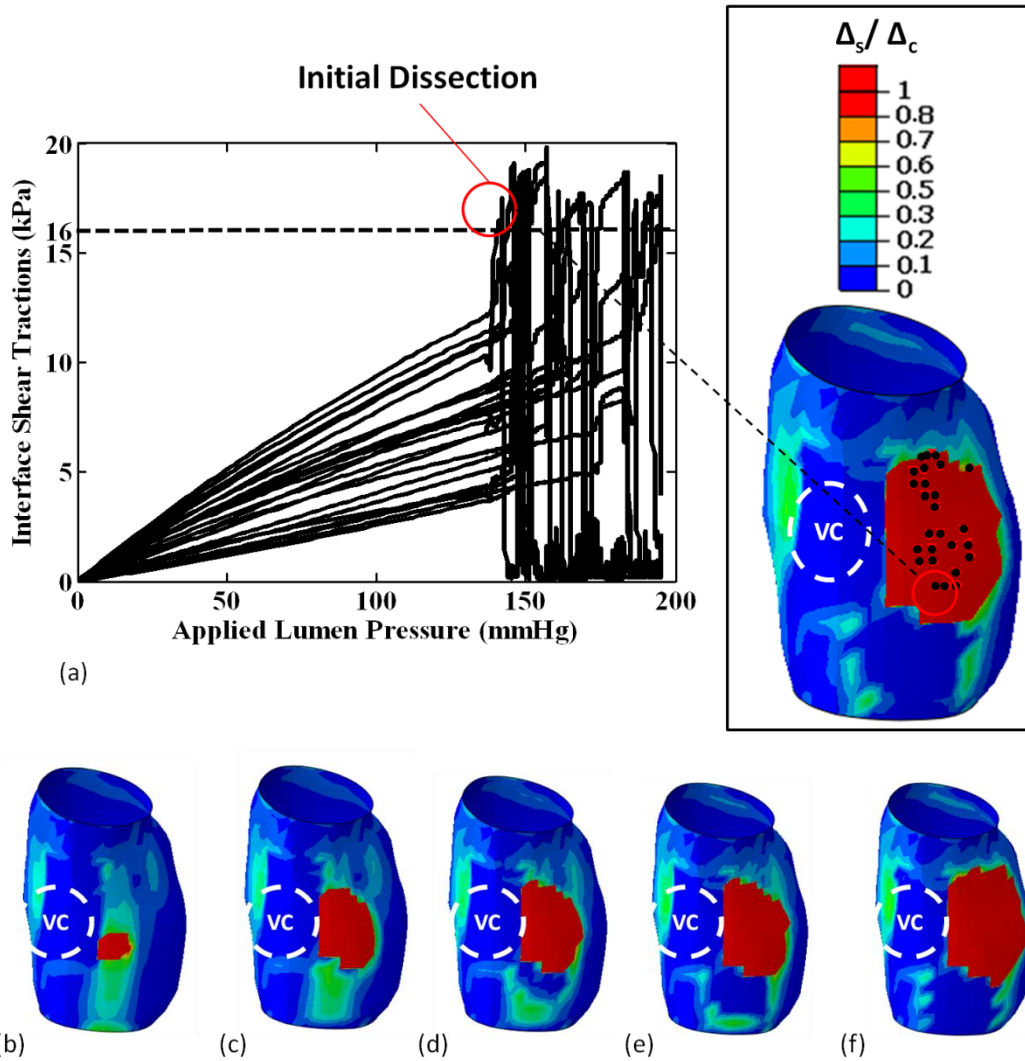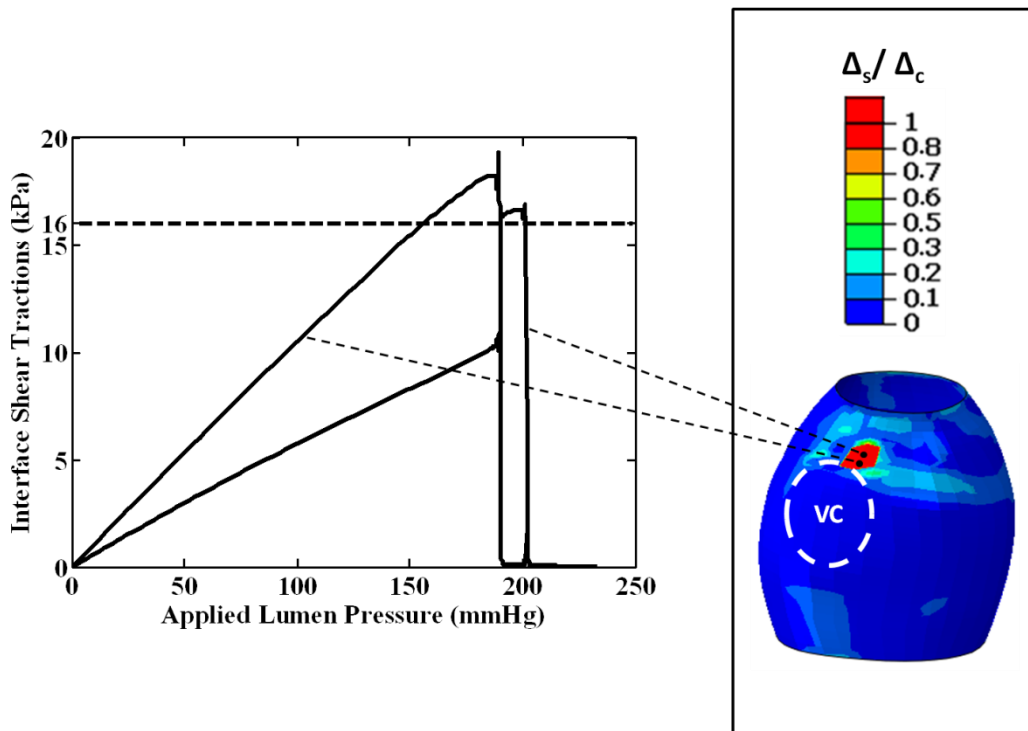

Figure 7-8: Computed interface shear traction as a function of applied lumen pressure at 2 nodes at the adventitia-media interface for geometry 3 when the intraluminal thrombus (ILT) is included. A region in which the critical cohesive characteristic distance is exceeded ($\Delta_s / \Delta_c > 1$) is shown on the right together with the position of the vertebral column (VC). Individual wall layer properties are chosen for the intima, media and adventitia layers.
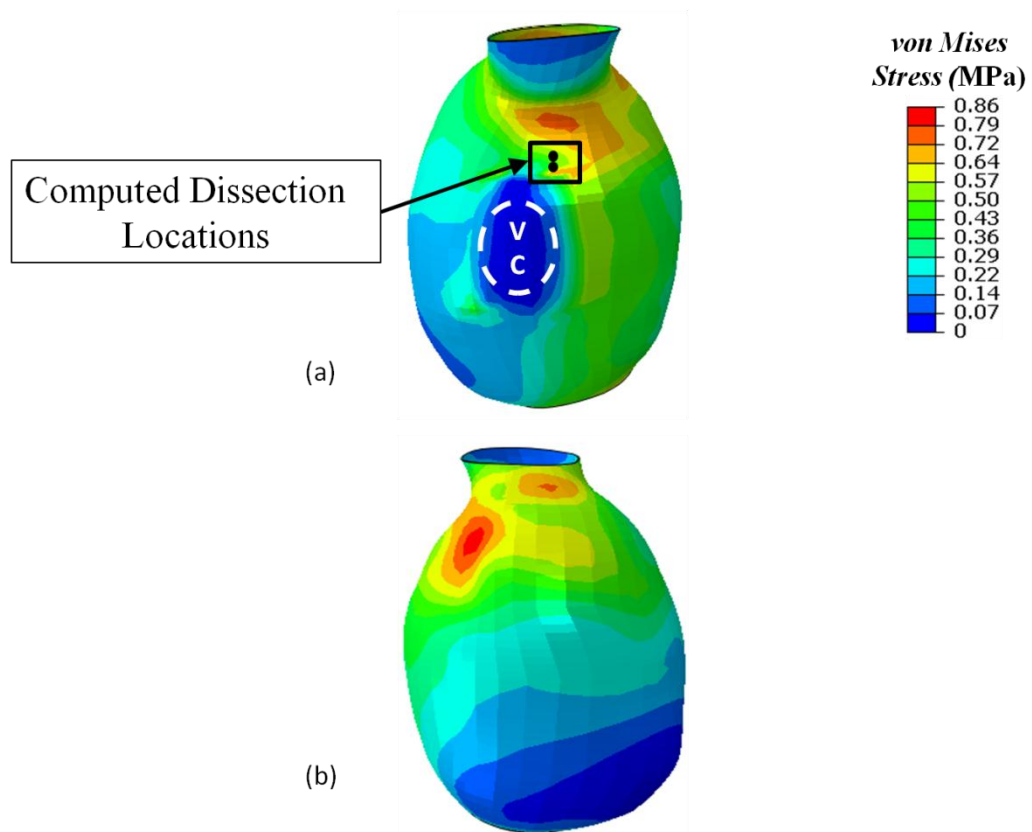
Figure 7-9: Distribution of computed von Mises stress in the adventitia layer, on the (a) posterior and (b) anterior AAA sides, at an applied lumen pressure of 188mmHg for geometry 3 where the intraluminal thrombus (ILT) is included. The computed region of interlayer dissection at the adventitia-media interface does not coincide with regions of peak von Mises stress. Individual wall layer properties are chosen for the intima, media and adventitia layers. The position of the vertebral column (VC) is also indicated.
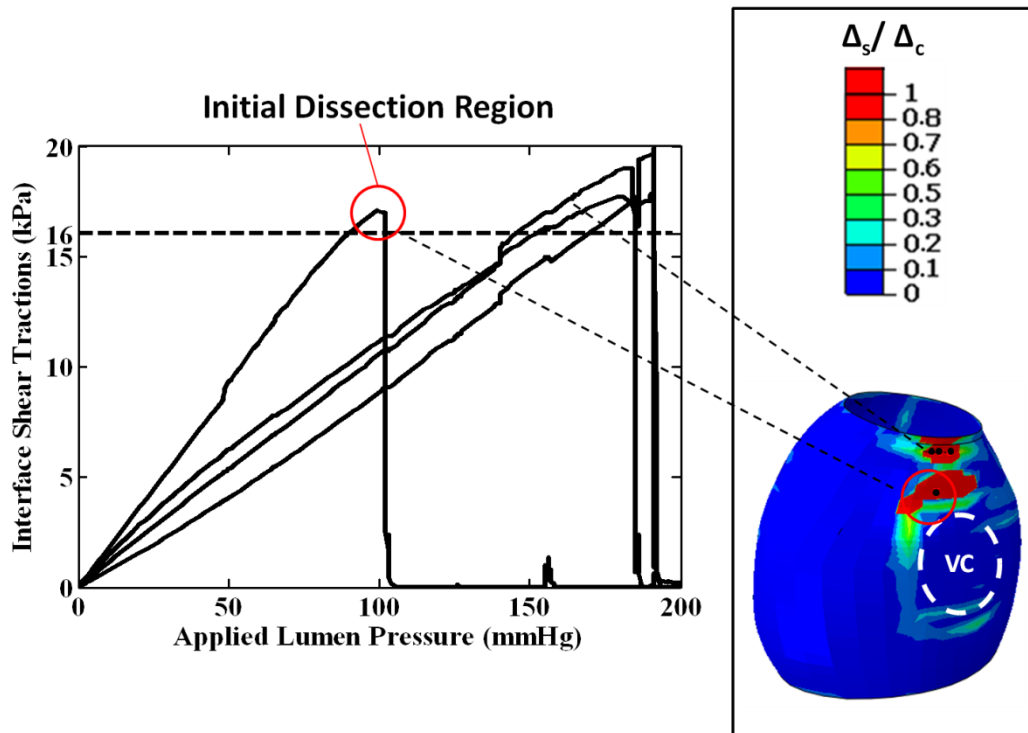
Figure 7-10: Computed interface shear traction as a function of applied lumen pressure at 4 nodes at the adventitia-media interface for geometry 3 when the intraluminal thrombus (ILT) is omitted. Two regions in which the critical cohesive characteristic distance is exceeded ($\Delta_s/\Delta_c > 1$) are shown on the right together with the position of the vertebral column (VC). The initial computed dissection region is also indicated. Individual wall layer properties are chosen for the intima, media and adventitia layers.
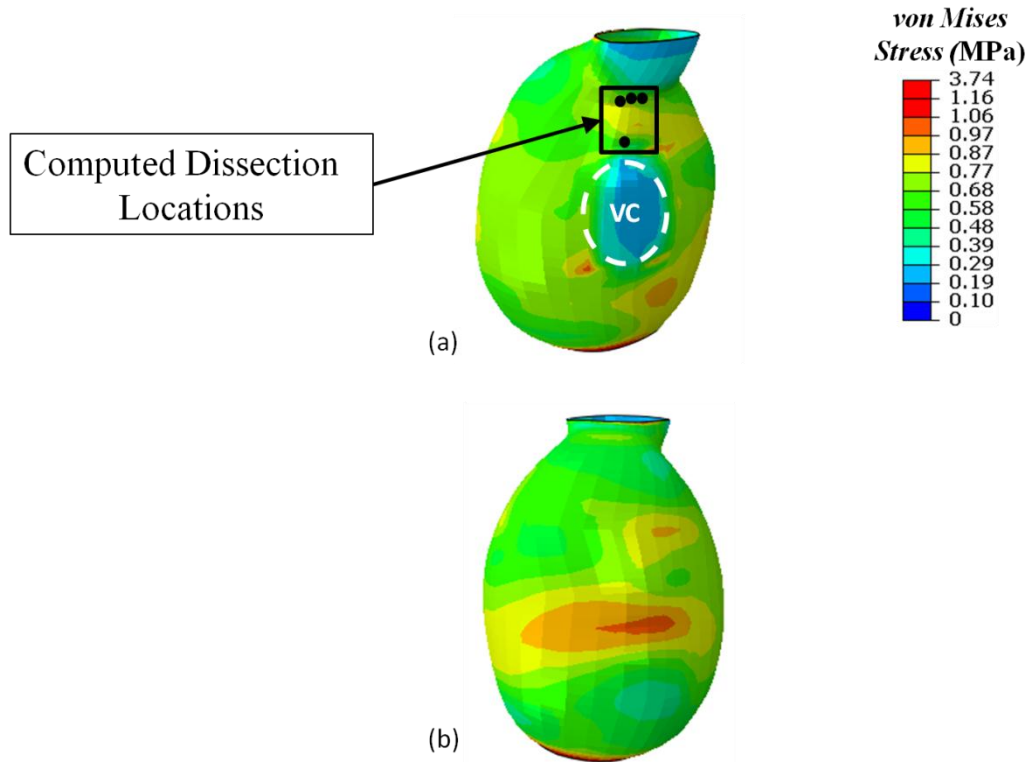
Figure 7-11: Distribution of computed von Mises stress in the adventitia layer, on the (a) posterior and (b) anterior sides, at an applied lumen pressure of 105mmHg for geometry 3 where the intraluminal thrombus (ILT) is omitted. Computed regions of interlayer dissection at the adventitia-media interface do not coincide with regions of peak von Mises stress. Individual wall layer properties are chosen for the intima, media and adventitia layers. The position of the vertebral column (VC) is also indicated.
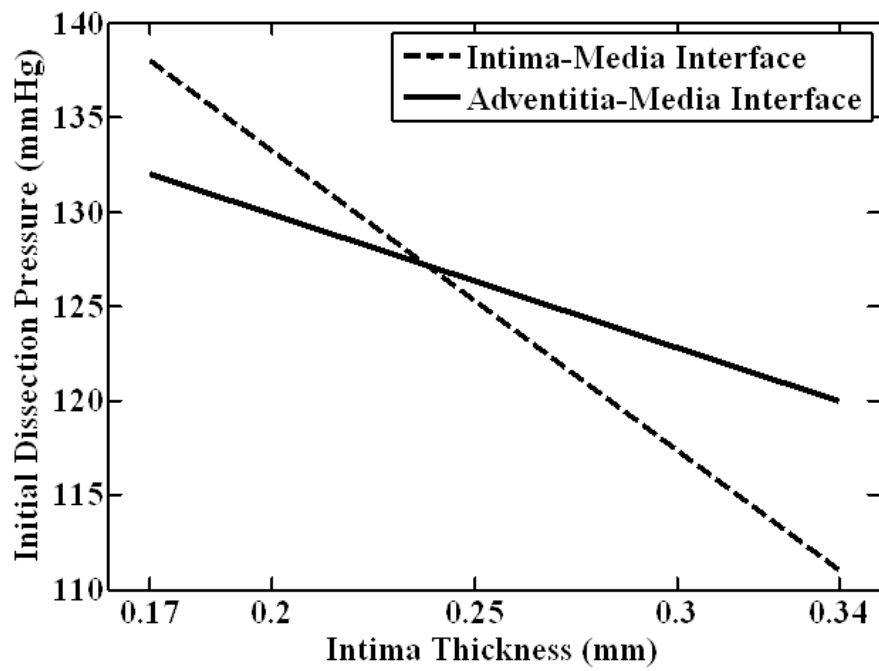
Figure 7-20: Initial computed dissection pressure (mmHg) at the intima-media and adventitia-media interface as a function of intima thickness (mm) for geometry 1. $E_{intima} = 2.9 MPa$.

		A-M dissection (132mmHg)		I-M dissection (138mmHg)	
Geometry 1	AAA wall layer	Adventitia	Media	Media	Intima
	Peak von Mises stress (MPa)	0.672	0.101	0.106	0.192
	Location of peak von Mises Stress	Upper anterior	Upper anterior	Upper anterior	LR
	Offset distance (mm)	~15	~22	~32	~7
		A-M dissection (150mmHg)		**I-M dissection (142mmHg)**	
Geometry 2	AAA wall layer	Adventitia	Media	Media	Intima
	Peak von Mises stress (MPa)	**1.06**	0.18	0.16	0.24
	Location of peak von Mises Stress	LL close to VC	LL close to VC	LL close to VC	LL close to VC
	Offset distance (mm)	~26	~26	~47	~46
		A-M dissection (188mmHg)			
Geometry 3	AAA wall layer	Adventitia	Media		
	Peak von Mises stress (MPa)	0.78	0.119		
	Location of peak von Mises Stress	Upper anterior	Upper anterior		
	Offset distance (mm)	~55	~54		

Table 7-1: This table illustrates that peak von Mises stress locations do not coincide with the locations of dissection initiation. Offset distance is the distance from the initial dissection point to the point of peak von Mises stress. A-M and I-M refer to the adventitia-media and intima-media

interfaces respectively. Areas LR and LL refer to lateral right and lateral left AAA locations respectively while VC refers to the vertebral column. Values are shown for AAAs in which the intraluminal thrombus (ILT) is included.

	Intima thickness=0.17mm		Intima thickness=0.34mm	
E_{intima}	2.9MPa	5.8MPa	2.9MPa	5.8MPa
A-M	132 (LR)	131 (LR)	120 (LR)	117 (LR)
I-M	138 (LR) 168 (ANT)	146 (LR)	115 (LR) 111 (LL)	118 (LR)

Table 7-2: Table summarising the influence of intima thickness and intima stiffness (E_{intima}) on initial dissection pressure and location for geometry 1. A-M and I-M refer to the adventitia-media and intima-media interfaces respectively. Areas LR, LL and ANT refer to lateral right, lateral left and anterior AAA locations respectively. All pressures are given in mmHg.

8 Computational Investigation of Endothelial Cell Delamination

8.1 Introduction

The reorientation of cells seeded onto flexible substrates subjected to cyclic tensile strain has received much attention in recent years (Ives et al., 1986; Dartsch and Betz, 1989; Wang et al., 1995; Wang et al., 2001; Wang et al., 2004; Kaunas et al., 2005; Kamotani et al., 2008; Hao et al., 2009; Balestrini et al., 2010). The cellular morphology and the actin cytoskeleton have been reported to align in the direction of minimum substrate strain (Dartsch and Betz, 1989; Iba et al., 1991; Wang et al., 1995; Wang et al., 2001; Balestrini et al., 2010).

For example, in the study of Wang et al. (1995), human melanocytes were grown on rectangular culture dishes subjected to unidirectional cyclic stretching at a frequency of 1Hz for 24 hours. Cells were reported to align in the direction of minimum strain. In the study of Wang et al. (2001), human endothelial cells were seeded on deformable silicone membranes. The cells were subjected to three types of cyclic stretching; simple elongation, pure uniaxial stretching and equi-biaxial stretching. In all cases, it was reported that the cells aligned in the direction of minimum substrate strain. This study also revealed that the rate and extent of early cell reorientation depended mostly on the stretching magnitude and not on the stretch frequency. Similarly in the work of Balestrini et al. (2010), dermal fibroblasts aligned in a direction away from the direction of principal strain when seeded on flexible-bottomed culture wells. These studies suggest that cells reorient to minimise the strain acting on them. However, the specific mechanisms involved to produce such behaviour are not well understood. A number of computational frameworks have been proposed to investigate the mechanism of cell reorientation (Wang et al., 1995; Civelekoglu et al., 1998; Wang, 2000; McGarry et al., 2005; Na et al., 2007; Hsu et al., 2009).

In this chapter the biomechanical response of an endothelial cell on a cyclically stretching silicone substrate is simulated. CZMs are utilised to model cell-

substrate interface behaviour. It is demonstrated that mixed-mode separation occurs at the cell-substrate interface when the work of tangential separation exceeds the work of normal separation ($\emptyset_t > \emptyset_n$). In particular, it is shown that the use of the potential-based Xu-Needleman (XN) model (Xu and Needleman, 1993) at the cell-substrate interface results in the computation of repulsive normal tractions. Further, it is demonstrated that the modified potential-based (MP) model, presented in Chapter 3, significantly decreases the computation of such non-physical repulsive tractions. A three-dimensional active stress fibre formulation (Deshpande et al., 2006; Ronan et al., 2012b) is used to simulate active remodelling and contractility of the cell cytoplasm. Simulations reveal that incorrect treatment of mixed-mode behaviour at the cell-substrate interface has a significant effect on prediction of stress fibre remodelling in the cell cytoplasm. In Section 8.2, the cell-substrate finite element model and the constitutive formulation used to describe active cell contractility are presented. In Section 8.3, the results of the simulations are reported with particular focus on the implications of incorrect mixed-mode interface behaviour.

8.2 Methods

8.2.1 Finite Element Model

The cell geometry, shown in Figure 8-1, is based on the experimental data of Caille et al. (2002) for endothelial cells. The cell is attached to a silicone substrate which is cyclically stretched from 0-10% nominal axial strain via a sinusoidally varying displacement boundary condition at a frequency of 1Hz, based on experimental boundary conditions (Wang et al., 1995; Wang et al., 2001; Moretti et al., 2004; Kaunas et al., 2005; Na et al., 2007; Hsu et al., 2009). One quarter of the cell and substrate geometries are modelled due to the use of symmetry boundary conditions. The silicone substrate is assumed to behave as a linear elastic material with a Poisson's ratio of 0.4 and a Young's modulus of 0.25MPa (McGarry et al., 2005).

Cohesive zone formulations are used to simulate the cell-substrate interface. Specifically, the XN, MP and NP1 formulations, presented in Chapter 3, are considered. This application primarily relies on the potential-based CZMs (XN and MP) due to the possibility of cell debonding and rebonding during cyclic substrate stretching. Only potential-based models formally ensure that the net interface work is zero if a closed loop of mixed-mode debonding and rebonding is followed. A simulation using the non-potential-based NP1 formulation is also provided for comparison. The cohesive zone models are implemented in Abaqus Standard software (V.6.8-1, Abaqus Inc., RI, USA) via a user-defined interface subroutine (UINTER). Characteristic interface lengths of $\delta_n = 25nm$ and $\delta_t = 35.36nm$ are assumed based on ligand-receptor bond lengths reported in literature (Chan et al., 1999; Dong and Lei, 2000). A mode I interface strength of $\sigma_{max} = 4\,kPa$ is chosen based on experimental measurements of bond strength and bond density (Thoumine et al., 2000). It is assumed that the mode II strength is higher than mode I strength at the cell-substrate interface, so that $\tau_{max} = 20\,kPa$ (corresponding to $q \approx 3$ for the XN model). The exponential shape of the normal traction-separation curve for the three models considered in this study (XN, MP and NP1 formulations) is similar to an experimentally measured force-

deformation curve for an isolated ligand-receptor bond (Leckband and Israelachvili, 2001), providing motivation for the use of such models at the cell-substrate interface (Figure 8-2). It is worth noting that traction-separation relationship under pure mode I and pure mode II conditions is identical for all cohesive zone formulations. Critically, however, differences between the mixed-mode behaviour of the models has a pronounced effect on predicted cell debonding, and consequently on cell remodelling.

8.2.2 Constitutive Formulation for the Active Behaviour of the Cell Actin Cytoskeleton

The actin cytoskeleton, which comprises contractile stress fibres, plays a critical role in the active bio-mechanical behaviour of a cell. Stress fibres are formed in response to signalling cascades in the cell cytoplasm which lead to the assembly of the phosphorylated myosin and polymerized actin filaments. Cross-bridge cycling between the myosin motor proteins and actin filaments generates active contractility in the actin cytoskeleton. Several experimental studies have demonstrated that a reduction in cell tension leads to the dissociation of stress fibres (Franke et al., 1984; Kolega, 1986; Burridge and Chrzanowska-Wodnicka, 1996; Tan et al., 2003; Thomopoulos et al., 2005).

In the present study, an active bio-chemo-mechanical model, proposed by Deshpande et al. (2006) is used to simulate the formation, remodelling and contractility of the actin cytoskeleton. Using a three-dimensional (3D) numerical implementation of this framework developed by Ronan et al. (2012b), stress fibre formation at each integration point in the cell cytoplasm is computed in 400 evenly spaced directions in 3D space. Each discrete direction is defined by two angles ω and ϕ. Theoretically stress fibres can form in an infinite number of directions at any point in the cell, but it has been demonstrated that a converged solution is obtained when the number of directions considered is greater than 200 (Ronan et al., 2012b).

The signal-induced formation and tension-dependent dissociation of the stress fibres is governed by a first order kinetic equation (Equation 8.1) in terms of the dimensionless stress fibre activation level, η (Deshpande et al., 2006).

$$\dot{\eta}(\phi, \omega) = \left[1 - (\eta(\phi, \omega))\right]Ck_f - \left[1 - \frac{\sigma(\phi, \omega)}{\sigma_0(\phi, \omega)}\right](\eta(\phi, \omega))k_b \qquad (8.1)$$

The first term on the right hand side of the above equation drives the assembly of a stress fibre in response to a time dependent signal C. k_f is a forward reaction rate constant. The second term drives the dissociation of the stress fibre when the stress fibre tension, $\sigma(\phi, \omega)$ is lower than the isometric tension $\sigma_0(\phi, \omega)$. k_b is the backwards reaction rate constant. The isometric tension is proportional to the stress fibre activation level, such that;

$$\sigma_o(\phi, \omega) = \sigma_{max}\eta(\phi, \omega) \qquad (8.2)$$

where the model parameter σ_{max} represents the isometric tension of a fully activated stress fibre. As previously stated, stress fibre tension is generated by the cross-bridge cycling of actin-myosin pairs (Warshaw et al., 1990) resulting in a contractile behaviour similar to that of skeletal muscle. This behaviour is captured using the following Hill-like relation between stress fibre tension $\sigma(\phi, \omega)$ and strain rate $\dot{\varepsilon}(\phi, \omega)$

$$\frac{\sigma(\phi, \omega)}{\sigma_0(\phi, \omega)} = \begin{cases} 0 & \frac{\dot{\varepsilon}(\phi, \omega)}{\dot{\varepsilon}_0} < -\frac{\eta(\phi, \omega)}{k_v} \\ 1 + \frac{k_v}{\eta(\phi, \omega)}\frac{\dot{\varepsilon}(\phi, \omega)}{\dot{\varepsilon}_0} & -\frac{\eta(\phi, \omega)}{k_v} \leq \frac{\dot{\varepsilon}(\phi, \omega)}{\dot{\varepsilon}_0} \leq 0 \\ 1 & \frac{\dot{\varepsilon}(\phi, \omega)}{\dot{\varepsilon}_0} > 0 \end{cases} \qquad (8.3)$$

where the model parameters k_v and $\dot{\varepsilon}_0$ determine the slope of the Hill curve (Hill, 1938). It should be noted that stress fibres yield when lengthening ($\dot{\varepsilon}_0 > 0$). This active formulation is placed in parallel with a passive hyperelastic material model which represents the non-contractile elements of the cell cytoplasm, including intermediate filaments and microtubules. Material parameters for the active and passive components of the cell material model are taken from McGarry et al. (2009) and Ronan et al. (2012b).

8.3   Results and Discussion

Figure 8-3 shows the evolution of normal traction, (T_n) and separation,(Δ_n) at a point A (Figure 8-1) at the leading edge of the cell during the first five substrate cycles. As the substrate is stretched, nodes at the front of the cell undergo mixed-mode debonding, as illustrated for point A in Figure 8-1. Firstly, considering the results computed by the XN model (Figure 8-3 (a)): During the first cycle, point A undergoes mixed-mode separation with the normal traction increasing up to a value of $T_n \approx 0.9\sigma_{max}$ and then decreasing as the node fully debonds (pure mode I debonding would result in a higher peak normal traction of $T_n = \sigma_{max}$). A repulsive traction is computed for a brief period. The normal traction then vanishes and the normal separation undergoes a rapid increase to a peak value of $\sim 30\delta_n$ when the substrate is fully stretched to 10% nominal strain. As the substrate stretch decreases during the second half of the cycle the normal separation decreases. However, the cell surface at point A does not return to the substrate at the end of the cycle, with a separation of $\sim 5\delta_n$ being computed when the substrate returns to 0% nominal strain. Clearly, in Figure 8-3(a), this end of cycle separation ($\Delta_n > 0$) is accompanied by repulsive normal tractions ($T_n < 0$). As discussed in Chapter 3 of this thesis, such repulsive normal tractions can be computed in potential-based models under mixed-mode conditions if the work of tangential separation exceeds the work of normal separation ($\emptyset_t > \emptyset_n$). As the substrate stretching resumes at the start of the second cycle the repulsive traction disappears, but it should be noted that the peak traction during the stretching phase of the second cycle is considerably lower than that of the first cycle as the node is already partially debonded due to the computation of repulsive forces at the end of the first cycle. As highlighted in Figure 8-3(a), repulsive tractions prevent the cell from contacting the substrate at point A at the end of every subsequent cycle.

Tractions and separations at point A computed using the MP model (Figure 8-3(b)) reveal a markedly different pattern to those computed using the XN model. During the initial substrate stretching in the first cycle the behaviour is almost identical to the XN predictions with normal traction increasing up to a

value of $T_n \approx 0.9\sigma_{max}$ and then decreasing, marking the onset of mixed-mode debonding. Following debonding, a small repulsive force ($T_n \approx -0.05\sigma_{max}$) is computed for a brief period after which the traction disappears and the normal separation rapidly increases until the substrate is fully stretched. During the second half of the first cycle, when the substrate strain is reduced from 10% to 0%, point A returns to the substrate surface. As no damage is included in the model, the node rebonds in a mixed-mode fashion, with a peak normal traction of $T_n \approx 0.9\sigma_{max}$ being computed during rebonding. At the end of the cycle, point A contacts the substrate surface and then slightly overcloses into the substrate. This over-closure is appropriately penalised by negative normal tractions. It is important that such negative normal tractions which penalise (negative) normal over-closure are not confused with the repulsive negative normal tractions computed by the XN model in Figure 8-3(a) at the end of the cycle which coincide with positive normal separation. During the second and subsequent cycles for the MP model (Figure 8-3(b)), point A goes through a similar debonding and rebonding cycle, with peak tractions of $T_n \approx 0.9\sigma_{max}$ being computed twice per cycle and extremely small repulsive tractions being computed only for a brief period following nodal debonding.

Tractions and separations computed at point A using the non-potential-based (NP1) formulation are shown in Figure 8-3(c). Again, during initial substrate stretching in the first cycle the behaviour is almost identical to the XN and MP predictions with normal traction increasing up to a peak value of $T_n \approx 0.9\sigma_{max}$ marking the onset of mixed-mode debonding. Since repulsive tractions cannot be computed for non-potential-based formulations, mixed-mode cell reattachment is computed at the end of each substrate cycle. Similar to the MP model, over-closure is appropriately penalised by negative normal tractions.

Figure 8-3 presents traction and separation history for a single node at the leading edge of the cell. Figure 8-4 reveals the full extent of repulsive normal tractions computed by the XN model. Specifically, Figure 8-4 (a)-(c) shows the computed normal tractions, normal displacements and effective tangential tractions

computed at the cell-substrate interface for the XN and MP models at the end of the third cycle when the substrate has returned to 0% nominal strain. In the case of the XN model, significant regions of unphysical repulsive normal tractions are computed around the outer perimeter of the contact region (characterised as regions where positive normal separations are coincident with negative normal tractions, as distinct from regions in which over-closure is being penalised, where both normal separations and normal tractions are negative). In contrast, no unphysical repulsive normal tractions are computed for the MP model when the substrate returns to 0% nominal strain and normal separations are close to zero throughout the interface, indicating a complete re-adhesion of the cell to the substrate. As can be seen in Figure 8-4(c), the repulsive normal tractions in the XN simulation have a pronounced affect on the tangential tractions at the cell-substrate interface, with minimal computed tractions at the leading edge of the cell at 0% nominal substrate strain. In contrast, tangential tractions are computed at the leading edge of the cell for MP following full cell reattachment.

Figure 8-5 shows the predicted remodelling of stress fibres at the base of the cell over 30 loading cycles using the MP model. Prior to initiation of cyclic substrate stretching an equilibrium stress fibre distribution is computed in response to an exponentially decaying signal in the cell cytoplasm on a static substrate. As expected in the absence of applied external substrate loading, an axisymmetric stress fibre distribution occurs in the cell (Figure 8-5(a)). No debonding occurs during this stage of the simulation as the interface tractions generated by the contractile actin cytoskeleton are an order of magnitude lower than the interface strength. Subsequent cyclic substrate stretching in the x-direction results in cyclic debonding and rebonding of significant regions of the cell-substrate interface (as shown in Figure 8-3) but little change in stress fibre distribution following one and three cycles (Figure 8-5(b, c)). However, following 10 cycles (Figure 8-5(d)) it can be observed that stress fibre dissociation begins to occur. A clear pattern of stress fibre redistribution emerges following 20 cycles (Figure 8-5(e)), whereby stress fibres remain intact in the regions of lowest cyclic strain rate. In highlighted region 1, stress fibre shortening in the *x*-direction during the unloading half cycle

results in tension reduction and dissociation. It should be noted that region 2 debonds during substrate stretching and reattaches to the substrate towards the end of the unloading half cycle (as shown in Figure 8-4(b)). Therefore stress fibres in this region experience a reduced period of shortening and tension reduction during unloading half cycles, leading to a slower rate of dissociation. Region 3 undergoes stress fibre shortening in the z-direction during cell stretching due to the Poisson's effect, leading to dissociation. By 30 cycles (Figure 8-5(f)) a distinct band of stress fibres are computed from the centre of the cell to the cell periphery at an angle of ~60° to the stretching (x) direction. Further dissociation is also computed in region 2 following 30 cycles, all be it at a slower rate due to debonding and rebonding. Figure 8-6 demonstrates that significant stress fibre remodelling occurs throughout the entire cell cytoplasm, and not just at the base of the cell as shown in Figure 8-5. The prediction that stress fibres align at ~60° is strongly supported by experimental findings (Wang et al., 1995; Wang et al., 2001). This direction corresponds to the direction of minimum strain rate for a silicone substrate with a Poisson's ratio of 0.4. This pattern of stress fibre alignment is not predicted by the XN model, as repulsive normal tractions during the unloading half cycles prevents reattachment of the cell to the substrate, as shown in Figure 8-3(a). Therefore stress fibres in region 3 are not subjected to shortening during any period of the unloading half cycles and no dissociation occurs in this region.

8.4 Conclusion

In this chapter mixed-mode separation of an endothelial cell on a cyclically stretching silicone substrate is simulated. It is demonstrated that mixed-mode separation occurs at the cell-substrate interface when the work of tangential separation exceeds the work of normal separation ($\emptyset_t > \emptyset_n$). A three-dimensional active stress fibre formulation (Deshpande et al., 2006; Ronan et al., 2012b) is used to simulate active remodelling and contractility of the cell cytoplasm. Simulations reveal that the use of the Xu-Needleman (XN) model at the cell-substrate interface results in the computation of significant regions of repulsive normal tractions, preventing the readhesion of the cell to the substrate during

substrate unloading half-cycles. The implications of the computation of unphysical repulsive forces are clearly demonstrated in terms of unphysical prediction in cell-substrate contact and erroneous prediction of associated remodelling of the actin cytoskeleton.

In contrast, negligible repulsive tractions are computed at the cell-substrate interface during mixed-mode cell deformation following the application of the modified potential (MP) formulation allowing for the computation of significant cytoskeletal remodelling with full cell reattachment computed at the end of each strain cycle. Simulations suggest that significant changes in stress fibre remodelling are not observed until 30 strain cycles where the dominant stress fibre bundling direction is computed to be at an angle of approximately 60° to the stretching direction. Experimental studies demonstrate that following ~10,000 cycles both the actin cytoskeleton and the cell morphology align in the direction of minimum substrate strain (Wang et al., 2001). For silicon substrates this corresponds to ~70° (as dictated by a Poisson's ratio of ~0.4). Full cell reattachment is also predicted using the NP1 formulation, where no repulsive forces are computed.

The use of a CZM to model cell adhesion has previously been undertaken in the literature (McGarry et al., 2005). However, the modelling of the cell-substrate interface using a passive cohesive zone framework represents a significant simplification. Cell-substrate adhesion entails traction-dependent binding of high-affinity integrins to ligands, leading to focal adhesion assembly, as detailed in the thermodynamically consistent framework of Deshpande et al. (2008). Additionally, the kinetics of bond formation and rupture has been the subject of a number of studies (Bell, 1978; Evans, 1985; Dembo et al., 1988; Dong and Lei, 2000; Freund and Lin, 2004). As the focus of this chapter is on the mixed-mode behaviour of path-independent potential-based models, the cell-substrate interface is treated as a passive entity, with debonding and readhesion being governed exclusively by an interface potential. The implementation of a mixed-mode active cell-substrate interface model is beyond the scope of the study presented in this chapter and has recently been reported elsewhere (Ronan et al., 2012a).

267

8.5   References

Balestrini, J. L., Skorinko, J. K., Hera, A., Gaudette, G. R.&Billiar, K. L. (2010) Applying controlled non-uniform deformation for in vitro studies of cell mechanobiology. *Biomechanics and Modeling in Mechanobiology,* 9, 329-344.

Bell, G. I. (1978) Models for the specific adhesion of cells to cells. *Science,* 200, 618.

Burridge, K.&Chrzanowska-Wodnicka, M. (1996) Focal adhesions, contractility, and signaling. *Annual review of cell and developmental biology,* 12, 463-519.

Caille, N., Thoumine, O., Tardy, Y.&Meister, J.-J. (2002) Contribution of the nucleus to the mechanical properties of endothelial cells. *Journal of Biomechanics,* 35, 177-187.

Chan, B. P., Bhat, V. D., Yegnasubramanian, S., Reichert, W. M.&Truskey, G. A. (1999) An equilibrium model of endothelial cell adhesion via integrin-dependent and integrin-independent ligands. *Biomaterials,* 20, 2395-2403.

Civelekoglu, G., Tardy, Y.&Meister, J. J. (1998) Modeling actin filament reorganization in endothelial cells subjected to cyclic stretch. *Bulletin of mathematical biology,* 60, 1017-1037.

Dartsch, P. C.&Betz, E. (1989) Response of cultured endothelial cells to mechanical stimulation. *Basic research in cardiology,* 84, 268-281.

Dembo, M., Torney, D. C., Saxman, K.&Hammer, D. (1988) The reaction-limited kinetics of membrane-to-surface adhesion and detachment. *Proceedings of the Royal Society of London. Series B, Biological Sciences*, 55-83.

Deshpande, V. S., McMeeking, R. M.&Evans, A. G. (2006) A bio-chemo-mechanical model for cell contractility. *Proceedings of the National Academy of Sciences,* 103, 14015-14020.

Deshpande, V. S., Mrksich, M., McMeeking, R. M.&Evans, A. G. (2008) A bio-mechanical model for coupling cell contractility with focal adhesion formation. *Journal of the Mechanics and Physics of Solids,* 56, 1484-1510.

Dong, C.&Lei, X. X. (2000) Biomechanics of cell rolling: shear flow, cell-surface adhesion, and cell deformability. *Journal of Biomechanics,* 33, 35-43.

Evans, E. A. (1985) Detailed mechanics of membrane-membrane adhesion and separation. I. Continuum of molecular cross-bridges. *Biophysical Journal,* 48, 175-183.

Franke, R. P., Grafe, M., Schnittler, H., Seiffge, D., Mittermayer, C.&Drenckhahn, D. (1984) Induction of human vascular endothelial stress fibres by fluid shear stress.

Freund, L. B.&Lin, Y. (2004) The role of binder mobility in spontaneous adhesive contact and implications for cell adhesion. *Journal of the Mechanics and Physics of Solids,* 52, 2455-2472.

Hao, Y., Xu, C., Sun, S.&Zhang, F. (2009) Cyclic stretching force induces apoptosis in human periodontal ligament cells via caspase-9. *Archives of Oral Biology,* 54, 864-870.

Hill, A. V. (1938) The heat of shortening and the dynamic constants of muscle. *Proceedings of the Royal Society of London. Series B, Biological Sciences,* 126, 136-195.

Hsu, H. J., Lee, C. F.&Kaunas, R. (2009) A dynamic stochastic model of frequency-dependent stress fiber alignment induced by cyclic stretch. *PloS one,* 4, e4853.

Iba, T., Maitz, S., Furbert, T., Rosales, O., Widmann, M. D., Spillane, B., et al. (1991) Effect of cyclic stretch on endothelial cells from different vascular beds. *Circulatory shock,* 35, 193.

Ives, C. L., Eskin, S. G.&Mcintire, L. V. (1986) Mechanical effects on endothelial cell morphology: in vitro assessment. *In Vitro Cellular & Developmental Biology-Plant,* 22, 500-507.

Kamotani, Y., Bersano-Begey, T., Kato, N., Tung, Y. C., Huh, D., Song, J. W., et al. (2008) Individually programmable cell stretching microwell arrays actuated by a Braille display. *Biomaterials,* 29, 2646-2655.

Kaunas, R., Nguyen, P., Usami, S.&Chien, S. (2005) Cooperative effects of Rho and mechanical stretch on stress fiber organization. *Proceedings of the National Academy of Sciences of the United States of America,* 102, 15895.

Kolega, J. (1986) Effects of mechanical tension on protrusive activity and microfilament and intermediate filament organization in an epidermal epithelium moving in culture. *The Journal of cell biology,* 102, 1400-1411.

Leckband, D.&Israelachvili, J. (2001) Intermolecular forces in biology. *Quarterly Reviews of Biophysics,* 34, 105-267.

Leckband, D. E., Schmitt, F. J., Israelachvili, J. N.&Knoll, W. (1994) Direct force measurements of specific and nonspecific protein interactions. *Biochemistry,* 33, 4611-4624.

McGarry, J. P., Fu, J., Yang, M. T., Chen, C. S., McMeeking, R. M., Evans, A. G., et al. (2009) Simulation of the contractile response of cells on an array of micro-posts. *Philosophical Transactions of the Royal Society A: Mathematical, Physical and Engineering Sciences,* 367, 3477-3497.

McGarry, J. P., Murphy, B. P.&McHugh, P. E. (2005) Computational mechanics modelling of cell-substrate contact during cyclic substrate deformation. *Journal of the Mechanics and Physics of Solids,* 53, 2597-2637.

Moretti, M., Prina-Mello, A., Reid, A. J., Barron, V.&Prendergast, P. J. (2004) Endothelial cell alignment on cyclically-stretched silicone surfaces. *Journal of Materials Science: Materials in Medicine,* 15, 1159-1164.

Na, S., Meininger, G. A.&Humphrey, J. D. (2007) A theoretical model for F-actin remodeling in vascular smooth muscle cells subjected to cyclic stretch. *Journal of Theoretical Biology,* 246, 87-99.

Ronan, W., Deshpande, V. S., McMeeking, R. M.&Patrick McGarry, J. (2012a) Cellular contractility and substrate elasticity: a numerical investigation of the actin cytoskeleton and cell adhesion. *Submitted August 2012. .*

Ronan, W., Deshpande, V. S., McMeeking, R. M.&Patrick McGarry, J. (2012b) Numerical investigation of the active role of the actin cytoskeleton in the compression resistance of cells. *Journal of the Mechanical Behavior of Biomedical Materials*.

Tan, J. L., Tien, J., Pirone, D. M., Gray, D. S., Bhadriraju, K.&Chen, C. S. (2003) Cells lying on a bed of microneedles: an approach to isolate mechanical force. *Proceedings of the National Academy of Sciences of the United States of America,* 100, 1484.

Thomopoulos, S., Fomovsky, G. M.&Holmes, J. W. (2005) The development of structural and mechanical anisotropy in fibroblast populated collagen gels. *Journal of Biomechanical Engineering,* 127, 742.

Thoumine, O., Kocian, P., Kottelat, A.&Meister, J. J. (2000) Short-term binding of fibroblasts to fibronectin: optical tweezers experiments and probabilistic analysis. *European Biophysics Journal,* 29, 398-408.

Wang, H., Ip, W., Boissy, R.&Grood, E. S. (1995) Cell orientation response to cyclically deformed substrates: Experimental validation of a cell model. *Journal of Biomechanics,* 28, 1543-1552.

Wang, J. H. C. (2000) Substrate Deformation Determines Actin Cytoskeleton Reorganization: A Mathematical Modeling and Experimental Study. *Journal of Theoretical Biology,* 202, 33-41.

Wang, J. H. C., Goldschmidt-Clermont, P., Wille, J.&Yin, F. C. P. (2001) Specificity of endothelial cell reorientation in response to cyclic mechanical stretching. *Journal of Biomechanics,* 34, 1563-1572.

Wang, J. H. C., Yang, G., Li, Z.&Shen, W. (2004) Fibroblast responses to cyclic mechanical stretching depend on cell orientation to the stretching direction. *Journal of Biomechanics,* 37, 573-576.

Warshaw, D. M., Desrosiers, J. M., Work, S. S.&Trybus, K. M. (1990) Smooth muscle myosin cross-bridge interactions modulate actin filament sliding velocity in vitro. *The Journal of cell biology,* 111, 453-463.

Xu, X. P.&Needleman, A. (1993) Void nucleation by inclusion debonding in a crystal matrix. *Modelling and Simulation in Materials Science and Engineering,* 2, 417-418.

8.6   Tables and Figures
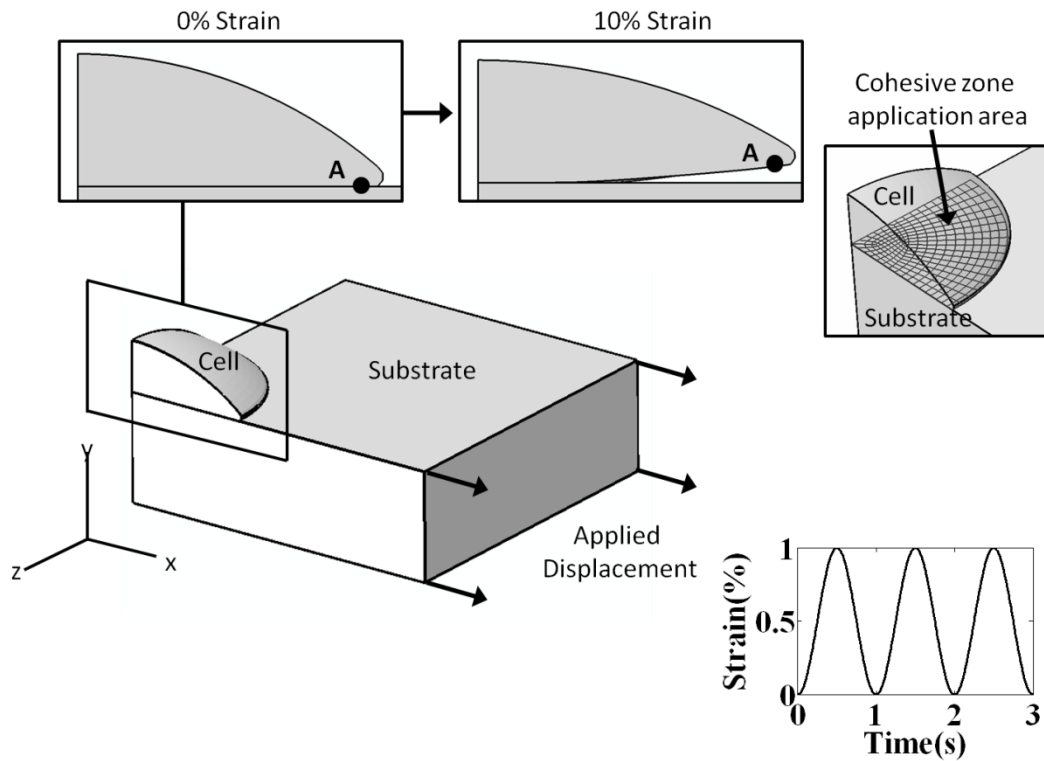
Figure 8-1: Axisymmetric geometry of cell and substrate model. Arrows indicate the direction of cyclic substrate deformation. The inserts show the deformed geometry of the cell at 10% strain. Point A indicates a node at the cell-substrate interface where mixed-mode separation is computed. The cohesive zone application area is also highlighted.

Removed due to copyright
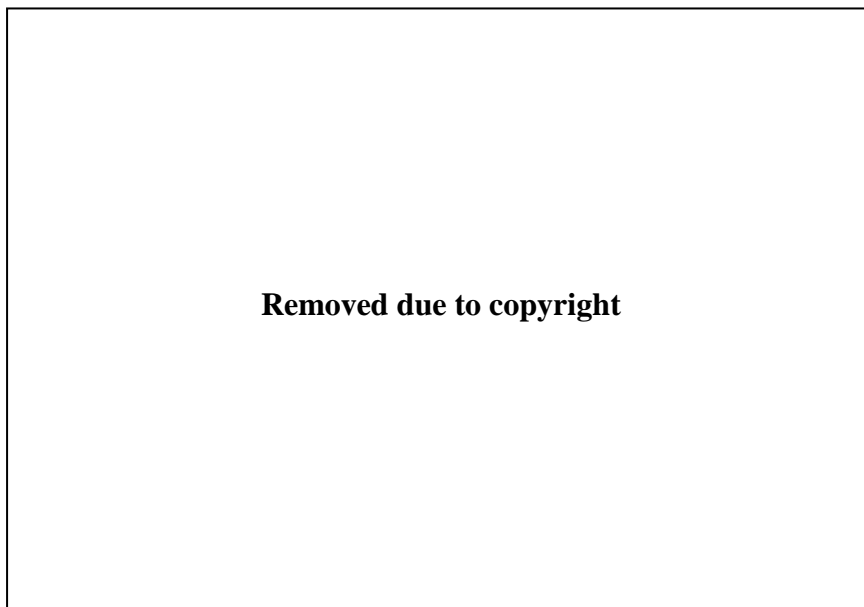
Figure 8-2: Experimental tension measurement of an isolated ligand-receptor bond (Leckband and Israelachvili, 2001) motivating the use of an exponential form of cohesive zone model.
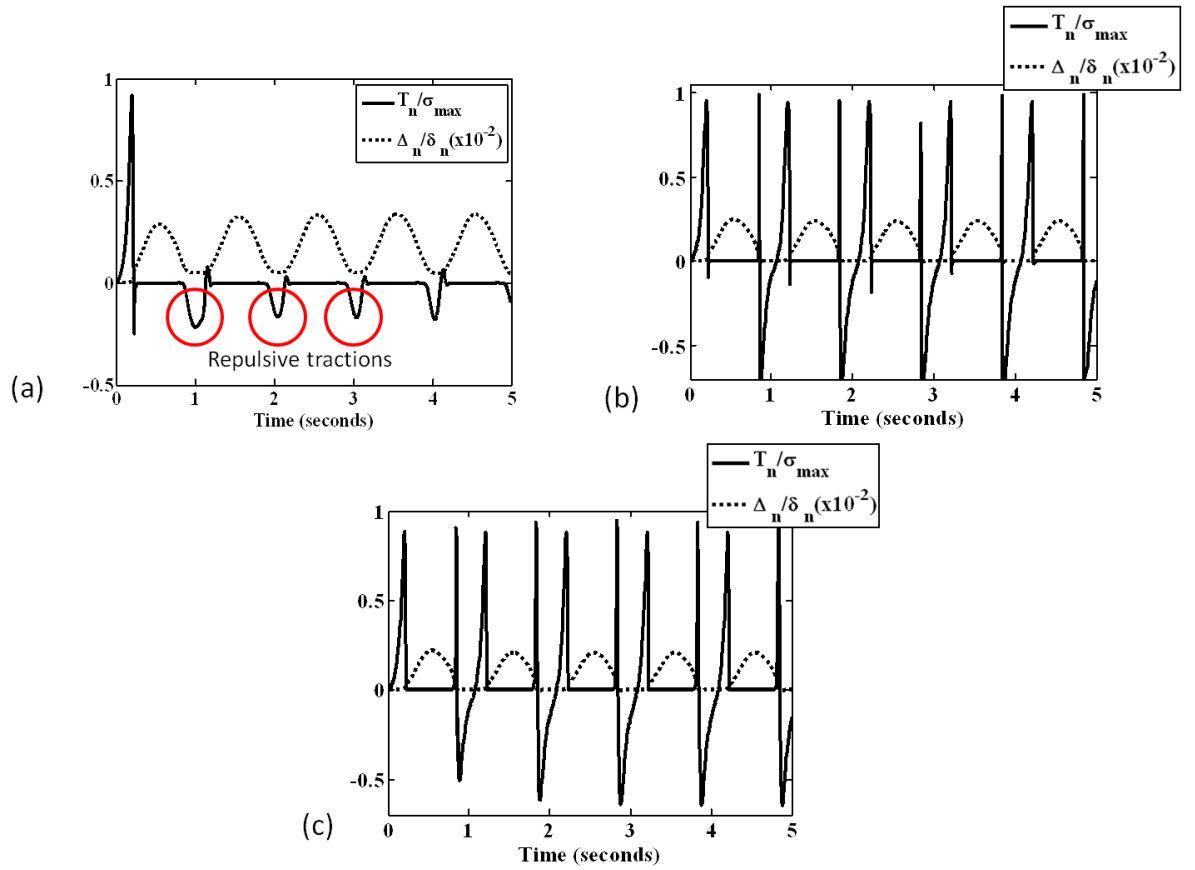
Figure 8-3: Normalised normal traction (T_n/σ_{max}) and normalised normal separation (Δ_n/δ_n) as a function of time for (a) the XN (b) MP ($m = 1$) and (c) NP1 cohesive zone models. Repulsive normal tractions are highlighted in the case of the XN model.
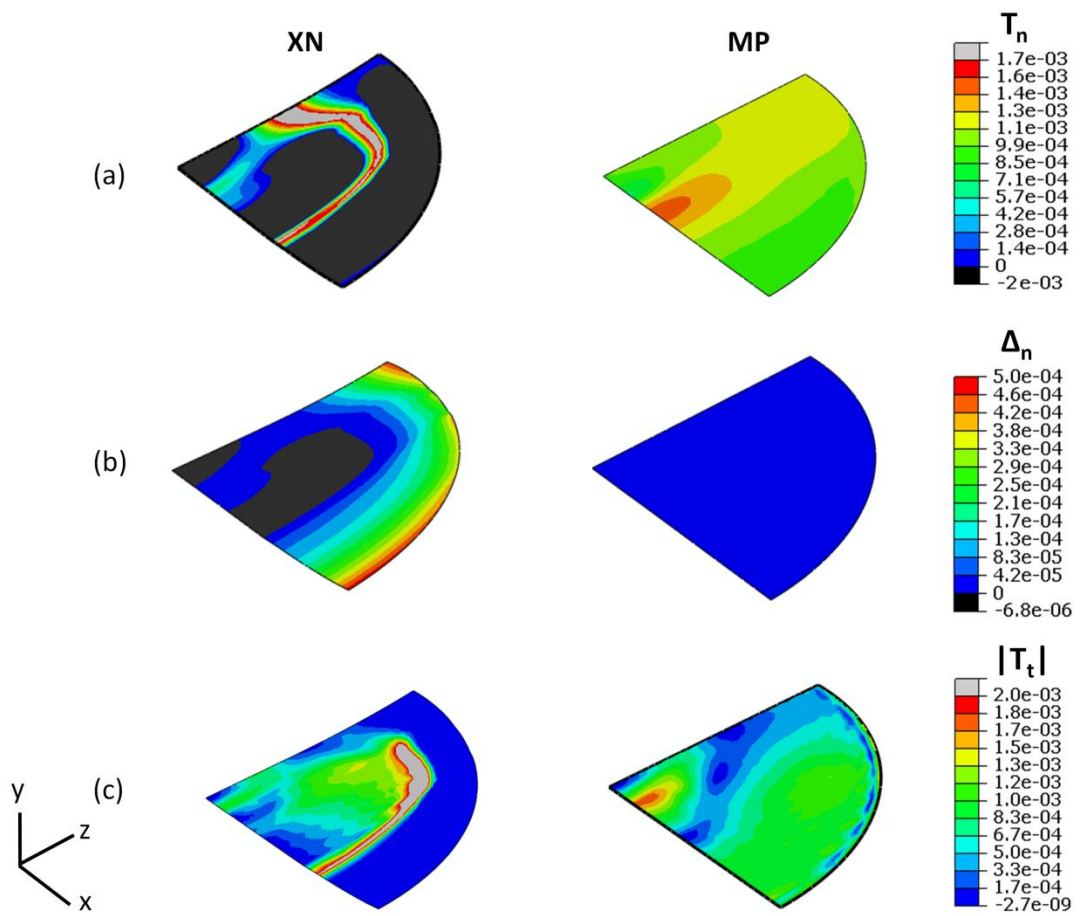
Figure 8-4: (a) Computed normal tractions (T_n); (b) Computed normal displacements (Δ_n); (c) Computed effective tangential tractions ($|T_t|$) for XN and MP (m=1) cohesive zone models. Results are shown at 0% substrate strain following 3 substrate strain cycles.
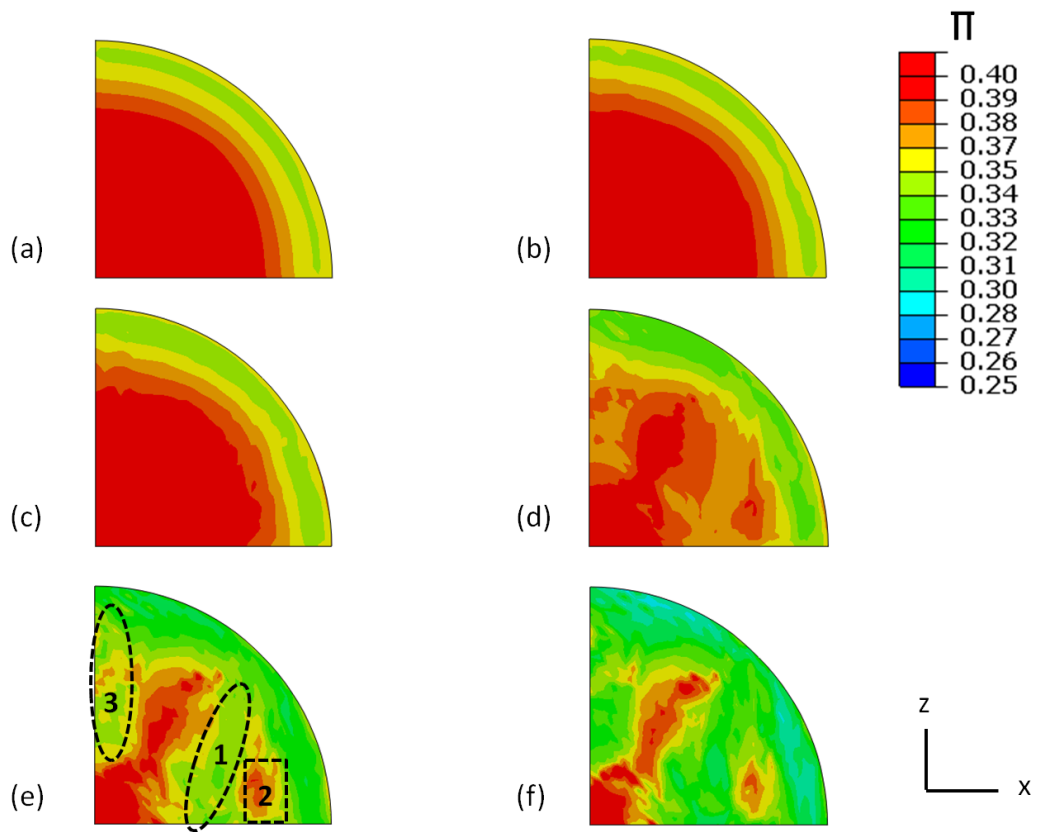
Figure 8-5: Computed dominant stress fibre bundling direction (Π) at the cell interface surface for the MP model following (a) equilibrium; (b) 1 cycle; (c) 3 cycles; (d) 10 cycles; (e) 20 cycles; (f) 30 cycles. In all cases cyclic loading is applied in the x-direction.
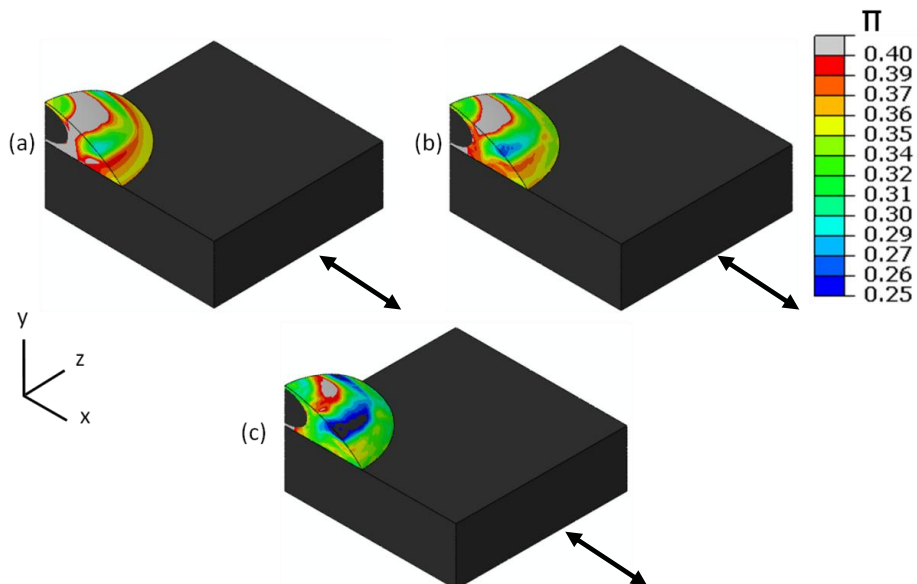
Figure 8-6: Computed dominant stress fibre bundling direction (Π) in the cell geometry for the MP model following (a) equilibrium; (b) 10 cycles; (c) 30 cycles. The loading direction is also indicated.

9 Concluding Remarks

The main objective of this thesis was to perform a rigorous analysis of potential-based and non-potential-based cohesive zone formulations under mixed-mode conditions and to predict failure in cardiovascular applications using the presented formulations. Detailed discussions and interpretation of results are presented in each technical chapter of the thesis (Chapters 3, 4, 6, 7, 8). This final chapter presents an overview of the key findings of the thesis in the broad context of cohesive zone modelling and cardiovascular biomechanics.

In **Chapter 3**, a comprehensive theoretical analysis of potential-based and non-potential-based cohesive zone models (CZMs) is carried out. Much of this theoretical work involves a complete analysis of the frequently implemented Xu-Needleman (XN) (Xu and Needleman, 1993) potential-based CZM, significantly expanding on the initial work of Abdul-Baqi and Van der Giessen (2001) and van den Bosch et al. (2006). To the best of the author's knowledge, no comprehensive analysis of the commonly implemented XN CZM has previously been carried out in which the complete range of diverse interface behaviour under mixed-mode separation and mixed-mode over-closure has been characterised. Several experimental studies have reported that the work of normal $(\emptyset_n)$ and tangential $(\emptyset_t)$ separation required for interfacial fracture are different (Dollhofer et al., 2000; Warrior et al., 2003; Yang et al., 2001). For example, Hutchinson and Suo (1992) reported that the mode II fracture toughness is four times higher than the mode I fracture toughness for an epoxy-plexiglass interface. The analysis of Chapter 3 demonstrates that derivation of traction-separation relationships from the XN potential function results in non-physical behaviour under mixed-mode conditions when $\emptyset_t \neq \emptyset_n$. A modified potential-based model (MP model) is then considered, and it is demonstrated that the MP model partially addresses a number of limitations associated with the XN CZM. Essentially, an additional coupling parameter in this potential function reduces the zone in which unphysical interface

behaviour is computed under mixed-mode conditions. In contrast to the XN CZM, it is demonstrated that the MP model can significantly reduce the computation of unphysical repulsive normal tractions during mixed-mode separation when $\emptyset_t > \emptyset_n$. Considering that the work of tangential separation ($\emptyset_t$) has been reported to be greater than the work of normal separation in several experimental studies, as mentioned above, the MP formulation is shown to provide a significant improvement on the XN model for mixed-mode applications. However, it must be stated that no potential-based model can fully eliminate unphysical mixed-mode interface behaviour if $\emptyset_t > \emptyset_n$. In order to overcome this problem, previous studies which use potential-based models have set the value of normal traction to zero if repulsive tractions emerge from the potential function (Park et al., 2009; Sørensen and Kirkegaard, 2006). However, this approach of abandoning the potential function for certain displacement fields means that the cohesive zone model can no longer be defined as a potential-based framework as the net work done if the interface follows a closed displacement loop will not necessarily be zero.

It is demonstrated that non-potential-based CZMs must be implemented to fully eliminate the possible computation of repulsive normal tractions during mixed-mode separation if $\emptyset_t > \emptyset_n$. Theoretical analysis of the non-potential-based cohesive zone model of van den Bosch et al. (2006) (VB CZM) reveals that it fails to provide physically realistic behaviour under mixed-mode over-closure. In order to correct the unphysical behaviour of the VB CZM in mixed-mode over-closure, two non-potential-based models (NP1 and NP2) are considered, and it is demonstrated that both of these formulations provide physically reasonable coupling under mixed-mode separation and over-closure. Finally, a formulation which offers the possibility of mode-independent work of separation is considered whereby coupling terms are based on the separation magnitude (SMC model). The analyses presented in this study provide valuable guidance for future development and implementation of CZMs for problems involving mixed-mode separation and over-closure.

Chapter 4 extends on the theoretical analysis presented in Chapter 3 by providing a computational assessment of cohesive zone performance in mixed-mode over-closure and separation. Firstly, simulations are performed to assess the performance of each CZM under traction-controlled mode mixity. Specifically, traction distributions at the interface of a bi-layered arch are considered. An analytical solution has been developed (Parry and McGarry, 2012) whereby the traction magnitude is constant along the arch, but mode mixity is a function of position on the arch interface with a symmetric sinusoidal distribution of normal and shear tractions from the top to the bottom of the arch. Finite element simulations in Chapter 4 reveal that in cases where the coupling terms in a cohesive zone formulation result in a bias towards mode I or mode II separation, the analytical solution is not reproduced. The normal-tangential coupling terms in each cohesive zone formulation are found to significantly affect computed tractions and debonding patterns at the arch interface with most CZMs exhibiting a bias towards either mode I or mode II separation prior to coating debonding. Proportional separations corresponding to the analytical solution at all points along the interface are computed only for the SMC formulation. This computational assessment of mixed-mode CZM performance demonstrates that predicted debonding patterns are highly sensitive to normal-tangential coupling terms in a CZM for a traction controlled interface such as a bi-layered arch.

In order to assess the performance of CZMs under conditions of mixed-mode over-closure, the behaviour of a coating on the compressive region of a cardiovascular stent during stent deployment is also simulated in this chapter. It is shown that the VB model (van den Bosch et al., 2006) fails to correctly penalise mixed-mode coating over-closure (compression) leading to incorrect prediction coating stress and, subsequently, coating buckling. In contrast, the NP1 and NP2 formulations correctly penalise mixed-mode coating compression during stent expansion and predict similar coating buckling patterns to those observed experimentally for commercially available stents (Basalus and von Birgelen, 2010). Chapter 4 provides a challenging computational assessment of the mode sensitivity of CZMs presented in Chapter 3, both in over-closure and in

separation. Having established the suitability of the SMC CZM for mode-sensitive interface separation and the robustness of the NP2 CZM for mixed-mode over-closure, these models are implemented to describe interface behaviour for the first two applications (stent coating delamination and aneurysm dissection), with the SMC CZM being used in separation and the NP2 model being used in over-closure.

An assessment of the traction distributions along the interface between a cardiovascular stent and coating is presented in **Chapter 6**. Interface traction distributions are initially assessed in the absence of interface debonding. Additionally, it is demonstrated that coating debonding patterns are highly dependent on material properties, stent deployment levels and geometry. A 2D unit cell reference configuration of a stent and coating geometry is used based on the dimensions of commercially available stent designs (Regar et al., 2001). Firstly, an elastic stent is considered in order to develop an initial fundamental understanding of interface traction behaviour. When interface tractions are assessed for a range of strut lengths, stent thicknesses and coating thicknesses, it is shown that peak normal tractions exceed peak tangential tractions at low stent deployment whereas peak tangential tractions exceed peak normal tractions at high stent deployment. Considering that stents are typically subjected to high levels of deployment, these results suggest that mode II coating debonding should be carefully considered. The simulation of a short strut results in reduced normal tractions and increased tangential tractions along the stent-coating interface whereas a longer strut results in an increased rotation at the base of the stent arch, reducing the tangential tractions and increasing the normal tractions. Stent-coating interface tractions are shown to increase with increasing coating thickness. These results suggest that antiproliferative drugs such as sirolimus and paclitaxel should be delivered, if possible, via thinner coatings. Interface tractions are also shown to increase with increasing stent thickness. The influence of stent thickness on interface tractions is particularly relevant based on the fact that clinical studies have suggested that thinner stents reduce restenosis rates (Kastrati et al., 2001; Pache et al., 2005; Turco et al., 2008). In the second part of Chapter 6 interface

traction distributions are presented for an elastic-plastic stent. It is shown that for a very thin elastic-plastic stent, interface tractions are not significantly influenced by stent strain hardening moduli, while coating stiffness again has a significant influence on computed tractions. In contrast, the computed tractions are highly dependent on both stent strain hardening moduli and coating stiffness for a stent thickness typical of commercially available stents. Simulations reveal that the location and mechanism of initial coating debonding is highly dependent on interface strength and the ratio of peak normal to tangential traction, suggesting that rigorous bench-side testing experiments should be carried out to quantify the mode I and mode II fracture toughness of a stent-coating interface.

This thesis demonstrates that the mechanisms of coating debonding are quite complex and depend on numerous stent, coating and interface design criteria. Numerous experimental studies using scanning electron microscopy have reported extensive delamination of polymer coatings from the stent surface during deployment (Otsuka et al., 2007; Levy et al., 2009; Basalus and von Birgelen, 2010; Wiemer et al., 2010). It has been suggested that coating damage may play a key role in late stent thrombosis (Hoffmann et al., 2002; Wang et al., 2002; Balakrishnan et al., 2005; Iakovou et al., 2005; Otsuka et al., 2007; Levy et al., 2009). It is reasonable to suggest that additional clinical complications may arise as a result of coating damage including micro-embolism formation, impaired drug delivery and obstruction of blood flow. Currently, the FDA does not provide guidelines for computational analysis and design techniques for coated stents, despite the aforementioned clinical implications of coating debonding. The simulations of Chapter 6 provide valuable insight into the stress-state at the stent-coating interface as a function of the stent design parameters. Such analyses allow for a more reliable assessment of the limits relating to safe implantation of coated stents.

In **Chapter 7**, dissection between the arterial wall layers of an abdominal aortic aneurysm (AAA) is simulated. The prediction of AAA interlayer dissection using a cohesive zone formulation is a unique approach that has not previously been

simulated. Three patient-specific AAA geometries are reconstructed from CT scans. Firstly, it is demonstrated that the distribution of computed interlayer traction is highly dependent on the prescribed material properties. Additionally, omission of the intraluminal thrombus (ILT), which is reported to be present in over 70% of AAAs, is found to have a significant influence on the location of maximum interface tractions. The location of initial interlayer dissection is found to be highly dependent on the specific AAA geometry considered. Importantly, in most cases, initial interalyer dissection is not predicted to occur in the same locations as peak wall stresses. A mortality rate of 90% is associated with the rupture of AAAs. However, the reliable evaluation of the rupture risk of a specific AAA does not currently exist. In all cases the surgeon is presented with a dilemma: to operate and risk surgical complications or to carefully monitor the growth of the AAA. While previous computational models have attempted to predict the likelihood of AAA rupture based on the magnitude and location of maximum von Mises stress in the AAA wall, the initiation mechanisms and underlying mechanics of AAA rupture are poorly understood. It has been suggested in numerous studies that shear dissection between the layers of the AAA wall could play a role in AAA rupture (Ring, 2000; Phillippi et al., 2011; Pasta et al., 2011; Raghavan et al., 2011). However, the simulations presented in Chapter 7 demonstrate that locations of inter layer dissection do not necessarily coincide with locations of maximum von Mises stress in the AAA wall. Therefore traditional approaches to predicting rupture location based on von Mises stress concentrations must be questioned. The use of CZMs with CT derived geometries to predict interlayer dissection, as developed in this thesis, could potentially guide the future surgical assessment of AAA rupture potential.

The biomechanical response of an endothelial cell on a cyclically stretching silicone substrate is simulated in **Chapter 8**. As both cell debonding and rebonding can occur in this cyclic application, only the potential-based XN (Xu and Needleman, 1993) and MP formulations are considered so that no net interface work is performed if a point on the cell interface undergoes a closed loop where it debonds and then rebonds to its initial position on the substrate. Mixed-

mode separation of the cell from the substrate is computed when the prescribed work of tangential separation exceeds the work of normal separation ($\emptyset_t > \emptyset_n$). Active remodelling and contractility of the cell cytoplasm is described by a three-dimensional active stress fibre formulation (Deshpande et al., 2006; McGarry et al., 2009; Ronan et al., 2012). It is demonstrated that differences between the mixed-mode behaviour of the models has a pronounced effect on predicted cell debonding, and consequently on cell remodelling. Implementation of the XN model results in the computation of non-physical repulsive normal tractions which prevent cell rebonding during the unloading half cycles. In contrast, when the MP CZM is used to model the cell-substrate interface non-physical repulsive normal tractions are not computed and the cell rebonds to the substrate at the end of each cycle. When the MP CZM is used, significant changes in stress fibre remodelling are observed following 30 cycles with the dominant stress fibre bundling direction corresponding to experimentally observed cell realignment at ~70° to the stretching direction (Wang et al., 2001). The reorientation of cells seeded onto flexible substrates subjected to cyclic tensile strain has received much attention in recent years. The cellular morphology has been reported to align in the direction of minimum substrate strain (Dartsch and Betz, 1989; Iba et al., 1991; Wang et al., 1995; Wang et al., 2001; Balestrini et al., 2010). The findings of this chapter demonstrate that the XN CZM can introduce non-physical repulsive normal tractions at the cell-substrate interface while the MP model does not suffer from this drawback, and hence provides a prediction of cytoskeletal remodelling that corresponds closely to experimental observations.

9.1   Limitations and Future Directions

There are a number of limitations in the work presented in this thesis. The CZMs used in this work were not validated experimentally and were instead motivated by previous studies. A number of experiments could be performed to directly validate the cohesive zone formulations. For example, T-peel tests of commercially available stent coating could be performed to determine the shape and cohesive zone parameters of the cohesive zone formulation used in Chapter 6. In Chapter 7, where interlayer dissection is predicted in aneurysm geometries, lap shear tests could be used to characterise the mode II fracture strength of aortic tissue. Inflation testing of aortic ring specimens could be carried out to investigate the mechanism of arterial fracture in healthy and diseased tissue. Aditionally, damage was neglected in the cohesive zone formulations employed in this work. The incorporation of damage variables could produce altered interface failure predictions in the computational analyses and should be considered in future work. Furthermore, no rate dependence was included in the CZMs used in this work which could also influence predicted failure patterns. In Chapter 6, coating delamination was considered only one side (tensile side) of the stent unit cell. In contrast to this work where only one unit cell design was considered, future work should investigate different delamination patterns for a number of different stent unit cell architectures. In Chapter 7, a passive hyperelastic material model was used to describe the aneurysm wall. In reality, the evolution of an aneurysm involves complex remodelling of collagen and elastin fibres in the media and adventitia layers. Future work should incorporate an active remodelling framework for the aneurysm wall. For the cell contractility model presented in Chapter 8, no active model was included to describe the mechanism of cell debonding and rebonding. In reality, cell-substrate adhesion entails traction-dependent binding of high-affinity integrins to ligands, leading to focal adhesion assembly (Deshpande et al. (2008)). The implementation of an active cell-substrate interface model has recently been reported elsewhere (Ronan et al., 2012a).

In conclusion, the theoretical analysis presented in this thesis provides valuable guidance for future development and implementation of potential and non-potential-based CZMs for problems involving mixed-mode separation and over-closure. The implementation of mixed-mode cohesive zone models for cardiovascular applications provide novel insight relating to: Debonding of stent coatings during deployment; Interlayer dissection of arterial tissue in AAAs; Debonding, rebonding and cytoskeletal remodelling in endothelial cells during cyclic stretching.

9.2   References

Abdul-Baqi, A.&Van Der Giessen, E. (2001) Indentation-induced interface delamination of a strong film on a ductile substrate. *Thin Solid Films,* 381**,** 143-154.

Balakrishnan, B., Tzafriri, A. R., Seifert, P., Groothuis, A., Rogers, C.&Edelman, E. R. (2005) Strut position, blood flow, and drug deposition. *Circulation,* 111**,** 2958-2965.

Balestrini, J. L., Skorinko, J. K., Hera, A., Gaudette, G. R.&Billiar, K. L. (2010) Applying controlled non-uniform deformation for in vitro studies of cell mechanobiology. *Biomechanics and Modeling in Mechanobiology,* 9**,** 329-344.

Basalus, M. W. Z.&Von Birgelen, C. (2010) Benchside testing of drug-eluting stent surface and geometry. *Interv. Cardiol.,* 2**,** 159-175.

Dartsch, P. C.&Betz, E. (1989) Response of cultured endothelial cells to mechanical stimulation. *Basic research in cardiology,* 84**,** 268-281.

Deshpande, V. S., McMeeking, R. M.&Evans, A. G. (2006) A bio-chemo-mechanical model for cell contractility. *Proceedings of the National Academy of Sciences,* 103**,** 14015-14020.

Deshpande, V. S., Mrksich, M., McMeeking, R. M.&Evans, A. G. (2008) A bio-mechanical model for coupling cell contractility with focal adhesion formation. *Journal of the Mechanics and Physics of Solids,* 56, 1484-1510.

Dollhofer, J., Beckert, W., Lauke, B.&Schneider, K. (2000) Fracture mechanical characterisation of mixed-mode toughness of thermoplast/glass interfaces. *Computational Materials Science,* 19**,** 223-228.

Hoffmann, R., Mintz, G. S., Haager, P. K., Bozoglu, T., Grube, E., Gross, M., et al. (2002) Relation of stent design and stent surface material to subsequent in-stent intimal hyperplasia in coronary arteries determined by intravascular ultrasound. *The American journal of cardiology,* 89**,** 1360-1364.

Hutchinson, J. W.&Suo, Z. (1992) Mixed mode cracking in layered materials. *Advances in applied mechanics,* 29**,** 191.

Iakovou, I., Schmidt, T., Bonizzoni, E., Ge, L., Sangiorgi, G. M., Stankovic, G., et al. (2005) Incidence, predictors, and outcome of thrombosis after successful implantation of drug-eluting stents. *JAMA: the journal of the American Medical Association,* 293**,** 2126-2130.

Iba, T., Maitz, S., Furbert, T., Rosales, O., Widmann, M. D., Spillane, B., et al. (1991) Effect of cyclic stretch on endothelial cells from different vascular beds. *Circulatory shock,* 35**,** 193.

Kastrati, A., Mehilli, J., Dirschinger, J., Dotzer, F., Schuhlen, H., Neumann, F. J., et al. (2001) Intracoronary stenting and angiographic results: strut thickness effect on restenosis outcome (ISAR-STEREO) trial. *Circulation,* 103**,** 2816-2821.

Levy, Y., Mandler, D., Weinberger, J.&Domb, A. J. (2009) Evaluation of drug-eluting stents' coating durability-"Clinical and regulatory implications. *Journal of Biomedical Materials Research Part B: Applied Biomaterials,* 91**,** 441-451.

McGarry, J. P., Fu, J., Yang, M. T., Chen, C. S., McMeeking, R. M., Evans, A. G., et al. (2009) Simulation of the contractile response of cells on an array of micro-posts. *Philosophical Transactions of the Royal Society A: Mathematical, Physical and Engineering Sciences,* 367**,** 3477-3497.

Otsuka, Y., Chronos, N. A. F., Apkarian, R. P.&Robinson, K. A. (2007) Scanning electron microscopic analysis of defects in polymer coatings of three commercially available stents: comparison of BiodivYsio, Taxus and Cypher stents. *Journal of Invasive Cardiology,* 19**,** 71.

Pache, J., Dibra, A., Mehilli, J., Dirschinger, J., Schomig, A.&Kastrati, A. (2005) Drug-eluting stents compared with thin-strut bare stents for the reduction of restenosis: a prospective, randomized trial. *European Heart Journal,* 26**,** 1262-1268.

Park, K., Paulino, G. H.&Roesler, J. R. (2009) A unified potential-based cohesive model of mixed-mode fracture. *Journal of the Mechanics and Physics of Solids,* 57**,** 891-908.

Parry, G.&McGarry, P. (2012) An analytical solution for the stress state at stent-coating interfaces. *Journal of the Mechanical Behavior of Biomedical Materials,* 10**,** 183-196.

Pasta, S., Phillippi, J. A., Gleason, T. G.&Vorp, D. A. (2011) Effect of aneurysm on the mechanical dissection properties of the human ascending thoracic aorta. *The Journal of Thoracic and Cardiovascular Surgery,* 143**,** 460-467.

Phillippi, J. A., Pasta, S.&Vorp, D. A. (2011) Biomechanics and Pathobiology of Aortic Aneurysms. *Biomechanics and Mechanobiology of Aneurysms***,** 67-118.

Raghavan, M. L., Hanaoka, M. M., Kratzberg, J. A., Higuchi, M. D. L.&Da Silva, E. S. (2011) Biomechanical failure properties and microstructural content of ruptured and unruptured abdominal aortic aneurysms. *Journal of Biomechanics,* 44**,** 2501-2507.

Regar, E., Sianos, G.&Serruys, P. W. (2001) Stent development and local drug delivery. *British medical bulletin,* 59**,** 227.

Ring, W. S. (2000) Congenital Heart Surgery Nomenclature and Database Project: aortic aneurysm, sinus of Valsalva aneurysm, and aortic dissection. *The Annals of thoracic surgery,* 69**,** 147-163.

Ronan, W., Deshpande, V. S., McMeeking, R. M.&Patrick McGarry, J. (2012) Numerical investigation of the active role of the actin cytoskeleton in the compression resistance of cells. *Journal of the Mechanical Behavior of Biomedical Materials*.

Ronan, W., Deshpande, V. S., McMeeking, R. M.&Patrick McGarry, J. (2012a) Cellular contractility and substrate elasticity: a numerical investigation of the actin cytoskeleton and cell adhesion. *Submitted August 2012*.

Sørensen, B. F.&Kirkegaard, P. (2006) Determination of mixed mode cohesive laws. *Engineering Fracture Mechanics,* 73**,** 2642-2661.

Turco, M. A., Ormiston, J. A., Popma, J. J., Hall, J. J., Mann, T., Cannon, L. A., et al. (2008) Reduced Risk of Restenosis in Small Vessels and Reduced Risk of Myocardial Infarction in Long Lesions With the New Thin-Strut TAXUS Liberté Stent: 1-Year Results From the TAXUS ATLAS Program. *JACC: Cardiovascular Interventions,* 1**,** 699-709.

van den Bosch, M. J., Schreurs, P. J. G.&Geers, M. G. D. (2006) An improved description of the exponential Xu and Needleman cohesive zone law for mixed-mode decohesion. *Engineering Fracture Mechanics,* 73**,** 1220-1234.

Wang, F., Stouffer, G. A., Waxman, S.&Uretsky, B. F. (2002) Late coronary stent thrombosis: early vs. late stent thrombosis in the stent era. *Catheterization and cardiovascular interventions,* 55**,** 142-147.

Wang, H., Ip, W., Boissy, R.&Grood, E. S. (1995) Cell orientation response to cyclically deformed substrates: Experimental validation of a cell model. *Journal of Biomechanics,* 28**,** 1543-1552.

Wang, J. H. C., Goldschmidt-Clermont, P., Wille, J.&Yin, F. C. P. (2001) Specificity of endothelial cell reorientation in response to cyclic mechanical stretching. *Journal of Biomechanics,* 34**,** 1563-1572.

Warrior, N. A., Pickett, A. K.&Lourenco, N. S. F. (2003) Mixed-Mode Delamination-Experimental and Numerical Studies. *Strain,* 39**,** 153-159.

Wiemer, M., Butz, T., Schmidt, W., Schmitz, K. P., Horstkotte, D.&Langer, C. (2010) Scanning electron microscopic analysis of different drug eluting stents after failed implantation: from nearly undamaged to major damaged polymers. *Catheterization and cardiovascular interventions,* 75**,** 905-911.

Xu, X. P.&Needleman, A. (1993) Void nucleation by inclusion debonding in a crystal matrix. *Modelling and Simulation in Materials Science and Engineering,* 2**,** 417-418.

Yang, Q. D., Thouless, M. D.&Ward, S. M. (2001) Elastic-plastic mode-II fracture of adhesive joints. *International Journal of Solids and Structures,* 38**,** 3251-3262.

Appendix A

A.1 Additional Theory Formulations

A.1.1 Introduction

Theoretical formulations employed in this work, either directly or indirectly, are outlined in this chapter. The principles of continuum mechanics are presented in Section A.1.2 while the implicit finite element solution method is presented in Section A.1.3. The theoretical formulations provided in this section are largely based on the Abaqus, 2009 Theory Manual.

A.1.2 Continuum Mechanics Principles

A.1.2.1 Notation

In this section, scalars, vectors and matrices are utilised to describe some of the fundamental theories in continuum mechanics. A simple format for the representation of these entities is used so that the equations can be represented more concisely and to develop a more general understanding of their physical meaning. A scalar value is represented by 'a'. A vector can be represented by $\boldsymbol{a}$ or $\lfloor a \rfloor$. A second-order tensor or matrix is represented by $\boldsymbol{a}$ or $[a]$. A fourth-order tensor is represented by $\boldsymbol{A}$. Vectors and matrices, although written using the same form of notation, are differentiated by the context in which they are used. $\boldsymbol{a}^T$ signifies use of a vector, $\boldsymbol{a}$, in a 'row' format.

Vectors and tensors can be written in terms of their components which are associated with an axis system, defined by a set of base vectors in each point in space. For example, a vector, $\boldsymbol{a}$, can be defined as;

$$\boldsymbol{a} = a^1 \boldsymbol{e}_1 + a^2 \boldsymbol{e}_2 + a^3 \boldsymbol{e}_3 \tag{A.1}$$

where a^1, a^2 and a^3 are the components of $\boldsymbol{a}$ associated with base vectors $\boldsymbol{e_1}$, $\boldsymbol{e_2}$ and $\boldsymbol{e_3}$. The above equation can be simplified to;

$$\boldsymbol{a} = a^\alpha \boldsymbol{e_\alpha} \tag{A.2}$$

Similarly, instead of representing a matrix, $\boldsymbol{a}$, in component form where;

$$\begin{aligned}
\boldsymbol{a} &= \boldsymbol{e_1} a^{11} \boldsymbol{e_1} + \boldsymbol{e_1} a^{12} \boldsymbol{e_2} + \boldsymbol{e_1} a^{13} \boldsymbol{e_3} \\
&\quad \boldsymbol{e_2} a^{21} \boldsymbol{e_1} + \boldsymbol{e_2} a^{22} \boldsymbol{e_2} + \boldsymbol{e_2} a^{23} \boldsymbol{e_3} \\
&\quad \boldsymbol{e_3} a^{31} \boldsymbol{e_1} + \boldsymbol{e_3} a^{32} \boldsymbol{e_2} + \boldsymbol{e_3} a^{33} \boldsymbol{e_3}
\end{aligned} \tag{A.3}$$

the component form of a matrix can be simplified to (Flugge, 1972);

$$\boldsymbol{a} = \boldsymbol{e_\alpha} a^{\alpha\beta} \boldsymbol{e_\beta} \tag{A.4}$$

The dot product of two vectors is denoted by;

$$a = \boldsymbol{b}.\boldsymbol{c} \tag{A.5}$$

Matrix multiplication is denoted by;

$$\boldsymbol{a} = \boldsymbol{b}.\boldsymbol{c} \tag{A.6}$$

The cross product of two vectors is defined by;

$$\boldsymbol{a} = \boldsymbol{b} \times \boldsymbol{c} \tag{A.7}$$

The scalar product of two matrices is denoted by;

$$a = \boldsymbol{b} : \boldsymbol{c} \tag{A.8}$$

A.1.2.2 Deformation and Strain

The equations describing deformation are based on the movement of a particle of material in the current configuration, **x** relative to the initial configuration, **X**. The location history of the particle can be written as;

$$\mathbf{x} = \mathbf{x}(\mathbf{X}, \mathrm{t}) \tag{A.9}$$

If we consider two neighbouring particles located at **X** and **X**+d**X** in the initial configuration, then in the current configuration;

$$d\boldsymbol{x} = \frac{\partial \boldsymbol{x}}{\partial \boldsymbol{X}}.d\boldsymbol{X} \tag{A.10}$$

The matrix;

$$F = \frac{\partial x}{\partial X} \tag{A.11}$$

is known as the deformation gradient where;

$$dx = F.dX \tag{A.12}$$

Considering an infinitesimal gauge length dX around a particle initially at X, the initial and current lengths of the particle can be measured by;

$$dL^2 = d\mathbf{X}^T.d\mathbf{X} \text{ and } dl^2 = d\mathbf{x}^T.d\mathbf{x} \tag{A.13}$$

The stretch ratio or measure of strain at this gauge length is;

$$\lambda = \frac{dl}{dL} = \sqrt{\frac{dx^T.dx}{dX^T.dX}} \tag{A.14}$$

If $\lambda = 1$, the point of material has undergone rigid body motion only and there is no strain at this gauge length. From Equation (A.12);

$$dx^T.dx = dX^T.F^T.F.dX \tag{A.15}$$

So that Equation (A.14) becomes;

$$\lambda^2 = \frac{dX^T}{\sqrt{dX^T.dX}}.F^T.F.\frac{dX}{\sqrt{dX^T.dX}} = N^T.F^T.F.N \tag{A.16}$$

where N is a unit vector in the direction of gauge length dX. This equation can be used to measure the exact stretch ratio associated with any direction, N, at any material point defined by the initial or reference configuration. Stationary values of the stretch ratio, λ^2, can be obtained by solving the variational equation;

$$\delta\{N^T.F^T.F.N - p(N^T.N - 1)\} = 0 \tag{A.17}$$

where p is a Lagrange multiplier, used to retain the constraint;

$$N^T.N = 1 \tag{A.18}$$

when $N^T.N = 1$;

$$(\boldsymbol{F}^T.\boldsymbol{F} - p\boldsymbol{I}).\boldsymbol{N} = 0 \qquad \text{(A.19)}$$

By letting $\boldsymbol{n}_1, \boldsymbol{n}_2, \boldsymbol{n}_3$ be unit vectors in the initial configuration corresponding to $\boldsymbol{N}_1, \boldsymbol{N}_2, \boldsymbol{N}_3$ in the reference configuration;

$$\mathbf{n_1} = 1/\lambda_1 \, \mathbf{F}.\mathbf{N_1} \, ... \qquad \text{(A.20)}$$

Then;

$$\boldsymbol{n}_1^T.\boldsymbol{n}_2 = 1/\lambda_1\lambda_2 \, (\boldsymbol{N}_1^T.\boldsymbol{F}^T.\boldsymbol{F}.\boldsymbol{N}_2) = 1/\lambda_1\lambda_2 \, (\lambda_2^2 \boldsymbol{N}_1^T.\boldsymbol{N}_2) = 0 \qquad \text{(A.21)}$$

Since $\boldsymbol{n}_1, \boldsymbol{n}_2$ and $\boldsymbol{n}_3$ are unit vectors;

$$\boldsymbol{n}_1 = \boldsymbol{R}.\boldsymbol{N}_1, \quad \boldsymbol{n}_2 = \boldsymbol{R}.\boldsymbol{N}_2, \quad \boldsymbol{n}_3 = \boldsymbol{R}.\boldsymbol{N}_3 \qquad \text{(A.22)}$$

Where $\boldsymbol{R}$ is the pure rigid body rotation matrix and has the property $\boldsymbol{R}^T = \boldsymbol{R}^{-1}$. Therefore, it is possible to isolate the rigid body rotation and stretch of a particle by comparing the principle stretch directions in the current and reference configurations.

Strain in one-dimension is considered next. The magnitude of strain is zero at $\lambda = 1$. Often, the stretch ratio on its own is not sufficient to yield an accurate measure of strain. In one dimension, the strain, ε, can be defined in terms of the stretch ratio, λ, by;

$$\varepsilon = f(\lambda) \qquad \text{(A.23)}$$

By using a Taylor series expansion in the unstrained state ($\lambda = 1$), the strain can be expanded to;

$$\varepsilon = f(1) + (\lambda - 1)\frac{df}{d\lambda} + \frac{1}{2!}(\lambda - 1)^2 \frac{d^2 f}{d\lambda^2} + \cdots \qquad \text{(A.24)}$$

So that $f(1) = 0$ in the unstrained state. This technique provides a more accurate method for determining the strain magnitude. For very small strains, the higher order terms in the Taylor series are negligible and the overall strain tends towards $f(1)$. Many different strain measures are implemented such as;

Nominal strain (Biot's strain);

$$f(\lambda) = \lambda - 1 \tag{A.25}$$

If L is the reference gauge length and l is the current gauge length for a uniaxial specimen, this strain is given as $l/L - 1$.

Logarithmic strain is commonly implemented to describe metal plasticity. It is often used for these materials due to the fact that the elastic portion of strain is usually small. It is given as;

$$f(\lambda) = ln(\lambda) \tag{A.26}$$

The Green strain is often implemented for problems involving large motions but small strains. It can be generalised to a strain tensor in any 3-D motion and this tensor can be computed directly from the deformation gradient without the need for computing principal stretch directions and ratios. The Green strain is given as;

$$f(\lambda) = \frac{1}{2}(\lambda^2 - 1) \tag{A.27}$$

A.1.2.3 Finite Rotation

In Abaqus/Standard software, the components of the rotation vector, $\boldsymbol{\phi}$, are stored as degrees of freedom 4, 5 and 6 at a node where rotation is required. $\boldsymbol{\phi}$ consists of a rotation magnitude,$(\phi = \|\boldsymbol{\phi}\|)$ and a rotation axis, $\boldsymbol{P} = \boldsymbol{\phi}/\|\boldsymbol{\phi}\|$. Rotation is interpreted as a rotation by ϕ radians about the axis, $\boldsymbol{P}$. The rotation matrix is defined by using the rotation vector, $\boldsymbol{\phi}$, in addition to the skew-symmetric matrix,$\widehat{\boldsymbol{\phi}}$;

$$\widehat{\boldsymbol{\phi}}.\boldsymbol{\phi} = \mathbf{0} \text{ and } \widehat{\boldsymbol{\phi}}.\mathbf{v} = \boldsymbol{\phi} \times \mathbf{v}, \text{ for all vectors } \mathbf{v} \tag{A.28}$$

If $= \{\phi^1, \phi^2, \phi^3\}^T$, then;

$$[\widehat{\boldsymbol{\phi}}] = \begin{bmatrix} 0 & -\phi^3 & \phi^2 \\ \phi^3 & 0 & -\phi^1 \\ -\phi^2 & \phi^1 & 0 \end{bmatrix} \tag{A.29}$$

A.1.2.4 Rate of Deformation and Strain Increment

The velocity of a material particle is;

$$v = \frac{\partial x}{\partial t} \tag{A.30}$$

which defines the rate of change of a fixed material particle in the spatial position x. The difference in velocity between two neighbouring particles in the current configuration is given as;

$$dv = \frac{\partial v}{\partial x} \cdot dx = L \cdot dx \tag{A.31}$$

where $L = \partial v / \partial x$ is the current configuration velocity gradient. Since $dx = F \cdot dX$;

$$dv = L \cdot dx = L \cdot F \cdot dX \tag{A.32}$$

where F is the deformation gradient. L takes account of the material strain rate and rate of spin and can be decomposed into two parts; a symmetric strain rate matrix and an antisymmetric spin (rotation) rate matrix. The symmetric strain rate matrix is defined as;

$$D = \frac{1}{2}(L + L^T) = \frac{1}{2}\left(\left[\frac{\partial v}{\partial x}\right] + \left[\frac{\partial v}{\partial x}\right]^T \right) \tag{A.33}$$

The spin rate matrix is defined as;

$$W = \frac{1}{2}(L - L^T) = \frac{1}{2}\left(\left[\frac{\partial v}{\partial x}\right] - \left[\frac{\partial v}{\partial x}\right]^T \right) \tag{A.34}$$

A.1.2.5 Equilibrium Equations

Letting V denote a material volume in the current configuration and S denote the surface bounding the volume, the surface traction on any point on S can be denoted by the force, t, and the body force acting at any point in the material volume denoted as f. The force equilibrium for the volume of material is then given as;

$$\int_S \boldsymbol{t}dS + \int_V \boldsymbol{f}dV = 0 \qquad (A.35)$$

The Cauchy or true stress matrix, $\boldsymbol{\sigma}$, at a point on the surface, S is given by;

$$\boldsymbol{t} = \boldsymbol{n}.\boldsymbol{\sigma} \qquad (A.36)$$

where $\boldsymbol{n}$ is the unit outward normal to the surface at the point. Therefore, Equation (A.35) can be written as;

$$\int_S \boldsymbol{n}.\boldsymbol{\sigma} \, dS + \int_V \boldsymbol{f}dV = 0 \qquad (A.37)$$

The application of Gauss's theorem to the surface integral gives;

$$\int_S \boldsymbol{n}.\boldsymbol{\sigma} \, dS = \int_V \left(\frac{\partial}{\partial \boldsymbol{x}}\right).\boldsymbol{\sigma}dV \qquad (A.38)$$

The differential equation for translational equilibrium can then be defined as;

$$\left(\frac{\partial}{\partial \boldsymbol{x}}\right).\boldsymbol{\sigma} + \boldsymbol{f} = 0 \qquad (A.39)$$

By taking moments about the origin, moment equilibrium can be written as;

$$\int_S (\boldsymbol{x} \times \boldsymbol{t}) \, dS + \int_V (\boldsymbol{x} \times \boldsymbol{f}) \, dV = 0 \qquad (A.40)$$

Use of the Gauss theorem shows that the true Cauchy stress matrix must be symmetric;

$$\boldsymbol{\sigma} = \boldsymbol{\sigma}^T \qquad (A.41)$$

So that at each material point there are only six independent stress components. The above equation assumes that there are no point couples acting on the volume in which case symmetry property of Equation (A.41) would no longer be valid.

A.1.2.6 Stress Measures

The internal virtual work rate takes into account the symmetric part of the velocity gradient, $\boldsymbol{D}$ and Cauchy stress, $\boldsymbol{\sigma}$ such that;

$$\int_V \boldsymbol{\sigma} : \boldsymbol{D}dV = \int_{V^0} J\boldsymbol{\sigma} : \boldsymbol{D}dV^0 \qquad (A.42)$$

where $J = dV/dV^0$, known as the Jacobian, defines the volume change from the reference configuration. The standard Green strain matrix is defined as;

$$\varepsilon^G = \frac{1}{2}(\boldsymbol{F}^T.\boldsymbol{F} - \boldsymbol{I}) \qquad (A.43)$$

with respect to the reference configuration. The rate of Green strain is defined as;

$$\dot{\varepsilon}^G = \frac{1}{2}(\dot{\mathbf{F}}^T.\mathbf{F} + \mathbf{F}^T.\dot{\mathbf{F}}) = \mathbf{F}^T.\mathbf{D}.\mathbf{F} \qquad (A.44)$$

and therefore;

$$\mathbf{D} = \mathbf{F}^{-T}.\dot{\varepsilon}^G.\mathbf{F}^{-1} \qquad (A.45)$$

The work rate per unit volume can then be defined as;

$$dW^0 = J\boldsymbol{\sigma}:\mathbf{D} = J\boldsymbol{\sigma}:(\mathbf{F}^{-T}.\dot{\varepsilon}^G.\mathbf{F}^{-1}) \qquad (A.46)$$

From this equation, the stress measure, $\boldsymbol{S}$, known as the second Piola-Kirchoff stress tensor can be defined as;

$$\boldsymbol{S} = J\boldsymbol{F}^{-1}.\boldsymbol{\sigma}.\boldsymbol{F}^{-T} \qquad (A.47)$$

which is used to describe material subjected to large rotations but small strains. $\boldsymbol{S}$ can also be written in terms of the rotation, $\boldsymbol{R}$, of the principal axis of deformation as;

$$\boldsymbol{S} = \boldsymbol{R}^T.\boldsymbol{\sigma}.\boldsymbol{R} \qquad (A.48)$$

A.1.2.7 Hyperelasticity

Strain energy potentials are used to describe hyperelastic materials in Abaqus/Standard software. The strain energy potentials define the strain energy stored in the material per unit reference volume as a function of the strain at a point in the material. Numerous strain energy potentials exist to model incompressible isotropic elastomers including the Arruda Boyce form, the Marlow form, the neo-Hookean form, the Ogden form, the Mooney Rivlin form, the

polynomial form, the reduced polynomial form the Yeoh form and the Van der Walls form. The Yeoh and neo-Hookean forms can be viewed as special cases of the reduced polynomial model.

The form of the neo-Hookean strain energy potential is;

$$U = C_{10}(\bar{I}_1 - 3) + 1/D_1 (J^{el} - 1)^2 \tag{A.49}$$

where U is the strain energy per unit reference volume; J^{el} is the elastic volume ratio; C_{10} and D_1 are temperature-dependent material parameters; $\bar{I}_1$ is the first deviatoric strain invariant defined as;

$$\bar{\lambda}_1^2 + \bar{\lambda}_2^2 + \bar{\lambda}_3^2 \tag{A.50}$$

where the deviatoric stretches $\bar{\lambda}_i = J^{-1/3}\lambda_i$. J is the total volume ratio and λ_i are the principal stretches. The initial shear and bulk moduli are given by;

$$\mu_0 = 2C_{10}, \qquad K_0 = 2/D_1 \tag{A.51}$$

The temperature-dependent material parameters are related to the Young's modulus, E, and poisons ratio, v, by;

$$C_{10} = \frac{E}{4(1+v)}, \; D_1 = \frac{6(1-2v)}{E} \tag{A.52}$$

Hyperelastic materials are often incompressible or near incompressible. The relative compressibility of a material can be assessed by the ratio of the initial bulk modulus, K_0, to the initial shear modulus, μ_0 and in terms of the poisons ratio since

$$v = \frac{3K_0/\mu_0 - 2}{6K_0/\mu_0 + 2} \tag{A.53}$$

Abaqus/Standard computes the initial bulk modulus from the initial shear modulus by;

$$D_1 = \frac{2}{K_0} = \frac{3(1-2v)}{\mu_0(1+v)} \tag{A.54}$$

Using x to define the current position of a material point and X to represent the reference position of the same point, the deformation gradient, F, is defined as;

$$F = \frac{\partial x}{\partial X} \tag{A.55}$$

The total volume change at the point is defined by the Jacobian, J;

$$J = \det(F) \tag{A.56}$$

For simplicity, the deformation gradient with the volume change eliminated is defined as;

$$\bar{F} = J^{-1/3} F \tag{A.57}$$

The left Cauchy-Green strain tensor of $\bar{F}$ is defined as;

$$\bar{B} = \bar{F} \bar{F}^T \tag{A.58}$$

The first deviatoric strain invariant, $\bar{I}_1$, is defined as;

$$\bar{I}_1 = trace(\bar{B}) = I{:}\bar{B} \tag{A.59}$$

where I is a unit matrix.

The second strain invariant is defined as;

$$\bar{I}_2 = \frac{1}{2}\left(\bar{I}_1^2 - trace(\bar{B}.\,\bar{B})\right) \tag{A.60}$$

The gradient of the displacement variation regarding the current position is defined as;

$$\delta L = \frac{\partial \delta u}{\partial x} \tag{A.61}$$

The gradient of the displacement variation is divided into symmetric and anti-symmetric parts. The virtual rate of deformation is the symmetric part of δL where;

$$\delta D = sym(\delta L) = \frac{1}{2}(\delta L + \delta L^T) \tag{A.62}$$

The anti-symmetric part of δL is the virtual rate of spin where;

$$\delta W = asym(\delta L) = \frac{1}{2}(\delta L - \delta L^T) \tag{A.63}$$

A.1.2.8 Viscoelasticity

For linear isotropic viscoelasticity;

$$\boldsymbol{\sigma}(t) = \int_0^t 2G(\tau - \tau')\, \dot{e}\, dt' + \boldsymbol{I} \int_0^t K(\tau - \tau')\, \dot{\phi}\, dt' \tag{A.64}$$

where e and ϕ are the mechanical deviatoric and volumetric strains respectively; G is the shear modulus and K is the bulk modulus. τ is the reduced time. The reduced time is defined in terms of the actual time, t by;

$$\tau = \int_0^t \frac{dt'}{A_\theta\big(\theta(t')\big)} \tag{A.65}$$

where θ is the temperature and A_θ is the shift function. If $A_\theta = 1$, then the reduced time, τ is equal to the actual time, t.

A standard linear solid model can be used to represent both bulk and shear behaviour for a linear, isotropic viscoelastic material. In Abaqus/Standard software, the bulk and shear functions, $K(t)$ and $G(t)$, can be defined individually in terms of a series of exponentials known as the Prony series;

$$K(\tau) = K(\infty) + \sum_{i=1}^{n_K} K_i\, e^{-\tau/\tau_i^K} \tag{A.66}$$

$$G(\tau) = G(\infty) + \sum_{i=1}^{n_G} G_i\, e^{-\tau/\tau_i^G} \tag{A.67}$$

where $K(\infty)$ and $G(\infty)$ are the long-term bulk and shear moduli respectively, τ is the relaxation modulus, τ_i^K and τ_i^G are the bulk and shear relaxation moduli. The Prony series parameters (g^p, k^p, τ) can be defined directly for each term in the Prony series;

$$K(t) = \frac{K(\infty)\left(1 - k^p\left(1 - exp^{-\frac{t}{\tau}}\right)\right)}{(1 - k^p)} \tag{A.68}$$

$$G(t) = \frac{G(\infty)\left(1 - g^p\left(1 - exp^{-\frac{t}{\tau}}\right)\right)}{(1 - g^p)} \tag{A.69}$$

where g^p is the modulus ratio of the first term in the Prony series expansion of the shear relaxation modulus and k^p is the modulus ratio of the first term in the Prony series expansion of the bulk relaxation modulus.

A.1.2.9 Isotropic Elasto-Plasticity

The elastic response must always be small in cases where these constitutive models are used. Usually, plasticity is used to describe deformation in materials such as metals, polymer, crushable foams and concrete, where the elastic strain is usually negligible. Both rate-independent and rate-dependent plasticity constitutive models are based on the same numerical technique in Abaqus/Standard. Rate-independent plasticity is usually used to model the deformation response of metal and some other materials at low temperature and low strain rates. Elastic-plastic models are based on the assumption that the deformation can be divided into elastic and plastic parts. In the most basic and general form, this equation can be expressed as;

$$\boldsymbol{F} = \boldsymbol{F}^{el}.\boldsymbol{F}^{pl} \tag{A.70}$$

Where $\boldsymbol{F}$ is the entire deformation gradient, $\boldsymbol{F}^{el}$ is the recoverable and $\boldsymbol{F}^{pl}$ is the unrecoverable portion of deformation at a point under consideration. An additive strain decomposition can be used to formulate the plasticity model;

$$\dot{\varepsilon} = \dot{\varepsilon}^{el} + \dot{\varepsilon}^{pl} \tag{A.71}$$

where $\dot{\varepsilon}$ is the total mechanical strain rate, $\dot{\varepsilon}^{el}$ is the elastic strain rate and $\dot{\varepsilon}^{pl}$ is the plastic strain rate. Equation (A.71) is a consistent approximation of Equation Equation (A.70) when elastic strains are infinitesimal and when strain rate measure equals the rate of deformation;

$$\dot{\varepsilon} = sym\left[\frac{\partial \boldsymbol{v}}{\partial \boldsymbol{x}}\right] \tag{A.72}$$

The elastic part of the response can be derived from an elastic strain energy density potential and the stress defined by;

$$\boldsymbol{\sigma} = \frac{\partial U}{\partial \varepsilon^{el}} \tag{A.73}$$

where U is the strain energy density function and $\boldsymbol{\sigma}$ is the true (Cauchy) stress.

In an isotropic elasto-plasticity model, the volume strain is defined as;

$$\varepsilon_{vol} = trace(\varepsilon) \tag{A.74}$$

and the deviatoric strain is

$$\boldsymbol{e} = \varepsilon - \frac{1}{3}\varepsilon_{vol}\,\boldsymbol{I} \tag{A.75}$$

In the case of linear and isotropic elasticity, the bulk modulus, K, and shear modulus, G, can be used to describe the constitutive response;

$$K = \frac{E}{3(1-2v)} \tag{A.76}$$

and

$$G = \frac{E}{2(1+v)} \tag{A.77}$$

Elasticity can be expressed in terms of volumetric component as;

$$p = -K\varepsilon_{vol} \tag{A.78}$$

where p is the equivalent pressure stress and is also defined as;

$$p = -\frac{1}{3}trace(\boldsymbol{\sigma}) \tag{A.79}$$

Elasticity can also be defined in terms of the deviatoric component as;

$$\boldsymbol{S} = 2G\boldsymbol{e}^{el} \tag{A.80}$$

where $\boldsymbol{S}$ is the deviatoric stress and also defined as;

$$\boldsymbol{S} = \boldsymbol{\sigma} + p\boldsymbol{I} \tag{A.81}$$

The plastic flow rule is defined as;

$$d\boldsymbol{e}^{pl} = d\bar{e}^{pl}\boldsymbol{n} \tag{A.82}$$

where

$$n = \frac{3}{2}\frac{S}{q} \; ; q = \sqrt{\frac{3}{2}S{:}S} \tag{A.83}$$

and $d\bar{e}^{pl}$ is the equivalent plastic strain rate. The material must satisfy a uniaxial-stress, plastic-strain relationship for plasticity. For rate-independent material, the yield condition is;

$$q = \sigma^0 \tag{A.84}$$

where σ^0 is the yield stress and is a function of the temperature (θ) and equivalent plastic strain$(\bar{e}^{pl})$. For isotropic hardening, the yield surface changes size uniformly in all directions so that the yield stress increases or decreases in all strain directions as plastic strain progresses. If isotropic hardening is defined, the yield stress, σ^0, can be represented as a tabular function of plastic strain and temperature or other predefined variables.

For rate-dependent material, the equivalent plastic strain rate is defined by the uniaxial flow rate definition;

$$\dot{e}^{pl} = h(q, \bar{e}^{pl}, \theta) \tag{A.85}$$

where h is a known function. Integrating by the backward Euler method gives;

$$\Delta\bar{e}^{pl} = \Delta t h(q, \bar{e}^{pl}, \theta) \tag{A.86}$$

The general uniaxial form for both the rate-independent and the rate-dependent models is;

$$q = \bar{\sigma}(\bar{e}^{pl}) \tag{A.87}$$

Where $\bar{\sigma}$ is obtained through inversion of Equation (A.86) for the rate-dependent model and $\bar{\sigma} = \sigma^0$ for the rate-independent model.

A.1.3 Implicit Finite Element Solution Method

In the context of finite element methods, the word "implicit" refers to the method by which the finite element model is updated from time t to $t+\Delta t$. A fully implicit procedure means that the state at $t+\Delta t$ is determined based on information at time $t+\Delta t$, whereas the explicit method solves for $t+\Delta t$ based on information at time t.

A range of solution procedures are used by implicit finite element solvers. A form of the Newton-Raphson (N-R) method is the most common and is presented here. For illustrative purposes, the small strain case is presented and matrix/vector notation is used. When solving a quasi-static boundary value problem, the principle of virtual work is a fundamental equation upon which this method is based;

$$\int_V \delta\boldsymbol{\varepsilon}^T \boldsymbol{\sigma} dV = \int_S \delta\mathbf{u}^T \mathbf{t} dS \tag{A.88}$$

where the equilibrium is enforced on a reference volume, V, which is bounded by a surface, S. $\boldsymbol{\sigma}$ and $\mathbf{t}$ are the stress and surface traction vectors respectively, while $\delta\boldsymbol{\varepsilon}$ and $\delta\mathbf{u}$ are the virtual strain and virtual displacement vectors. Consider the integrals of Equation (A.88) taken over a finite element mesh with individual elements "e" of volume V_e and surface S_e. Within each element one has the following finite element interpolation:

$$\delta\boldsymbol{\varepsilon} = \mathbf{B}_e \delta\mathbf{u}_e \tag{A.89}$$

and

$$\delta\mathbf{u} = \mathbf{N}_e \delta\mathbf{u}_e \tag{A.90}$$

where $\mathbf{N}_e$ and $\mathbf{B}_e$ are the element shape function and shape function gradient matrices, respectively. Substituting these into Equation (A.88) and rearranging, the following expression is generated:

$$\sum_e \int_{V_e} \delta\mathbf{u}_e^T \mathbf{B}_e^T \boldsymbol{\sigma}(\mathbf{u}_e) dV = \sum_e \int_{S_e} \delta\mathbf{u}_e^T \mathbf{N}_e^T \mathbf{t} dS \tag{A.91}$$

where the summation is over all elements in the finite element mesh. Note that the stress matrix is dependent on the elemental vector of nodal displacements, $\mathbf{u}_e$. Performing the summation, which in effect means assembling elemental quantities into global quantities, and eliminating the arbitrary virtual quantities yields the following global expression:

$$\int_V \mathbf{B}^T \boldsymbol{\sigma}(\mathbf{u}) dV = \int_S \mathbf{N}^T \mathbf{t} dS \tag{A.92}$$

where $\mathbf{u}$ is the global nodal displacement vector for the mesh. A set of global equations in $\mathbf{u}$ for the out of balance force, $\mathbf{G}$, can then be assembled;

$$\mathbf{G}(\mathbf{u}) = \int_V \mathbf{B}^T \boldsymbol{\sigma}(\mathbf{u}) dV - \int_S \mathbf{N}^T \mathbf{t} dS = 0 \tag{A.93}$$

In general for non-linear problems involving non-linear constitutive laws and/or non-linear boundary conditions Equation (A.93) is non-linear, and is usually solved by incremental methods, where loads/displacements are applied in time steps, Δt, up to an ultimate time, t_{final}.

Within each increment, the state of the analysis is updated iteratively using the N-R method from time t to time $t+\Delta t$ to solve for $\mathbf{u}^{t+\Delta t}$. An estimation of the roots of Equation (A.93) is made, such that for the ith iteration:

$$\delta \mathbf{u}_{i+1} = \mathbf{u}_{i+1}^{t+\Delta t} - \mathbf{u}_i^{t+\Delta t} = -\left(\frac{\partial \mathbf{G}(\mathbf{u}_i^{t+\Delta t})}{\partial \mathbf{u}}\right) \mathbf{G}(\mathbf{u}_i^{t+\Delta t}) \tag{A.94}$$

where $\mathbf{u}_i^{t+\Delta t}$ is the vector of nodal displacements for the ith iteration at time $t+\Delta t$. The partial derivative on the right hand side of the equation is the Jacobian matrix of the governing equations and can be referred to as the global stiffness matrix, $\mathbf{K_G}$. Equation A.94 is manipulated and inverted to produce a system of linear equations:

$$\mathbf{K_G}\left(\mathbf{u}_i^{t+\Delta t}\right) \delta \mathbf{u}_{i+1} = -\mathbf{G}\left(\mathbf{u}_i^{t+\Delta t}\right) \tag{A.95}$$

Equation (A.95) must be solved, for each iteration, for the change in incremental displacements, $\delta \mathbf{u}_{i+1}$. In order to solve for $\delta \mathbf{u}_{i+1}$ the global stiffness matrix, $\mathbf{K_G}$,

must be inverted. Although, this is a computationally expensive operation, iteration ensures that a relatively large time increment can be used while maintaining accuracy of solution. Following iteration i, $\delta\mathbf{u}_{i+1}$ has been determined and a better approximation of the solution has been made, $\mathbf{u}_{i+1}^{t+\Delta t}$, through Equation A.93. This in turn is used as the current approximation to the solution for the subsequent iteration ($i+1$).

The accuracy of the method depends on the accurate evaluation of $\mathbf{G}\big(\mathbf{u}_i^{t+\Delta t}\big)$ for each iteration, which in turn depends on the accurate evaluation of $\boldsymbol{\sigma}\big(\mathbf{u}_i^{t+\Delta t}\big)$. The latter of these two quantities requires an accurate stress update algorithm to be in place to calculate the stresses for each iterative estimate of the displacements, $\mathbf{u}_i^{t+\Delta t}$. The accuracy of the solution is also dictated by the convergence criterion where the updated value for $\mathbf{G}$ must be less than a tolerance value. Complications can arise in an analysis that has a highly non-linear stress-strain response or where there is contact and sliding between two surfaces. For a complex problem it can be difficult to predict how long it will take to solve or even if convergence will occur at all.

Abaqus/Standard uses a form of the N-R iterative solution method to solve for the incremental set of equations. Formulating and inverting the Jacobian matrix is the most computationally expensive process. Several variations on the N-R method exist to improve the solution time. The modified Newton method is the most commonly used alternative and is suitable for non-linear problems. The Jacobian is only recalculated occasionally and in cases where the Jacobian is unsymmetric it is not necessary to calculate an exact value for it. The modified Newton method converges quite well using a symmetric estimate of the Jacobian.

A.1.4 References

Abaqus (2009) Abaqus Theory Manual, Version 6.9-1,. *User Documentation, Dassault Systems*.

Flugge, W. (1972) *Tensor analysis and continuum mechanics*, Springer-Verlag Berlin.

Appendix B

B.1 Stent Parameter Sensitivity and Mesh Sensitivity Analysis

Figure B-1(a) shows the maximum normal interface traction $\left(T_{n,max}/E_c\right)$ computed at $\theta = 0$ as a function of arch deployment (Σ_a) using the mesh density of 181760 elements and a mesh density in which the element length is halved (727680 elements). At all levels of stent deployment, the higher density mesh results in a negligible percentage change (less than 1%) in computed traction. This clearly demonstrates that the mesh element length used in the current study is sufficiently accurate. Figure B-1(b) shows the computed interface traction $\left(T_{n,max}/E_c\right)$ computed at $\theta = 0$ as a function of interface length (δ/R). δ/R ratios of, $4\text{x}10^{-5}, 4\text{x}10^{-4}, 4\text{x}10^{-3}$ and $4\text{x}10^{-2}$ are considered. For a radial distance (R) of $100\mu m$, these ratios correspond to interface lengths of $4\text{x}10^{-3}$, $4\text{x}10^{-2}$, $4\text{x}10^{-1}$ and $4\mu m$. It is clear that the characteristic interface length has no influence on computed interface tractions at small $(\Sigma_a = 0.004)$, medium $(\Sigma_a = 0.2)$ and finite $(\Sigma_a = 0.4)$ arch deformation. 4-noded bilinear plane strain quadrilateral elements (CPE4) were utilised for the meshed stent and coating geometries.
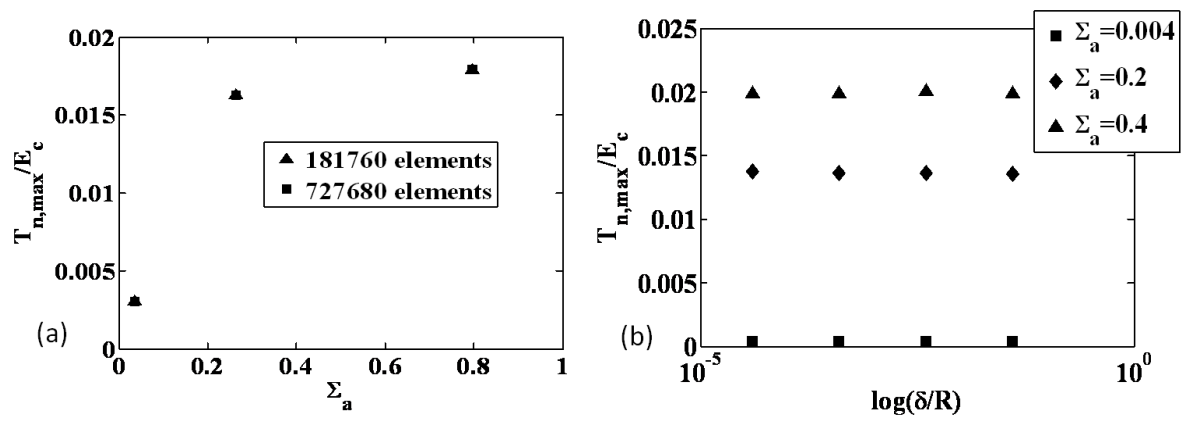
Figure B-1: Maximum normalised normal traction $\left(T_{n,max}/E_c\right)$ computed at $\theta = 0$ as a function of (a) arch deformation (Σ_a) for two mesh densities and (b) normalised characteristic interface length $(\delta = \delta_n = \delta_t)$ at three levels of arch deformation (Σ_a). E_c is the coating stiffness. R is the radial distance to the stent-coating interface.

B.2 Abdominal Aortic Aneurysm-Mesh Sensitivity Analysis

Figure B-2 shows the peak von Mises stress $\left(\sigma_{mises,max}\right)$ computed in the adventitia layer as a function of applied lumen pressure. An increase in finite element mesh density from approximately 5000 to 50000 elements results in only a ~2% increase in the computed stress. Therefore, considering computational efficiency, a mesh density of approximately 5000 elements is used for all analyses presented in Chapter 7. 8-noded linear brick elements (C3D8) are used for all aneurysm simulations.
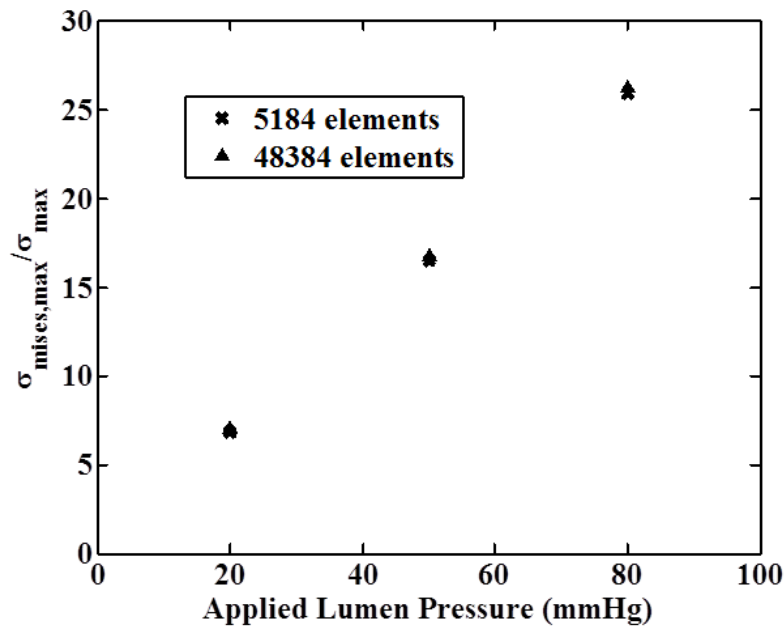
Figure B-2: Peak von Mises stress normalised by prescribed interface strength $\left(\sigma_{mises,max}/\sigma_{max}\right)$ as a function of applied lumen pressure for two mesh densities. $E_{intima} = 2.9MPa$, $\sigma_{max} = 17Kpa$, $\delta_n = \delta_t = 10\mu m$.

Appendix C

C.1 Rotational Constraint at the Base of the Stent Struts

Certain stent designs may effect a rotational constraint at the bottom of the struts (Figure C-1), e.g. a repeating diamond arrangement of struts. This constraint results in a significant increase in tangential traction for all deployment levels and also results in a normal compression at the stent–coating interface at the bottom of the arch. When strut rotation is prevented, peak tangential tractions exceed peak normal tractions, even at a low of stent deployment ($\Sigma_a = 0.028$) (Figure C-2 (a)), for a short strut length ($L/R = 0.5$). The patterns of computed traction for a medium deployment level ($\Sigma_a = 0.228$), Figure C-2(b)) are reasonably similar to those presented for a low deployment level. At a high level of deployment ($\Sigma_a = 0.335$), peak tangential traction significantly exceeds the peak computed normal tractions for a shorter strut ($L/R = 0.5$) with $|T_{t,max}/T_{n,max}| > 4$. Additionally, significant coating compression is computed for $L/R = 0.5$ from $1 \leq x/R \leq 1.9$. Constraining arch rotation clearly results in an increase in computed tangential tractions and decrease in normal tractions computed along the stent-coating interface.

(a)　　　　　　　　　　　　　　　　　(b)
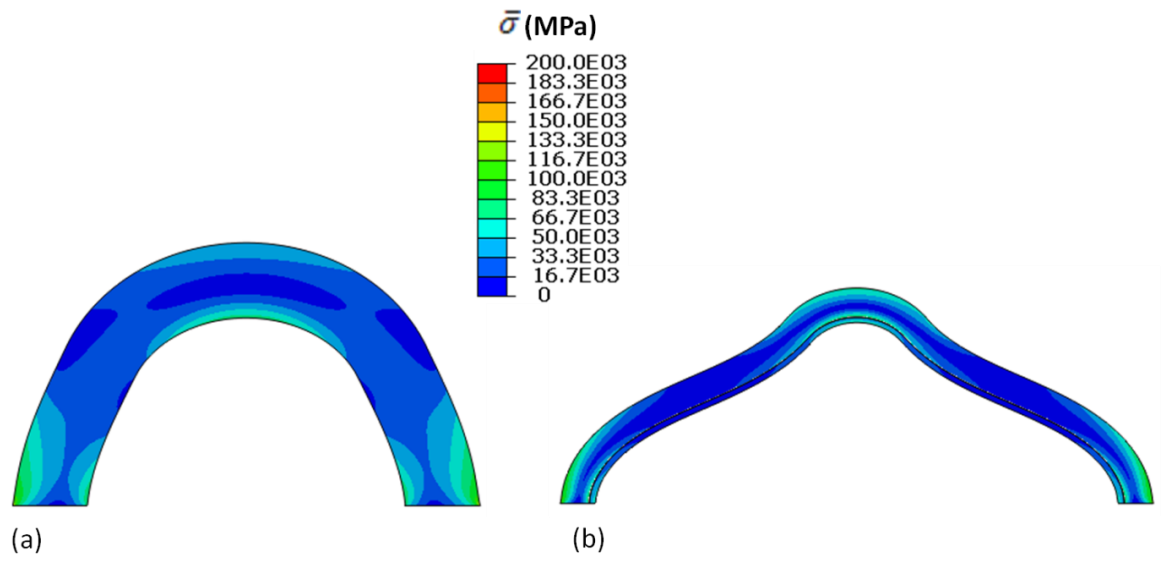
Figure C-1:von Mises $(\bar{\sigma})$ stress distribution on the deformed geometry for (a) $L/R = 2$ and (b) $L/R = 10$ at an arch deployment of $\Sigma_a = 0.335$. A boundary condition is imposed on the bottom edges of the stent strut to prevent edge rotation.
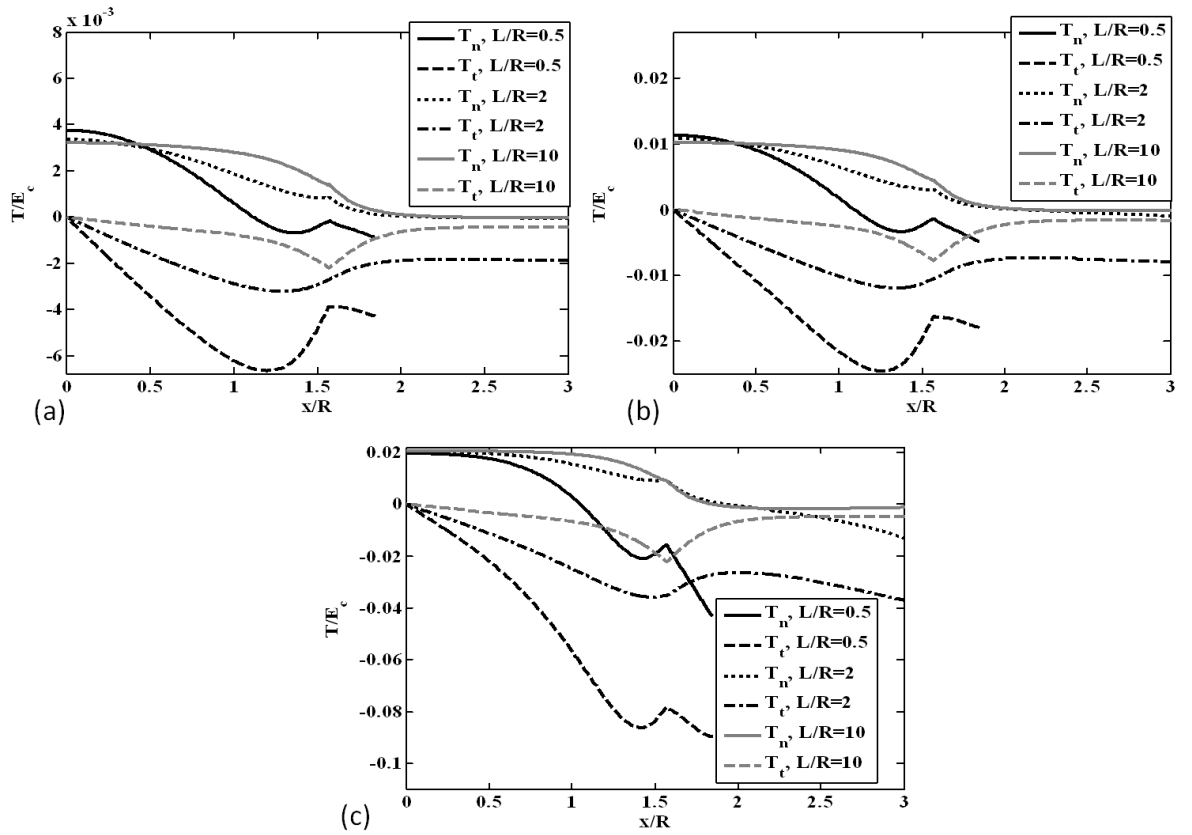
Figure C-2: Computed normal (T_n) and tangential (T_t) tractions along the stent-coating interface for a range of strut lengths for (a) low deployment $(\Sigma_a = 0.028)$ (b) medium deployment $(\Sigma_a = 0.228)$ and (c) high deployment $(\Sigma_a = 0.335)$. Boundary conditions are imposed on the strut ends to prevent rotation. E_c=200GPa, E_s=500GPa $\sigma_{max}/E_c = \tau_{max}/E_c = 2$, $h_1/R = 0.2$, $h_2/R = 1$.

Appendix D

D.1 Abdominal Aortic Aneurysm (AAA) Histology

D.1.1 Introduction

In this section, the reported histology of healthy aorta and diseased AAA tissue is presented. In the case of the AAA tissue, both layer specific and general histological features are presented.

D.1.2 Histology- Healthy Aorta

The intima is made of endothelium resting on a basal lamina and a subendothelial connective tissue layer. Endothelial cells are elongated in the direction of blood flow. The subendothelial layer contains elastic fibres and type I collagen fibrils, fibroblasts and small smooth muscle-like myointimal cells. With age, these myointimal cells accumulate lipid and can lead to atherosclerotic change in the intima. Thickening of the intima progresses with age and is more marked in the distal rather than the proximal segment of the aorta. An internal elastic lamina lies between the intima and the media. The media consists of a layered structure of fenestrated layers of elastic (elastic lamellae), interlamellar smooth muscle cells (SMC's), collagen and fine elastic fibres. Some 75% of the mass of the media consists of SMC's, which run circumferentially around the vessel wall. The SMC's serve as the contractile machinery in the medial layer. In addition to collagen and elastic fibres, the adventitial layer contains flattened fibroblasts, macrophages, mast cells, lymphatic vessels and nerve bundles. It is composed of thick bundles of collagen fibrils arranged in helical structures (Standring, 2008).

D.1.3 Histology-Aneurysm (layer-specific)

The transition from healthy AA tissue to diseased AAA tissue is associated with significant changes in each arterial layer. Additionally, it has been reported that a in an intraluminal thrombus (ILT) in approximately 70% of AAAs (Vande Geest et al., 2006). SEM images from three different intraluminal thrombus regions were analysed by Wang et al. (2001). Specifically, tissue samples from the luminal, medial and abluminal regions were assessed. A significant difference in tissue composition was reported based on the region analysed. In the luminal region, fibrin fibres were clearly identifiable, arranged into primary thick fibrin bundles and fine secondary structures crosslinking the primary bundles. In the medial region many of the fibrin fibres were degenerated. It was reported that all of the fibrin fibres were degenerated in the abluminal region, with the ILT in this region showng little or no structure at all. A porous ILT structure was reported by Gasser et al. (2009) where histological slices from 7 ILT's were assessed. Larger pores were reported in the abluminal layer when compared to the luminal layer. ILT's from 24 patients were histologically assessed by Adolph et al. (1997). Large pores(cavities) were reported throughout the entire thickness of the ILT tissue. Additionally, T-cells, neutrophils, macrophages, platelets and red blood cells were detected throughout the thickness of the ILT tissue. T-cells and macrophages were quantified in the luminal region of the ILT suggesting that the ILT is a biologically active structure and may play a significant role in the pathogenesis of AAAs. It was reported by Busuttil et al. (1982) that elastase activity is significantly higher in aneurysmal tissue, particularly in the intima and medial layers. Kazi et al. (2003) reported inflammatory cells (macrophages and T-cells) in the intimal layer with apoptosis of cells in the thrombus-covered intimal layer also confirmed. However, it has been reported that elsewhere that a recognisable intimal layer does not exist in a AAA wall (Holmes et al., 1995; Vorp, 2007). A significant reduction in elastin and SMC content in the medial layer has been reported (Busuttil et al., 1982; Kazi et al., 2003). Interestingly, the work of Kazi et al. (2003) showed that SMC's were more necrotic and apoptotic in thrombus-covered AAA tissue as opposed to AAA tissue where no thrombus resided.

The research of Freestone et al. (1995) involved the analysis of AAA tissue samples for the activity of matrix metalloproneises (MMPs). MMPs are enzymes which play an important role in the remodelling of extra cellular matrix components (mainly elastin and collagen in aorta). The histological feature most clearly associated with enlarging aneurysm diameter was a higher density of inflammatory cells in the adventitia. Specifically, macrophages and B lymphocytes were identified in this layer. It was concluded that the proliferation of inflammatory cells into the adventitial layer along with the upregulation of metalloproteinases, including gelatinase B, could contribute to the rapid growth and rupture of larger aneurysm.

D.1.4 Histology- Aneurysm (general)

Menashi et al. (1987) tested for collagen content in AAA and non AAA tissue. Patients were categorised according to age and sex. It was found that the overall collagen content increased from 62% to 84% for AAA tissue which was suggested to be the result of preferential elastin degradation. A subgroup of three patients with a significant family history of aneurysm exhibited a lower amount of type 3 collagen in aortic media, suggesting that abnormalities in type 3 collagen mat be one of the genetic factors which can lead to the development of AAAs. Rizzo et al. (1989) concluded that neither patients with a family history of aneurysms nor those without a history of aneurysm formation had collagen type I or type II deficiency. Collagen types I and III were measured following tissue digestion with cyanogen bromide. Overall levels of collagen content were reported to be increased as well as evidence of fragmented elastin in the AAA tissue. However, Minion et al. (1994) suggested an increase in both elastin and collagen content in AAA tissue and Gandhi et al. (1994), did not support the hypothesis of a cross-linking deficiency in the elastin of AAAs. Smooth muscle cells play a crucial role in aortic medial layer architecture and matrix remodelling. The work of Lopez-Candales et al. (1997) involved immunohistochemistry analysis on pathological and non-pathological human abdominal aortic tissue specimens (N=21) in order to evaluate SMC density levels (α smooth muscle cell actin and direct cell counts).

In situ end labelling (ISEL) of fragmented DNA was used to detect apoptotic cells and it was subsequently evaluated that approximately 30% of the AAA wall cells were apoptotic. P53 protein levels increased 4fold in AAA tissue compared to non AAA tissue. It was also found that smooth muscle cell density decreased by 74% in AAA tissue compared to controls (n=10). These findings were corroborated by Henderson et al. (1999) where an increase in smooth muscle cell apoptosis and decrease in the density of smooth muscle cells in AAA tissue were reported. An increase in elastolysis in AAA tissue was reported by Wilson et al. (2001). Sixty two male patients of median age were prospectively studied. An increase in overall collagen turnover was reported for AAA tissue -increased collagen turnover is associated with reduced distensibility. A procollagen 3-N-terminal propeptide (PIINP) was used in this study to quantify overall collagen turnover. A significant reduction in the concentration of elastin crosslinking in AAA tissue was reported in the work of Carmo et al. (2002). It was also reported that collagen crosslinks were 350% higher in AAA tissue than in control tissue. However, the markers indicating the levels of overall collagen and elastin content reduced suggesting that the synthesis of new collagen and elastin fibres is inhibited in pathological AAA tissue leading to the progression of the disease. However, an increase in collagen content and a decrease in elastin content was reported for AAA tissue in the research of Sakalihasan et al. (1993). Research conducted by Wilson et al. (2005), suggested that the concentration of MMP-8 was significantly raised in AAA tissue compared to healthy tissue. TIMP1 and TIMP2 (tissue inhibitors of metalloproteinases) expression was significantly reduced in AAA tissue compared to control samples. It was concluded that the high concentration of MMP-8 in aortic aneurysms could present a potent pathway for collagen degradation and subsequently aneurysm formation and expansion. It was also suggested that the loss of elastin can initiate the development of the AAA but it is the loss of collagen which leads to continued expansion.

D.1.5 References

Adolph, R., Vorp, D. A., Steed, D. L., Webster, M. W., Kameneva, M. V.&Watkins, S. C. (1997) Cellular content and permeability of intraluminal thrombus in abdominal aortic aneurysm. *Journal of vascular surgery,* 25**,** 916-926.

Busuttil, R. W., Rinderbriecht, H., Flesher, A.&Carmack, C. (1982) Elastase activity: the role of elastase in aortic aneurysm formation. *Journal of Surgical Research,* 32**,** 214-217.

Carmo, M., Colombo, L., Bruno, A., Corsi, F. R. M., Roncoroni, L., Cuttin, M. S., et al. (2002) Alteration of elastin, collagen and their cross-links in abdominal aortic aneurysms. *European Journal of Vascular & Endovascular Surgery,* 23**,** 543-549.

Freestone, T., Turner, R. J., Coady, A., Higman, D. J., Greenhalgh, R. M.&Powell, J. T. (1995) Inflammation and matrix metalloproteinases in the enlarging abdominal aortic aneurysm. *Arteriosclerosis, Thrombosis, and Vascular Biology,* 15**,** 1145.

Gandhi, R. H., Irizarry, E., Cantor, J. O., Keller, S., Nackman, G. B., Halpern, V. J., et al. (1994) Analysis of elastin cross-linking and the connective tissue matrix of abdominal aortic aneurysms. *Surgery,* 115**,** 617.

Gasser, T. C., Martufi, G., Auer, M., Folkesson, M.&Swedenborg, J. (2009) Micromechanical Characterization of Intra-luminal Thrombus Tissue from Abdominal Aortic Aneurysms. *Annals of Biomedical Engineering***,** 1-9.

Henderson, E. L., Geng, Y. J., Sukhova, G. K., Whittemore, A. D., Knox, J.&Libby, P. (1999) Death of smooth muscle cells and expression of mediators of apoptosis by T lymphocytes in human abdominal aortic aneurysms. *Circulation,* 99**,** 96.

Holmes, D. R., Liao, S., Parks, W. C.&Hompson, R. W. (1995) Medial neovascularization in abdominal aortic aneurysms: A histopathologic marker of aneurysmal degeneration with pathophysiologic implications. *Journal of vascular surgery,* 21**,** 761-772.

Kazi, M., Thyberg, J., Religa, P., Roy, J., Eriksson, P., Hedin, U., et al. (2003) Influence of intraluminal thrombus on structural and cellular composition of abdominal aortic aneurysm wall. *Journal of vascular surgery,* 38**,** 1283-1292.

Lopez-Candales, A., Holmes, D. R., Liao, S., Scott, M. J., Wickline, S. A.&Thompson, R. W. (1997) Decreased vascular smooth muscle cell density in medial degeneration of human abdominal aortic aneurysms. *The American journal of pathology,* 150**,** 993.

Menashi, S., Campa, J. S., Greenhalgh, R. M.&Powell, J. T. (1987) Collagen in abdominal aortic aneurysm: typing, content, and degradation. *Journal of vascular surgery: official publication, the Society for Vascular Surgery [and] International Society for Cardiovascular Surgery, North American Chapter,* 6**,** 578.

Minion, D. J., Davis, V. A., Nejezchleb, P. A., Wang, Y., Mcmanus, B. M.&Baxter, B. T. (1994) Elastin is increased in abdominal aortic aneurysms. *The Journal of surgical research,* 57**,** 443.

Rizzo, R. J., Mccarthy, W. J., Dixit, S. N., Lilly, M. P., Shively, V. P., Flinn, W. R., et al. (1989) Collagen types and matrix protein content in human abdominal aortic aneurysms. *Journal of vascular surgery: official publication, the Society for Vascular Surgery [and] International Society for Cardiovascular Surgery, North American Chapter,* 10**,** 365.

Sakalihasan, N., Heyeres, A., Nusgens, B. V., Limet, R.&Lapiere, C. M. (1993) Modifications of the extracellular matrix of aneurysmal abdominal aortas as a function of their size. *European journal of vascular surgery,* 7**,** 633.

Standring, S. (2008) *Gray's anatomy*, Churchill Livingstone, Elsevier.

Vande Geest, J. P., Sacks, M. S.&Vorp, D. A. (2006) A planar biaxial constitutive relation for the luminal layer of intra-luminal thrombus in abdominal aortic aneurysms. *Journal of Biomechanics,* 39**,** 2347-2354.

Vorp, D. A. (2007) Biomechanics of abdominal aortic aneurysm. *Journal of Biomechanics,* 40**,** 1887-1902.

Wang, D. H. J., Makaroun, M., Webster, M. W.&Vorp, D. A. (2001) Mechanical properties and microstructure of intraluminal thrombus from abdominal aortic aneurysm. *Journal of Biomechanical Engineering,* 123**,** 536.

Wilson, K. A., Lindholt, J. S., Hoskins, P. R., Heickendorff, L., Vammen, S.&Bradbury, A. W. (2001) The Relationship Between Abdominal Aortic Aneurysm Distensibility and Serum Markers of Elastin and Collagen Metabolism. *European Journal of Vascular and Endovascular Surgery,* 21**,** 175-178.

Wilson, W. R. W., Schwalbe, E. C., Jones, J. L., Bell, P. R. F.&Thompson, M. M. (2005) Matrix metalloproteinase 8 neutrophil collagenase in the pathogenesis of abdominal aortic aneurysm. *British Journal of Surgery,* 92**,** 828-833.

Appendix E

E.1 User Subroutines Used to Define Surface Interaction Behaviour

E.1.1 2D-UINTER

```fortran
      subroutine
uinter(stress,ddsddr,flux,ddfddt,ddsddt,ddfddr,
     1      statev,sed,sfd,spd,svd,scd,pnewdt,rdisp,drdisp,
     2
temp,dtemp,predef,dpred,time,dtime,ciname,slname,msname,
     3
props,coords,aLocalDir,drot,area,chrLngth,node,ndir,nstatv,
     4      npred,nprops,mcrd,kstep,kinc,kit,linper,lOpenClose,
     5      lState,lSdi,lPrint)
c
      include 'aba_param.inc'
c
      dimension
stress(ndir),ddsddr(ndir,ndir),flux(2),ddfddt(2,2),
     $
ddsddt(ndir,2),ddfddr(2,ndir),statev(nstatv),rdisp(ndir),
     $
drdisp(ndir),temp(2),dtemp(2),predef(2,npred),dpred(2,npred),
     $
time(2),props(nprops),coords(mcrd),aLocalDir(mcrd,mcrd),
     $      drot(2,2)
      character*80 ciname,slname,msname
      REAL*8 LN,LT,k,UTEST

          Q1=1.D0
          Q0=0.0000000000000000E+00
```

```fortran
c
          SMAX=PROPS(1)
          LN=PROPS(2)
          LT=PROPS(3)
          TMAX=PROPS(4)
          ZETA=PROPS(5)


c
       UN=RDISP(1)*-1.
       UT=RDISP(2)
c      UM=RDISP(3)
c
       DUN=DRDISP(1)*-1.
       DUT=DRDISP(2)
c       DUM=DRDISP(3)
c
       U=UN/LN
c       write(6,*)'UN=',UN
c     write(6,*)'u=',u
       V=UT/LT
c       write(6,*)'UT=',UT
c     write(6,*)'v=',v
c       W=UM/LT
c
c
       if (UN.GT.Q0)THEN
C     if (UN.GT.LN/1000)THEN
C     APPLY SMC
c
       TN=SMAX*EXP(Q1)*(U)*EXP(-SQRT((U*U)+(V*V)))
     $+(ZETA*SMAX*DUN/(DTIME*LN))
c
c      write(6,*)'TN=',TN
       TT=TMAX*EXP(Q1)*V*EXP(-SQRT((U*U)+(V*V)))
     $+(ZETA*TMAX*DUT/(DTIME*LT))
c      write(6,*)'TT=',TT
ccccccccccccccccccccccccccccccccccccccccccccccccccccccccccccccccccc
ccccccc
C     jabobian
```

```fortran
c        if (u.eq.0) then
c        DDSDDR(1,1)=SMAX*exp(1-sqrt(V*V+U*U))+(ZETA*SMAX/LN/DTIME)
c        else
         DDSDDR(1,1)=SMAX*EXP(Q1-SQRT(V*V+U*U))/LN-
(SMAX*UN*UN*EXP(Q1-SQRT
     $(V*V+U*U)))/(LN*LN*LN*SQRT(V*V+U*U))+(ZETA*SMAX/LN/DTIME)
c
c        write(6,*)'DDSDDR(1,1)',DDSDDR(1,1)
         DDSDDR(1,2)=(SMAX*UN*UT*EXP(Q1-SQRT(V*V+U*U)))/
     $(SQRT(V*V+U*U)*LN*LT*LT)
c        write(6,*)'DDSDDR(1,2)',DDSDDR(1,2)
c
c        write(6,*)'DDSDDR(1,2)',DDSDDR(1,2)
         DDSDDR(2,1)=(TMAX*UN*UT*exp(Q1-SQRT(V*V+U*U)))/
     $(LN*LN*LT*SQRT(V*V+U*U))
c        write(6,*)'DDSDDR(2,1)',DDSDDR(2,1)
c        endif
c        write(6,*)'DDSDDR(2,1)',DDSDDR(2,1)
         DDSDDR(2,2)=TMAX*EXP(Q1-SQRT(V*V+U*U))/LT-
     $(TMAX*UT*UT*EXP(Q1-SQRT(V*V+U*U)))/(LT*LT*LT*SQRT(V*V+U*U))
     $+(ZETA*TMAX/LT/DTIME)
c
c        endif
         ELSE
c        APPLY NP2 FORMULATION
          UTEST=1.0
             k=SQRT(2.)-1.

         TN=SMAX*EXP(Q1)*(U)*EXP(-U)*EXP(-SQRT(V*V)*k)
     $+(ZETA*SMAX*DUN/(DTIME*LN))
c*EXP(-SQRT(W*W)*k)
c        write(6,*)'TN=',TN
         TT=TMAX*V*EXP(Q1)*EXP(-SQRT(V*V))*EXP(-U*k)
     $+(ZETA*TMAX*DUT/(DTIME*LT))
c*EXP(-SQRT(W*W))
c        write(6,*)'TT=',TT
c         TM=TMAX*W*EXP(Q1)*EXP(-SQRT(V*V))*EXP(-U*k)
c      $+(ZETA*TMAX*DUM/(DTIME*LT))
c  *EXP(-SQRT(W*W))
```

319

```fortran
c         write(6,*)'TM=',TM
CCCCCCCCCCCCCCCCCCCCCCCCCCCCCCCCCCCCCCCCCCCCCCCCCCCCCCCCCCCCCCCCCCCCCC
CCCCCCCC
C      jabobian
       DDSDDR(1,1)=(smax*exp(-(k*abs(UT))/abs(LT)-
     $UN/LN+1))/LN-(smax*UN*exp(-(k*abs(UT))/abs(LT)
     $-UN/LN+1))/(LN*LN)+(ZETA*SMAX/LN/DTIME)
c
c         write(6,*)'DDSDDR(1,1)',DDSDDR(1,1)
       DDSDDR(1,2)=(k*smax*UN*sign(UTEST,UT)*exp(-
     $(k*abs(UT))/abs(LT)-UN/LN+1))/(abs(LT)*LN)
c
c         write(6,*)'DDSDDR(1,2)',DDSDDR(1,2)
c                     DDSDDR(1,3)=(k*smax*UN*SIGN(UTEST,UM)*exp(-
(k*abs(UM))/abs(LT)-
c      $(k*abs(UT))/abs(LT)-UN/LN+1))/(abs(LT)*LN)
c
c         write(6,*)'third jac comp',third jac comp
       DDSDDR(2,1)=(k*tmax*UT*exp(-abs(UT)/abs(LT)-
     $(k*UN)/LN+1))/(LT*LN)
C
c         write(6,*)'DDSDDR(2,1)',DDSDDR(2,1)
c
       DDSDDR(2,2)=(tmax*exp(-abs(UT)/abs(LT)-
     $(k*UN)/LN+1))/LT-(tmax*(UT)*SIGN(UTEST,UT)*exp(-
abs(UT)/abs(LT)-
     $(k*UN)/LN+1))/(LT*abs(LT))+(ZETA*TMAX/LT/DTIME)
c
c         write(6,*)'DDSDDR(2,2)',DDSDDR(2,2)
       ENDIF
c         write(6,*)'AFTER JACOBIAN=',AFTER JACOBIAN
       STRESS(1)=TN*-1.
       STRESS(2)=TT
c      STRESS(3)=TM


       STATEV(1)=TN
       STATEV(2)=TT
       STATEV(3)=sqrt(TN*TN+TT*TT)
       STATEV(4)=UN
```

```fortran
      STATEV(5)=UT
      STATEV(6)=sqrt(UN*UN+UT*UT)
C
      write(6,*)'***********************************************
*****'
C
      RETURN
      END


C
```

E.12 3D-UINTER

```fortran
      subroutine
uinter(stress,ddsddr,flux,ddfddt,ddsddt,ddfddr,
     1      statev,sed,sfd,spd,svd,scd,pnewdt,rdisp,drdisp,
     2
temp,dtemp,predef,dpred,time,dtime,ciname,slname,msname,
     3
props,coords,aLocalDir,drot,area,chrLngth,node,ndir,nstatv,
     4      npred,nprops,mcrd,kstep,kinc,kit,linper,lOpenClose,
     5      lState,lSdi,lPrint)
c
      include 'aba_param.inc'
c
      dimension
stress(ndir),ddsddr(ndir,ndir),flux(2),ddfddt(2,2),
     $
ddsddt(ndir,2),ddfddr(2,ndir),statev(nstatv),rdisp(ndir),
     $
drdisp(ndir),temp(2),dtemp(2),predef(2,npred),dpred(2,npred),
     $
time(2),props(nprops),coords(mcrd),aLocalDir(mcrd,mcrd),
     $      drot(2,2)
      character*80 ciname,slname,msname
      REAL*8 LN,LT,k,UTEST

          Q1=1.D0
          Q0=0.0000000000000000E+00
c
          SMAX=PROPS(1)
          LN=PROPS(2)
          LT=PROPS(3)
          TMAX=PROPS(4)
          ZETA=PROPS(5)


c
      UN=RDISP(1)*-1.
      US=RDISP(2)
              UM=RDISP(3)
              UT=sqrt(US*US+UM*UM)
```

322

```
c
        DUN=DRDISP(1)*-1.
        DUS=DRDISP(2)
                DUM=DRDISP(3)
                DUT=sqrt(DUS*DUS+DUM*DUM)
c
        U=UN/LN
c        write(6,*)'UN=',UN
c      write(6,*)'u=',u
        V=UT/LT

        UTEST=1.0
          k=SQRT(2.)-1.

                if (ut.ne.0.0000000000000000E+00)then

        TN=SMAX*EXP(Q1)*(U)*EXP(-U)*EXP(-SQRT(V*V)*k)
     $+(ZETA*SMAX*DUN/(DTIME*LN))

        TT=TMAX*V*EXP(Q1)*EXP(-SQRT(V*V))*EXP(-U*k)
     $+(ZETA*TMAX*DUT/(DTIME*LT))
        TS=TT*(US/UT)
        TM=TT*(UM/UT)




CCCCCCCCCCCCCCCCCCCCCCCCCCCCCCCCCCCCCCCCCCCCCCCCCCCCCCCCCCCCCCCCCCCCC
CCCCCCCC
C     jabobian
c                xDDSDDR(1,1)
c
     DTNDUN=(smax*exp(-(k*abs(UT))/abs(LT)-
     $UN/LN+1))/LN-(smax*UN*exp(-(k*abs(UT))/abs(LT)
     $-UN/LN+1))/(LN*LN)+(ZETA*SMAX/LN/DTIME)
c                DTNDUN=DTNDUN
c
c                xDDSDDR(1,2)
c
```

```fortran
      DTNDUT=(k*smax*UN*sign(UTEST,UT)*exp(-
     $(k*abs(UT))/abs(LT)-UN/LN+1))/(abs(LT)*LN)


C                 xDDSDDR(2,1)
C
      DTTDUN=(k*tmax*UT*exp(-abs(UT)/abs(LT)-
     $(k*UN)/LN+1))/(LT*LN)
C
C                     xDDSDDR(2,2)
C
      DTTDUT=(tmax*exp(-abs(UT)/abs(LT)-
     $(k*UN)/LN+1))/LT-(tmax*(UT)*SIGN(UTEST,UT)*exp(-
abs(UT)/abs(LT)-
     $(k*UN)/LN+1))/(LT*abs(LT))+(ZETA*TMAX/LT/DTIME)
C
C
C22
                        DTSDUS1=((US/UT)*(US/UT))*DTTDUT
                        DTSDUS2=(((UT*UT)-(US*US))/(UT*UT*UT))*TT
                        DTSDUS=(DTSDUS1+DTSDUS2)
C
C33
                        DTMDUM1=((UM/UT)*(UM/UT))*DTTDUT
                        DTMDUM2=(((UT*UT)-(UM*UM))/(UT*UT*UT))*TT
                        DTMDUM=(DTMDUM1+DTMDUM2)
C
C23
                        DTSDUM1=((US/UT)*(UM/UT))*DTTDUT
                        DTSDUM2=((-(US*UM))/(UT*UT*UT))*TT
                        DTSDUM=(DTSDUM1+DTSDUM2)
C
C32
                        DTMDUS1=((US/UT)*(UM/UT))*DTTDUT
                        DTMDUS2=((-(US*UM))/(UT*UT*UT))*TT
                        DTMDUS=(DTMDUS1+DTMDUS2)
C
C12
                        DTNDUS=(US/UT)*DTNDUT
C13
```

324

```fortran
                              DTNDUM=(UM/UT)*DTNDUT
C21
                              DTSDUN=(US/UT)*DTNDUT
C31
                              DTMDUN=(UM/UT)*DTNDUT

                        else
C
                        TN=0.D0
                        TS=0.D0
                        TM=0.D0
C
                        DTNDUN=0.d0
                        DTNDUS=0.d0
                        DTNDUM=0.d0
                        DTSDUN=0.d0
                        DTSDUS=0.d0
                        DTSDUM=0.d0
                        DTMDUN=0.d0
                        DTMDUS=0.d0
                        DTMDUM=0.d0
C
C
                        endif
C
                        DDSDDR(1,1)=DTNDUN
                        DDSDDR(1,2)=DTNDUS
                        DDSDDR(1,3)=DTNDUM
                        DDSDDR(2,1)=DTSDUN
                        DDSDDR(2,2)=DTSDUS
                        DDSDDR(2,3)=DTSDUM
                        DDSDDR(3,1)=DTMDUN
                        DDSDDR(3,2)=DTMDUS
                        DDSDDR(3,3)=DTMDUM

                        STRESS(1)=TN*-1.
                        STRESS(2)=TS
                        STRESS(3)=TM
```

325

```fortran
      STATEV(1)=TN
      STATEV(2)=TS
      STATEV(3)=TM
      STATEV(4)=TT
      STATEV(5)=SQRT(TN*TN+TT*TT)
      STATEV(6)=UN
      STATEV(7)=US
      STATEV(8)=UM
      STATEV(9)=UT
      STATEV(10)=SQRT(UN*UN+UT*UT)
C

      RETURN
      END
```